MOBILIZATION AND NATURAL ATTENUATION OF ARSENIC IN ACID MINE DRAINAGE (AMD)

PhD Thesis

Department of Geotechnical Engineering and Geo-Sciences (ETCG)
Technical University of Catalonia (UPC)

María Pilar Asta Andrés

Supervisor: Dr. Jordi Cama i Robert

Institute of Environmental Assessment and Water Research (IDAEA), CSIC

March, 2009

This thesis has been funded by the Spanish Government with a FPI grant, contract REN 2003-09590-C04-02: “Drenaje ácido de mina: Prevención, atenuación natural y tratamiento pasivo”. The research of this thesis was developed mainly in the Institute of Earth Sciences “*Jaume Almera*”-CSIC.

A mi madre y a mi hermano.

A J.P.

Abstract

Acid mine drainage (AMD) generated by sulfide oxidative dissolution is a major cause of water contamination world-wide. Arsenic is one of the main AMD pollutants whose concentration can reach up to hundreds of mg L^{-1}, i.e. 5-6 orders of magnitude higher than the limit of 10 μg L^{-1} for potable water established by the European Union in 1998. This thesis is concerned with the impact of arsenic mobilization along AMD discharges.

Oxidation of As-bearing sulfides such as arsenopyrite (AsFeS), As-rich pyrite (FeS_2) or marcasite (FeS_2) is one of the main sources of arsenic release. The first part of this thesis is focused on the dissolution kinetics of arsenopyrite and marcasite at acidic to neutral pH using long term flow-through experiments. The effects of pH, dissolved oxygen and temperature on their dissolution were assessed. The respective dissolution rate laws were proposed on the basis of the steady-state rates, taking into consideration the slight pH effect and the strong dissolved oxygen effect on dissolution. The incorporation of these rate laws into the kinetic databases of geochemical and reactive transport codes allows us to obtain better realistic simulations.

The environmental impact of released arsenic into waters depends on its natural attenuation. The arsenic oxidation state is considered given that the main process that controls the fate and mobility of aqueous arsenic is arsenate sorption onto precipitated Fe-phases. The second part of the thesis discusses arsenic oxidation and arsenic sorption.

Oxidation was studied by means of batch experiments under abiotic and biotic conditions at typical AMD water pH and water composition. Simultaneous oxidation of Fe(II) to Fe(III) and arsenite to arsenate occurs under biotic conditions, the former mediated by bacteria, and the latter by the presence of Fe(III). Under abiotic conditions, oxidation of arsenite to arsenate in the presence of Fe(III) is slow, but is enhanced by increasing dissolved Fe(III) and chloride concentrations in the presence of light. Arsenic sorption at AMD sites, and hence arsenic attenuation, occurs via arsenate sorption on new iron-oxyhydroxide and iron-oxyhydroxide-sulphate precipitates (mainly, schwertmannite ($Fe_8O_8(OH)_{5.5}(SO_4)_{1.25}$), jarosite ($KFe_3(SO_4)_2(OH)_6$) and goethite (FeOOH)). The sorption capacity of goethite and jarosite was studied and compared with the one reported for schwertmannite. To this end, batch experiments were conducted using synthetic powders of K-jarosite and goethite at highly acidic pH. In the absence of competitive effects of other anions, K-jarosite presented better removal efficiency for arsenate, and ionic strength and pH had little effect on the sorption capacity of the two minerals. In contrast, these sorption capacities diminished considerably in the presence of sulfate, which is the main anion in AMD waters.

A deeper understanding of the dominant mechanisms controlling arsenic content in waters demands the study of the processes not only under laboratory but also under natural conditions. Accordingly, the third part of this thesis deals with the arsenic attenuation processes in a natural system. To this end, the acidic water and sediments of the abandoned Tinto Santa Rosa mine discharge, located in the Iberian Pyritic Belt, were studied. The most striking feature of the water was a pH decrease accompanied by a systematic decrease in ferrous iron, total iron, arsenite, arsenate and total arsenic concentration. Additionally, bed-stream sediments showed high arsenic contents. The main processes that control the fate and mobility of arsenic in waters in the field were iron and arsenic oxidation, precipitation of Fe(III)-minerals and sorption of As(V) onto them. A 1-D reactive transport model using the PHREEQC code was used to explain and quantify the aforementioned processes that had been studied previously under laboratory conditions.

Resumen

El drenaje de aguas ácidas de mina generado a partir de la oxidación de sulfuros metálicos es una de las principales causas de contaminación del agua a nivel mundial. De entre los principales contaminantes asociados a estos drenajes, el arsénico es uno de los más importantes, pudiendo alcanzar concentraciones de hasta cientos de mg L^{-1}. Estos valores superan en 5-6 órdenes de magnitud el valor máximo establecido de 10 μg L^{-1} por la Unión Europea en 1998 para las aguas potables. En esta tesis, se estudia la movilidad del arsénico asociado a estos drenajes ácidos de mina y su impacto medioambiental.

Una de las principales fuentes de arsénico en las aguas es la oxidación de sulfuros ricos en As, como son la arsenopirita (AsFeS), la pirita rica en arsénico (FeS_2) o la marcasita (FeS_2). En la primera parte de esta tesis, se ha estudiado la cinética de disolución de arsenopirita y marcasita mediante experimentos de flujo continuo de larga duración. Con esta metodología, la influencia del pH, del oxígeno disuelto y de la temperatura han sido examinados. Asimismo, se han propuesto leyes de velocidad que contemplan el leve efecto que ejerce el pH y la gran influencia del oxígeno en las velocidades de disolución de ambos minerales. Las leyes de disolución obtenidas pueden ser incorporadas en códigos de transporte reactivo, permitiendo obtener cálculos y predicciones más realistas.

Una vez liberado, el impacto medioambiental del arsénico depende de su atenuación natural. En este sentido, el principal proceso que controla la movilidad del arsénico acuoso es la adsorción. Debido a la gran influencia que ejerce el estado de oxidación del arsénico en la adsorción éste es un factor clave a considerar. En la segunda parte de la tesis, los procesos de adsorción y oxidación del arsénico han sido investigados. La oxidación ha sido estudiada mediante experimentos de tipo "*batch*" en condiciones abióticas y bióticas, en aguas con pH y composición similares a las encontradas en los medios naturales afectados por el drenaje ácido de mina. Según los resultados obtenidos, en condiciones bióticas el As(III) es oxidado abióticamente por el Fe(III) generado simultáneamente por oxidación catalizada por bacterias. Aunque la oxidación de As(III) a As(V) por el hierro es muy lenta, el proceso se acelera cuando se incrementa la concentración de Fe(III) o la de cloro en presencia de luz.

La adsorción del arsénico en los drenajes ácidos, y por tanto su atenuación, tiene lugar por la adsorción de As(V) en los nuevos oxihidroxidos e oxihidroxisulfatos de hierro que se forman en este tipo de medios, como la schwertmanita ($Fe_8O_8(OH)_{5.5}(SO_4)_{1.25}$), la goetita (FeOOH) o la jarosita ($KFe_3(SO_4)_2(OH)_6$). La capacidad de adsorción de la goetita y jarosita han sido examinadas y comparadas con las obtenidas previamente por otros autores para la schwertmanita. Con tal objetivo, se han realizado experimentos tipo *batch* con goetita y jarosita sintética en condiciones de pH muy ácido. En ausencia de los efectos competitivos de otros aniones, la jarosita potásica presenta mayor eficiencia en la remoción del arsenato de la solución. Por otro lado, se ha observado que el pH y la fuerza iónica no ejercen apenas influencia en el proceso de adsorción del arsenato en ambos minerales. Sin embargo, la presencia de sulfato, principal anión en las aguas ácidas de mina, provoca una importante disminución en las capacidades de adsorción.

Un conocimiento completo de los mecanismos dominantes que controlan el arsénico en las aguas requiere del estudio de los procesos involucrados, no sólo bajo condiciones de laboratorio, sino también en condiciones naturales. Por tanto, la tercera parte de esta

tesis se ha centrado en el estudio de los procesos de atenuación natural que tienen lugar en un sistema natural. Con este objetivo, se han estudiado tanto el agua como los sedimentos de la descarga ácida de la mina abandonada de Tinto Santa Rosa (situada en la Faja Pirítica Ibérica). Las principales características observadas en el sistema natural son una disminución del pH, acompañada de un decrecimiento sistemático en el Fe(II), en el hierro total, en el As(III), en el As(V) y en el arsénico total. Adicionalmente, se ha observado que los sedimentos del fondo del arroyo presentan elevadas concentraciones de arsénico. Según las características del sistema, los principales procesos que controlan la movilidad del arsénico en las aguas de campo estudiadas son la oxidación del hierro y del arsénico, la precipitación de minerales de Fe(III) y la adsorción del As(V) en estos minerales. Un modelo de transporte reactivo 1-D, realizado mediante el código de modelización geoquímica PHREEQC, se empleó para explicar y cuantificar los procesos previamente mencionados y que habían sido anteriormente estudiados en condiciones de laboratorio.

Resum

L'anomenat drenatge àcid de mina (AMD) ve generat per l'oxidació de sulfurs i és causa major de contaminació d'aigües a nivell mundial. L'arsènic és un del principals contaminants la concentració del qual pot assolir centenars de mgL^{-1}, és a dir, de 5 a 6 ordres de magnitud més gran que el límit de potabilitat per a l'aigua ($10\mu g\ L^{-1}$) establert per la UE en 1998. En aquesta tesi, s'estudia l'impacte de la mobilització de l'arsènic al llarg de descàrregues de drenatge àcid de mina.

L'oxidació de sulfurs que contenen arsènic (tal com l'arsenopirita (AsFeS), la pirita rica en arsènic (FeS_2) o la marcassita (FeS_2) és una de les principals fonts d'alliberament d'arsènic a l'aigua. En la primera part de la tesi, s'ha estudiat la cinètica de dissolució de l'arsenopirita i de la marcassita a pHs àcids i neutre, utilitzant reactors de flux continu, i s'han valorat els efectes del pH, de l'oxigen dissolt i de la temperatura en la dissolució d'ambdós sulfurs. A partir de les velocitats en estat estacionari establertes, es proposen les respectives lleis de dissolució que tenen en compte el lleu i el fort efecte del pH i de l'oxigen dissolt, respectivament, en llur dissolució. La incorporació d'aquestes lleis cinètiques en les bases de dades del codis geoquímics i de transport reactitu permeten fer prediccions molt més realistes.

L'impacte mediambiental causat per l'arsènic alliberat a les aigües depèn de la seva atenuació natural. El principal procés que controla el destí i la mobilitat de l'arsènic aquós

és l'adsorció de l'arsenat en fases de ferro precipitades. Per tant, cal tenir en compte el paper que juga l'estat d'oxidació de l'arsènic. En la segona part de la tesi, shan estudiat tant l'oxidació de l'arsènic com l'adsorció de l'arsènic. L'oxidació s'estudia en condicions abiòtiques i biòtiques a pH i composició típics d'aigües àcides de mina, fent servir experiments de tipus *batch*. S'hi mostra com en condicions biòtiques tenen lloc simultàniament l'oxidació de Fe(II) a Fe (III) i d'arsenit a arsenat, de manera que mentre els bacteris governen la primera, el contingut de Fe(III) domina la segona. En condicions abiòtiques, l'oxidació d'arsenit a arsenat en presència de Fe(III) és lenta, tot i que augmenta augmentant la presència de Fe(III) i de clorur amb llum de dia.

L'adsorció d'arsènic en llocs d'AMD, i per tant l'atenuació d'arsènic, ocorre mitjançant l'adsorció d'arsenat en precipitats formats per oxi-hidròxids i oxi-hidròxid-sulfats de ferro (principalment schwertmannita ($Fe_8O_8(OH)_{5.5}(SO_4)_{1.25}$), K-jarosita ($KFe_3(SO_4)_2(OH)_6$) i goetita (FeOOH)). S'han estudiat les capacitats d'adsorció de la jarosita i de la goetita i s'han comparat amb la de la schwertmannita. Amb aquest propòsit es van fer experiments de tipus *batch* a pH molt àcid i amb mostres sintetitzades de K-jarosita i de goetita. Sense la competència d'altres anions, la capacitat de la jarosita per eliminar arsenat és més alta que la de la goetita. També s'ha vist que la força iònica té un escàs efecte en l'adsorció d'ambdós minerals, però que la presència de sulfat, que és l'anió més abundant en aigües àcides de mina, minva llurs capacitas d'adsorció.

Cal conèixer bé els mecanismes dominants que controlen el contingut d'arsènic en les aigües, no només en condicions de laboratori, sinó també en les condicions de camp. Per tant, en la tercera part de la tesi s'han estudiat el processos d'atenuació de l'arsènic en un sistema natural. Amb aquest objetiu s'han caracterizat exhaustivament l'aigua i els sediments del rierol provinent de la mina abandonada Tinto Santa Rosa, situada a la Faixa Pirítica Ibèrica (IPB). La característica dominant de l'aigua del rierol és un descens del pH aigües avall que va acompanyat d'un decreixement sistemàtic de les concentracions de ferro ferrós i de ferro total, d'arsenit i d'arsenat, així com d'arsènic total. A més a més, els sediments de llit mostren contiguts alts d'arsènic. Els principals

mecanismes que dominen el destí i la mobilitat de l'arsènic en aquestes aigües de camp són l'oxidació del ferro i de l'arsènic i la precipitatió de compostos de Fe(III) que adsorbeixen l'arsenat. S'ha proposat un model unidimensional de trasnport reactiu, utilitzant el codi PHREEQC, per explicar i quantificar els processos mencionats que han estat estudiats en condicions de laboratori.

Agradecimientos

Estos últimos años han sido para mí unos de los más importantes, intensos y fascinantes de toda mi vida. Durante este tiempo he tenido la enorme suerte y la oportunidad de conocer a gente excelente que me ha ayudado desinteresadamente dando lo mejor de sí mismos para que este trabajo pudiese llegar a su fin. Quiero dedicar unas palabras de agradecimiento a todas estas personas, que de manera directa o indirecta, han contribuido en este trabajo.

En primer lugar quiero agradecer a mi director de tesis, el Dr. Jordi Cama el haber confiado en mí para desarrollar este trabajo y el haberme dado la oportunidad de trabajar en este grupo. Quiero también darle las gracias por sus revisiones y comentarios durante la realización de la tesis. Asimismo, quiero agradecer al Dr. Carlos Ayora sus aportes, críticas, comentarios y sugerencias durante el desarrollo de esta investigación.

A la Dra. Gabriela Román-Ross quiero agradecerle, no sólo el haberme dado la oportunidad de emplear y aprender junto a ella la técnica del XAFS, sino el haber estado siempre dispuesta a corregirme un capítulo de la tesis o darme un consejo, además quiero agradecerle su amabilidad y sus palabras de ánimo durante algunos de los momentos más críticos del desarrollo de esta tesis.

Estoy enormemente agradecida al Dr. Kirk Nordstrom y a Blaine McClesckey por todo su apoyo, ayuda y hospitalidad durante mi estancia en Boulder. Gracias por darme la oportunidad de vivir una experiencia inolvidable como fue la de Yellowstone, por enseñarme muchísimas cosas y transmitirme vuestra pasión por la geoquímica, y también por apreciarme y valorarme. Muchísimas gracias a los dos.

Quiero agradecer a Javier Giménez y María Martínez de Ingeniería Química de la UPC su gran ayuda con la parte de adsorción, su amabilidad y disponibilidad y también todos sus consejos, revisiones y explicaciones.

Quiero dar las gracias a los técnicos de los Serveis Cientificotècnics de la Universidad de Barcelona (Eva Prats, Ana Dominguez, Lorenzo Calvo, Eva Pelegrí, Toni Padró, Xavi Llovet, Joan Gamez) y a los del instituto *"Jaume Almera*" (Josep Elvira, Mercé Cabañas, Rafael Bartrolí, Silvia Rico y Sandra Toro) a los que he estado dando la lata a lo largo de estos años y a los que debo gran parte del trabajo de esta tesis.

Estoy muy agradecida al Dr. Ignasi Queralt del Instituto "*Jaume Almera"* por su ayuda con la fluorescencia, al Dr. Andrew Gault y al Dr. John M. Charnock por su colaboración con el EXAFS y también a la Dra. María José Ruiz, siempre dispuesta a echarme una mano con los análisis aún estando en la fase final de su tesis. Asimismo, quiero dar las gracias al Dr. Antoni Roig de la Universidad "*Jaume I*" de Castellón por su amabilidad y su ayuda con los análisis de especiación de arsénico y al Dr. Javier Sánchez-España del IGME por tomar y enviarme las muestras con las que trabajé en Boulder. Quiero agradecer también a Araceli Garrido sus consejos y explicaciones durante la toma de contacto con las isotermas de adsorción.

Quiero dar las gracias a mis amigos y compañeros del grupo de hidrogeoquímica del instituto "*Jaume Almera*", a Patricia, Tobías, Clara, José Luis Mogollón, Esteban, Marco Boi, Arantxa, Francesco, Esther y Ana por la asistencia en las tareas de laboratorio, por acompañarme al campo, por los buenos consejos, por los ánimos y porque muchas cosas de las que he aprendido a lo largo de todos estos años han sido, sin duda, gracias a vosotros. En este sentido quiero resaltar la ayuda de Patricia y Tobias, ya que gracias a sus consejos, explicaciones, revisiones y sugerencias, he conseguido por fin, finalizar esta tesis. A todos ellos les agradezco esos momentos de reunión, risas y terapias de grupo en el bar de geo. Quiero agradecer también a Javier Pérez y en especial a Vanessa Ouro toda su ayuda en el laboratorio porque, aunque he pasado muchas y largas horas en ese recinto del sótano, seguro hubieran sido muchas más sin su ayuda.

Siempre estaré en deuda con mis compañeros de la Universidad de Huelva: Manu, Awi, José Miguel y Rafa siempre dispuestos a acompañarme y ayudarme durante las campañas de campo, a enviarme unas muestras o a resolver todas mis dudas. También a Daniel Sánchez Rodas por sus explicaciones sobre la especiación de arsénico y por solucionarme vía mail todas mis incertidumbres sobre este tema.

A Maria José Gimeno y Luis Auqué con quienes comencé mis andanzas por el mundo de la investigación y que han estado ahí siempre para escucharme, aconsejarme, ayudarme y animarme. Gracias, os debo un montón!

Quiero agradecer a mis compañeros de despacho (Jorge, Isaac, Miguel, Maricruz, Marco, Cris, Michael...) esos raticos de risas y de desahogo tan necesarios para seguir adelante.

Estoy muy agradecida a la gente tan maravillosa que conocí durante mis estancias en USA (María Guedez e Iñaki, María Rovira y David, Rosa e Ignacio, Grace y Juan, Oscar y *mi* Gis, Sarah, Karen y Sandrine) con la que compartí momentos inolvidables y me hicieron sentir como en casa aún a miles de Km. de mi hogar.

Muchísimas gracias a mis amigos del "*ghetto de geólogos maños y agregados*" Vicent, Sara, Clara, Ángel, María, Nuria, Pili, Miriam, Fabio, Juanmi, Manolo, Cris, Patricia, Iván, Raquel, Laura, Antonio y Ruth, menos mal que habéis estado aquí conmigo todo este tiempo. Os voy a echar muchísimo de menos!

A mis amigos de Zaragoza, Vivi y Javi, Esther, Rakel y Fer, Rocío, Jorge, Angelito y Manu, Gemi y Diego, Marina y Juan, Vir, Cris, Coral y Rosana por haber estado ahí siempre que os he necesitado, por vuestro cariño y vuestro apoyo.

Mis últimos agradecimientos, no por ello menos importantes, son para mi familia por todo su apoyo y comprensión y en especial a mi madre, el haber logrado finalizar esta tesis también es fruto de su trabajo de muchos años.

Y finalmente, gracias J.P., por haber compartido conmigo todos estos años, por toda tu ayuda, apoyo, comprensión y ánimos. Jamás lo hubiera logrado sin ti.

Table of contents

List of figures

List of Tables

Chapter 1

Introduction

Oxidation of pyrite and other minor sulfides is the major contributor of hydrogen ions in mine waters. The purely natural process of "Acid Rock Drainage" (ARD) is often intensified by human activities related to mining and mineral processing (Acid Mine Drainage or AMD). Oxidation of sulfide minerals not only creates acidity but it also releases metals and sulfate into waters giving rise to a major environmental issue. These polluting discharges can persist during long periods once the mining activity is over (Strömberg and Banwart, 1994). AMD is therefore considered to be one of the main causes of contamination of hydrological resources (Nordstrom and Alpers, 1999).

AMD is mainly generated by oxidation of pyrite (FeS_2), which is the most common sulfide mineral, and by other sulfides in the presence of water and oxygen (e.g. Stumm and Morgan, 1996). Pyrite dissolution can be expressed as:

$$FeS_2 + H_2O + 3.5O_2 \Rightarrow Fe^{2+} + 2SO_4^{2-} + 2H^+ \quad (1.1)$$

During dissolution, pyrite reacts with dissolved oxygen and water to produce ferrous iron, sulfate and acidity. If there is enough oxygen in the system the ferrous iron released by pyrite dissolution is oxidized to ferric iron according to the following reaction:

$$Fe^{2+} + 0.25O_2 + H^+ \Rightarrow Fe^{3+} + 0.5H_2O \quad (1.2)$$

This reaction has been termed the "rate determining" step for the overall sequence because it is very slow at low pH (< 4) (Singer and Stumm, 1970). However, the presence of catalytic microorganisms can increase the rate of iron oxidation by several orders of magnitude (Nordstrom and Southam, 1997; Schrenk *et al.*, 1998). The ferric iron generated could precipitate as iron hydroxides and other Fe(III) compounds, producing more acidity according to the reaction:

$$Fe^{3+} + 3H_2O \Rightarrow Fe(OH)_3 + 3H^+ \quad (1.3)$$

in addition, Fe^{3+} dissolves pyrite producing more acidity, sulfate and Fe^{2+} according to the reaction:

$$FeS_2 + 14Fe^{3+} + 8H_2O \Rightarrow 15Fe^{2+} + 2SO_4^{2-} + 16H^+ \quad (1.4)$$

At very low pH in some acid mine drainages, high concentrations of a wide range of solutes are found, including arsenic and iron. Arsenic concentrations in these drainages can be as high as hundreds of mg L^{-1}. Arsenopyrite (FeAsS) is the dominant arsenic mineral in most As-bearing natural occurrences and therefore most responsible for elevated arsenic concentrations at surface sites (Smedley *et al.*, 1996). Likewise, oxidation of other As-bearing sulfides, such as pyrite and marcasite, can release high arsenic concentrations, since arsenic is present in their respective structures in the ranges of 100-77000 mg kg^{-1} and 20-126000 mg kg^{-1} (Smedley and Kinniburgh. 2002).

The Iberian Pyritic Belt (IPB) is one of the largest massive sulfide provinces on the planet, whose original reserves were in the order of 1700 million tonnes (Sáez *et al.* 1999). Centuries of extraction and exploitation have left kilometers of galleries, numerous pits, waste dumps and mine waste (e.g. tailings) where oxidation of sulfides occurs. As a result, the area is totally degraded and the Tinto and Odiel rivers are currently two of the most polluted rivers in Spain (Olías *et al.*, 2004; Sarmiento *et al.*, 2006; Nieto *et al.*, 2007; Sarmiento *et al.*, 2009) owing to the longevity of the contamination processes of AMD (Younger, 1997). In these massive sulfide deposits, arsenic can be found in arsenical pyrite (with up to 0.4% of As), and in some accessory minerals such as arsenopyrite and marcasite. Despite the large amounts of these sulfides in the IPB and despite the high arsenic release due to their oxidation, aqueous arsenic is naturally attenuated in rivers and streams impacted by AMD.

The aim of the present thesis is to study the arsenic cycle in AMD waters in the context of sulfide mining (e.g. Iberian Piritic Belt) in an attempt to improve predictability of arsenic behaviour. Accordingly, the following processes were studied: (i) the sulfide oxidation process that governs the arsenic release to water and (ii) the natural processes involved in the removal of arsenic in AMD streams under laboratory and field conditions.

The first part of the thesis deals with the dissolution of arsenopyrite and marcasite given that this dissolution releases arsenic to AMD waters. Owing to the importance of pyrite in the formation of acid mine drainage, pyrite dissolution kinetics has received a great deal of attention (Smith and Schumate, 1970; Wiersma and Rimstidt, 1984; McKibben and Barnes, 1986; Nicholson *et al.*, 1988; Moses and Herman, 1991; Williamson and Rimstidt, 1994; Domènech *et al.*, 2002; Descostes *et al.*, 2004; Pérez-López *et al.*, 2007). Arsenopyrite dissolution has also been studied. The effects of temperature, Fe^{3+} concentration, the presence of bacteria (*Acidithiobacillus ferrooxidans*), pH and of particle size on the oxidative dissolution of arsenopyrite have been reported, either in relation to aqueous chemistry studies (Gagen, 1987; Breed *et al.*, 1997; Ruitenberg *et al.*, 1999;

McGuire *et al.*, 2001; Craw *et al.*, 2003; Yu *et al.* 2004; Tallant and McKibben, 2005, Walker *et al.*, 2006, Yu *et al.* 2007 and McKibben *et al.*, 2008) or to arsenopyrite surface spectroscopy research, mainly by X-ray Photoelectron Spectroscopy (XPS) (Buckley and Walker, 1988; Richardson and Vaughan, 1989; Nesbitt *et al.*, 1995; Nesbitt and Muir, 1998; Hacquard *et al.*, 1999, and Mikhlin *et al.*, 2006). Fewer studies have focused on marcasite dissolution. Mathews and Robins (1972, 1974); Wiersma (1982) and Wiersma and Rimstidt (1984) studied the oxidation of mixtures of pyrite and marcasite. Most recently, Rimstidt and Vaughan (2003) studied the differences in reactivity of pyrite and marcasite. In addition, several X-ray Photoelectron Spectroscopy (XPS) studies have focused on the evolution of marcasite surfaces during oxidation (Rinker *et al.* 1997; Pratt *et al.* 1998; Uhlig *et al.* 2001; Elsetinow *et al.*, 2003; Harmer and Nesbitt, 2004).

However, these data on arsenopyrite and marcasite dissolution are of limited use when the long-term dissolution of arsenopyrite and marcasite is to be considered in wider ranges of pH, temperature and dissolved oxygen content.

Accordingly, the first objective of this thesis is to study the dissolution kinetics of arsenopyrite and marcasite by assessing the effects that the AMD environmental factors (pH, dissolved oxygen and temperature) have on arsenic release in the long-term. Thus, dissolution rate laws are proposed to quantify the arsenic release in the AMD impacted areas. Likewise, the dissolution of arsenopyrite and marcasite was studied at pH higher than the typical ones in AMD in an effort to gain a greater understanding of the treatment systems.

The second part of the thesis discusses the natural attenuation of arsenic released from its source and the physical, chemical and biological processes that are responsible for arsenic mitigation.

The natural attenuation of arsenic in AMD areas takes place as the formation of new precipitates, such as schwertmannite ($Fe_8O_8(OH)_{5.5}(SO_4)_{1.25}$), jarosite ($KFe_3(SO_4)_2(OH)_6$), and goethite (FeOOH), effectively sorb As(V), reducing the arsenic content in waters

(Fukushi, *et al.* 2003a; Sánchez-España *et al.* 2005a; Gault *et al.*, 2005; Acero *et al.*, 2006; Lee and Chon, 2006). In fact, these iron phases play an important role in the removal of trace elements from solution by adsorption and co-precipitation (Benjamin, 1983; Johnson, 1986; Stumm and Sulzberger, 1992; Bigham *et al.*, 1994; Webster *et al.*, 1998).

Schwertmannite sorption has been the subject of a large number of works given the capacity of this mineral to sorb trace metals (Fukushi *et al.*, 2003b; Fukushi *et al.*, 2004; Regenspurg and Peiffer, 2005). Sorption of arsenic on goethite has also been studied by Grossl and Sparks (1995), Matis *et al.* (1997), Dixit and Hering (2003), Lehmann *et al.* (2005), and Giménez *et al.* (2007) among others. Studies of arsenic sorption onto jarosite are less abundant, and jarosite sorption capacity remains unknown.

Natural arsenic attenuation depends on the arsenic oxidation state; As(V) is sorbed more strongly than As(III) to Fe(III) oxides and hydroxides at acid pH (Hsia *et al.*, 1992; Bowell, 1994; Wilkie and Hering, 1996). Although As(III) is primarily released by dissolution of arsenopyrite (Yu *et al.*, 2007; Cama *et al.*, 2008), the presence of high concentrations of Fe and As-oxidizing bacteria in AMD environments appear to oxidize As(III) to As(V) rapidly (Cherry *et al.*, 1979; Wakao *et al.*, 1988, Emett and Khoe, 2001; Hug *et al.*, 2001; Bednar *et al.*, 2002; Leblanc *et al.*, 2002; Bruneel *et al.*, 2003), favoring arsenic sorption onto the iron precipitates. Hence, changes in the iron oxidation state play a central role in arsenic mobilization in these aqueous systems since ferrous iron oxidation facilitates the formation of Fe(III) precipitates, and arsenite oxidation favors arsenate sorption onto these Fe(III) precipitates.

Currently, there are few data on the simultaneous oxidation of iron and arsenic in pH and water chemistry conditions similar to those of acid mine drainage. Likewise, arsenic sorption processes at very low pH (e.g. pH < 3) are poorly documented. In an attempt to better understand and predict arsenic behaviour in streams and rivers impacted by AMD, the oxidation of iron and arsenic and the arsenate sorption in these precipitates were studied. Therefore, the second objective of this thesis is to characterize the main processes involved in natural attenuation of arsenic: iron and arsenic oxidation

and arsenic sorption onto Fe(III) precipitates under laboratory conditions that emulate AMD field conditions.

The last part of the thesis is focused on arsenic mobilization in the acidic discharge of the abandoned Tinto Santa Rosa mine in the Iberian Pyritic Belt (SW, Spain). The arsenic behavior is modeled using the quantified parameters involved in the distinct arsenic related processes that were studied under laboratory conditions.

1.1 Thesis outline

This thesis is composed of seven chapters including the introduction. All the chapters are based on published papers or manuscripts that are currently in preparation for publication or under review by international peer-reviewed journals. The thesis is divided into three parts. Each part corresponds to one of the aforementioned objectives.

Part I (Chapter 2) deals with quantification of arsenic release, yielding arsenopyrite and marcasite dissolution rate laws. The effect of pH, dissolved oxygen and temperature on the long-term dissolution rates is studied by means of flow-through experiments. The evolution of the reacting surfaces is discussed.

Part II (Chapters 3 and 4) is devoted to the processes involved in natural attenuation of arsenic. Chapter 3 describes the simultaneous oxidation of As(III) and Fe(II) and As(III) oxidation by Fe(III) under laboratory conditions similar to those found in AMD waters. In chapter 4, the arsenate sorption onto goethite and jarosite is compared with the sorption capacity of schwertmannite.

Part III (Chapters 5 and 6) addresses the third objective of the thesis: a field study and modeling of the processes involved in the natural attenuation of arsenic in the Tinto Santa Rosa acid discharge in the Iberian Pyritic Belt (SW, Spain). The chemistry of waters and sediments of the stream is discussed. Chapter 6 describes the geochemical model of

the discharge using the PHREEQC code. The processes involved in the arsenic mitigation observed in the field are quantified.

Chapter 7 provides a summary of the main contributions of this thesis.

Part I

Sulfide dissolution

Chapter 2

Dissolution kinetics of arsenopyrite and marcasite

Inorganic aqueous arsenic release is an environmental and human health concern world-wide (Ferguson, 1990; Aposhian *et al.*, 2004; Rosman *et al.* 2004; Bunnell *et al.*, 2007). Elevated levels of arsenic have been found in natural waters in many areas around the world (Nordstrom, 2002; Smedley and Kinniburgh, 2002).

Arsenopyrite is the dominant arsenic mineral in most As-bearing natural occurrences and therefore the main responsible for elevated arsenic concentrations at surface sites (Smedley *et al.*, 1996). Nonetheless, the oxidation of other sulfides, such as pyrite and marcasite, could release high arsenic concentrations because arsenic could be present in their structures in the ranges of 100-77000 mg kg^{-1} and 20-126000 mg kg^{-1} for pyrite and marcasite, respectively (Smedley and Kinniburgh, 2002).

Very high concentrations of arsenic (even hundreds of mg L^{-1}) could be found in acid mine drainage (AMD) and acid rock drainage (ARD) as a result of the weathering of As-bearing sulfides (Nodstrom and Alpers, 1999; Lazareva *et al.*, 2002; Casiot *et al.*, 2003a; Frau and Ardau, 2003; Casiot *et al.*, 2005; Lee *et al.*, 2005; Lee and Chon, 2006; Pfeifer *et al.*,

2007). An important case of arsenic mobilization related to AMD is the Iberian Pyrite Belt (IPB) in the SW of Spain and S of Portugal, which is one of the most important massive sulfide provinces in the world. This region contains a large number of abandoned sulfide mines, open pits, galleries, tailings and sulfide-sludge ponds that generate creeks with acidic water with high levels of arsenic that reach up to 40 mg L^{-1} (Sánchez-España *et al.*, 2005b; Sánchez-Rodas *et al.*, 2005; Sarmiento *et al.*, 2005; Acero *et al.*, 2006; Asta *et al.*, 2007; Sarmiento *et al.*, 2007; Asta *et al.*, 2008a). Dissolved oxygen promotes dissolution of arsenopyrite (AsFeS) and arsenical pyrite ($Fe(As,S)_2$) with the consequent As release into run-off water (Williams, 2001; Lazareva *et al.*, 2002; Smedley and Kinniburgh, 2002; Casiot *et al.*, 2003a; Frau and Ardau, 2003; Welch and Stollenwerk, 2003; Lee *et al.*, 2005; Pfeifer *et al.*, 2007). Other examples of arsenic contaminated groundwaters are probably attributed to oxidation of arsenopyrite and As-bearing sulfides in non acidic waters at pH ranging from 7-9 in the Madrid Tertiary detrital aquifer (central Spain) (Hernández-García and Custodio, 2004) or in groundwater with near neutral pH at Ester dome (Fairbanks, Alaska), where dissolved arsenic concentration appears to be controlled by oxidation of arsenopyrite in the near-surface environment (Verplanck et al., 2007). Smedley *et al.* (2007) have recently reported arsenic contamination in circumneutral-pH groundwaters in Proterozoic basement rocks in Burkina Faso. Thus, there are also other scenarios where higher pH (neutral or alkaline) is common. For example, acid generation may be artificially attenuated by adding alkaline substances to the AMD producing materials (Pérez-López *et al.*, 2007), which results in acid neutralization. Similarly, hydrometallurgical techniques such as cyanidation have been conducted at high pH producing alkaline waters in contact with mine residues (Salzsauler *et al.*, 2005).

Because pyrite is usually the most abundant sulfide mineral in ARD and AMD environments the kinetics of pyrite oxidation under acidic to neutral conditions have been studied for over two decades (Wiersma and Rimstidt, 1984; McKibben and Barnes, 1986; Nicholson *et al.* 1988; Moses and Herman, 1991; Williamson and Rimstidt, 1994; Domènech *et al.*, 2002; Descostes *et al.*, 2004; Pérez-López *et al.*, 2007; Asta *et al.* 2008b).

Similarly, the effects of different environmental factors on arsenopyrite oxidative dissolution, such as temperature, Fe(III) concentration, presence of bacteria (*Acidithiobacillus ferrooxidans*), pH and particle size have been reported in the literature, either related to aqueous chemistry studies (Breed *et al.*, 1997; Ruitenberg *et al.*, 1999; McGuire *et al.*, 2001; Craw *et al.,* 2003; Yu *et al.* 2004; Tallant and McKibben, 2005; Walker *et al.*, 2006; Yu *et al.* 2007 and McKibben *et al.*, 2008) or to arsenopyrite surface spectroscopy research, mainly by X-ray Photoelectron Spectroscopy (XPS) (Buckley and Walker, 1988; Richardson and Vaughan, 1989; Nesbitt *et al.*, 1995; Nesbitt and Muir, 1998; Hacquard *et al.*, 1999, and Mikhlin *et al.*, 2006). This extensive literature is indicative of the important role of arsenopyrite oxidative dissolution in different geochemical environments, from AMD to metallurgical processes, and groundwater contamination. However, far few studies have focused on the dissolution kinetics of marcasite. Mathews and Robins (1972, 1974) studied the oxidation of mixtures of pyrite and marcasite by ferric iron and dissolved oxygen. According to these authors when pyrite-marcasite mixtures were oxidized by ferric iron the rate was proportional to the ratio of ferric to total iron. When the pyrite-marcasite mixtures were oxidized by oxygen, the pH effect over a very limited acidic range (pH -0.1-1.2) was negligible and the results yielded a 0.81 order of dependence on dissolved oxygen concentration. Wiersma and Rimstidt (1984) found a first-order dependence on ferric iron concentrations for pyrite and marcasite. Rimstidt and Vaughan (2003) studied the differences in reactivity of pyrite and marcasite and concluded that the variations in the crystal structure caused only small differences in the dissolution rates (less than one order of magnitude). In addition, several X-ray Photoelectron Spectroscopy (XPS) studies focused on the evolution of marcasite surfaces during oxidation (Rinker *et al.* 1997; Pratt *et al.* 1998; Uhlig *et al.* 2001; Elsetinow *et al.*, 2003; Harmer and Nesbitt, 2004). Rinker *et al.* (1997) conducted batch experiments and analyzed marcasite surfaces using XPS and AES (Auger electro spectroscopy), reporting a dissolution rate at pH 3. According to Uhlig *et al.* (2001) the S2p spectrum of fracture surfaces of marcasite consists of four main contributions, assigned to bulk sulfur dimers, surface dimers, surface monosulfide and short chained polysulfides at the surface.

Elsetinow *et al.* (2003) investigated a synthetic thin film of marcasite by means of XPS and AFM (Atomic Force Microscope) and found that the S2p spectral region was dominated by disulfide groups and polysulfides.

Despite their valuable insights into arsenopyrite and marcasite dissolution, most of these studies focused their attention on the first few hours of dissolution and not on the steady-state dissolution. The short duration of batch experiments usually renders much faster dissolution rates than the ones obtained after months (or years) of interaction with solutions. In line with this affirmation, a decrease in the concentrations with time has been described for many sulfides, such as pyrite (Domènech *et al.*, 2002), chalcopyrite and sphalerite (Malmström and Colin 2004; Acero *et al.* 2007a; Acero *et al.* 2007b; Acero *et al.* 2009) or galena (Cama and Acero, 2005; Acero *et al.* 2007c) but also for other types of minerals (Metz and Ganor, 2001; Brandt *et al.*, 2003).

High concentrations at the beginning of the experiments are due to either dissolution of an outer layer of the reacting mineral, which may be altered by grinding or cleaving, or to dissolution of microparticles with higher specific surface areas than the bulk sample (Lasaga, 1998). Hence, apparent rates obtained by short batch experiments, which are based on those initially high concentrations, are always faster than the steady-state rates obtained in flow-through experiments. Therefore, the apparent rates obtained in batch experiments, which are only based on the initial dissolution of arsenopyrite and marcasite, are not applicable for predicting arsenopyrite dissolution in scenarios where an extended interaction with solutions is expected (e.g. in the pores of mine tailings, in acid streams or aquifers).

The aim of the present chapter is to study the kinetics of arsenopyrite and marcasite oxidative dissolution at different oxidizing conditions by assessing the effects of environmental factors, such as pH, dissolved oxygen and temperature in order to evaluate and quantify the As release in long-term conditions. To this end, forty-two stirred and non-stirred flow-through experiments were carried out at 25-70ºC and dissolved O_2 concentrations in the range of 0.2 to 8.7 mg L^{-1} and over the pH range of 1 to

9. X-ray photoelectron spectroscopy (XPS) and scanning electron microscopy (SEM) examinations of the samples were carried out before and after experiments to characterize mineral surfaces after dissolution. This study is useful in the quantification of the extent of arsenic mobility and pollution at field sites where sulfide oxidation is the dominant control of arsenic release.

2.1 Materials and Methods

2.1.1 Sample characterization

The arsenopyrite samples used in this study were obtained from Martinet skarn mineralization (East Pyrenees range), and the marcasite samples are from the carbonate-hosted Zn-Pb deposits of Reocin (Cantabria, Spain).

Powder samples were examined by X-ray diffraction (XRD) using Cu Kα radiation over a 2θ range from 0 to 60 degrees and using a scan speed of 0.0014 degrees 2θ per second. (XRD). Patterns of the samples showed that mineral samples were monomineralic. Electron microprobe analyses were performed on multiple points of the samples using a Cameca SX-50 equipment with an accelerating voltage of 20 kV and a beam current of 15nA. The atomic composition based on these analyses was Fe 33.3±0.2% and S 66.7±0.2% (FeS_2) for marcasite, and Fe 33.5±0.1, As 32.1±0.4 and S 34.4±0.4 for arsenopyrite (yielding an average chemical formula of $Fe_{1.0}As_{0.94}S_{1.05}$). These results confirmed the high purity of the samples.

Mineral fragments of the minerals were crushed in an agate mortar and sieved to a size fraction of 10 to 100 μm. The specific surface areas of the ground samples were determined by the BET method (Brunauer *et al.*, 1938) using 5-point N_2 adsorption isotherms with a Micromeritics ASAP 2000 surface area analyzer. Measured specific areas were found to be 0.9 ± 0.1 $m^2\ g^{-1}$ for marcasite and 0.6 ± 0.1 $m^2\ g^{-1}$ for arsenopyrite. No attempt to remove the microparticles (<1μm) attached to grain surfaces resulting from grinding was made. In long-term flow-through experiments, it is not necessary to

pretreat the samples to obtain the steady-state dissolution rate since the possible effect of the particle size is corrected by normalizing the rates by the final specific surface area.

Unreacted and reacted powders were examined by Scanning Electron Microscopy (SEM) using a JEOL JSM-840 microscope and a field-emission scanning microscope Hitachi H-4100FE.

XPS surface examination of the initial and reacted powdered samples mounted on carbon conductive tabs was carried out with a Physical Electronics (PHI) 5500 spectrometer using a monochromatic X-ray source (with an Al Kα line of 1486.6 eV energy and 350 W) placed perpendicular to the analyzer axis and calibrated using the 3d5/2 line of Ag with a width of 0.8 eV and a binding energy of 368.3 eV. All these measurements were made in an ultra high vacuum (UHV) chamber (pressure between $6.6 \cdot 10^{-11}$ and $6.6 \cdot 10^{-12}$ atm). The analyzer pass energy was 23 eV. An electron flood gun at low energies (below 25 eV) was used for charge compensation. Comparison of the relative positions of the different peaks in all the studied spectra indicated that charge shifting could be considered uniform. Spectra are shown as raw data corrected by adjusting the C1s peak (corresponding to adventitious carbon, to a binding energy of 284.6 eV) because of the charge of the sample. Given the lack of sample cooling while acquiring the measurements, loss of elemental sulfur could occur. Therefore, the presence or absence of elemental sulfur is discussed below. Atomic concentrations of arsenic, iron and sulfur were determined from the XPS peak areas divided by atomic sensitivity factors following the Shirley background substraction. A deconvolution of the spectra into different components was carried out. Each spectrum was fitted by means of an iterative least-squares procedure with Gaussian bands. The proportion of each surface species was then determined as a function of the areas covered by each band. However, a systematic quantification of the different iron species present in the samples is not presented here because of the low signal-to-noise ratio in most of the XPS spectra for these peaks. Only the approximate position of the observed sulfur species will be described below.

Surfaces of raw arsenopyrite powder and some powders retrieved at the end of the runs at different pH were examined by MicroRaman spectroscopy, revealing traces of quartz and pyrite at the surface. MicroRaman measurements were carried out in back scattering geometry by using the polarized 514.5 nm line of an Argon-ion laser. Raman scattering measurements were performed in air at room temperature with a triple spectrometer Jobin-Yvonne Dilor integrated system with a spectral resolution of about 1 cm^{-1}. The power density at the sample was set between 5 and 10 mW mm^2. Acquisition time was between 30 and 120 s depending of the quality of the spectra that were recorded in the Stokes region by a 1200 grooves/mm grating monochromator and CCD detector system. A confocal microscope Olympus B-201 was used, with an objective 100× with 0.90 numerical aperture. The spatial resolution was less than 1 μm. In order to verify the homogeneity of the samples and the reproducibility of the reported data, all the measurements were repeated at different random points of the samples.

2.1.2 Solutions and analysis

All input solutions were prepared by mixing the respective analytical reagents and Millipore MQ water (18.2 MΩ·cm). The analytical-grade reagents in the acidic solutions (pH 1 and 3) were HCl and H_2SO_4 (95-97%). Reagents $FeSO_4 \cdot 7H_2O$ and H_2SO_4 (95-97%) were used to prepare the 0.01M Fe^{2+} in a H_2SO_4 solution. Input solution of pH 5.7 only consisted of Millipore MQ water (18.2 $M\Omega \cdot$ cm). The solution of pH 7.6 was prepared with KH_2PO_4 and NaOH, and pH 9 solution consisted of $Na_2B_4O_7 \cdot H_2O$.

Total concentrations of metals and sulfur in input and output solutions were analyzed by Inductively Coupled Plasma Atomic Emission Spectroscopy (ICP-AES, Thermo Jarrel-Ash with CID detector and a Perkin Elmer Optima 3200 RL). Detection limits for As, Fe and S were $1.3 \cdot 10^{-6}$, $3.6 \cdot 10^{-7}$ and $3.1 \cdot 10^{-6}$ mol L^{-1}, respectively. The accuracy in ICP-AES measurements was estimated to be around 3 %. Ferrous and total dissolved iron concentrations in output solutions with pH < 3.5 were determined by colorimetry using the ferrozine method (To *et al.*, 1999) in a UV–VIS HP Spectrophotometer within

one month of sampling. Fe(III) was taken as the difference between Fe(tot) and Fe(II). The quality of the results was assured by measuring several standards, blanks and duplicates. Fe(tot) concentrations matched ICP-AES results within 5%.

Input and output solution pH was measured at experimental temperature on an unstirred aliquot of solution using a Crison meter combination electrode with temperature compensation. Calibration was made with standards of 2, 4, 7 and 9.21 pH buffer solutions. Input and output solution pH was the same within error (±0.05 pH units).

The concentration of dissolved oxygen in the reacted solutions was measured in some representative experiments by luminescent dissolved oxygen using a Hach HQ10 portable dissolved oxygen meter. Luminescent dissolved oxygen measurements were made in dark conditions and the accuracy at room temperature (22±3ºC) is 5%.

Redox potential was measured by an Orion combination Pt/Ag-AgCl redox electrode. The measurements were corrected by the Standard Hydrogen Electrode (S H E). Reliable redox potential measurements could not systematically be obtained because of considerable drifting in the recorded values with time. This drifting could be due to the low concentrations of aqueous species in the output solutions, to the presence of $H_2S_{(g)}$ or to the absence of a clearly dominant redox couple (Nordstrom, 2000). When it was possible to carry out the measurements the Eh was between 0.2 and 0.7 V.

2.1.3 Flow through experiments

Experiments were performed using stirred and non-stirred flow-through Lexan reactors with a reaction chamber of 35 mL in volume, as shown in Figure 2.1. The reaction cells consisted of two chambers separated by a fine mesh (5 μm) on which the powder sample and a teflon stir bar (in the stirred experiments) were placed together. The flow rate used in the experiments ranged between 0.03-0.05 mL min^{-1}, which allowed residence times of

10-20 h. Solutions were filtered with a 0.45 μm nylon membrane at the top and bottom of the reactor.

Reactors were fully immersed in a thermostatic water-bath held at constant temperature (25, 50 and 70±1°C). In the experiments carried out at input dissolved oxygen concentrations lower than 8.7 mg L^{-1}, output solutions, pumps and flow-through cells were enclosed in a glove box with the corresponding O_2/N_2 gas mixtures (4.5% O_2 in N_2 for the experiment with 2.0 mg L^{-1} of input dissolved oxygen and pure N_2 for the experiments with 0.2 mg L^{-1} of input dissolved oxygen).

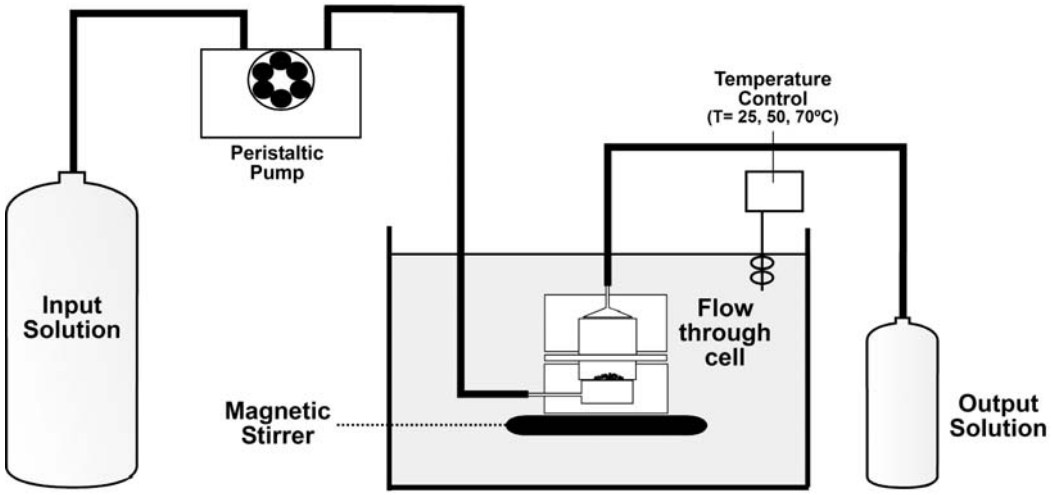

Figure 2.1. Schematic representation of the experimental setup.

Steady-state conditions were considered to be attained when differences in the metal concentration of the output solution were within ± 10% for at least 200 h in consecutive leachate samples. After the experiment, the reacted samples were collected, rinsed with double-dionized water, dried at room temperature and stored in closed microvials until examination by SEM, XPS and determination of their BET specific area.

2.1.4 Calculation of dissolution rates at pH < 6

The dissolution rate in steady state, *Rate* (mol m^{-2} s^{-1}), was based on the release of As, Fe and S according to the expression:

$$Rate = \frac{q(c_i - c_i^o)}{A\nu_i} \quad (2.1)$$

where c_i and c_i^o are the out and in-flowing concentrations of the element *i* (mol As, Fe or S m^{-3}), ν_i is the stoichiometry coefficient of Fe, As or S in the dissolution reaction, *A* is the surface area (m^2) and *q* is the fluid volume flux through the system ($m^3\ s^{-1}$). The error associated with the calculated dissolution rates was estimated by the Gaussian error propagation method (Barrante, 1974) to range from 12 to 25% and it was dominated by the uncertainty of BET surface area measurements (±10-15%).

2.1.5 Calculation of dissolution rates at pH > 6

At pH higher than 6, it is expected that Fe(II) released from arsenopyrite and marcasite dissolution oxidizes quickly to Fe(III) (Singer and Stumm, 1970), and that Fe(III)-bearing phases precipitate on mineral surfaces, coating the grains as dissolution proceeds. This process is satisfactorily described by the shrinking core model (SCM) and was already applied to pyrite oxidation at basic pH (Nicholson *et al.*, 1990). The model assumes spherical particle shape, and according to Wen (1968), the process of dissolution-coating can be divided into three successive steps: diffusion of reactant ($O_{2(aq)}$ in our case) from the bulk solution to the external surface of the coating, diffusion of $O_{2(aq)}$ through the coating volume, and finally $O_{2(aq)}$-induced dissolution of the unreacted core. $O_{2(aq)}$ consumption at the core surface gives rise to a concentration gradient across the coating.

To simplify the system, we assume that diffusion in water is much faster than through the solid coating, and that the unreacted core shrinks much more slowly than the time needed to reach steady-state diffusion across the coating. This means that, except in the early steps of dissolution, the coating acts as the slow barrier for the whole process, and the dissolution rate decreases as the coating accumulates.

At the onset of the experiment, when no coating is still developed, surface reaction is the step that controls the overall process. It is assumed that the mineral dissolution rate (mol m^{-2} s^{-1}) is linearly dependent on oxygen activity:

$$Rate = k\rho a_{O2} \tag{2.2}$$

where k is a mass transfer dissolution constant (m s^{-1}), ρ is the molar density of arsenopyrite and marcasite (37850 and 40632 mol m^{-3}, respectively), and a_{O2} is the input $O_{2(aq)}$ activity. When the coating is developed, and the overall process is controlled by oxygen diffusion through the coating, mineral dissolution depends on the oxygen flux:

$$Rate = \frac{1}{\nu_{ox}} D \frac{\partial C}{\partial r} \tag{2.3}$$

where ν_{ox} is O_2 stoichiometry in the arsenopyrite and marcasite dissolution reaction (see below), and D is the effective diffusion coefficient of the coating (m^2 s^{-1}). According to Wen (1968), the time required to react a specified molar fraction of arsenopyrite, X, can be calculated on the basis of the step that controls the overall process:

- dissolution at the surface of the unreacted core (at the onset of the experiment):

$$t = \frac{\nu_{ox} R \rho}{kC}\left[\, 1 - (1 - X)^{1/3} \right] \tag{2.4}$$

- diffusion across the coating:

$$t = \frac{\nu_{ox} R^2 \rho}{6DC}\left[\, 1 - 3(1 - X)^{2/3} + (1 - X) \,\right] \tag{2.5}$$

where R is initial radius of the particle (m) and D is the effective diffusion coefficient of the coating. Total time of the overall process is obtained by adding the times of the two steps. For each specific time, the molar fraction of arsenopyrite dissolved, X, was calculated from the integrated solute concentration (e.g. sulfate) over time divided by the initial mass of arsenopyrite. Hence, the values of k and D were obtained for each

experiment as their best fit in eqs. (2.4) and (2.5). As shown by eqs. (2.4) and (2.5), the values of k and D depend on the value of the initial radius R. Assuming an initial existence of a homogeneous population of particles, the value of R for this population was estimated according to the expression:

$$R = \frac{3}{A_{BET}\rho M} \tag{2.6}$$

where A_{BET} is the specific surface area (0.6 and 0.9 $m^2\ g^{-1}$ for arsenopyrite and marcasite respectively) and M is arsenopyrite and marcasite molar mass (162.7 g mol^{-1} and 119.98 g mol^{-1}, respectively). As the measured BET specific surface areas are 0.6 and 0.9 $m^2\ g^{-1}$ for arsenopyrite and marcasite respectively, equivalent values of R are 0.8 and 0.7 μm. Although these values are outside the range of the measured particle size (10-100 μm) as the amount of dissolved sulfide is low, the BET specific surface is more representative of the mineral surface than the geometrical surface. Hence, these values ensure the direct transformation of the product $k \cdot \rho$ into a dissolution rate constant (mol $m^{-2}\ s^{-1}$), as obtained for low pH experimental rates (eq. 2.1), and as obtained from many experiments conventionally bound to BET surface measurements (see Brantley, 2008).

2.2 Results

2.2.1 Results based on solution chemistry

Variations with time of the output metals and S concentrations in some representative flow-through experiments with different pH are depicted in Figs. 2.2 and 2.3. The duration of the experiments varied from 600 to 4500 h. In the experiments carried out at pH < 6, steady-state conditions were attained after 300-1200 h and the duration of steady state varied exceeding 300 h. In the experiments carried out at pH range 7.5-9 steady state was not attained, and the output concentration decreased with time. The conditions of all experiments are shown in Tables 2.1, 2.2, 2.3 and 2.4. The residence time in the reactors was between 15 and 20 h, depending on the flow rate (0.03-0.05 mL min^{-1}). Calculated

Table 2.1. Experimental conditions, steady-state values and arsenopyrite dissolution rates based on steady-state values and based on the Shrinking Core Model (SCM) and arsenic concentration at acidic pH. Initial BET area of unreacted arsenopyrite is 0.61 $m^2 g^{-1}$.

Experiment	Stirring	Electrolyte	Flow rate	pH	input DO	T	S	Fe	As	Stoichiometry			Final BET	initial mass	final mass	R_{As}	log R_{As}	R_{Fe}	log R_{Fe}	log Rate SCM_{As}
			(mL min^{-1})		(mg L^{-1})	(ºC)		(µM)		Fe/As	S/As	Fe/S	($m^2 g^{-1}$)	(g)		(mol $m^{-2} s^{-1}$)				
ASP-25-1	no	H_2SO_4	0.040	1.0	8.7	25	99877	32.76	29.38	1.1	-	-	0.54	0.5014	0.4875	$7.4 \cdot 10^{-11}$	-10.1	$8.2 \cdot 10^{-11}$	-10.1	-10.6
ASP-25-2	no	H_2SO_4	0.040	2.7	8.7	25	963	41.34	34.66	1.1	-	-	0.40	0.5028	0.4962	$1.3 \cdot 10^{-10}$	-9.9	$1.4 \cdot 10^{-10}$	-9.9	-9.7
ASP-25-3	no	HCl	0.037	1.2	8.7	25	18.37	38.43	34.50	1.1	0.5	2.1	0.77	0.5039	0.4912	$5.7 \cdot 10^{-11}$	-10.2	$6.2 \cdot 10^{-11}$	-10.2	-10.1
ASP-25-4	no	HCl	0.038	3.1	8.7	25	18.37	30.96	29.67	1.0	0.6	1.7	0.65	0.5076	0.4930	$5.9 \cdot 10^{-11}$	-10.2	$6.1 \cdot 10^{-11}$	-10.2	-10.0
ASP-25-12	yes	HCl	0.041	1.1	8.7	25	27.76	53.97	50.33	1.1	0.5	1.9	0.63	0.8002	0.7330	$7.5 \cdot 10^{-11}$	-10.1	$8.1 \cdot 10^{-11}$	-10.1	-10.0
ASP-25-13	yes	HCl	0.026	2.9	8.7	25	85.02	108.41	95.93	1.1	0.9	1.3	0.74	0.8002	0.7060	$7.8 \cdot 10^{-11}$	-10.1	$8.8 \cdot 10^{-11}$	-10.1	-10.0
ASP-25-5	no	HCl	0.034	1.3	2.0	25	4.34	9.16	7.69	1.2	0.6	1.2	0.43	0.5034	0.5013	$2.0 \cdot 10^{-11}$	-10.7	$2.4 \cdot 10^{-11}$	-10.6	-10.8
ASP-25-24	no	HCl	0.036	3.1	2.0	25	22.69	22.51	17.42	1.3	1.3	1.0	0.60	0.7991	0.7911	$2.2 \cdot 10^{-11}$	-10.7	$2.8 \cdot 10^{-11}$	-10.6	-10.6
ASP-25-25	no	HCl	0.038	1.1	2.0	25	22.93	18.89	15.64	1.2	1.0	0.8	0.49	0.8068	0.7992	$2.5 \cdot 10^{-11}$	-10.6	$3.0 \cdot 10^{-11}$	-10.5	-10.7
ASP-25-6	no	Fe^{2+}&H_2SO_4	0.038	1.2	8.7	25	124520	10070	21.49	-	-	-	0.61	0.4937	0.4829	$4.7 \cdot 10^{-11}$	-10.3	-	-	-10.0
ASP-25-7-a	no	HCl	0.037	3.0	0.2	25	*b.d.l*	0.75	*b.d.l*	1.1	-	-	0.73	0.5014	0.5006	-	-	$1.3 \cdot 10^{-12}$	-11.9	-
ASP-25-7-b	no	HCl	0.036	3.0	2.0	25	3.62	4.83	4.55	1.1	0.8	1.3	0.73	0.5014	0.4991	$7.6 \cdot 10^{-12}$	-11.1	$8.1 \cdot 10^{-12}$	-11.1	-11.1
ASP-25-7-c	no	HCl	0.036	3.0	8.7	25	12.53	17.53	16.85	1.0	0.7	1.4	0.73	0.5014	0.4935	$2.8 \cdot 10^{-11}$	-10.6	$2.9 \cdot 10^{-11}$	-10.5	-10.5
ASP-25-32	no	HCl	0.014	1.1	0.2	25	9.81	7.83	4.38	1.8	1.7	0.8	0.33	0.8090	0.8075	$2.1 \cdot 10^{-12}$	-11.7	$3.7 \cdot 10^{-12}$	-11.4	-11.3
ASP-25-34-a	yes	HCl	0.046	1.2	2.0	25	8.89	16.38	14.80	1.1	0.6	1.8	0.48	0.8239	0.8121	$2.3 \cdot 10^{-11}$	-10.6	$2.6 \cdot 10^{-11}$	-10.6	-10.3
ASP-25-34-b	yes	HCl	0.048	1.3	0.2	25	3.89	4.38	3.03	1.1	1.3	1.1	0.48	0.8239	0.8085	$4.9 \cdot 10^{-12}$	-11.3	$7.0 \cdot 10^{-12}$	-11.2	-11.2
ASP-50-1	no	HCl	0.033	1.1	8.7	50	29.12	54.27	51.84	1.0	0.6	1.9	0.66	0.5016	0.4742	$8.9 \cdot 10^{-11}$	-10.0	$9.4 \cdot 10^{-11}$	-10.0	-9.8
ASP-50-4	no	HCl	0.035	2.9	8.7	50	34.41	54.91	56.30	1.0	0.6	1.6	0.50	0.8037	0.7763	$6.9 \cdot 10^{-11}$	-10.2	$6.7 \cdot 10^{-11}$	-10.2	-9.6
ASP-70-1	no	HCl	0.037	1.0	8.7	70	27.78	35.80	31.08	1.2	0.9	1.3	0.46	0.5011	0.4785	$8.6 \cdot 10^{-11}$	-10.1	$9.9 \cdot 10^{-11}$	-10.0	-9.4
ASP-70-5	no	HCl	0.026	1.2	8.7	70	41.94	41.28	30.97	1.3	1.3	1.0	0.51	0.8039	0.7898	$2.8 \cdot 10^{-11}$	-10.5	$3.8 \cdot 10^{-11}$	-10.4	-9.3
ASP-25-8	no	HCl	0.038	5.2	8.7	25	36.90	25.93	33.72	0.8	1.1	0.7	0.63	0.5066	0.4702	$7.3 \cdot 10^{-11}$	-10.1	$5.6 \cdot 10^{-11}$	-10.3	-10.0
ASP-25-9	no	DDW	0.036	5.5	8.7	25	15.45	4.06	18.03	0.2	0.8	0.3	0.67	0.5023	0.4851	$3.2 \cdot 10^{-11}$	-10.5	$7.3 \cdot 10^{-12}$	-11.1	-10.2
ASP-25-23	y	DDW	0.035	5.8	8.7	25	91.24	35.05	66.12	0.5	1.4	0.4	0.59	0.8039	0.7754	$8.4 \cdot 10^{-11}$	-10.1	$4.5 \cdot 10^{-11}$	-10.3	-10.0
ASP-25-19-a	no	DDW	0.040	5.6	0.2	25	4.80	0.62	1.30	0.5	2.2	0.1	0.61	0.8033	0.8024	$1.7 \cdot 10^{-12}$	-11.8	$8.4 \cdot 10^{-13}$	-12.1	-11.2
ASP-25-19-b	no	DDW	0.033	5.6	8.7	25	71.11	15.24	60.41	0.3	1.2	0.2	0.61	0.8033	0.7875	$6.9 \cdot 10^{-11}$	-10.2	$1.7 \cdot 10^{-11}$	-10.8	-10.5
ASP-70-4	no	DDW	0.030	4.4	8.7	70	61.51	23.98	47.43	0.5	1.3	0.4	0.65	0.8002	0.7796	$4.6 \cdot 10^{-11}$	-10.3	$2.3 \cdot 10^{-11}$	-10.6	-9.7

b.d.l.: below detection limit

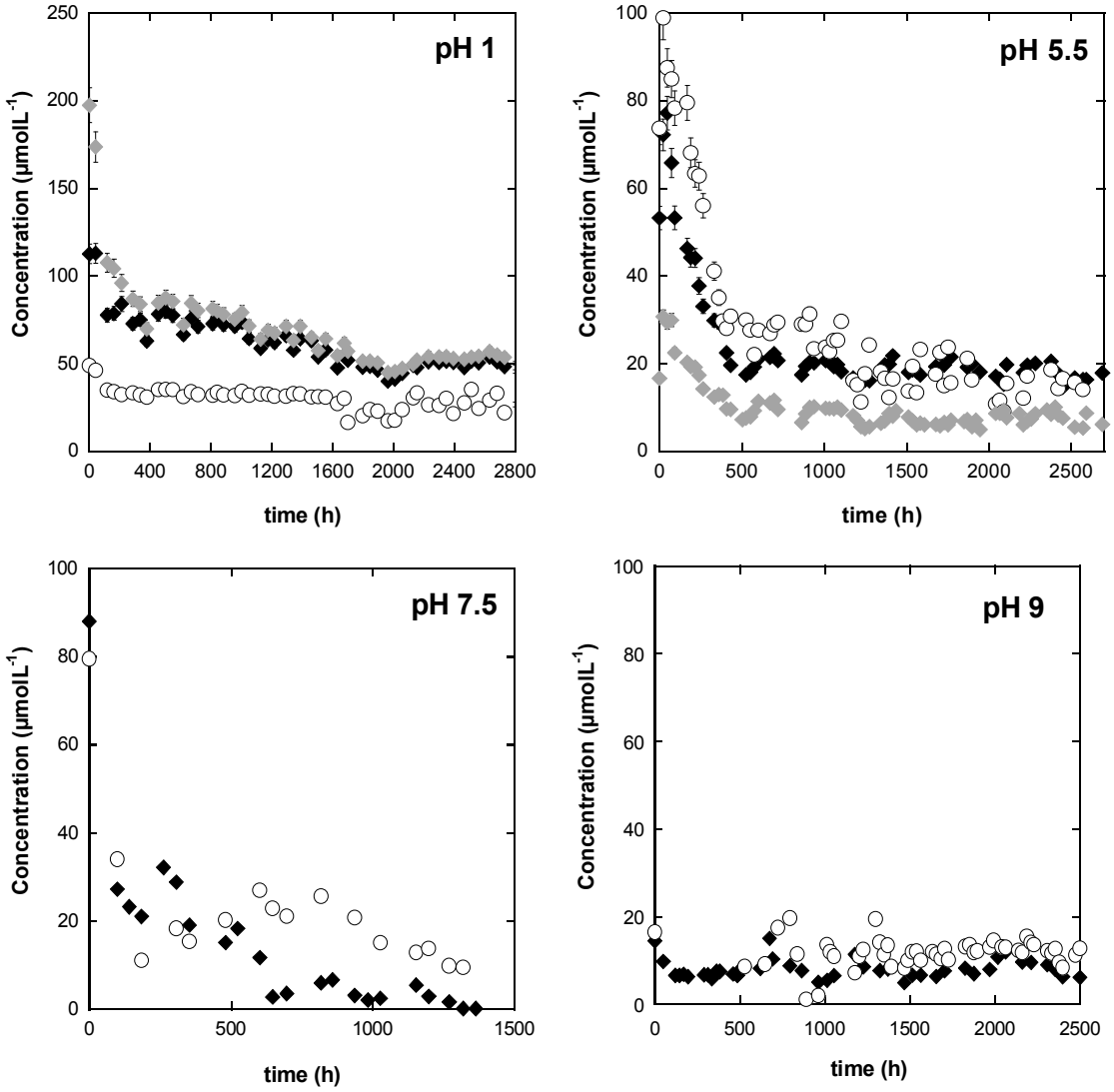

Figure 2.2. Variation in total iron (grey rhombi), arsenic (black rombhi) and sulphur (circles) as a function of time in arsenopyrite representative experiments at different pH and 8.7 mgL^{-1} of O_2-dissolved and 25 °C. Initial concentrations for the experiments are not depicted for the sake of significance of the vertical scale at basic pH, and iron concentration is not depicted because it was below detection limit.

total dissolved mineral mass throughout the experiments was usually less than 10%. As shown in Figs. 2.2 and 2.3, concentrations of arsenic, iron and sulfur in the output solutions were highest at the start of the experiments, subsequently decreasing. The high concentrations at the start of the experiments were probably due to dissolution of external layers of the ground mineral or to dissolution of highly reactive microparticles

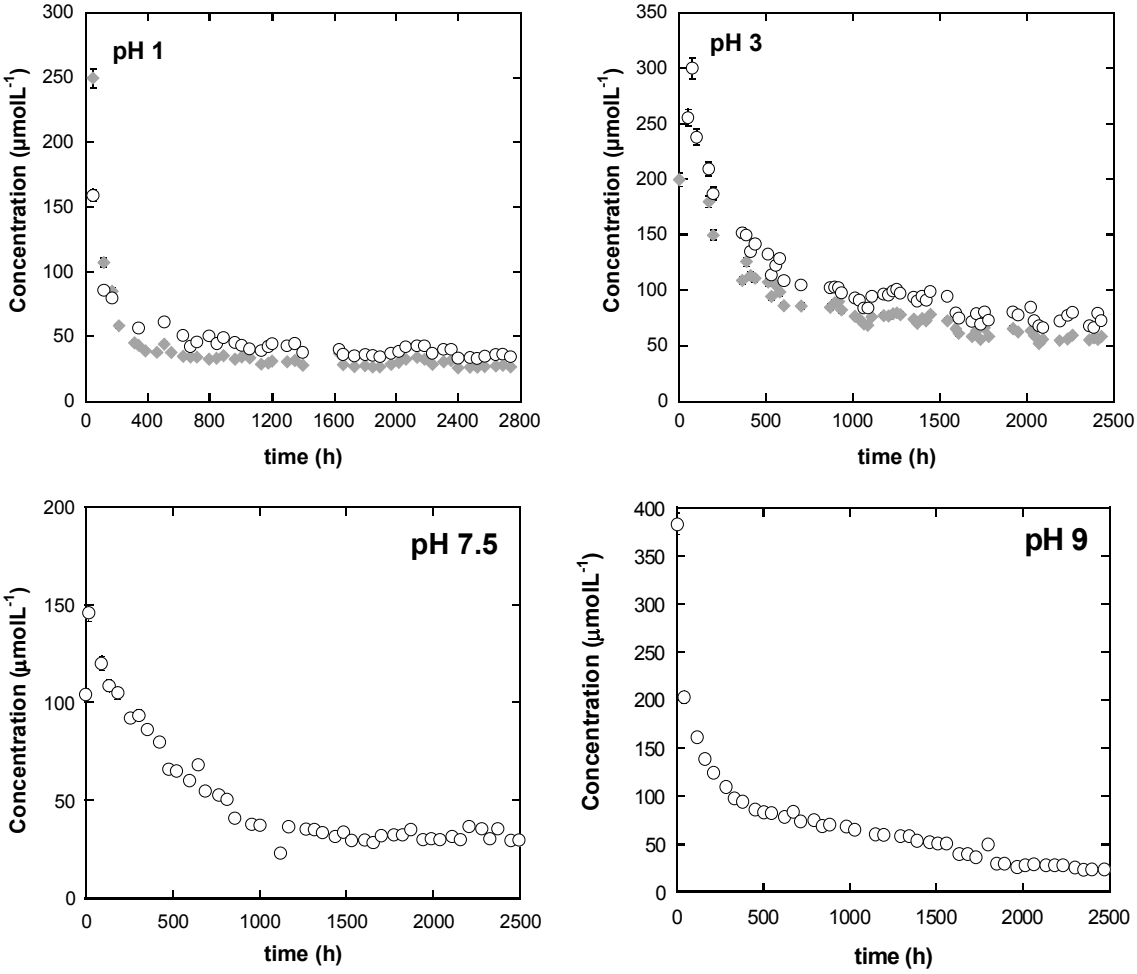

Figure 2.3. Variation in total iron (circles) and sulfur (rhombi) as a function of time in two marcasite representative experiments at pH 1, 3, 7.5 and 9 and 25ºC and 8.7 mg L^{-1} of dissolved oxygen. The concentration differences at acidic pH are mainly due to the different flow rate of the experiments. Initial concentrations for the experiments are not depicted for the sake of significance of the vertical scale at basic pH iron is not depicted because it was below detection limit.

(Lasaga, 1998) (Fig. 2.4). Additionally, preferential dissolution in cracks and other mineral defects during the early stages of the experiments can cause high initial concentrations (Borda *et al.*, 2004). The fact that a mineral dissolves apparently faster at the start of the experiment and the fact that steady states are attained after some time (in this work from 300 to 1200 h) highlight the need to carry out flow-through instead of short batch experiments. Long-term experiments are needed to predict the sulfide dissolution in scenarios where an extended interaction with solutions is expected (e.g. acid streams or

Table 2.2. Experimental conditions and arsenopyrite dissolution rates obtained by the SCM based on output arsenic and sulfur concentrations at circumneutral and basic pH. Initial BET area of unreacted pyrite is 0.61 $m^2 g^{-1}$.

Experiment	Stirring	Duration	Electrolyte	Flow rate	pH	Input DO	T	Final BET area	initial mass	final mass	R_{As}	log R_{As}	R_S	log R_S
		(h)		(mL min^{-1})		(mg L^{-1})	(ºC)	($m^2 g^{-1}$)	(g)		(mol $m^{-2} s^{-1}$)			
ASP-25-10	no	2643	KH_2PO_4	0.034	7.5	8.7	25	1.08	0.5027	0.5005	$6.7 \cdot 10^{-12}$	-11.2	$3.2 \cdot 10^{-11}$	-10.5
ASP-25-21	yes	1699	KH_2PO_4	0.036	7.5	8.7	25	1.24	0.8040	0.7957	$5.0 \cdot 10^{-11}$	-10.3	$5.3 \cdot 10^{-11}$	-10.3
ASP-25-11	no	2683	$Na_2B_4O_7 \cdot H_2O$	0.031	9.1	8.7	25	0.71	0.5064	0.5014	$2.2 \cdot 10^{-11}$	-10.7	$3.6 \cdot 10^{-11}$	-10.4
ASP-25-15	yes	3312	$Na_2B_4O_7 \cdot H_2O$	0.032	8.9	8.7	25	0.68	0.8040	0.7925	$1.9 \cdot 10^{-11}$	-10.7	$3.1 \cdot 10^{-11}$	-10.5

Table 2.3. Experimental conditions and marcasite dissolution rates based on steady-state values and SCM at acidic pH. Initial BET surface area is 0.9 $m^2 g^{-1}$.

Experiment	Stirring	Electrolyte	Flow rate	pH	input DO	T	S	Fe	Fe/S	Final BET	initial mass	final mass	$Rate_{Fe}$	log ($Rate_{Fe}$)	log Rate SCM_{Fe}
			(mL min^{-1})		(mg L^{-1})	(ºC)	(µM)			($m^2 g^{-1}$)	(g)		(mol $m^{-2} s^{-1}$)		
MRC-1	no	HCl	0.029	3.0	8.7	25	71.03	58.44	0.8	0.62	0.5001	0.4564	$1.0 \cdot 10^{-10}$	-10.0	-10.1
MRC-2	yes	HCl	0.028	3.0	8.7	25	105.28	85.80	0.8	0.79	0.8007	0.7536	$6.7 \cdot 10^{-11}$	-10.2	-9.9
MRC-3	no	HCl	0.044	1.1	8.7	25	18.81	20.58	1.1	0.54	0.5001	0.4714	$6.1 \cdot 10^{-11}$	-10.2	-10.5
MRC-4	yes	HCl	0.039	1.0	8.7	25	47.00	34.00	0.7	0.66	0.8002	0.7686	$4.3 \cdot 10^{-11}$	-10.4	-10.4
MRC-50-1	yes	HCl	0.039	2.8	8.7	50	109.56	64.37	0.6	0.42	0.7502	0.7010	$1.4 \cdot 10^{-10}$	-9.9	-9.8
MRC-50-2	yes	HCl	0.027	1.0	8.7	50	107.38	100.80	0.9	0.71	0.8062	0.7507	$7.8 \cdot 10^{-11}$	-10.1	-9.9
MRC -70-1	yes	HCl	0.037	1.4	8.7	70	120.00	113.00	0.9	0.54	0.8004	0.7721	$1.6 \cdot 10^{-10}$	-9.8	-9.8
MRC-5a	no	HCl	0.046	1.2	2.0	25	13.47	16.56	1.2	0.46	0.8068	0.7962	$3.2 \cdot 10^{-11}$	-10.5	-10.6
MRC-5-b	no	HCl	0.045	1.3	0.2	25	4.35	5.40	1.2	0.46	0.7962	0.7957	$1.1 \cdot 10^{-11}$	-11.0	-11.2
MRC-6-a	no	HCl	0.049	3.3	2.0	25	101.41	64.41	0.6	1.50	0.8035	0.7769	$4.5 \cdot 10^{-11}$	-10.4	-10.4
MRC-6-b	no	HCl	0.063	2.9	0.2	25	10.48	19.89	1.9	1.50	0.7986	0.7744	$1.9 \cdot 10^{-11}$	-10.7	-10.6
MRC-7	no	HCl	0.033	3.1	0.2	25	*bdl*	6.56	-	0.51	0.5064	0.5036	$1.4 \cdot 10^{-11}$	-10.9	-11.1
MRC-8	no	H_2SO_4	0.033	2.2	8.7	25	5844	84.30	-	0.68	0.8000	0.7553	$8.9 \cdot 10^{-11}$	-10.0	-9.9
MRC-9	no	H_2SO_4	0.032	1.5	8.7	25	37579	86.23	-	0.62	0.8004	0.7607	$9.7 \cdot 10^{-11}$	-10.0	-9.9
MRC-10	no	HCl	0.034	2.0	8.7	25	65.33	73.03	0.8	0.58	0.7997	0.7454	$9.2 \cdot 10^{-11}$	-10.0	-9.9

bdl: below detection limit

pores of mine tailings). Sulfur concentrations, in the acid output solutions, were lower than metal concentrations (Figs. 2.2, 2.3; Tables 2.1, 2.3). $H_2S_{(g)}$ odour was detected during the collection of marcasite acid output solutions; although the presence of $H_2S_{(g)}$ can not be ruled out, it was not detected during the collection of arsenopyrite acid output solutions. It is worth noting that, at acid pH, although the measured dissolution reaction could be stoichiometric, the dissolved sulfur concentrations do not reflect the stoichiometry of the bulk mineral. The deficit of dissolved sulfur in acidic solutions has been observed in many studies on sulfide dissolution (Lochmann and Pedlik, 1995; Weisener *et al.*, 2003; Malmström and Collin, 2004; Weisener *et al.*, 2004; Acero *et al.*, 2007b); pyrite (Domènech *et al.*, 2002); pyrrhotite (Janzen *et al.*, 2000); galena (De Giudici and Zuddas, 2001; Cama and Acero, 2005; Cama *et al.*, 2005); arsenopyrite (Tallant and McKibben, 2005; McKibben *et al.*, 2008) and marcasite (Rinker *et al.*, 1997). Hence, at acid pH dissolution rates of arsenopyrite and marcasite are based only on dissolved iron and arsenic concentrations (Tables 2.1 and 2.3).

At pH > 3 the oxidative dissolution of iron sulfides may lead to precipitation of iron (hydr)oxides. The results showed that aqueous iron was partially depleted at mildly acidic pH (4.4 to 5.8) and totally depleted at neutral-basic pH (7.5 to 9) ($[Fe]_{out}$ was below the detection limit). In the case of arsenopyrite, arsenic output concentrations were lower than sulfur in the mildly acidic to basic pH range (Tables 2.1, 2.2; Fig. 2.2). Therefore, for experiments at pH higher than 3, the arsenopyrite and marcasite dissolution rates were computed from the output S concentration.

The saturation state of the output solution at the end of each experiment was calculated using the PHREEQC code (Parkhurst and Appelo, 1999) and WATEQ database (Ball and Nordstrom, 1991). Data for scorodite ($FeAsO_4 \cdot 2H_2O$) are those revised by Krause and Ettel (1988). At pH 1-3, output solutions were undersaturated with respect to native sulfur, S-bearing phases and Fe-oxy-hydroxides (Tables 2.5 and 2.6).

Table 2.4. Experimental conditions and marcasite dissolution rates obtained by the SCM and output sulfur concentration at neutral and basic pH. Initial BET surface area is 0.9 $m^2 g^{-1}$.

Experiment	Stirring	Electrolyte	Flow Rate	pH	input DO	T	Final BET area	initial mass	final mass	$Rate_S$	log ($Rate_S$)
			(mL min^{-1})		(mg L^{-1})	(ºC)	($m^2 g^{-1}$)	(g)		(mol $m^{-2} s^{-1}$)	
MRC-11	no	DDW	0.030	7.2	8.7	25	1.35	0.5064	0.5055	$8.6 \cdot 10^{-11}$	-10.1
MRC-12	no	KH_2PO_4	0.029	7.4	8.7	25	0.94	0.8064	0.7931	$1.3 \cdot 10^{-10}$	-9.9
MRC-14	no	$Na_2B_4O_7 \cdot H_2O$	0.031	9.1	8.7	25	1.11	0.8029	0.7803	$2.2 \cdot 10^{-10}$	-9.7

Thus, precipitation of these phases is not thermodynamically favored. In arsenopyrite output solutions, in the pH range of 4.4 to 5.8, assuming that total iron was ferric iron, supersaturation with respect to scorodite and Fe-oxy-hydroxide phases, such as ferryhidrite, goethite and lepidocrocite occurred. At pH > 7, although aqueous iron was depleted, calculations were run by using a very low iron concentration ($1x10^{-7}$ M), yielding arsenopyrite and marcasite output solutions supersaturated with respect to several iron oxy-hydroxides (Tables 2.5 and 2.6).

2.2.2 Morphology of reacted solids

A comparison of SEM photographs of samples before and after reacting in acidic and basic pH is shown in Figures 2.4 and 2.5. At acidic pH it is observed that after the experiments most of the microparticles have been dissolved. The comparison at neutral - basic pH reveals the precipitation of new Fe-bearing phases (Fig. 2.5). The smooth surface and sharp edges of the unreacted minerals contrast with the surface of reacted grains at pH > 3 as it is shown in the SEM micrographs (Figs. 2.4 and 2.5). The comparison of the initial samples (Fig. 2.4) to the reacted samples at neutral-basic pH revealed that some grains were covered by a discontinuous product-layer like a coarse granulation (Fig. 2.5). The formation of secondary iron precipitates on reacted pyrite and arsenopyrite surfaces at neutral-basic pH has been reported in earlier works (Koslides and Ciminelli, 1992; Bonnissel-Gissinger *et al.*, 1998; Pérez-López *et al.*, 2007).

Table 2.5. Saturation indices of the arsenopyrite output solutions with respect to As and Fe bearing minerals.

Experiment	pH	Arsenopyrite (FeAsS)	Arsenolite (As_2O_3)	As_2O_5	Scorodite ($FeAsO_4{:}2H_2O$)	Schwertmannite ($Fe_8O_8(OH)_{4.5}(SO_4)_{1.75}$)	Goethite (α-FeOOH)	Lepidocrocite (γ-FeOOH)	Magnetite (Fe_3O_4)	Maghemite (γ-Fe_2O_3)	Ferryhidrite ($Fe(OH)_{3(a)}$)	Elemental Sulfur
ASP-25-1	1.0	-219.2	-51.5	-15.7	-13.0	-115.0	-11.2	-13.3	-31.4	-30.9	-17.1	-92.2
ASP-25-2	2.8	-220.2	-52.6	-16.8	-7.2	-71.7	-4.9	-7.2	-14.6	-18.2	-10.8	-96.6
ASP-25-3	1.2	-222.3	-51.4	-15.6	-10.8	-104.2	-9.1	-11.4	-26.3	-26.6	-15.0	-96.1
ASP-25-4	3.1	-222.2	-53.3	-17.5	-6.4	-66.6	-3.8	-6.2	-11.7	-16.0	-9.7	-99.0
ASP-25-12	1.2	-221.9	-51.1	-15.3	-10.8	-105.3	-9.3	-11.5	-26.6	-27.0	-15.2	-95.8
ASP-25-13	2.9	-219.6	-51.9	-16.2	-6.2	-68.6	-4.3	-6.6	-11.7	-16.9	-10.2	-98.0
ASP-25-5	1.3	-221.7	-52.0	-17.0	-11.3	-103.6	-8.9	-11.2	-26.3	-26.2	-14.8	-95.7
ASP-25-24	3.0	-220.0	-52.8	-17.8	-6.8	-67.9	-4.0	-6.4	-12.5	-16.5	-9.9	-97.6
ASP-25-25	1.0	-220.7	-51.3	-16.3	-11.9	-109.5	-9.8	-12.0	-28.5	-28.0	-15.7	-94.6
ASP-25-6	1.2	-216.7	-51.8	-16.0	-12.8	-112.9	-10.9	-13.1	-28.1	-30.3	-16.8	-92.3
ASP-25-7-a	3.0	-226.4	-54.8	-20.6	-8.2	-77.9	-4.0	-6.4	-14.0	-16.4	-9.9	-102.6
ASP-25-7-b	3.0	-222.1	-54.0	-19.0	-7.3	-68.7	-4.0	-6.3	-13.0	-16.3	-9.9	-98.4
ASP-25-7-c	3.0	-222.8	-53.6	-17.9	-6.8	-68.0	-4.0	-6.4	-12.5	-16.4	-9.9	-99.0
ASP-25-32	1.2	-219.0	-51.6	-17.4	-11.9	-106.0	-9.3	-11.5	-27.4	-27.0	-15.2	-93.9
ASP-25-34-a	1.2	-221.0	-51.4	-16.4	-11.2	-105.0	-9.1	-11.4	-26.7	-26.7	-15.0	-95.3
ASP-25-34-b	1.3	-219.7	-52.0	-17.8	-11.6	-103.2	-8.8	-11.1	-26.5	-26.0	-14.7	-94.4
ASP-50-1	1.1	-202.7	-47.1	-14.9	-11.0	-107.0	-8.6	-11.7	-24.2	-27.3	-15.4	-87.6
ASP-50-4	2.9	-201.8	-48.2	-16.1	-7.0	-74.2	-4.1	-7.1	-11.2	-18.2	-10.8	-89.9
ASP-70-1	1.0	-190.0	-44.8	-15.1	-11.6	-110.5	-8.5	-12.1	-23.4	-28.1	-15.8	-81.9
ASP-70-5	1.2	-189.6	-44.8	-15.1	-11.1	-106.7	-8.0	-11.7	-22.1	-27.2	-15.3	-81.9
ASP-25-8	5.2	-231.0	-57.2	-21.5	2.7	15.9	7.2	4.9	7.4	6.1	1.4	-102.8
ASP-25-9	5.5	-233.1	-58.3	-22.6	1.6	10.3	6.7	4.4	5.9	5.1	0.8	-103.8
ASP-25-23	5.8	-231.5	-57.8	-22.1	3.1	20.2	7.9	5.6	9.5	7.5	2.1	-103.6
ASP-25-19-a	5.6	-230.2	-59.3	-25.2	-0.4	3.5	6.0	3.7	4.2	3.7	0.1	-102.1
ASP-25-19-b	5.6	-231.6	-57.5	-21.8	2.7	16.4	7.4	5.1	7.9	6.5	1.5	-103.3
ASP-70-4	4.4	-229.1	-55.3	-19.6	2.7	11.8	6.4	4.0	4.8	4.3	0.5	-101.0
ASP-25-10	7.5	-241.8	-65.0	-29.9	-1.8	2.8	6.7	4.9	5.8	5.0	0.8	-108.4
ASP-25-21	7.5	-241.2	-64.9	-29.8	-1.7	3.5	6.7	4.9	5.8	5.0	0.8	-107.8
ASP-25-11	9.1	-247.1	-70.0	-35.1	-4.5	-3.1	6.5	4.4	5.2	4.6	0.6	-111.0
ASP-25-15	8.9	-246.3	-69.6	-34.6	-4.2	-1.7	6.6	4.5	5.4	4.8	0.7	-110.4

Table 2.6. Saturation indices of the marcasite output solutions with respect to Fe bearing minerals.

Experiment	pH	Marcasite FeS_2	Schwertmannite $(Fe_8O_8(OH)_{4.5}(SO4)_{1.75})$	Goethite (α–FeOOH)	Maghemite (γ–Fe_2O_3)	Ferryhidrite $(Fe(OH)_{3(a)})$	Hematite (α–Fe_2O_3)	Elemental Sulfur
MRC-1	3.0	-223.8	-70.0	-4.5	-17.3	-10.4	-7.0	-97.8
MRC-2	3.0	-223.7	-67.1	-4.1	-16.5	-10.0	-6.1	-98.0
MRC-3	1.1	-224.2	-109.6	-9.8	-28.0	-15.7	-17.3	-95.8
MRC-4	1.0	-223.2	-109.0	-9.8	-28.0	-15.7	-17.3	-95.4
MRC-50-1	2.8	-203.3	-74.6	-4.2	-18.5	-11.0	-6.4	-89.3
MRC-50-2	1.0	-202.3	-109.5	-9.1	-28.2	-15.8	-15.7	-86.9
MRC -70-1	1.4	-188.4	-100.6	-7.3	-25.8	-14.6	-12.3	-81.7
MRC-5a	1.2	-222.0	-104.5	-9.1	-26.6	-15.0	-16.0	-95.1
MRC-5-b	1.3	-220.5	-102.6	-8.8	-25.9	-14.6	-15.3	-94.4
MRC-6-a	3.3	-221.8	-63.5	-3.5	-15.4	-9.4	-5.0	-97.5
MRC-6-b	2.9	-217.5	-69.9	-4.5	-17.4	-10.4	-7.0	-95.2
MRC-7	3.1	-222.1	-67.4	-3.8	-16.1	-9.7	-5.7	-97.0
MRC-8	2.2	-219.4	-85.2	-6.9	-22.2	-12.8	-11.8	-95.0
MRC-9	1.5	-217.4	-103.3	-9.6	-27.5	-15.5	-17.1	-93.2
MRC-10	2.0	-222.6	-84.2	-6.5	-21.5	-12.4	-11.0	-96.4
MRC-11	7.2	-240.8	7.8	6.9	5.5	1.0	15.9	-106.4
MRC-12	7.4	-242.2	6.7	7.0	5.6	1.1	16.0	-107.3
MRC-14	9.1	-245.8	-0.4	6.8	5.2	0.9	15.6	-110.7

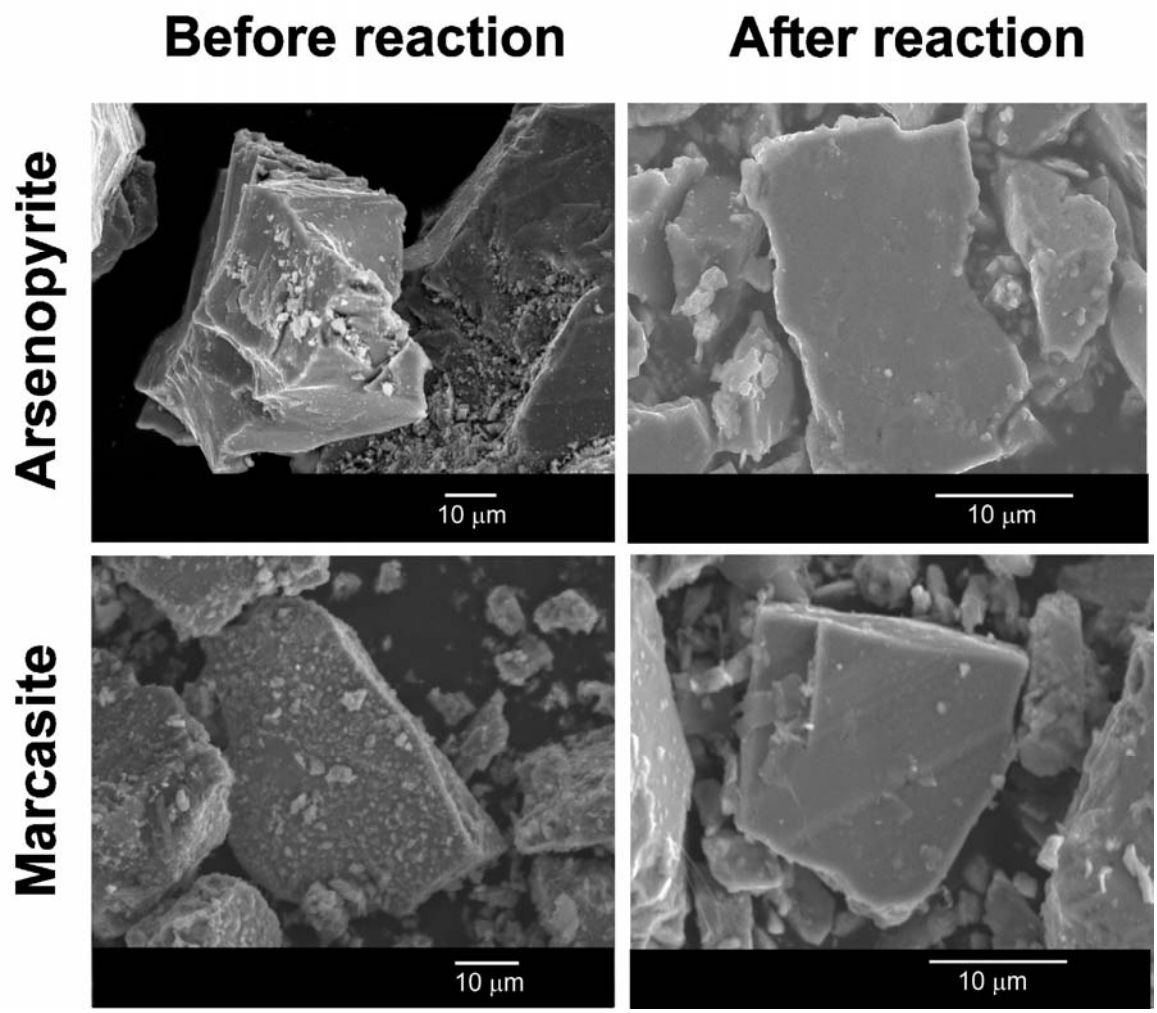

Figure 2.4. SEM images of freshly ground and sieved arsenopyrite and marcasite before experiments with attached microparticles and after dissolution at pH < 5 when microparticles are mostly dissolved.

2.2.3 Results based on surface spectroscopy

The results obtained by XPS examination of the samples before and after the flow-through experiments are summarized in Tables 2.7 and 2.8. The poor quality of the signal in the Fe2p region of the reacted arsenopyrite surfaces prevented the XPS identification of the iron surface species. The results show that, at acidic pH, arsenopyrite surface is enriched in arsenic and sulfur and marcasite in sulfur, whereas, at pH 4 to 9, the arsenopyrite surface is enriched in iron and arsenic and in iron in the case of marcasite, consistently with the solution results (Tables 2.1 and 2.2).

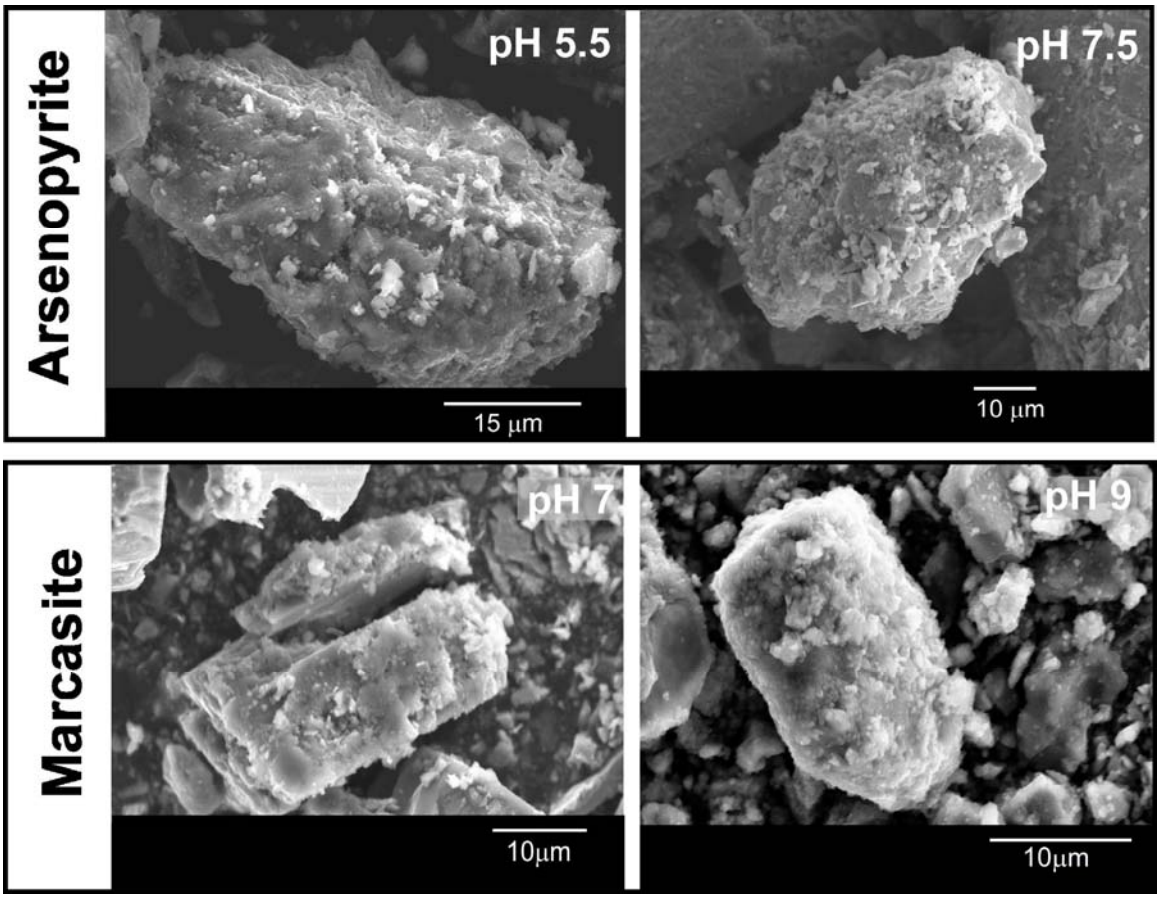

Figure 2.5. SEM images of the samples after representative flow-through experiments for the studied sulfides.

An examination of the S2p spectra of arsenopyrite reacted at acidic pH and 8.7 mg L^{-1} of DO (Fig. 2.6a) indicates the existence of three possible species at binding energies (BE) of approximately 161.3-161.7, 163.5-163.7 and 168.6-168.8 eV. These binding energies were identified as S^{2-}, polysulfides (S_n^{2-} where n≥2), and sulfate, respectively, according to the values reported in earlier studies (Buckley and Woods, 1985; Mycroft *et al.* 1990; Nesbitt and Muir, 1994; Pratt *et al.* 1994; Nesbitt *et al.*, 1995; Nesbitt and Muir, 1998; Hacquard *et al.* 1999). The detection of elemental S on the surfaces was practically impossible (i.e., this could not be confirmed or ruled out) owing to the technical limitations of the equipment used in the acquisition of the spectra. The examination of As3d peaks (Fig.2.6b) shows a major peak at approximately 45.3 eV, which corresponds to As(V) (Nesbitt and Muir, 1998). The shoulder of the low binding energy side may

Table 2.7. Results obtained from X-ray Photoelectron Spectroscopy (XPS) determinations on the initial and reacted arsenopyrite samples. Surface stoichiometry is represented by molar ratios.

Sample	pH	S	Fe (at. %) †	As	Fe/S	As/S	Fe/As
Initial FeAsS		*33.0*	*33.0*	*33.0*	*1*	*1*	*1*
ASP-25-1*	1.0	35.9	26.2	36.7	0.73	1.02	0.71
ASP-25-2*	2.7	35.1	20.7	42.1	0.59	1.20	0.49
ASP-25-3	1.2	37.5	27.5	34.2	0.73	0.91	0.80
ASP-25-4	3.1	34.7	28.7	35.6	0.83	1.03	0.81
ASP-25-23	5.8	17.2	41.4	38.4	2.40	2.23	1.08
ASP-25-11	9.1	33.8	47.4	18.9	1.40	0.56	2.51

† *Estimated normalizing out the rest of elements (oxygen and adventicious carbon)*
*H_2SO_4

indicate the contribution of As(-I) and As(II) species at binding energies of 41.3-41.7 eV and 43.3 eV, respectively (Buckley and Walker, 1988; Nesbitt *et al.*, 1995; Nesbitt *et al.*, 1998). Spectra of arsenopyrite surface after reacting at acidic pH and low input DO concentration (2 mg L^{-1}) showed that reduced sulfur and arsenic signals increased and the amount of the most oxidized species (As(V) and sulfates) decreased (Figs. 2.7 c,d).

Arsenopyrite XPS results in the pH range of 4.5-5.5 show changes with respect to the results obtained at acid pH. First, at this pH the amount of surface iron is higher than in the initial sample, which can be attributed to the presence of iron precipitates (e.g., Fe(III)-(hydr)oxides). In the S2p spectra two species are identified with an energy binding of 164.7 and 169.2 eV (Fig. 2.6e), which correspond to an intermediate oxysulfur (Schaufuss *et al.*, 2000) and sulfate, respectively. In the case of As3d peak the best fits of the spectra indicate the presence of a major contribution of As(V) and minor As(III) with peaks at 45.7 and 44 eV, respectively (Fig. 2.6f). In the range of pH 7-9, S2p spectra show that S(-I) oxidizes mainly to polysulfides, and the As3d spectra show a shoulder with binding energies in the range of 41.8-42 that may indicate the contribution of As(-I) and a major peak at approximately 45 eV, which corresponds to As(V) (Nesbitt and Muir, 1998) (Fig. 2.6g,h).

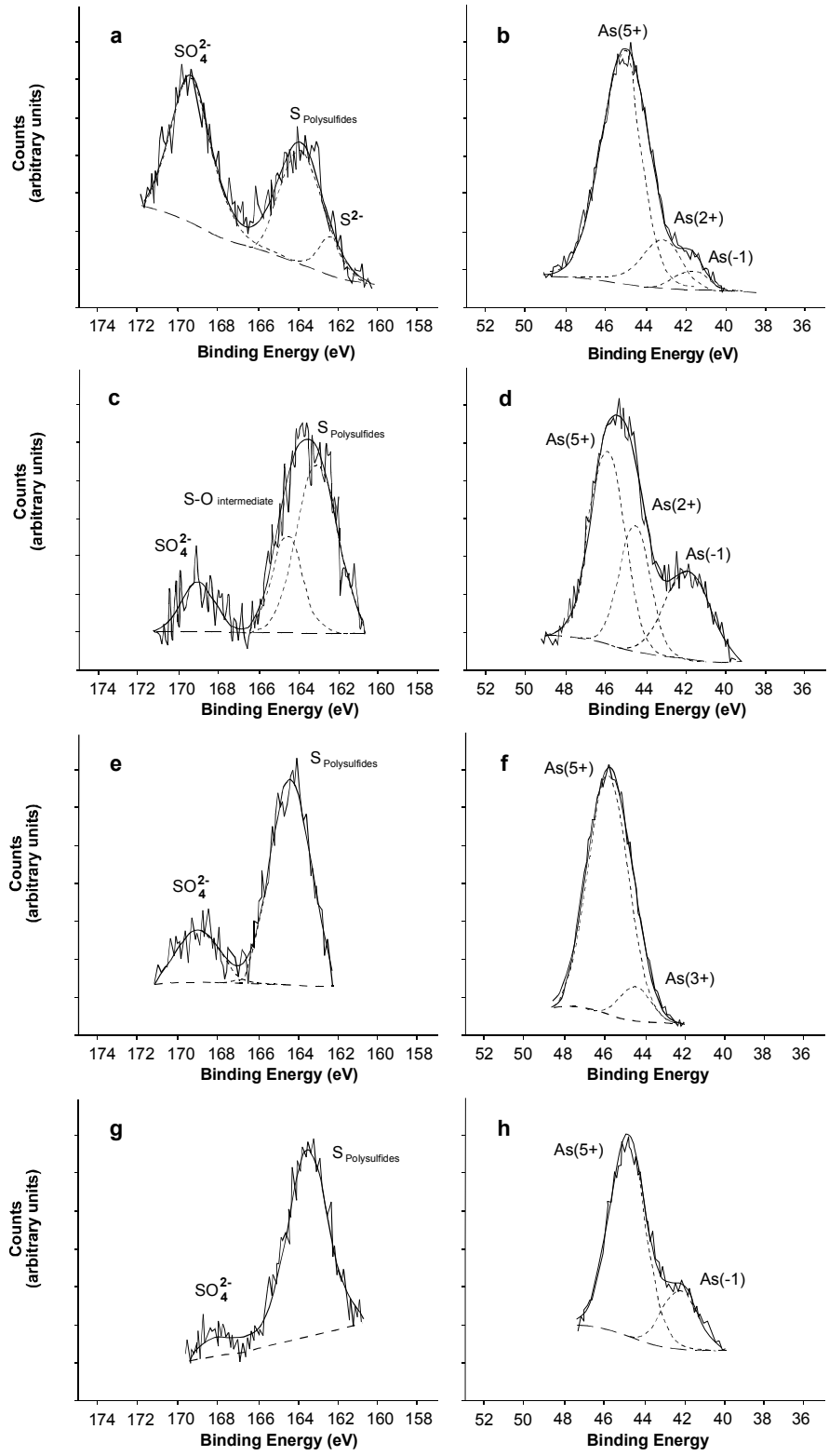

Figure 2.6. Curve fitted S2p and As3d spectra of arsenopyrite representative samples dissolved at 25ºC, 8.7 mg L^{-1} input DO and pH 3 (a) and (b); at 2 mg L^{-1} input DO and pH 3 (c) and (d); 8.7 mg L^{-1} input DO and pH 5.6 (e) and (f) and); 8.7 mg L^{-1} input DO and pH 7.

MicroRaman spectra for arsenopyrite are shown in Fig. 2.7. Reacted samples at acidic pH (1-3) show that the most intense peaks are at 472, 219 and 150 cm^{-1} (Fig. 2.7a). These peaks are attributed to elemental sulfur, whereas the other noticeable peaks are due to iron oxide and As_2O_3. This seems to indicate that, under acidic conditions, native sulfur could be a dominant surface species along with a minor amount of a stable phase iron oxide. MicroRaman spectra of samples reacted at pH 7 (Fig. 2.7b) show peaks that are associated with hematite, iron oxy(hydroxide), probably goethite, as well as traces of As-O and As_2O_3 (e.g., claudetite). Thus, secondary predominant surface species are pH dependent according to thermodynamics (e.g., see Brookins, 1988). It should be noted that native sulfur and iron oxy-hydroxides are very efficient Raman scatterers, i.e. the higher their crystallinity, the higher their Raman efficiency. Raman scattering involves hundreds of atomic layers below the surface.

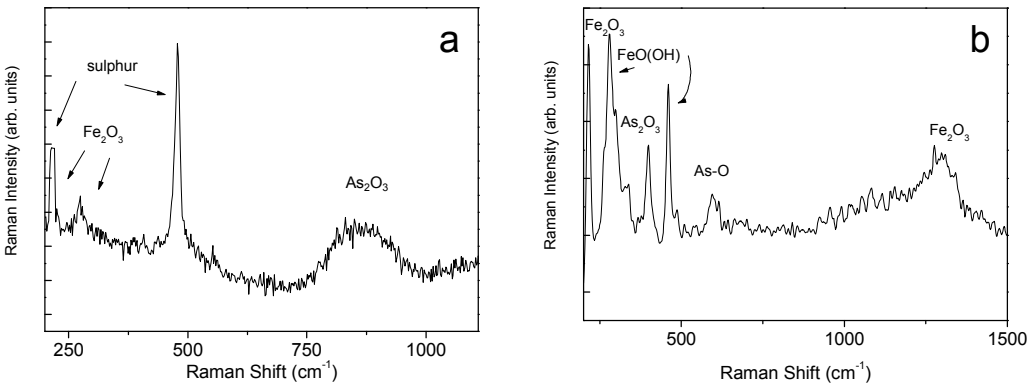

Figure 2.7. MicroRaman spectra of arsenopyrite samples reacted at 8.7 mg L^{-1} DO at 25 °C and at pH 3 (a); and pH 7 (b).

Hence, taking into account the saturation index of the output solution (Table 2.5) and the Raman microanalysis of the solids one can conclude that iron hydroxides such as goethite may be responsible for Fe depletion at pH higher than 5. Despite sulfur detection by Raman spectroscopy its formation at acidic pH in significant amounts is prevented by the subsaturated state of the solution.

Finally, As depletion at pH > 4 could be attributed to sorption on the Fe(III)-hydroxide surface. Accordingly, an estimation of the As sorption onto Fe-oxyhydroxide

Table 2.8. Results obtained from X-ray Photoelectron Spectroscopy (XPS) determinations on the initial and reacted marcasite samples. Surface stoichiometry is represented by molar ratios.

Sample	pH	S (at. %) †	Fe	Fe/S
Initial FeS_2	-	*67*	*33*	*0.50*
MRC-1	3.0	71	29	0.41
MRC-4	1.0	78	22	0.28
MRC-5	1.3	77	23	0.30
MRCS-70-1	1.4	75	25	0.33
MRC-50-2	1.0	76	24	0.32
MRC-12	7.4	43	57	1.33
MRC-14	9.1	33	67	2.04

† *Estimated normalizing out the rest of elements (oxygen and adventicious carbon)*

at pH range 4-9 was made on the basis of the Generalized Two layer-surface complexation model (Dzombak and Morel, 1990) using the PHREEQC code, a surface area of 600 $m^2\ g^{-1}$ (as described by Dzombak and Morel, 1990 for hydrous ferric oxide) and a surface site density of 2.3 sites nm^{-2} (Davis and Kent, 1990). Given the total amount of Fe-hydroxide, which was based on SO_4 released (< 0.1 g), the maximum amount of As(III) and As(V) sorbed was less than 10^{-9} mol As (at pH < 9.5). This arsenic amount was too low to account for the As that was retained in the experiments, which was higher than 1/5 Fe (i.e. 10^{-4} mol As). Therefore, the formation of an As phase seems to be responsible for As depletion at pH > 4. Based on the stoichiometry of our results, scorodite and/or pharmacosiderite could be responsible for As depletion. Beattie and Poling (1987) showed that, at pH values greater than 7, arsenopyrite oxidation results in the formation of secondary arsenic minerals such as pitticite [$Fe_2(AsO_4)(SO_4)OH{\cdot}2H_2O$) and pharmacosiderite ($6FeAsO_4{\cdot}2Fe(OH)_3{\cdot}12H_2O$). Similarly, Hacquard *et al.* (1999) observed the formation of an oxidation layer composed of Fe(III) arsenite and arsenate on the arsenopyrite surface after reacting with a solution of pH 10.

In the case of marcasite, an examination of the S2p spectra of samples after reacting in the range of pH studied (1-9) and 8.7 mg L^{-1} of dissolved oxygen (Fig. 2.8) suggests the existence of two possible species at binding energies of 163.0-163.8 eV and 168.2-169.3 eV. Based on the BE values reported in earlier studies (Buckley and Woods, 1987; Mycroft *et*

al. 1990; Nesbitt and Muir, 1994; Pratt *et al.* 1994; Nesbitt *et al.*, 1995; Nesbitt and Muir, 1998; Hacquard *et al.* 1999; Elsetinow *et al.*, 2003) the species identified at middle binding energies were attributed to either polysulfides or elemental sulfur, and the highest value was attributed to sulfates.

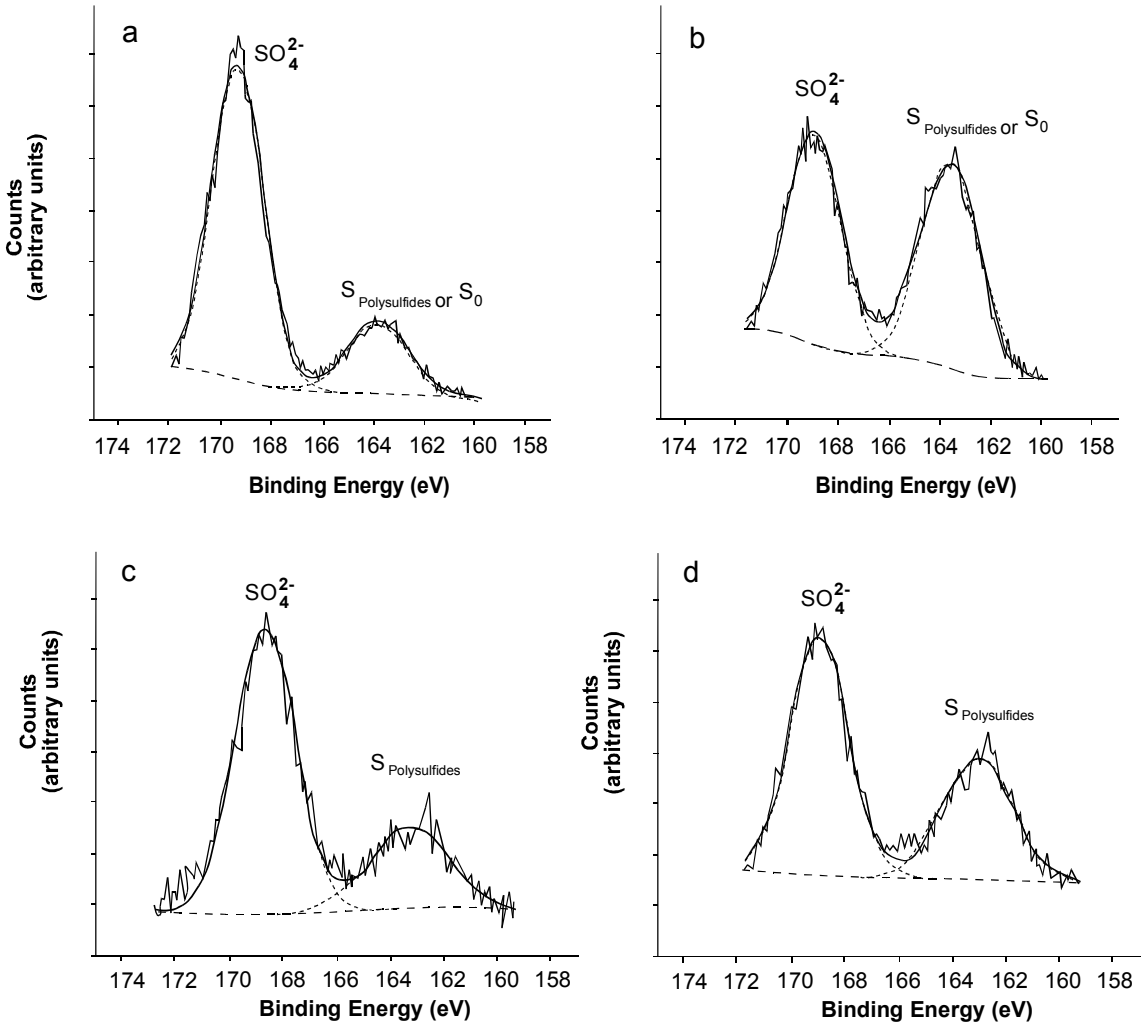

Figure 2.8. Curve fitted S2p spectra of representative samples after the flow through experiment at pH 1 (a), pH 3 (b), pH 7 (c) and pH 9 (d) and 8.7 mg L^{-1} of dissolved oxygen and 25ºC.

The surface Fe/S ratios obtained suggest an enrichment of sulfur in the reacted marcasite during dissolution at acidic pH (Table 2.8). These products are composed of polysulfides and sulfates, although the presence of elemental sulfur cannot be ruled out. This sulfur enrichment has been observed to develop in other reacted sulfides surfaces (Acero *et al.*, 2007a,b and c) and also in reacted marcasite by Rinker *et al.* (1997) who

observed the formation of a discontinuous S-rich and Fe deficient surface layer on dissolving marcasite. According to the variation in iron and sulfur aqueous concentrations durable steady states in all the experiments carried out were achieved, which suggests that the solid products on the reacted mineral surfaces do not seem to cause a progressive increase in marcasite passivation.

At neutral-basic pH the results show that marcasite surface is enriched in iron and according to the saturation indices obtained iron hydroxides such as goethite and ferrihydrite may be responsible for Fe depletion at pH 7-9.

2.3 Discussion

2.3.1 Evolution of the arsenopyrite and marcasite surfaces during dissolution

Inspection of the reacted samples confirmed that the arsenopyrite and marcasite surface undergoes critical variation as a function of pH, which influenced the overall oxidative dissolution of arsenopyrite and marcasite. At pH < 4 the overall oxidative dissolution of arsenopyrite (eq. 2.7) and marcasite (eq. 2.8) can be simplified as:

$$FeAsS_{(s)} + \frac{11}{4}O_{2(aq)} + \frac{3}{2}H_2O = Fe^{2+} + H_3AsO_3 + SO_4^{2-} \quad (2.7)$$

$$FeS_{2(s)} + H_2O + \frac{7}{2}O_{2(aq)} \Rightarrow Fe^{2+} + 2SO_4^{2-} + 2H^+ \quad (2.8)$$

Hence, steady-state dissolution rates were obtained at pH < 4 based on As and Fe release normalized with respect to final BET specific surface area (Tables 2.1 and 2.3). The dissolution rates obtained in the experiments carried out in H_2SO_4 (pH 1 and 3) were the same, within error, as the rates obtained in HCl. This agreement shows that the arsenopyrite and marcasite dissolution rates obtained in this study are applicable to

acidic environments with sulfate as the main anionic species (e.g., systems affected by acid mine drainage).

From pH 5 to 6, arsenopyrite dissolution yielded Fe/As and Fe/S aqueous ratios lower than one indicating that iron depletion during dissolution was incomplete (Fig. 2.2). Likewise, incomplete arsenic depletion was observed, giving 0.81 < S/As < 1.38. At pH ranging from 7 to 9, aqueous iron was completely depleted in both minerals (below the detection limit), and As depletion, higher than that at pH 5-6, was observed during arsenopyrite dissolution.

Therefore, at pH > 5 released ferrous iron rapidly oxidized to ferric iron, which precipitated as Fe-solid phases:

$$Fe^{2+} + \frac{1}{4}O_{2(aq)} + \frac{5}{2}H_2O = Fe(OH)_{3(s)} + 2H^+ \qquad (2.9)$$

In the case of arsenopyrite As(III) can be oxidized to As(V) by oxygen (eq. 2.10 at pH ≤ 7 and eq. 2.11 at pH > 7) (Tallman and Shaikh, 1980; Eary and Schramke, 1990; Walker *et al.*, 2006):

$$H_3AsO_3 + \frac{1}{2}O_{2(aq)} = H_2AsO_4^- + H^+ \qquad (2.10)$$

$$H_3AsO_3 + \frac{1}{2}O_{2(aq)} = HAsO_4^{2-} + 2H^+ \qquad (2.11)$$

To simplify, the variable S/As aqueous ratio (Table 2.2), can be interpreted as variable proportions in the formation of scorodite and $Fe(OH)_3$ phases:

$$Fe^{2+} + \frac{1}{4}O_{2(aq)} + HAsO_4^{2-} + \frac{3}{2}H_2O = FeAsO_4 \cdot 2H_2O_{(s)} \qquad (2.12)$$

The amorphous $Fe(OH)_3(s)$ may represent ferrihydrite, which could transform into hematite and/or goethite as pH increased from 5 to 13 (Schwertmann and Murad, 1983). This is a simplification and mixed phases (e.g. pharmacosiderite) can also be possible.

The precipitated Fe(III) and As-bearing phases in the case of arsenopyrite form a coating on the mineral grains as dissolution proceeds. As stated above, this process was modelled using the shrinking core model (SCM). Thus, the limiting process of arsenopyrite dissolution at pH > 4 is the diffusion of $O_{2(aq)}$ through the coating, resulting in the dissolution of the unreacted core of arsenopyrite and marcasite.

An important parameter that governs dissolution under the SCM is the stoichiometry of $O_{2(aq)}$ in the dissolution reactions (ν_{ox}), which according to the addition of eqs. 2.9, 2.10 or 2.11 (depending on pH) to eq. 2.7 and eq. 2.9 to 2.8 is 15/4 for arsenopyrite and marcasite.

An example of application of the SCM that simulates the variation in sulfate concentration versus time at pH 9 and 0.27 mol m^{-3} $O_{2(aq)}$ is depicted in Fig. 2.9. As expected, the early values are sensitive to k value, whereas the influence of D increases with time. The effect of coating can be observed in the plot. After 500 h only 1.7 mol % of initial marcasite was dissolved. However, had no coating been formed the dissolution of marcasite would have been 4.4 mol %. As discussed above, when the studied minerals dissolved at pH < 4 no precipitates were observed on their surfaces under SEM inspection. As expected, the variation of the solute concentration reached steady state after an initial time span (Figs. 2.2 and 2.3), and the dissolution rate constant can be calculated using eq. (2.1). Given that the removal of arsenopyrite and marcasite mass is constant in these experiments, their t-X plots show a linear trend, values of k (m s^{-1}) can also be estimated by fitting the experimental data to eq. (2.4). Since the initial radius is calculated assuming spherical particles from the BET specific surface area measured (eq. 2.6), the derived rate values (mol m^{-2} s^{-1}) (eq. 2.6) are practically coincident with the rate values obtained using steady state (eq. 2.1) (see Tables 2.1 and 2.3).

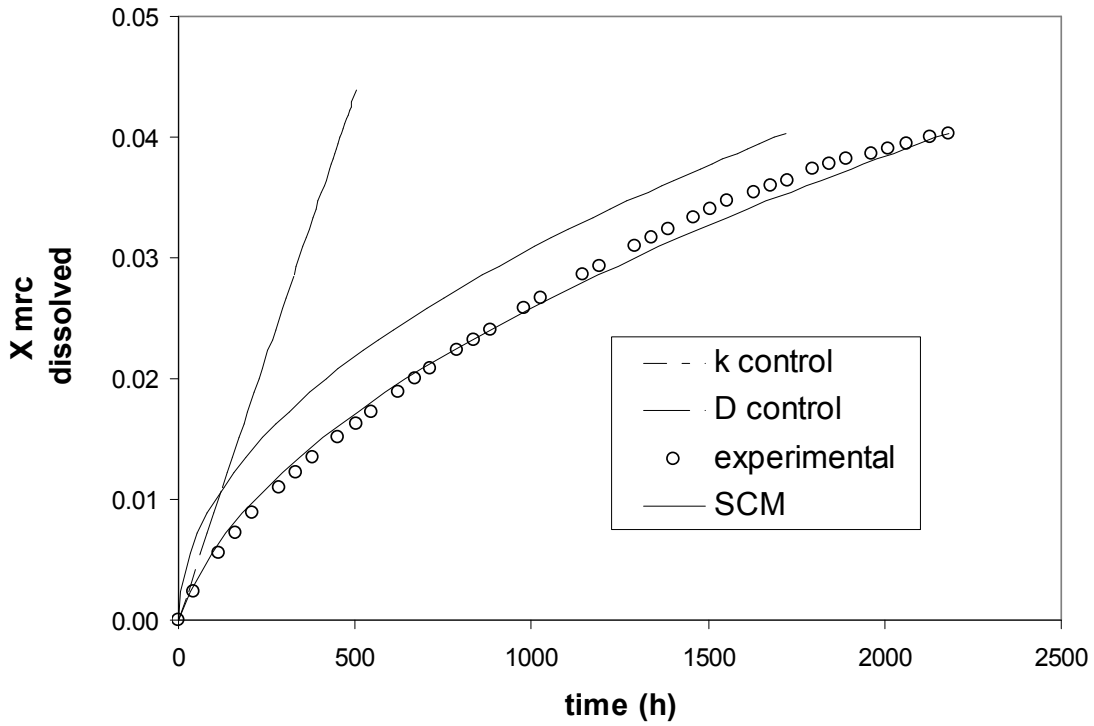

Figure 2.9. Evolution of the mole fraction of dissolved marcasite in an experiment carried out at pH 9 and 25ºC and 8.7 mgL^{-1} of dissolved oxygen. The curves are the plot of the process controlled by the surface dissolution step (eq. 2.4), by the diffusion across the coating step (eq. 2.5), and by the SCM model (addition of eq. 2.4 and 2.5).

The value of D estimated for the experiments that follow the SCM pattern varies within a range of 10^{-20}-10^{-15} m^2 s^{-1}. No variation with pH is apparent. Nicholson *et al.* (1988) estimated a D value for the coating of pyrite of $3 \cdot 10^{-16}$, which is in the higher range of our experimental results. As discussed above, the value of D depends on R^2 (the value assumed for initial radius, eq. 2.5), which in our case is smaller than that reported in the pyrite case. Furthermore, the D values estimated here are 5 to 10 orders of magnitude lower than the diffusion coefficient of $O_{2(aq)}$ in free water at 25°C (Wilke and Chang, 1955). This difference is too large to be attributed to porosity and tortuosity of a porous medium. On the other hand, these D values are higher than the diffusion coefficient values that are typical of solids (10^{-20} to 10^{-34} m^2 s^{-1}, Levine, 1978), but could be similar to those of poorly crystalline solids as suggested by Nicholson *et al.* (1988).

2.3.2 Effects of pH, DO and temperature on dissolution rates

Under far-from-equilibrium conditions, an empirically derived dissolution rate law that accounts for the effects that pH, dissolved oxygen and temperature exert on sulfide dissolution has been proposed as (McKibben and Barnes, 1986; Williamson and Rimstdit, 1994; Domènech *et al.*, 2002):

$$Rate = k \cdot a_{O2(aq)}^{n} \cdot \left(a_{H^+}\right)^{m} \tag{2.13}$$

where Rate is in mol m^{-2} s^{-1}, k is the dissolution rate constant, $a_{O2(aq)}$ and a_{H^+} are the activities of dissolved oxygen and hydrogen ions in solution. The factors m and n are the reaction orders of the reaction with respect to hydrogen ion activity and dissolved oxygen concentration in solution, respectively.

2.3.2.1 The effect of dissolved oxygen on dissolution rates

The dependence of arsenopyrite and marcasite dissolution rates on dissolved oxygen concentration was assessed at 25ºC and acidic pH (Tables 2.1 and 2.3, Fig. 2.10). The rates obtained are DO-dependent, decreasing when the dissolved oxygen concentration is diminished. This type of dependence has been reported for arsenopyrite (Yu *et al.*, 2007; McKibben *et al.*, 2008) and for pyrite (Nicholson *et al.*, 1988; Williamson and Rimstidt, 1994; Domènech et al, 2002). The reaction order with respect to dissolved oxygen at acidic pH was found to be 0.60 and 0.33 for arsenopyrite and marcasite dissolution, respectively (Fig. 2.10). The obtained values in this study are in the same order as the values reported by Smith and Schumate (1970) who found a value of 0.7 for a mixture of pyrite and marcasite, or Kamei and Ohmoto (2000), Manaka *et al.* (2000), and Manaka (2007) with values from 0.5 to 1 for pyrite, or McKibben (1984), Williamson and Rimstidt (1994) and Domènech *et al.* (2002) for pyrite (0.4-0.5±0.04) at pH 2-10. In the case of arsenopyrite, the obtained value is higher than those reported by Yu *et al.* (2007) (0.45±0.05) at pH 5.9 and McKibbben *et al.* (2008) (0.33±0.18) at pH 2-4.5.

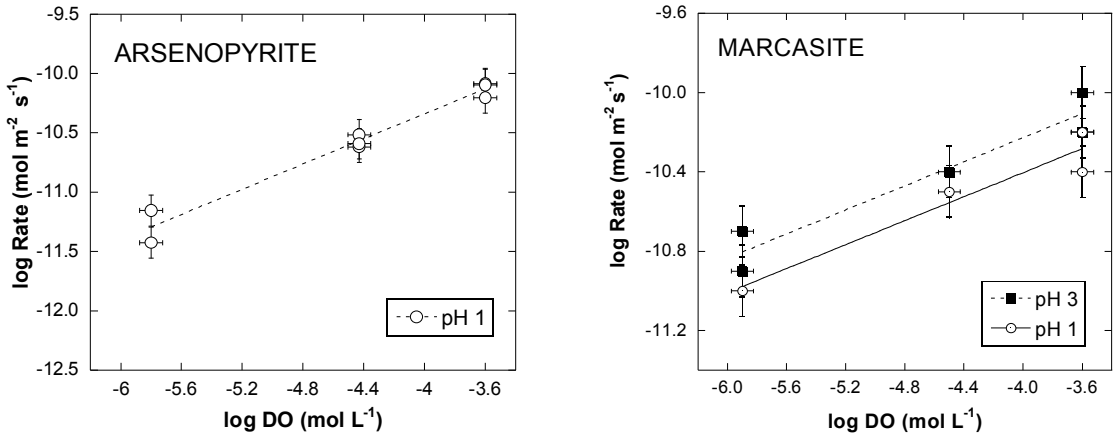

Figure 2.10. Arsenopyrite and marcasite dissolution rate dependence on dissolved oxygen at 25ºC.

2.3.2.2 The effect of temperature on the dissolution rates

The temperature dependence of dissolution rate generally follows the Arrhenius law:

$$Rate = Ae^{-E_{app}/RT} \tag{2.14}$$

where A is the pre-exponential factor, E_{app} is the apparent activation energy, R is the gas constant and T is the temperature (K). To obtain experimentally the apparent activation energy at acidic pH, experiments were carried out at 25, 50 and 70°C at pH 1 and 3 by maintaining constant both the pH and dissolved O_2 concentration (Tables 2.1, and 2.3 and Fig. 2.11).

The apparent activation energies for arsenopyrite and marcasite oxidation by oxygen in acidic conditions were 30.7 and 12.0 kJ mol^{-1}, respectively.

In the case of marcasite, the apparent activation energy obtained indicates that the overall dissolution mechanism appears to be a diffusion-controlled process. Values of the activation energy lower than 20 kJ mol^{-1} are usually associated with transport-controlled dissolution mechanisms (Lasaga, 1998; Brantley and Conrad, 2008). When the dissolution of a mineral is transport-controlled, it is expected to produce general rounding of the

grains, if the amount of mineral dissolved is significant, and variations in the dissolution rate if the stirring rate is changed (Berner, 1980). No change was observed in the shape of the grains after the experiments (Fig. 2.4) or in the dissolution rates obtained with and without stirring. At present there is no explanation for the apparent inconsistency between these observations and the low value obtained for the apparent activation energy. Rinker *et al.* (1997) reported a high E_{app} value for marcasite dissolution with respect to the one obtained in this study (Table 2.9), probably because of the short duration of their batch experiments (around 8 h) and the insufficient time to reach steady-state rates. Hence, the reported E_{app} is not comparable to the one obtained in our long-term flow through experiments.

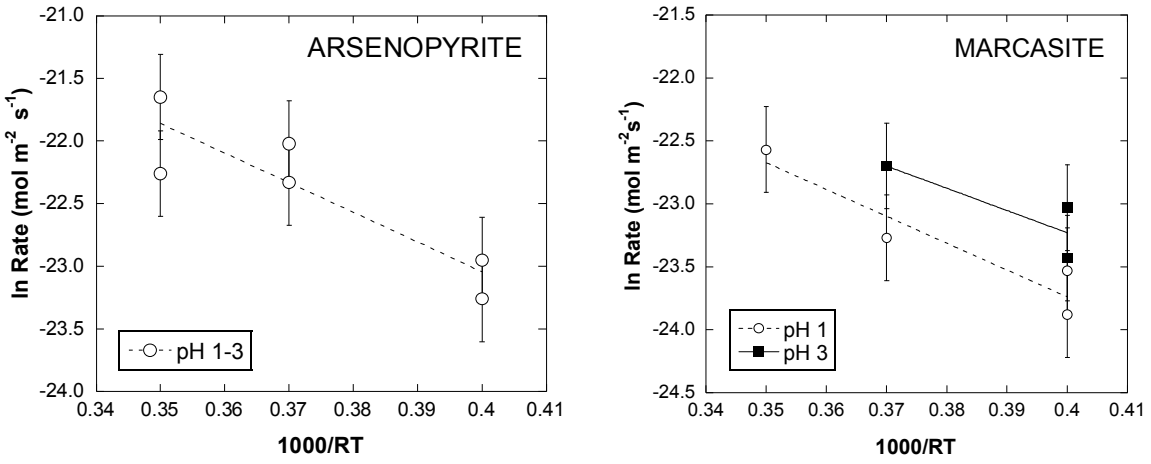

Figure 2.11. Arsenopyrite and marcasite dissolution rate dependence on temperature at 8.7 mg L^{-1} of dissolved oxygen.

In the case of arsenopyrite, Yu *et al.* (2007) using short-term flow reactors (6-8 h) reported E_{app} values (kJ mol^{-1}) of 43 (pH 1.8) and 57 (pH 5.9). McKibben *et al.* (2008) carrying out short-term batch experiments at pH 2-4.5 obtained a complicated non-Arrhenius behavior. The E_{app} value obtained in this study (30.7 kJ mol^{-1}) suggests that the arsenopyrite dissolution is a surface controlled process.

2.3.2.3 The effect of pH on dissolution rates

In the absence of other catalysts, the dissolution rate of a mineral within certain pH ranges, in which the dissolution mechanism does not change, is proportional to a fractional power of the H^+ activity according to:

$$R = ka_{H+}^{m} \tag{2.15}$$

where a_{H+} is the activity of hydrogen ion in the solution, m is the order of the reaction with respect to H^+, and k is a rate constant.

Fig. 2.12 plots logarithm of the rates vs. pH at 25ºC and dissolved O_2 concentration of 8.7 mg L^{-1}. From pH 1 to 4 the arsenopyrite and marcasite dissolution rate scarcely changes with pH. At pH 5-6 arsenopyrite dissolution rate is similar to that at pH < 4. Therefore, it suggests that hydrogen ion effect on the dissolution rates in this pH range is negligible. This result is consistent with the insignificant pH dependence reported previously by Yu *et al.* (2007) for arsenopyrite and by Williamson and Rimstdit (1994) and Domènech *et al.* (2002) for pyrite (see Table 2.9).

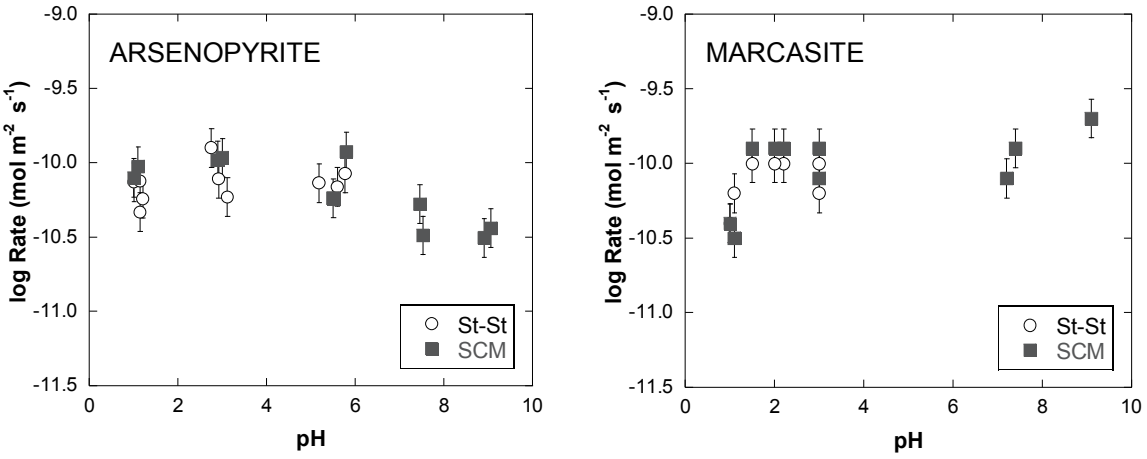

Figure 2.12. Arsenopyrite and marcasite dissolution rates versus pH at 25ºC of temperature and at 8.7 mgL^{-1} of dissolved oxygen based on steady-state (St-St) conditions and obtained using the Shrinking Core Model (SCM).

The effect of pH assessed in the range of 7-9, is in the order to study the conditions found in the treatments used in acid neutralization to remediate AMD contaminated sites. The results show that arsenopyrite, in the pH range of 7.5 to 9, dissolves slower than at acid pH. The same trend was observed by Yu *et al.* (2007) at pH 7-8. Marcasite was found to be independent on pH at the range of pH considered in this study.

2.3.3 Dissolution rate laws

Considering the effects of the environmental variables studied (pH, DO and temperature) on mineral dissolution, the reaction orders *n* and *m* and the apparent activation energy (E_{app}) and the rate dissolution constant (*k*), were estimated from multiple linear regression of the rates (Tables 2.1 and 2.3), yielding the following expression for the arsenopyrite dissolution rate laws at acidic pH:

$$R_{arsenopyrite}\,(mol\,m^{-2}\,s^{-1})_{25^\circ C} = 10^{-8.07\pm0.25}\cdot a_{O_2}^{0.60\pm0.05}\cdot a_{H^+}^{-0.05\pm0.05} \qquad (2.16)$$

$$R_{marcasite}\,(mol\,m^{-2}\,s^{-1})_{25^\circ C} = 10^{-9.10\pm0.14}\cdot a_{O_2}^{0.33\pm0.03}\cdot a_{H^+}^{-0.08\pm0.04} \qquad (2.17)$$

where the value of the Apparent Activation Energy has been found to be 30.7 and 12.0 kJ mol^{-1} for arsenopyrite and marcasite respectively at acid pH values.

A comparison of arsenopyrite dissolution kinetics and that of other As-bearing sulfides (arsenopyrite (AsFeS), orpiment (As_2S_3), realgar (AsS)) and pyrite is shown in Fig. 2.13. Table 2.9 gives the dissolution rates and kinetic parameters obtained in these studies of sulfides: pyrite (Williamson and Rimstidt, 1994; Domènech et al, 2002); orpiment and realgar (Lengke and Tempel, 2002, 2003), and arsenopyrite (Walker *et al.*, 2006; Yu *et al.*, 2007; McKibben *et al.*, 2008). It is important to highlight that different experimental setups and experimental conditions were used in these studies, and that dissolution processes and mechanisms of As-bearing sulfide dissolution may not be the same. Note that sulfide dissolution rates obtained in very short-term experiments (< 50 h)

are usually one order of magnitude faster (Yu *et al.*, 2007; McKibben *et al.*, 2008). Indeed, on the onset of our long-term experiments apparent dissolution rates were faster than steady-state rates. Thus, the advantage of the long-term experiments is that achievement of durable steady state (> 300 h) guarantees the reaction to proceed under steady mineral-solution conditions. Therefore, it is suggested that quantification of arsenopyrite oxidation at acidic mine wastes is appropriately obtained by the long-term experiments.

As shown in Table 2.9 marcasite dissolution rate obtained is lower than the rate proposed by Rinker *et al.* (1997). This difference may again be attributed to the shorter duration (less than 8 h) of the experiments in the work of Rinker *et al.* (1997).

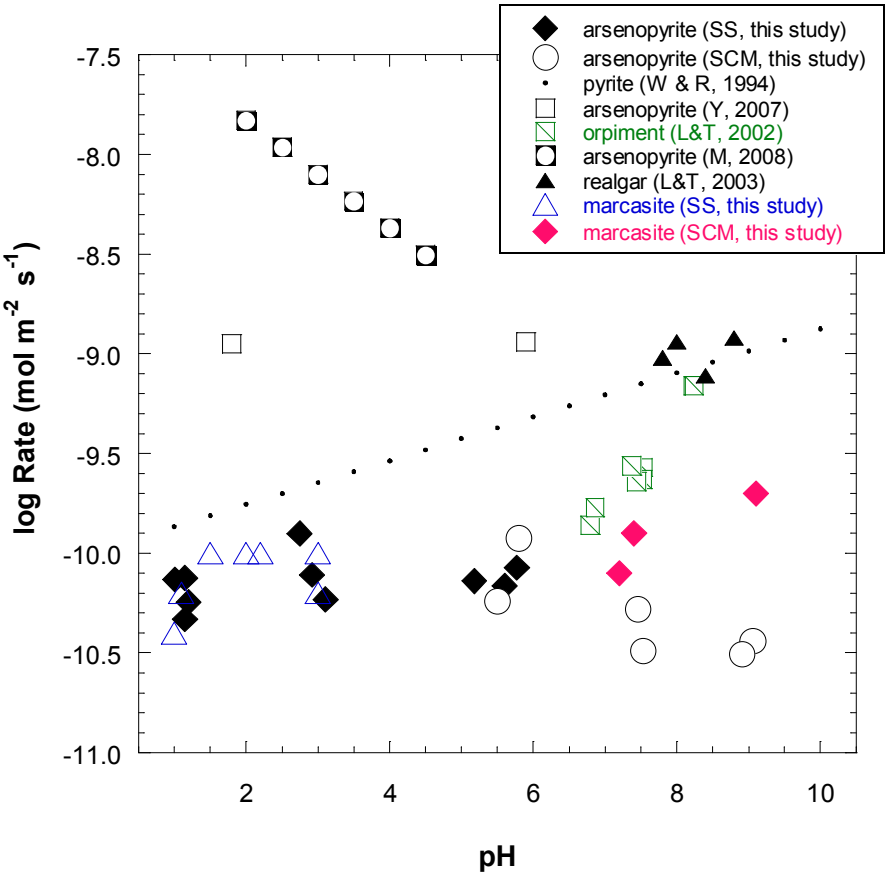

Figure 2.13. Comparison of arsenopyrite and marcasite oxidative dissolution rates obtained in the present study with rates of arsenopyrite, orpiment, natural realgar and pyrite found in the literature as a function of pH at 25°C and 8.7 mg L^{-1} DO. SS: Steady-state; SCM: Shrinking Core Model; W&R, 1994: Williamson and Rimstdit (1994); L&T, 2002: Lengke and Tempel (2002); L&T, 2003: Lengke and Tempel (2003); M, 2008: McKibben *et al.* (2008).

Table 2.9. As-bearing sulphide and pyrite dissolution rate laws obtained in earlier studies.

	Experiment type	pH	Temp.	DO	Activation Energy	Dissolution Rate	Duration experiment
			(ºC)	(mgL^{-1})	($kJ\ mol^{-1}$)	($mol\ m^{-2}\ s^{-1}$)	(h)
Arsenopyrite (FeAsS)							
Walker *et al*. (2006)	Mixed flow reactor	6.3-6.7	25	0.3-17	-	$r=10^{-10.14\pm0.03}$	30
Tallant and McKibben (2005)	Batch flow reactor	2-4.5	-	-	14.5	$r = k\ [O_{2(aq)}]^{0.40}\ a_{H+}^{\ 0.24}$	-
McKibben *et al.* (2008)	Batch flow reactor	2-4.5	10-40	-	-	$r = 10^{-6.11}[O_{2(aq)}]^{0.33(\pm0.18)}\ a_{H+}^{\ 0.27(\pm0.09)}$	-
Yu *et al*. (2007)	Mixed flow reactor	1.8-6.4	15-45	0.2-24.6	57	$r=10^{-(-2211\pm57)/T}\ [O_{2(aq)}]^{0.45\ (\pm0.05)}$	6-8
Orpiment (As_2O_3)							
Lengke and Tempel (2002)	Mixed flow reactor	6.8-8.2	25-40	6.4-17.4	59.1	$r = 10^{-11.77\ (\pm0.36)}\ [O_{2(aq)}]^{0.36\ (\pm0.09)}\ a_{H+}^{\ -0.47\ (\pm0.05)}$	~30
Lengke and Tempel (2001)	Mixed flow reactor*	6.9-7.9	25-40	7-19	16.8	$r_{As} = 10^{-16.77\ (\pm0.68)}\ [O_{2(aq)}]^{0.42(\pm0.07)}\ a_{H+}^{\ -1.26(\pm0.09)}$	~30
					16.3	$r_S=10^{-16.69\ (\pm0.67)}\ [O_{2(aq)}]^{0.35(\pm0.08)}\ a_{H+}^{\ -1.25(\pm0.09)}$	
Realgar (AsS)							
Lengke and Tempel (2003)	Mixed flow reactor	7.2-8.8	25-40	5.9-16.5	64.2	$r_{As} = 10^{-9.63\ (\pm0.41)}\ [O_{2(aq)}]^{0.51(\pm0.08)}\ a_{H+}^{\ -0.28(\pm0.05)}$	~30
					62.2	$r_S=10^{-9.74(\pm0.35)}\ [O_{2(aq)}]^{\ 0.54(\pm0.05)}\ a_{H+}^{\ -0.31(\pm0.04)}$	
	Mixed flow reactor*				124	$r = 10^{-13.65\ (\pm0.82)}\ [O_{2(aq)}]^{0.92\ (\pm0.08)}\ a_{H+}^{\ -1.09\ (\pm0.10)}$	~30
Marcasite (FeS_2)							
Rinker *et al*. (1997)	Batch reactor	3	25-35	8.7	71	$r = 4.25\cdot10^{-8}$	7.5
Pyrite (FeS_2)							
Domenech *et al*. 2002	Flow through reactor	2.5-4.7	22	0.1-4.3	-	$r = 10^{-7.8\ (\pm0.3)}\ [O_{2(aq)}]^{0.50\ (\pm0.04)}\ a_{H+}^{\ 0.10\ (\pm0.06)}$	1000
Williamson and Rimstdit (1994)	*Based in reported data*	2-10	-	-	-	$r = 10^{-8.19\ (\pm0.1)}\ [O_{2(aq)}]^{0.50\ (\pm0.04)}\ a_{H+}^{\ -0.11\ (\pm0.01)}$	-

* amorphous specimen

In line with this explanation, the dissolution rates obtained for marcasite and arsenopyrite in this work are in very good agreement with the rates obtained by Domènech *et al.* (2002) for pyrite, or Acero *et al.* (2007a,b,c, 2009) for sphalerite, chalcopyrite and galena based on long dissolution experiments. Likewise, the obtained rate laws obtained for both minerals and the influence exerted by pH and oxygen are similar than reported for pyrite by many authors such as Williamson and Rimstidt (1994) or Domènech *et al.* (2002), probably indicating that all these minerals present the same behavior under similar conditions.

2.4 Conclusions

In this chapter, dissolution rate laws applicable to the prediction of the long-term dissolution behavior of arsenopyrite and marcasite in environments undergoing acid drainage have been obtained.

Under the experimental conditions of this study the dissolution of arsenopyrite and marcasite dissolution is strongly affected by dissolved oxygen and slightly affected by temperature.

The low values obtained for the apparent activation energy for both sulfides in the studied conditions suggest that their dissolution kinetics is controlled by transport processes or mixed-controlled by surface reactions and transport processes.

In the light of the experimental results, two regions can be distinguished from arsenopyrite and marcasite oxidative dissolution: (1) an acidic region ($1 < pH < 5$) when aqueous iron is released to the solution and (2) at mildly acid to basic pH ($pH > 5$) when iron released precipitates.

The dissolution of both minerals in acid conditions creates a sulfur-enriched surface layer. This layer is mainly made up by polysulfides and sulfates in both minerals

although the presence of elemental sulfur can not be ruled out. However, these layers do not exert any passivating effect once the steady state is attained.

At midly acid to basic pH, the precipitation of Fe phases takes place. Fe-coating grows on the mineral surface and prevents the diffusion of aqueous species through it. Thus, steady state is not attained and the output concentration decreased with time. These results are representative of the conditions found in remediated sites: Fe-layers enhance mineral surface passivation, and in addition, the high stability of Fe oxy(hydroxide) at circumneutral pH provides a considerable retention capacity of toxic metal(oid)s, such as arsenic, that are in non-admissible levels in AMD.

The dissolution rates obtained for both minerals at atmospheric conditions in this work are similar, and also they are in good agreement with the reported rates for pyrite, sphalerite, chalcopyrite and galena based on long-term dissolution experiments. It is very common that the available dissolution rates for sulfide minerals are obtained in short-batch experiments. As shown by this study, the use of these rates may lead to an overestimation of the dissolution rates.

Part II

Natural attenuation processes

Chapter 3

Chemical oxidation processes

Arsenic is perhaps unique among the heavy metalloids and oxyanion-forming elements (e.g. As, Se, Sb, Mo, V, Cr, U, Re) in its sensitivity to mobilization at the pH values typically found in groundwaters (pH 6.5–8.5) and under both oxidizing and reducing conditions (Smedley and Kinniburgh, 2002). Arsenic can occur in the environment in several oxidation states (-3, 0, +3 and +5) but in natural waters it is mostly found in inorganic form as oxyanions of trivalent arsenite [As(III)] or pentavalent arsenate [As(V)]. Although organic As forms are produced by biological activity, mostly in surface waters, they are uncommon. However, they may occur where waters are significantly impacted by industrial activities (Smedley and Kinniburgh, 2002).

Aqueous arsenic species are controlled by pH and redox conditions. In most natural waters (pH ~ 4–10), the most widespread species are the neutral species H_3AsO_3 for arsenite, and $H_2AsO_4^-$ and $HAsO_4^{2-}$ for arsenate (Cullen and Reimer 1989). At acid pH range, the dominant species are H_3AsO_3 for arsenite and H_3AsO_4 and $H_2AsO_4^-$ for arsenate.

Very high concentrations of arsenic can be found in sulfide mining areas (e.g. IPB) owing to the oxidation of As-bearing sulfide minerals (e.g. As rich-pyrite and arsenopyrite) (Williams, 2001). Arsenic concentrations in these waters can reach up 5-6 orders of magnitude higher than the established limit of 10 μg L^{-1} for potable water (WHO, 2004).

Given that arsenopyrite is the dominant arsenic mineral in most As-bearing natural occurrences, it is mainly responsible for elevated arsenic concentrations at surface sites (Smedley *et al.*, 1996). At acidic pH, its dissolution can be expressed as:

$$FeAsS_{(s)} + \frac{11}{4}O_{2(aq)} + \frac{3}{2}H_2O = Fe^{2+} + H_3AsO_3 + SO_4^{2-} \qquad (3.1)$$

Dissolution of arsenopyrite mainly releases As(III) (Yu *et al.*, 2007; Cama *et al.*, 2008), which could be oxidised by O_2 (Tallman and Shaikh, 1980; Eary and Schramke, 1990) (eq. 3.2) and Fe(III) (Cherry *et al.*, 1979; Emett and Khoe, 2001; Hug *et al.*, 2001; Bednar *et al.*, 2002) (eq. 3.3):

$$H_3AsO_3 + \frac{1}{2}O_{2(aq)} = H_2AsO_4^- + H^+ \qquad (3.2)$$

$$2Fe^{3+} + H_3AsO_3 + H_2O \rightarrow 2Fe^{2+} + H_3AsO_4 + 2H^+ \qquad (3.3)$$

Although arsenite oxidation by oxygen and Fe(III) is slow, especially under acidic conditions, it may be catalyzed by the activity of bacteria (Wakao *et al.*, 1988; Leblanc *et al.* 2002; Bruneel *et al.*, 2003; Casiot *et al.*, 2003b; Duquesne *et al.*, 2007; Nakazawa and Hareyama, 2007) or by the presence of iron and illumination with near ultraviolet light (Emett and Khoe, 2001). There are some works on arsenic mobilization in acid drainages showing that arsenite oxidation in these environments is carried out at relatively significant rates during daytime (e.g. Sarmiento *et al.*, 2007).

Arsenite oxidation is of considerable importance since the resulting As(V) is less toxic than As(III), less soluble, and is sorbed more strongly than As(III) to Fe(III) oxides and hydroxides under acidic conditions (Bowell, 1994). Trapping of arsenic by iron minerals is an efficient natural attenuation process that considerably reduces the arsenic concentration in AMD waters.

Knowledge of the simultaneous occurrence of Fe(II) and As(III) oxidation, and of the oxidation rates is of great value in the prediction of iron and arsenic behavior in natural systems. The connection between iron and arsenic redox reactions play an important part in understanding the fate of arsenic in AMD environments since arsenic speciation and redox chemistry is reportedly controlled by Fe in solution in AMD systems (Daus *et al.*, 2002; Bednar *et al.*, 2005; Sarmiento *et al.*, 2007). Despite the significant role of these oxidation processes in the natural attenuation of arsenic, little work has been done on the simultaneous oxidation of iron and arsenic. This chapter therefore addresses the processes involved in arsenic oxidation under conditions similar to those found in AMD waters. To this end, batch experiments using field water samples and synthetic solutions were conducted under abiotic and biotic conditions at a controlled temperature and at varying concentrations of Fe(II) and Fe(III), sulfate and chloride in the presence and absence of light.

3.1 Materials and Methods

3.1.1 Site description and field sampling

The Iberian Pyritic Belt (IPB), which has been described as one of the largest massive sulfide deposit in the world, contained original reserves of the order of 1700 Mt (Sáez *et al.*, 1999) divided up into more than 80 massive sulfide deposits. Over several centuries of mining activity in this area has generated huge amounts of mining waste that continue to generate acidity and metal pollution affecting streams and rivers in the Tinto and Odiel drainage basins (Olías *et al.*, 2004; Nieto *et al.*, 2007; Sarmiento *et al.*, 2009).

Unfiltered water samples with bacterial slime (Fig. 3.1) were collected at two abandoned mines in the Iberian Pyritic Belt: San Telmo and Mina Esperanza, both located in the Odiel river basin. Water samples from the San Telmo abandoned mine were collected from water emanating from a sulfidic waste pile (Fig. 3.2a) on July 2007. Water pH of the samples was 2.55 at the moment of sampling. Water samples from Mina Esperanza were taken from water emerging from the adit mouth on June 2008 and the measured pH was 2.74 (Fig. 3.2b).

Figure 3.1. Photography that shows in detail the AMD water flowing from the Mina Esperanza adit mouth (Huelva, SW Spain) and bacterial slime. The water samples collected were used in the arsenic and iron oxidation experiments.

3.1.2 Solutions, analyses and mineral composition

All the reagents used to prepare the experimental and analytical solutions were of a purity at least equal to the reagent-grade standards of the American Chemical Society. Double-distilled water and re-distilled or trace metal grade acids were used in all preparations. The following reagents were used for the dissolved total arsenic and dissolved arsenite hydride generation atomic-absorption spectrometry (HG-AAS) analytical determinations: 10 percent (weight per volume) KI from Aldrich; 10 percent (weight per volume) L-Ascorbic Acid from Aldrich; NaOH from Fisher; $NaBH_4$ from

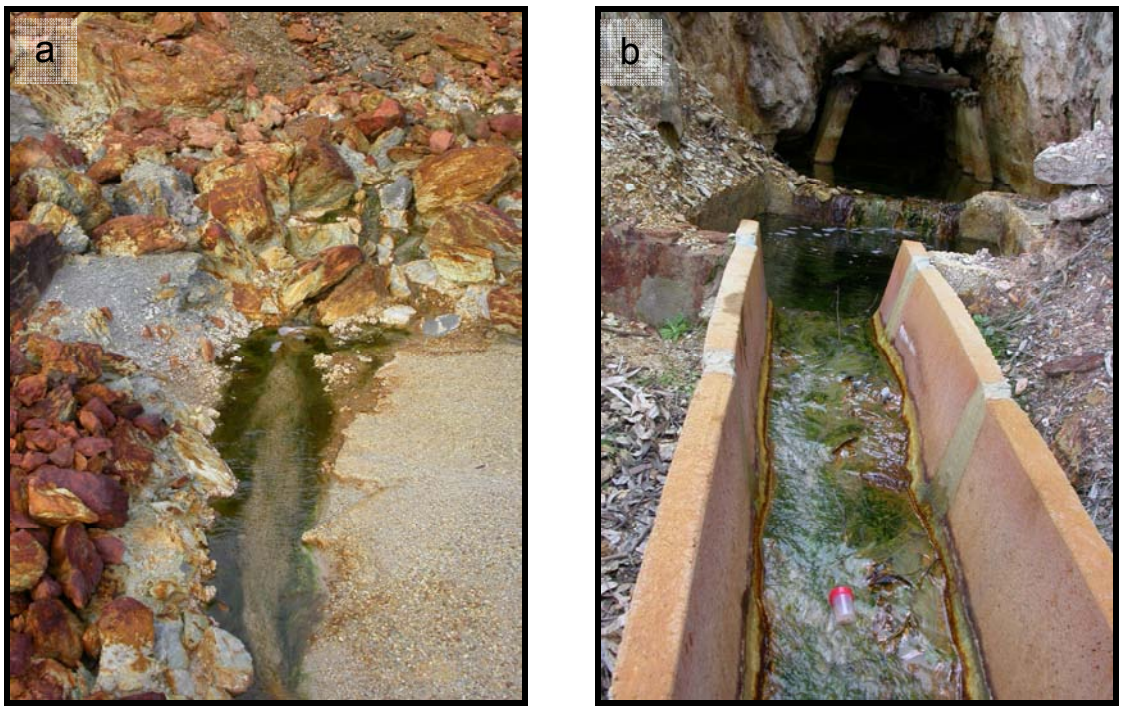

Figure 3.2. Photos of the sampling points: acid water emanating from a waste-rock pile in the San Telmo abandoned mine (a); and water emerging from the adit mouth of the abandoned Esperanza mine where samples were taken (b).

Fisher; trace metal grade HCl from Fisher; 1000 mg L^{-1} As(III) and 1000 mg L^{-1} As(V) from High Purity Standards. A standard arsenite stock solution of an As(III) concentration of 60 mg L^{-1} was prepared dissolving $NaAsO_2$ in double-distilled water.

Concentrations of total dissolved As (As(T)) and As(III) were determined by HG-AAS in water samples according to the methodology described in McCleskey *et al.* (2003). As(V) was calculated as the difference between As(T) and As(III). An atomic absorption spectrophotometer (Perkin-Elmer (PE) - AAnalyst 300) with an electrically heated quartz cell and a path length of 15-cm inline with a flow injection analysis system (FIAS; PE - FIAS 100), an autosampler (PE - AS90), and an arsenic electrodeless discharge lamp (EDL) attached to an EDL power supply (PE - EDL System 2) were used. The following spectrometer parameters were used: EDL current: 380 mv; wavelength: 193.7 nm; slit: 0.7 nm. Peak height was used for data processing. Sodium borohydride was prepared daily and filtered through a 0.45 μm polyvinylidene fluoride filter membrane using a vacuum

pump. The detection limits of the HGAAS analytical procedure used at the USGS National Research Laboratory in Boulder (Colorado, USA), are 0.1 μg L^{-1} for As(T) and 0.8 μg L^{-1} for As(III).

Ferrous and total dissolved iron concentrations were determined by colorimetry using the ferrozine method (Stookey, 1970; To *et al.*, 1999) in a Hewlett-Packard model 8452A diode array spectrometer with 1 cm cells at room temperature. The concentration of dissolved Fe(III) was determined by computing the difference between total dissolved iron and dissolved Fe(II). The detection limits are 1 and 2 μg L^{-1} for total and ferrous iron, respectively. However, if Fe(III) exceeds 50% of the total iron in a sample, Fe(II) is overestimated. On completion of our experiments, the quantity of dissolved Fe(III) was very high compared to dissolved Fe(II). Subsequently, when the Fe(III) concentration was higher than 50% of total iron, the colorimetric determination by Herrera *et al.* (1989) was used. This method is suitable for Fe(II) determination in bacterial leaching systems, where Fe(II) might be as low as 1% of total iron.

The concentration of total dissolved arsenic and iron was also measured by inductively coupled plasma optical emission spectrometer (ICP-OES) using the Leeman Lab Direct Reading Echelle equipment.

Sulfate and chloride concentrations were determined by HPLC (High Performance Liquid Chromatography) using a Dionex model 2010i ion chromatograph with AG4A guard and AS4A separator columns and Anion Self-Regenerating Suppressor-II.

Solution pH measurements were carried out on an unstirred aliquot of solution using an Orion Ross pH electrode (81-56) with temperature compensation after calibration with standard buffer solutions of pH 4 and 7.

The mineralogical composition of the precipitates formed during the experiments was determined by X-ray diffractometry (XRD) using a Bruker D5005 diffractometer with Cu Kα radiation. Powered samples were scanned from 0° to 60° 2θ with a continuous scan speed of 0.0014 degrees 2θ per second. Samples of precipitates were observed under

field-emission scanning electron microscopy (SEM) using a Hitachi H-4100FE with an intensity current of 10 kV.

3.1.3 Oxidation experiments

Biotic and abiotic batch experiments were performed in brown and dark polyethylene flask bottles of 250 mL and 125 mL. Bottles were immersed in a water bath at constant temperature (20 ± 2ºC) under atmospheric conditions. Bottles were periodically stirred in order to favor oxygenation.

Samples (1-5 mL) were taken regularly, filtered by 0.2 μm filters, preserved at 4ºC in the dark until analyses for As(III), total As, Fe(II) and total Fe. Arsenite determinations were also performed in the dark.

After the biotic experiments, the solids formed were retrieved, rinsed with double-dionized water, dried at room temperature and stored in closed microvials until SEM and XRD examinations.

3.1.3.1 Biotic oxidation experiments

Common bacteria from AMD water of Iberian Pyritic Belt were cultivated in a synthetic medium (9K medium) used to grow *Acidithiobacillus ferrooxidans.* This medium was prepared according to the composition of Silverman and Lundgren (1959) (see Table 3.1), adjusting its pH to 2.3.

In this study, two types of biotic experiments were carried out (Table 3.2): (1) 5 mL of field water samples that contained microbes were added to 250 mL of 9K culture media to enrich the cultures. 0.25 mL (experiments IPB-ME-1, IPB-ME-2, IPB-ME3, IPB-ME-4) and 0.1 mL of this enriched solution (experiment IPB-ME-5 and IPB-ME-6) were added to 250 mL of distinct solutions containing 100, 85, 50, 24 and 2.2 mg L^{-1} of ferrous iron (added as $FeSO_4$) and 800, 500, 490 and 250 μgL^{-1} of arsenite (added from the standard arsenite stock solution); (2) 250 mL solution of 9K culture medium were

Table 3.1. Composition of 1L of dissolution of 9K media prepared according to Silverman and Lundgren (1959).

Reagent	Amount (g)
$(NH_4)SO_4$	3.0
KCl	0.1
$KH_2PO_4 \cdot 3H_2O$	0.65
$MgSO_4 \cdot 7H_2O$	0.5
$Ca(NO_3)_2$	0.01
$FeSO_4 \cdot 7H_2O$	45

inoculated with 5 mL of field water sample and arsenite was added from the stock solution to reach a concentration of 800 μgL^{-1} (experiments IPB-ST-1 and IPB-ST-2). Experiments were carried out at sulfate concentrations of 487 to 17000 mg L^{-1}. Control experiments were run in synthetic solutions with the same concentrations of Fe(II), As(III) and sulfate without the addition of the enrichment medium.

3.1.3.2 Abiotic oxidation experiments

Abiotic oxidation of As(III) by Fe(III) was studied by means of H_2SO_4 synthetic lab solutions of pH 2.3 that were prepared using double-distilled water in either brown polyethylene flasks bottles for dark experiments or transparent for light experiments. Initial concentration of As(III) in the experiments ranged from 0.025 to 2.5 mg L^{-1}. Experiments were carried out with 1-350 mg L^{-1} of Fe(III), added as ferric sulfate, and 485 to 17000 mg L^{-1} of sulfate (Table 3.3). Chloride was added as NaCl to three experiments conducted at 140, 187 and 350 mg L^{-1} of Fe(III) and 2500 and 17000 mg L^{-1} of sulfate. Photoirradiation of the light experiments was carried out by a conventional lamp with light in the visible spectra (λ= 400-780 nm).

3.1.4 Geochemical calculations

Speciation-solubility calculations in this chapter were made with the geochemical code PHREEQC (Parkhurst and Appelo, 1999) using the WATEQ4F thermodynamic database

Table 3.2. Initial experimental conditions and arsenic oxidation rates obtained in presence of oxidizing bacteria.

Experiment	Initial experimental conditions					Rate constants		
	As(III)	Fe(II)	Fe:As	Sulfate	pH	As(III)	Fe(II)	
						k_{As}	$k_{Fe\ zero\ order}$	$k_{Fe\ first\ order}$
	μgL^{-1}	mgL^{-1}	molar ratio	mgL^{-1}		L mol^{-1} s^{-1}	$mol^{-1}L^{-1}s^{-1}$	s^{-1}
IPB-ST-1*	800	8500	15620	17000	2.3	*n.c*	$10^{-6.9}$	$10^{-4.1}$
IBP-ST-2*	800	8500	15513	17000		*n.c*	$10^{-7.0}$	-
IPB-ME-1	500	100	330	740		$10^{-2.2}$	$10^{-8.2}$	$10^{-3.9}$
IPB-ME-2	250	85	456	740		$10^{-2.8}$	$10^{-8.5}$	$10^{-4.0}$
IPB-ME-3	250	50	349	610		$10^{-2.7}$	$10^{-8.8}$	$10^{-4.5}$
IPB-ME-4	250	24	258	545		$10^{-2.5}$	$10^{-9.1}$	$10^{-4.6}$
IPB-ME-5	490	2.2	6.1	487	2.3	-	$10^{-9.4}$	$10^{-5.2}$
IPB-ME-6	480	2.2	6.1	487		-	$10^{-9.4}$	$10^{-5.2}$

* Oxidation rates obtained in 9K culture medium
ST stands for San Telmo samples
ME stands for Esperanza mine samples
n.c.: not calculated due to iron analytical uncertaintity during As(III) oxidation
k_{As} of the kinetic expression: $d[As(III)]/dt=k_{As}\ [As(III)][Fe(III)]$
$k_{Fe\ zero\ order}$ of the first zero expression: $-d[Fe(II)]/dt=k$
$k_{Fe\ first\ order}$ of the first order expression: $-d[Fe(II)]/dt=k_{Fe}\ [Fe(II)]\ a_{O2}$

(Ball and Nordstrom, 1991), which was enlarged with data from Bigham *et al.* (1996) and Yu *et al.* (1999) to account for schwertmannite solubility. In addition, using PHREEQC, the rate constants for iron and arsenic oxidation rates were obtained by fitting the experimental data to the kinetic expressions that will be discussed below.

3.2 Results and discussion

3.2.1 Oxidation of Fe(II) and As(III) in the presence of bacteria

Ferrous iron oxidation rate in AMD waters is controlled by the mine water pH, the amount of dissolved oxygen, and the presence of iron oxidizing bacteria. Abiotic Fe(II) oxidation is relatively slow and strongly inhibited at a pH less than approximately 4.5 (Ficklin and Mosier, 1999). However, in the presence of iron oxidizing bacteria, the oxidation rate of Fe(II) to Fe(III) increases by several orders of magnitude over the abiotic rate (Singer and Stumm, 1970).

Table 3.3. Initial experimental conditions in abiotic experiments carried out with different concentrations of Fe(III), sulfate and in presence and absence of light. Shadowed area corresponds to the experiments carried out in chloride solutions.

			Initial experimental conditions					Calculated rates		
	Experiment	Light	As(III)	Fe(III)	Sulphate	Fe:As	pH	Initial $Rate_{As}$ (k_{As})	$Rate_{As}$	k_{As}
			μgL^{-1}	mgL^{-1}		molar ratio		mol $L^{-1}s^{-1}$	mol $L^{-1}s^{-1}$	s^{-1}
This study	L10	Yes	2500	140	2500	75	2.3	$8.8 \cdot 10^{-8}$	$2.0 \cdot 10^{-12}$	$10^{-6.6}$
	L5	Yes	2000	350	17000	235		$6.1 \cdot 10^{-8}$	$1.5 \cdot 10^{-12}$	$10^{-7.0}$
	L17	Yes	2180	350	17000	215		$9.2 \cdot 10^{-9}$	$3.5 \cdot 10^{-12}$	$10^{-6.6}$
	B1	Yes	25	1	485	54		-	$3.8 \cdot 10^{-14}$	$10^{-6.8}$
	B2	Yes	25	10	500	537		$3.7 \cdot 10^{-10}$	$7.9 \cdot 10^{-14}$	$10^{-6.2}$
	B3	Yes	25	100	740	5366		$1.8 \cdot 10^{-9}$	-	-
	B4	Yes	250	1	485	5		-	$3.0 \cdot 10^{-13}$	$10^{-6.9}$
	B5	Yes	250	10	500	54		-	$3.9 \cdot 10^{-13}$	$10^{-6.8}$
	B6	Yes	250	100	740	537		$3.0 \cdot 10^{-9}$	$6.0 \cdot 10^{-13}$	$10^{-6.4}$
	B8	Yes	2500	10	500	5		-	$6.5 \cdot 10^{-12}$	$10^{-6.5}$
	B9	Yes	2500	100	740	54		-	$7.6 \cdot 10^{-12}$	$10^{-6.4}$
	NL1[(a)]	No	2500	187	4020	100	2.3	$9.7 \cdot 10^{-8}$	-	-
	NL2[(a)]	No	2370	200	4020	113		$8.8 \cdot 10^{-8}$	-	-
	NL7[(a)]	No	1350	187	17000	186		$5.4 \cdot 10^{-8}$	-	-
	NL2-Cl	No	1240	187	17000	202		[(b)]	-	-
		No							-	-
	L10-Cl	Yes	1000	140	2500	75		[(b)]	$1.2 \cdot 10^{-10}$ [(c)]	$10^{-5.4}$
		Yes							$3.4 \cdot 10^{-10}$ [(d)]	$10^{-4.5}$
	L5-Cl	Yes	1000	350	17000	235		[(b)]	$1.3 \cdot 10^{-10}$ [(c)]	$10^{-5.4}$
		Yes							$3.0 \cdot 10^{-10}$ [(d)]	$10^{-4.5}$
McClesckey *et al*. (2004)		Yes	20	1	0	54	1.3	-	$3.1 \cdot 10^{-13}$	-
		Yes	20	10	1000	543		-	$4.6 \cdot 10^{-14}$	-

(a) The initial arsenite oxidation rates are due to the experimental setup in the light.

(b) These experiments started without adding chloride.

(c) Experiments conducted with 0.05 gL^{-1} of Cl

(d) Experiments conducted with 8 gL^{-1} of Cl

Figure 3.3 shows the variation in concentration of Fe(II) and As(III) with time. It is observed that, even at low pH (pH 2.3), ferrous iron and arsenite concentrations decrease as oxidation to ferric iron and arsenate takes place. Oxidation of Fe(II) occurred rapidly, and, in the experiments with a very high initial Fe(II) concentration, an initial induction period of 150-300 h (Fig. 3.3 a) and of 50-70 h (Fig. 3.3 b) was observed. According to Nordstrom (2003) this is the time required for microbes to adapt to the new conditions after inoculation (lag phase). Thereafter, the population density is enough to affect the inorganic chemistry, resulting in a rapid decrease (Fig. 3.4). The high oxidation rate is represented by the steep decrease (slope) and is indicative of zero-order kinetics. The exponentially increasing rates (upper part of the curve) and the small but exponentially decreasing rates (lowest part of the curve) reflect first-order kinetics (Fig 3.4a). This

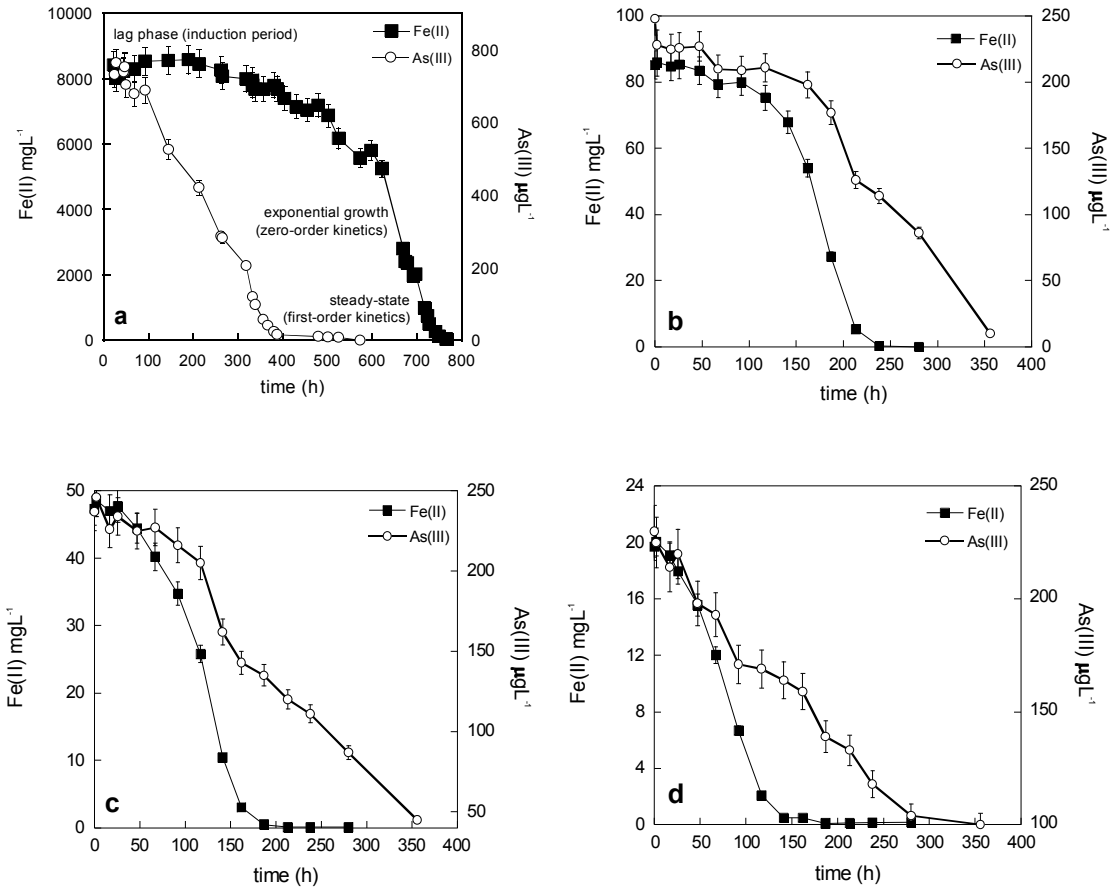

Figure 3.3. Evolution of Fe(II) and As(III) concentration during the biotic oxidation experiments carried out at different Fe(II) and As(III) concentrations.

evolution is observed in our experiments (Fig. 3.3 a-d) and corresponds to the main stages of microbial growth described by Nordstrom (2003): (1) initial lag phase; (2) exponential growth: the number of cells grown exponentially and the oxidation reaction kinetics is zero-order; (3) steady-state phase: achieved in the event of a limiting factor resulting in first-order reaction kinetics; (4) death phase: deceleration of the rate (Fig. 3.4b).

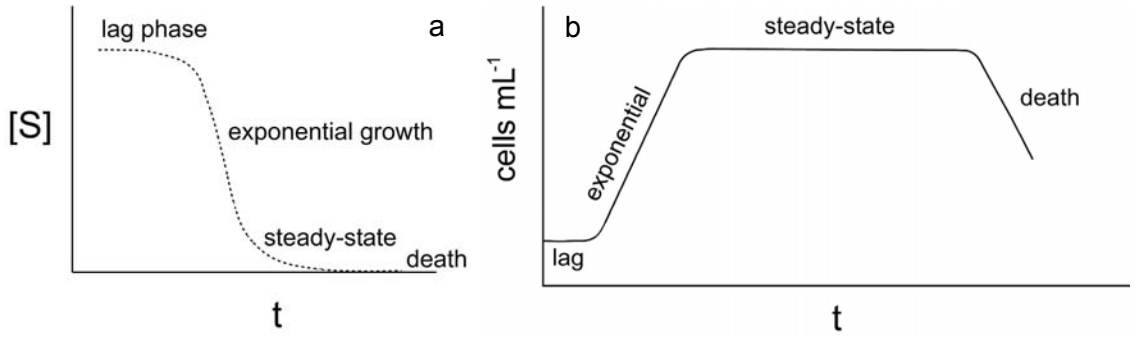

Figure 3.4. Typical curve of substrate evolution with time (a); schematic diagram of phases of microbial growth (b) (modified from Nordstrom, 2003).

The resulting ferrous iron oxidation rates were calculated using a combination of zero-order expression (eq. 3.4) and the first-order kinetic expression (eq.3.5) proposed by Singer and Stumm (1970):

$$r_{Fe(II)} = -\frac{d[Fe(II)]}{dt} = k_{zero\ order} \tag{3.4}$$

$$r_{Fe(II)} = -\frac{d[Fe(II)]}{dt} = k_{first\ order}[Fe(II)]\ a_{O_2} \tag{3.5}$$

where $r_{Fe(II)}$ is the oxidation rate expressed in mol L^{-1} s^{-1}, [Fe(II)] is the ferrous iron concentration (mol L^{-1}) at a time t (s), a_{O2} is the oxygen activity, $k_{zero\ order}$ (mol L^{-1} s^{-1}) is the rate coefficient of the zero-order kinetic expression and $k_{first\ order}$ (s^{-1}) of the first order kinetics. These constants were determined from the best-fit obtained by fitting the experimental results with the PHREEQC code (Table 3.2).

The resulting Fe(II) oxidation rates ranged from $10^{-6.9}$ mol L^{-1} s^{-1} to $10^{-9.4}$ mol L^{-1} s^{-1} (Table 3.2). These oxidation rates are within the values reported under comparable environmental conditions (pH=2-3, T=10-25°C) for bacterially mediated Fe(II) oxidation rates in AMD waters (e.g. 10^{-9} and 10^{-6} mol L^{-1} s^{-1}) (Kirby and Elder Brady, 1998; Nordstrom, 2003; Sánchez-España *et al.* 2007) with a proposed average value around

5×10^{-7} mol L^{-1} s^{-1} (Nordstrom and Alpers, 1999) and several orders of magnitude faster than abiotic rates (3×10^{-12} mol L^{-1} s^{-1}; Singer and Stumm, 1968). The differences in the oxidation rates obtained in our experiments could be attributed to the maximum concentration of bacterial cells achieved. According to Nordstrom (1985, 2003) the number of bacterial cells appears to be the limiting factor for iron-oxidation kinetics at least under field conditions.

In all experiments, As(III) concentration decreased drastically, reflecting to a certain degree Fe(II) behavior. Nonetheless, two trends were observed regarding As(III) behavior. First, in the experiments carried out with the highest As(III) and Fe(II) concentrations (9K medium) (Table 3.2), arsenic oxidation apparently commenced before iron oxidation, suggesting that two distinct microbial oxidations of arsenic and iron might occur independently (Fig. 3.3a). Second, in the experiments conducted with lower Fe(II) concentrations (Fig. 3.3b,c,d), the simultaneous oxidation curves of iron and arsenic suggest that the same microbes could oxidize both ferrous iron and arsenite. In contrast, in the abiotic control experiments with the same arsenic, iron and sulfate concentrations no decrease in Fe(II) and As(III) for 800 h was observed (Fig. 3.5).

The presence of As-oxidizing bacteria in AMD streams has been reported (Wakao *et al.*, 1988; Leblanc *et al.* 2002; Bruneel *et al.*, 2003; Casiot *et al.*, 2003b; Duquesne *et al.*, 2007; Nakazawa and Hareyama, 2007), and some authors have proposed that iron oxidizers (such as *A. ferrooxidans*) oxidized As(III) to As(V), which was immediately coprecipitated with Fe(III) oxyhidroxides (Leblanc *et al.*, 1996; Leonard *et al.*, 1999). However, the ability of iron-oxidizing bacteria to oxidize As(III) is still in contention. For example, Wakao *et al.*, (1988) discussed the capacity of *A. ferrooxidans* and *Leptospirillum* to oxidize arsenite.

Although the presence of arsenite-oxidizing bacteria appears to be a reasonable hypothesis to account for As(III) oxidation, it is worth noting that the analytical uncertainty of the Fe(II) concentration during the first hours is ca. 10%. Hence, a large concentration of Fe(III) could not have been determined (for example: 850, 10, 8.5 and 5 mg L^{-1} of Fe(III) could have been below the detection limit in experiments IPB-ST-1 or

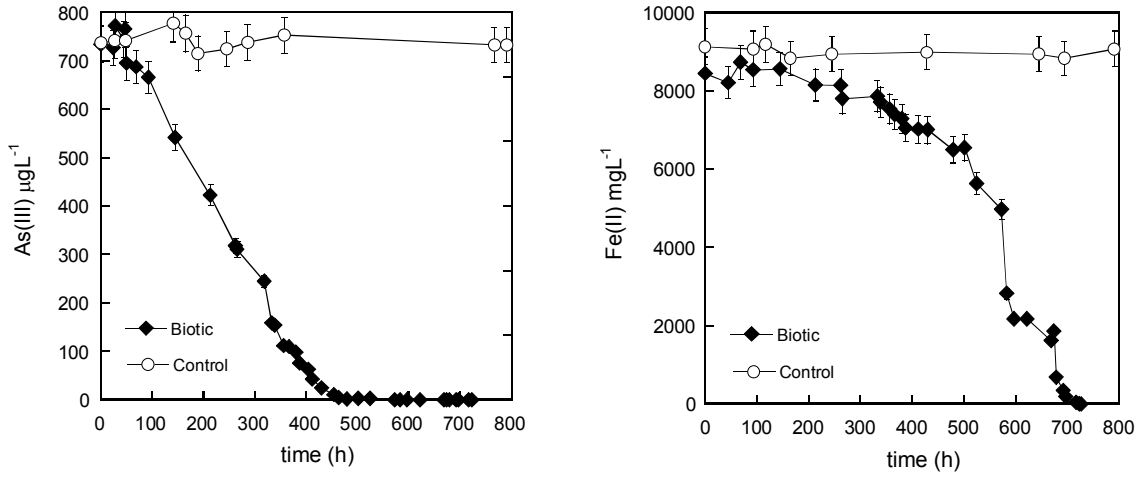

Figure 3.5. Evolution of As(III) and Fe(II) concentration during the abiotic and control oxidation experiment. No decrease in As(III) and Fe(II) was observed under sterile (abiotic) conditions.

IPB-ST-2, IPB-ME-1, IPB-ME-2 and IPB-ME-3, respectively; see Table 3.2). This undetected amount of Fe(III) would have been able to oxidize As(III) under these experimental conditions. Therefore, it is not easy to determine whether arsenic oxidation was catalyzed biotically or abiotically oxidized by Fe(III). In an attempt to clarify the role of bacteria in As(III) oxidation, two additional experiments were conducted in inoculated solutions but with low Fe(II) concentrations (2.2 mg L^{-1}) (Table 3.2: experiments IPB-ME-5 and IPB-ME-6). At this low ferrous iron concentration, As(III) oxidation was negligible, whereas Fe(II) was completely oxidized (Fig. 3.6), indicating that microbes in field water solutions are not As-oxidizer microbes. Thus, the As(III) oxidation observed in the experiments was catalyzed by the presence of Fe(III), which resulted from microbial oxidation of ferrous iron. Given that these findings indicated abiotic As(III) oxidation, even in the presence of iron-oxidizer microbes, abiotic experiments were conducted to study arsenic oxidation in the presence of Fe(III), sulfate, chloride and in the presence and the absence of light (see next section).

The variation of total arsenic with time was also studied in the biotic experiments. Total arsenic concentration and pH remained invariable when Fe(II) initial concentration was 100, 85, 50, 25 and 2.2 mg L^{-1} (Fig. 3.7a). However, when the initial ferrous iron concentration was 8500 mg L^{-1} (9K medium solution), total arsenic remained constant in

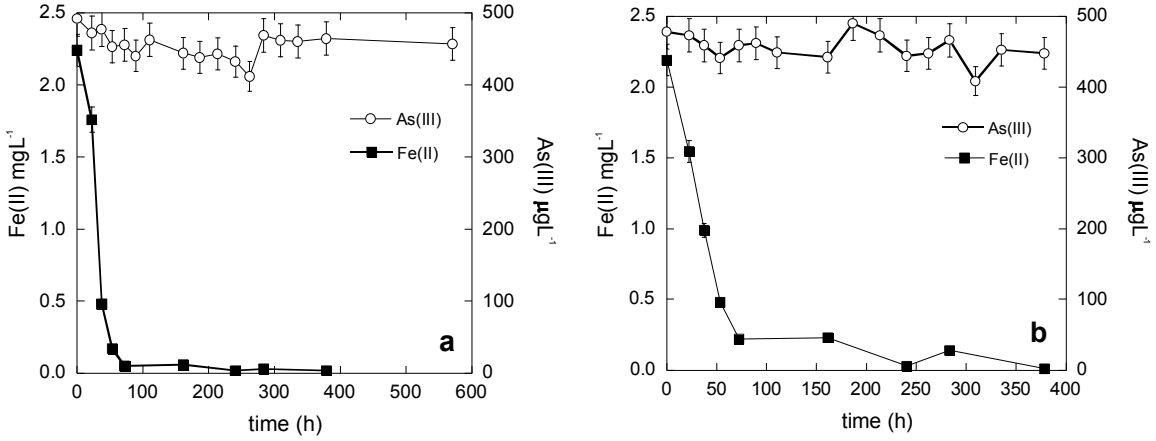

Figure 3.6. Evolution of As(III) and Fe(II) concentration during the experiments carried out with 2.2 mg L^{-1} of Fe(II) and 480 and 490 µg L^{-1} of As(III).

the first 145 h. Thereafter, total arsenic decreased together with As(III) oxidation until 350-380 h followed by a constant concentration for ca. 200 h. Finally, the total arsenic concentration reached the initial concentration at the end of the experiment (Fig. 3.7b).

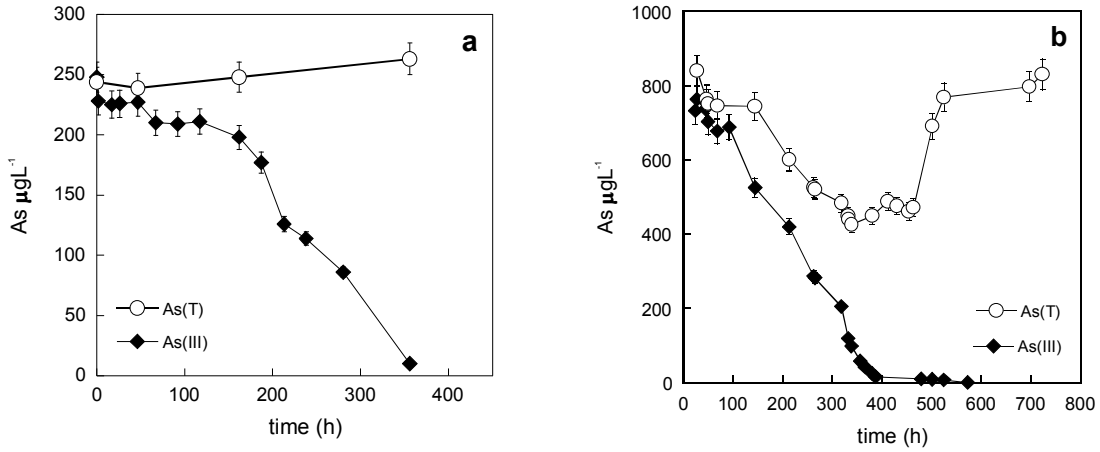

Figure 3.7. Variation in As(III) and total As concentration with time in two biotic oxidation experiments at 85 mg L^{-1} of initial Fe(II) (a); in 9K medium (8500 mg L^{-1} of initial Fe(II)) (b).

Fig. 3.8 depicts the pH variation in this experiment. In the first 400 h pH increases from 2.4 to 2.7, followed by a pH decrease to 2.2. The pH increase is a consequence of Fe(II) oxidation to Fe(III), which consumes protons whereas the pH decrease is due to Fe(III)

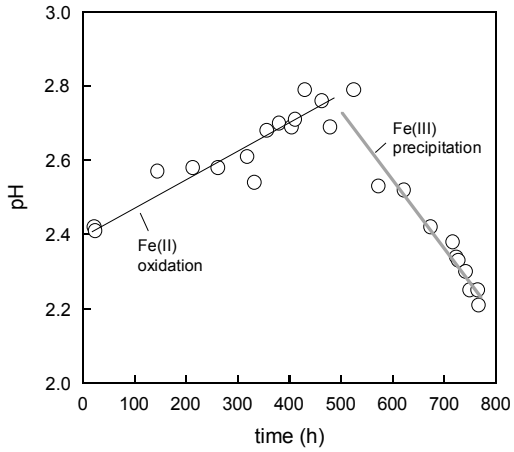

Figure 3.8. Variation in pH during the biotic oxidation experiment carried out at 8500 mg L^{-1} of initial Fe(II) (experiments IPB-ST1 and IPB-ST2 of Table 3.2).

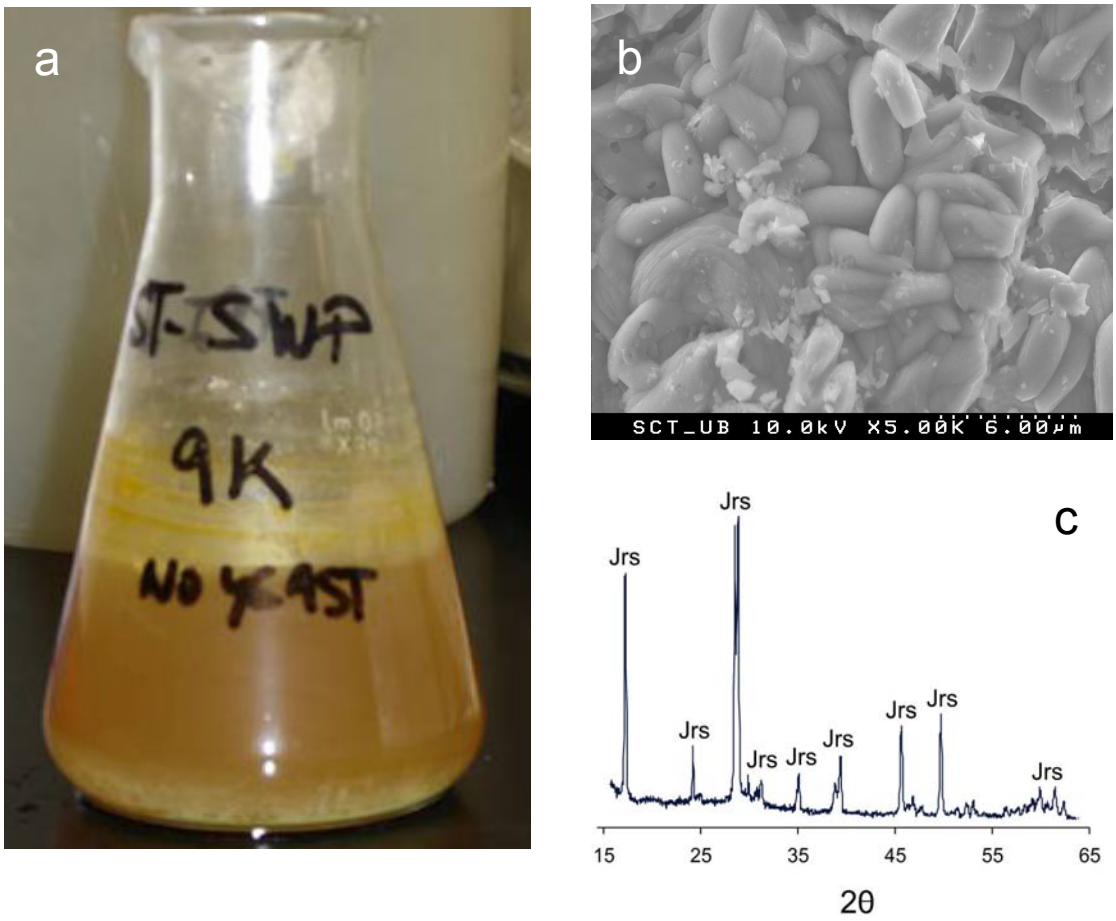

Figure 3.9. Precipitation of solid phases at the bottom flask during the experiments carried out in presence of bacteria (a); SEM image showing the Fe-precipitates (b) and XRD pattern (c) of the Fe(III) phase formed during the experiment (Jrs: jarosite).

hydrolysis and Fe(III) precipitation (Fig. 3.9a) (Nordstrom, 2003; Kupka *et al.*, 2007). SEM and XRD examinations of the retrieved precipitate in this experiment showed that it was merely formed by jarosite ($KFe_3(SO_4)_2(OH)_6$) (Fig. 3.9b and c). Wang *et al.* (2006) argue that schwertmannite ($Fe_8O_8(OH)_{5.5}(SO_4)_{1.25}$) is produced by biological oxidation of ferrous iron in cultures of iron-oxidizing bacteria, and owing to its instability, it can spontaneously transform to other phases including jarosite ($KFe_3(SO_4)_2(OH)_6$). This transformation is favored by aging, temperature and ammonium concentration in acid media. Although the 9K solution is supersaturated with respect to schwertmannite and jarosite as indicated by the PHREEQC calculations, direct precipitation of jarosite is not very probable since its formation at low temperature is slow (weeks to months). Furthermore, the precipitation of jarosite as the only Fe-phase present does not account for the arsenic behavior since arsenate sorption capacity of jarosite in the presence of high concentrations of sulfate (0.19 mol L^{-1} of sulfate in this experiment) is practically negligible. By contrast, schwertmannite transformation into jarosite would account for the behavior in the total arsenic concentration. Aqueous As(V) could be partially sorbed as schwertmannite precipitated. When schwertmannite transformed to jarosite, As(V) was released back to the solution as jarosite has a lower arsenate sorption capacity than schwertmannite in the presence of sulfate, as will be shown in the following chapter.

In summary, the experimental results suggest that the presence of an arsenite-oxidizing bacteria oxidizing arsenite to arsenate cannot be confirmed under the conditions of this study. It is shown that under these conditions (similar to those in AMD waters), arsenite oxidation is controlled by ferrous iron oxidation (Daus *et al.*, 2002; Bednar *et al.*, 2005; Sarmiento *et al.*, 2007), which is bacterially catalyzed by Fe-oxidizing microorganisms.

3.2.2 Abiotic arsenic oxidation

Arsenite oxidation was studied under abiotic conditions by means of batch experiments conducted at pH 2.3 in light and dark conditions, varying the concentrations of Fe(III), As(III), chloride and sulfate, which is the main anion in AMD waters (Table 3.3).

3.2.2.1 Oxidation of As(III) in Fe(III) solutions

Fig. 3.10 shows As(III) variation with time in atmospheric conditions in the presence of light (Fig. 3.10a-c) and in the absence of light (Fig. 3.10d).

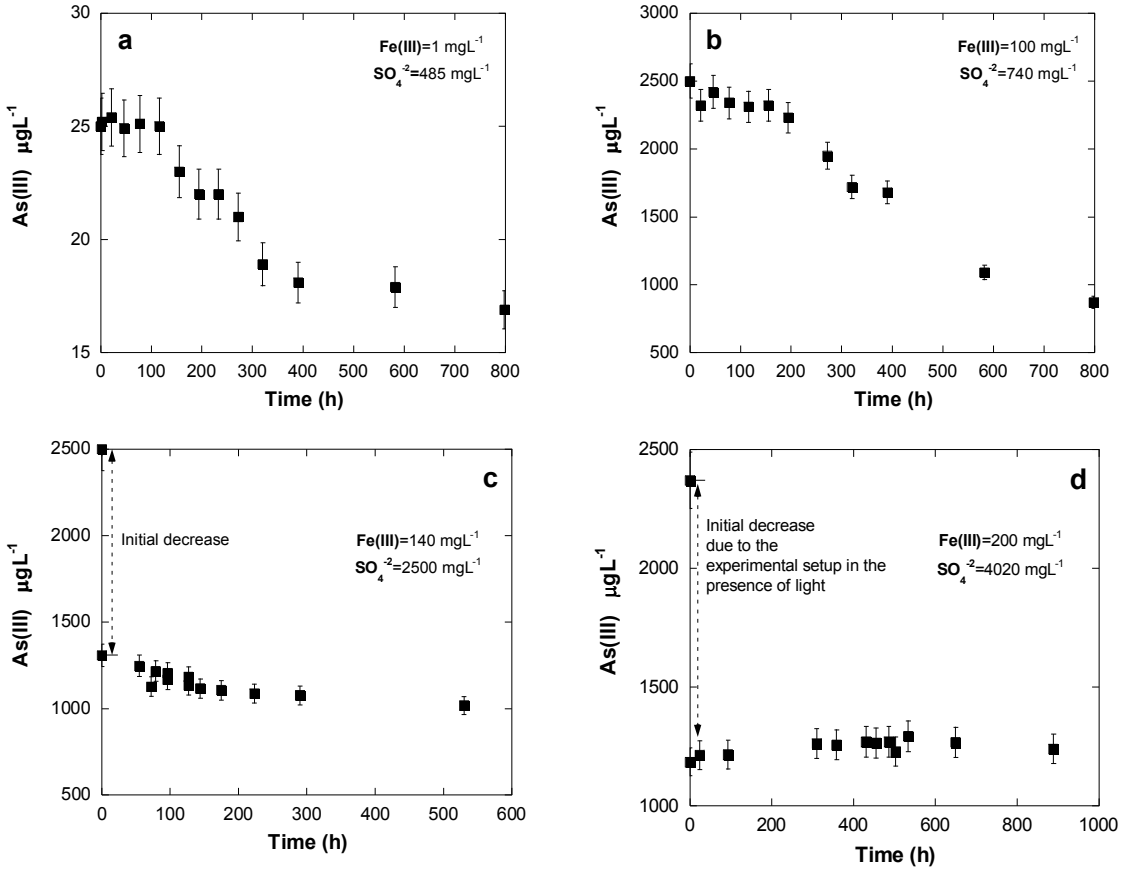

Figure 3.10. Abiotic arsenite oxidation by Fe(III) in some representative experiments at pH 2.3 in aerated solutions and in the presence of sulfate in light experiments (a, b, c) and dark experiments (d) (see Table 3.3).

In the experiments with an initial Fe(III)/As(III) molar ratio lower than 54, a gradual As(III) oxidation was observed (Fig. 3.10a,b), which went up by increasing the Fe(III) content. The As oxidation rate is calculated using a first-order kinetic expression:

$$r_{As(III)} = -\frac{d[As(III)]}{dt} = k[As(III)] \qquad (3.6)$$

where $r_{As(III)}$ is the oxidation rate expressed in mol L^{-1} s^{-1}, *k* is the oxidation rate coefficient (s^{-1}) and [As (III)] is the arsenite concentration (mol L^{-1}) after time *t*.

Thus, the oxidation rates in experiments B1, B5 and B9 with an initial Fe(III)/As(III) molar ratio of 54 went up from $3.8x10^{-14}$ to $7.6x10^{-12}$ mol L^{-1} s^{-1} by increasing the Fe(III) content from 1 to 100 (Table 3.3); in experiments B4 and B8 with an initial Fe(III)/As(III) molar ratio of 5, the oxidation rate went up from $3.0x10^{-13}$ to $6.5x10^{-12}$ mol L^{-1} s^{-1}, by increasing [Fe(III)] from 1 to 10 (Table 3.3).

A fast arsenite oxidation occurred at the start of the experiments with a high Fe(III)/As(III) molar ratio, i.e. a ratio higher than 54 (Fig. 3.10c,d). In this case, a zero-order kinetic expression was used to calculate the initial oxidation rate from:

$$r_{As(III)} = -\frac{d[As(III)]}{dt} = k \qquad (3.7)$$

where *k* is the oxidation coefficient (mol L^{-1} s^{-1}), [As (III)] is the arsenite concentration (mol L^{-1}) after time *t*. The yielded initial oxidation rates ranged from 3.7 x 10^{-10} to 9.7 to 10^{-8} mol L^{-1} s^{-1} (Table 3.3). This initial rapid oxidation was followed by a gradual arsenite oxidation (Fig. 3.10c) that was fitted using the first-order kinetic expression given in eq. 3.6. The oxidation rates obtained went up by increasing the Fe(III) content.

It appears that an initial Fe(III)/As(III) molar ratio higher than 54 yields fast arsenite oxidation rates under the present experimental conditions.

Log arsenic oxidation rates versus log Fe(III) concentration yield a linear dependence between the arsenite oxidation rate, R_{As}, and the Fe(III) concentration (Fig. 3.11). This is expressed as $R_{As} = k[Fe(III)]^n$ where k is a rate coefficient and n is the reaction order with respect to Fe(III) equal to 1.0±0.1. This oxidation rate-Fe(III) dependence was included in the calculations used to fit the observed arsenite oxidation as Fe(II) oxidized to Fe(III) (eqs. 3.4 and 3.5) in the biotic experiments (see Fig. 3.3):

$$r_{As(III)} = \frac{-d[As(III)]}{dt} = k\,[As(III)]\,[Fe(III)]^n \qquad (3.8)$$

where k is the oxidation coefficient ($mol^{-1}\ L^{-1}\ s^{-1}$), [As (III)] and [Fe(III)] are the arsenite and ferric iron concentrations (L^{-1}) after time t, and n is the reaction order with respect to ferric iron concentrations (1.0±0.1).

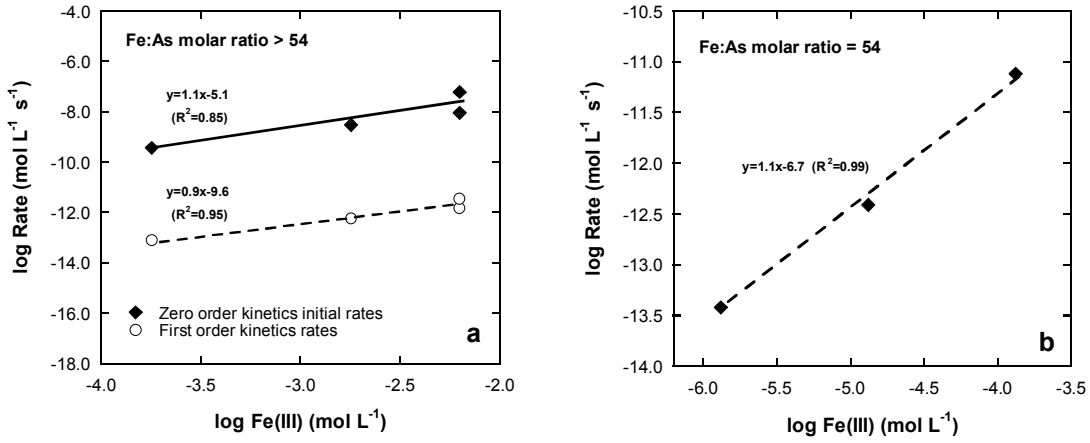

Figure 3.11. Log arsenic oxidation rates versus log Fe(III) concentration at high initial Fe:As molar ratio (>54) (experiments L5, L17, B2 and B3) (a) and initial Fe:As molar ratio of 54 corresponding (experiments B1, B5 and B9) (b).

Likewise, the arsenite oxidation rate-Fe(III) dependency was included in the calculations used to model the As (III) evolution along the AMD discharge discussed (the Tinto Santa Rosa discharge) in Chapter 6.

3.2.2.2 Influence of sulfate

The arsenite oxidation rates obtained in this study confirmed the inhibitory effect of sulfate on arsenite oxidation (Emett and Khoe, 2001; Bednar *et al.* 2005; McCleskey *et al.* 2004). The sulfate effect is observed after comparing our oxidation rates with those calculated from the data of McCleskey *et al.* (2004) with similar amounts of As(III) and Fe(III) and varying sulfate contents. The oxidation rate went up from $3.8x10^{-14}$ to $3.1x10^{-13}$ mol L^{-1} s^{-1} and from $4.6x10^{-14}$ to $7.9x10^{-14}$, by decreasing sulfate from 485 to 0 and from 1000 to 500 mg L^{-1}, respectively (experiments B1 and B2 and that of McCleskey *et al.* (2004) in Table 3.3).

3.2.2.3 Influence of light

According to Emett and Khoe (2001) photo-oxidation processes occur when light is absorbed by any species and a reactive free radical is produced. These authors observed that uncomplexed ferric ion (Fe^{3+}_{aq}), which only absorbs light below 300 nm, was found to be ineffective in oxidizing arsenic at acidic pH and in the absence of chloride. In our experiments at pH 2.3, iron speciation calculations carried out with the PHREEQC code showed that the hydrolysis of Fe(III) produced $Fe(III)OH^{2+}$. This species, in contrast to Fe^{3+}_{aq}, is an effective source of hydroxyl free radicals when arsenic oxidation occurs in a reaction mixture containing Fe(III) and no chloride at acid pH (Khoe *et al.*, 1986). This process is described via free-radical mechanism in which the rate of the initiation reaction is determined by the rate of photon absorption by dissolved Fe(III)-hydroxo species as shown in the following reactions:

$$Fe(III)(OH)^2 + h\nu \rightarrow Fe(II) + \cdot OH \qquad (3.9)$$

$$As(III) + \cdot OH \rightarrow As(IV) + OH^- \qquad (3.10)$$

$$As(IV) + O_2 + H+ \rightarrow As(V) + \cdot OH_2 \quad (3.11)$$

Although the presence of oxygen does not exert an influence on the photon-initiation reactions, it rapidly reacts with the intermediate as expressed in equation (3.11) (Kläning *et al.*, 1989).

Table 3.3 shows the arsenite oxidation rates obtained in abiotic conditions. In some experiments (L10, L5, L-17, NL-1, NL-2 and NL-7), a significant amount of As(III) was immediately oxidized when As(III) containing solution was mixed with the Fe(III) solution in the presence of light (Fig. 3.10c,d). This initial oxidation could be due to the presence of high concentrations of $Fe(III)OH^{2+}$ that were able to rapidly absorb photons, producing high reactive hydroxyl radicals. Thereafter, Fe(II) formed by photoreduction (eq. 3.7) could be slowly re-oxidized to Fe(III) by oxygen generating more $Fe(III)OH^{2+}$.

In the absence of light it was observed that after the immediate initial As(III) decrease at the start of the experiment in the presence of light, no further arsenite oxidation occurred (Fig. 3.10d). This finding confirms the results by Bednar *et al.* (2002) and McCleskey *et al.* (2004), who reported insignificant As(III) oxidation at acidic solutions in the absence of light. As(III) oxidation ceased owing to the absence of light that led to the non existence of hydroxyl radicals.

In the case of sulfate, it is reasonable to assume that the main anion in AMD waters exerts an inhibitory effect on arsenite oxidation in the presence of light given that it forms Fe(III)-complexes ($FeSO_4^+$), which do not produce reactive free-radicals necessary to produce the required As(IV) (Emett and Khoe, 2001).

3.2.2.4 Influence of chloride

Although AMD waters do not usually have high chloride concentrations, the chloride catalytic effect could play a key role in remediating the arsenic content in AMD contaminated environments. Therefore, since As(III) oxidation by Fe(III) seems to be very

slow, the effect of chloride on arsenite oxidation in the presence of Fe(III) and sulfate was studied by adding 0.05 g L^{-1} and 8 g L^{-1} of chloride in the presence and absence of light (Fig. 3.12; Table 3.3: experiments NL2-Cl, L10-Cl, L5-Cl). The results showed that the addition of chloride to the Fe(III)-sulfate solutions in the presence of light led to an increase in the As(III) oxidation (Fig. 3.12a).

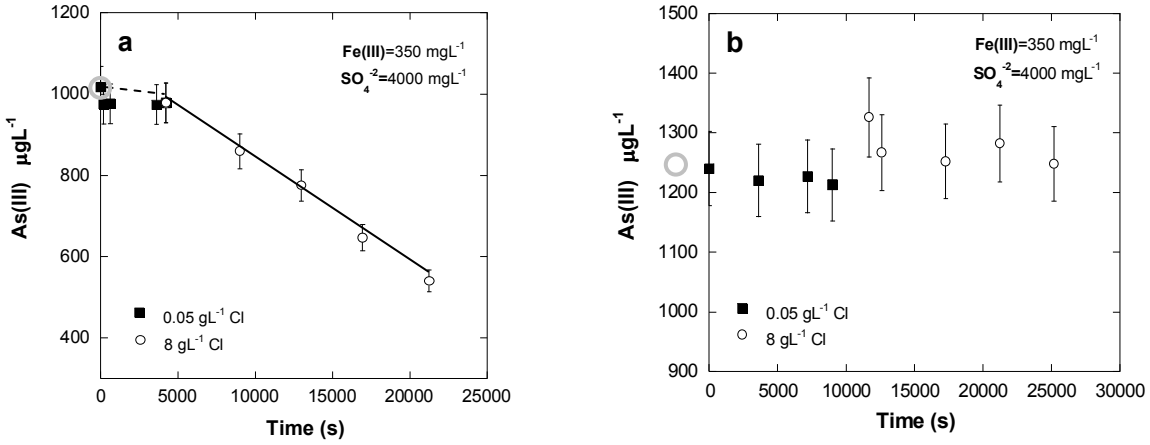

Figure 3.12. Oxidation of 1-1.2 mg L^{-1} of As(III) at pH 2.3 by Fe(III) in the presence of sulfate after the addition of 0.05 and 8 g L^{-1} of Cl. In the presence of light (a) and in dark (b). Grey circles indicate the As(III) concentration before adding chloride to solution.

The calculated oxidation rates were around 10^{-10} mol L^{-1} s^{-1}, which are one or two orders of magnitude higher than the rates in chloride-free solutions (10^{-13}-10^{-12} mol L^{-1} s^{-1}) and at the same Fe(III) and sulfate concentrations (e.g. compare experiments L10 with L10-Cl and L5 with L5-Cl of Table 3.3). Emett and Khoe (2001) attribute this catalytic effect on arsenite oxidation to the formation of Fe-chloride-complexes ($Fe(III)Cl^{2+}$), which absorb photons to produce highly oxidizing dichlororadicals:

$$Fe(III)(Cl)^2 + h\gamma \rightarrow Fe(II) + \cdot Cl \qquad (3.12)$$

$$Cl^- + \cdot Cl \rightarrow \cdot Cl_2^- \qquad (3.13)$$

In contrast, no effect of chloride was observed without light (Fig. 3.12b) since photoreactions were totally inhibited.

3.3 Conclusions

A deeper understanding of the Fe(II) and As(III) simultaneous oxidation processes and a quantification of their oxidation rates are of paramount importance in the prediction of iron and arsenic behavior in AMD waters.

Batch experiments under biotic and abiotic acid waters proved to be an efficient tool to study arsenite oxidation in the presence of bacteria and different contents of Fe(II), Fe(III), As(III) and sulfate and in the presence and absence of light.

At the low pH considered in this study, Fe(II) oxidation by oxygen is very slow (in the order of 10^{-12} mol L^{-1} s^{-1}). Nonetheless, iron and arsenite oxidize simultaneously in the presence of AMD microorganisms. The results suggest that Fe(II) oxidation is biotically catalyzed and that the resulting Fe(III) catalyzes As(III) oxidation to As(V). This mechanism invalidates the hypothesis that As(III) oxidation is mediated by bacteria. Fe-oxidizing microorganisms therefore play a major role in arsenite oxidation since arsenic speciation and sorption is controlled by iron in AMD waters.

As(III) oxidation in the presence of Fe(III) is accelerated by increasing Fe(III) and chloride concentrations in the presence of light. A fast arsenite oxidation occurred at the start of the experiments with a high Fe(III)/As(III) molar ratio, i.e. a ratio higher than 54 followed by a slow oxidation whereas at molar ratio lower than 54 a gradual As(III) oxidation was observed. In contrast, oxidation is inhibited by increasing the sulfate content and effectively stopped when the light is excluded. Strong complexing of Fe(III) by sulfate inhibits As(III) oxidation in the presence of light because absorption of photons by the Fe(III)-SO_4 complex does not produce a reactive free-radical which readily oxidizes As(III).

Chapter 4

Sorption processes

Most geochemical processes take place at the interface water-solid and involve the transfer of chemical elements between a fluid phase and a solid mineral phase. Solutes in natural waters are often taken up by the solids they contact without alteration of the solid. If the specific reaction responsible for uptake has not been identified the process is called *sorption*. Sorption of an element can occur through true *adsorption* (or surface complexation) or *co-precipitation* (forming a mixed precipitate or solid solution) (Parks, 1990).

Because of the interaction of aqueous metal ions with mineral particles in soil and sediment samples is immensely complex, studies of simplified model systems, such as that presented in this chapter, are required. Therefore, the problem is addressed in a series of simplified analog systems in which the number of variables and phases is controlled. The knowledge provided by these experiments is an approach of the complexity of the natural system and help us to understand the immobilization mechanism in the natural environment.

Surface and ground waters near mines of sulfide minerals are often heavily polluted. Waste materials containing residual sulfide minerals are piled up in tailings and may become oxidized giving rise to acid mine drainage (AMD) (Nordstrom and Alpers, 1999). This AMD releases large amounts of metals which remain soluble (Appleyard and Blowes, 1994), causing a major environmental problem.

The concentrations of arsenic, which is a potentially toxic trace element, in AMD can reach hundreds of mgL^{-1} (e.g. 850 mg L^{-1} in Richmond Mine, Iron Mountain, California; Nordstrom and Alpers, 1999) as a result of the oxidation of As-rich sulfides, such as arsenopyrite and As-rich pyrite. Although As(III) is mainly released from the dissolution of these minerals (Yu *et al.*, 2007; Cama *et al.*, 2008), the presence of As-oxidizing bacteria and oxidant agents such as Fe(III) oxidize As(III) to As(V) rapidly (Wakao *et al.*, 1988; Leblanc *et al.*, 2002; Bruneel *et al.*, 2003), which is sorbed more strongly than As(III) to Fe(III) oxides and hydroxides (Bowell, 1994).

Arsenic concentrations in AMD polluted areas are naturally attenuated by newly formed precipitates, such as schwertmannite ($Fe_8O_8(OH)_{5.5}(SO_4)_{1.25}$), K-jarosite ($KFe_3(SO_4)_2(OH)_6$) and goethite (FeOOH), which effectively sorb As(V) reducing As concentrations in waters (Fukushi, *et al.* 2003a; Gault *et al.*, 2005; Sánchez-España *et al.* 2005a,b; Acero *et al.*, 2006; Lee and Chon, 2006; Asta *et al.* 2007; Asta *et al.* 2008a). These minerals therefore play an important role in the removal of trace elements from solution by adsorption and co-precipitation (Benjamin, 1983; Johnson, 1986; Stumm and Sulzberger, 1992; Bigham *et al.*, 1994; Webster *et al.*, 1998).

These iron oxide precipitates formed in acid waters are initially poorly ordered minerals such as schwertmannite, which may spontaneously transform with time into goethite and jarosite. This transformation is observed under laboratory (Bigham *et al.* 1996; Kawano and Tomita, 2001; Jönson *et al.*, 2005; Acero *et al.*, 2006) and field conditions (Peine *et al.*, 2000; Gagliano *et al.*, 2004). The instability of schwertmannite has a significant impact on the water chemistry because the progressive transformation of the

As-bearing amorphous iron oxyhydroxides into more crystallized iron oxides leads to the release of arsenic to the water (Courtin-Nomade *et al.*, 2003).

A number of studies have measured the sorption of different pollutants on natural and synthetic iron oxide, hydroxide and oxyhydroxysulfate minerals. Because of its capacity for sorbing trace metals, schwertmannite sorption has been the subject of many studies (Courtin-Nomade *et al.*, 2003; Fukushi *et al.*, 2003a; Fukushi *et al.*, 2003b; Fukushi *et al.*, 2004; Regenspurg and Peiffer, 2005; Acero *et al.*, 2006).

Sorption of arsenic on goethite, even at relatively low pH has also been studied; Lehmann *et al.* (2005) reported a geochemical model for As(V) sorption on goethite at pH 3. Dixit and Hering (2003) observed that sorption of As(V) onto ferric oxides and goethite was more favorable than sorption of As(III) at pH below 5-6. The same trend was observed by Grossl and Sparks (1995), Matis *et al.* (1997), and Giménez *et al.* (2007). Moreover, the influence of other elements such as silicic acid or dissolved organic carbon (DOC) on As(V) sorption has been studied by Waltham and Eick (2002) and Gräfe and Sparks (2005). These authors suggested that the presence of silicic acid and organic acids could reduce the rate and the total quantity of arsenic adsorbed onto goethite. Works on arsenic sorption on jarosite are less abundant than the studies on sorption on goethite and schwertmannite. Tomioka (2006) observed that As(V) was sorbed on jarosite in the pH range 1-3, whereas As(III) remained in solution. Nonetheless, sorption capacity of jarosite is not reported. Gräfe *et al.* (2008) studied the co-sorption reaction products of arsenate and copper on goethite and natro-jarosite with extended X-ray absorption fine structure (EXAFS) spectroscopy.

Despite the large number of studies on arsenic sorption on such phases, data on the highly acidic conditions of AMD are lacking. Furthermore, the relative ability of jarosite and goethite to retain arsenic remains unclear (Acero *et al.*, 2006). Whereas some earlier studies claim that arsenic can remain immobilized in jarosite by replacing sulfur in sulfate tetrahedra (Savage *et al.* 2000, 2005; Gräfe *et al.*, 2008), other works show that arsenic is retained preferentially in goethite over jarosite (Strawn *et al.*, 2002).

In order to develop effective management strategies to remediate AMD impacted areas, it is necessary to quantify the arsenate sorption capacity of these precipitates at low pH. This enables us to understand and predict the arsenic behavior in streams, rivers and pit lakes and to determine the potential risk of releasing the sorbed arsenic under reductive conditions (e.g. pit and lake bottoms). The goal of this work is therefore to quantify the As(V) removed by jarosite and goethite at low pH (1.5-2.5). Given that jarosite and goethite coexist in different proportions in AMD precipitates, it is not easy to study the respective sorption capacity in natural samples. Synthetic jarosite and goethite were used separately to quantify the respective arsenic removal capacity. The effect of sulfate content and ionic strength variability on arsenic sorption was studied because sulfate is the main anion that competes with arsenate for surface sites and because the ionic strength could vary seasonally.

4.1 Materials and Methods

4.1.1 Solid synthesis and characterization

Sorption experiments were conducted with synthetic goethite and synthetic jarosite. Goethite synthesis was carried out following the Schwertmann and Cornell (1991) methodology. 180 mL of 5M KOH and 100 mL of 1M $Fe(NO_3)_2$ were mixed. The suspension was diluted to 2L with bidistilled water and aged for 60 h at 70°C. Thereafter, the suspension was washed and dried at 50°C. K-Jarosite was synthesized according to Baron and Palmer (1996), dissolving 5.6 g of KOH and 17.2 g of $Fe_2(SO_4)_3 \cdot 5H_2O$ in 100 mL of DDW at 95°C and 1 atm. The solution was placed in a covered beaker on a hot plate and stirred continuously. After 4 h, the precipitate settled and the supernatant solution was decanted. The precipitate was then washed several times with ultrapure water (18.2 $M\Omega \cdot$ cm) and dried at 110°C for 24 h. The synthesized solids were identified by means of X-ray diffraction (XRD) using a Bruker D5005 diffractometer with Cu Kα radiation and scanned from 0° to 60° 2θ with a continuous scan at a rate of 0.0014 degrees 2θ per second. The surface area was measured using a Micromeritics Gemini 2370 surface area

analyzer. The BET-determined initial surface area of goethite and jarosite was 29.4±1.9 m^2 g^{-1} and 2.3±0.3 m^2 g^{-1}, respectively, using 5-point N_2 adsorption isotherms.

In addition, using measured iron, potassium, sulfur and arsenic concentrations, the saturation indices (SI) of reacted solution were calculated employing the PHREEQC code (Parkhurst and Appello, 1999) and thermodynamic database WATEQ4F (Ball and Nordstrom, 1991).

4.1.2 Experimental methodology

The As(V) stock solution used in the sorption experiments were prepared from reagent grade $Na_2HAsO_4 \cdot 7H_2O$ (Sigma). Initial As(V) concentrations ranged from $3x10^{-5}$ to $1x10^{-2}$ mol dm^{-3}. H_2SO_4 (95-97%) and HCl were used to acidify the experiments with and without sulfate, respectively.

The influence of sulfate on As(V) sorption was studied by simultaneously adding As(V) and sulfate (as Na_2SO_4) stock solutions to sorbent suspensions prepared in the pH range of 2.3-2.5.

A given amount of solid (0.05 g) was put in contact with 20 cm^3 of metal solution in stoppered polyethylene bottles at room temperature (22±1°C). The bottles were stirred continuously for 50 h. Thereafter, samples were filtered through 0.20 μm pore size filters. Concentrations of iron, arsenic, potassium and sulfur were determined by Inductively Coupled Plasma Atomic Emission Spectrometry (ICP-AES) when iron and arsenic concentrations exceeded the ICP-AES detection limit ($1.3x10^{-6}$ and $3.5x10^{-6}$ mol dm^{-3} for arsenic and iron, respectively). Graphite Furnace Atomic Absorption Spectrometry (GFAAS) was used for lower concentrations.

The pH of the solutions was measured at equilibrium (pH_{eq}) using a Crison pH-meter combination electrode with temperature compensation. The calibration of the pH was carried out with standard buffer solutions of pH 2 and pH 4. The accuracy was ±0.02 pH units (± 4.5% in H^+ activity).

Different series of batch experiments were conducted to quantify the arsenic removal by goethite and jarosite following this experimental methodology:

i Variation of the As(V) sorption as a function of the arsenic concentration in solution (between $3x10^{-5}$ and $1x10^{-2}$ mol dm^{-3}) at 0.15 mol dm^{-3} ionic strength and pH 1.5-2.5.

ii Variation of the pH (1.5-2.5) on As(V) sorption.

iii Variation of ionic strength. In most experiments the ionic strength was 0.15 mol dm^{-3} (NaCl), but two additional experiments were carried out at 0.02 mol dm^{-3} (NaCl) (see below).

iv Variation of the As(V) sorption as a function of sulfate concentration in solution (between $5x10^{-3}$ to $2.8x10^{-1}$ mol dm^{-3}).

The concentration attached to the solid, $\{As\}_S$ in mol m^{-2}, was calculated by the difference between the initial concentration of arsenic added to the solution, $[As]_0$, and the equilibrium concentration, $[As]_{eq}$, and normalized with the surface area (SA, in m^2) to volume (V, in dm^3) according to the equation:

$$\{As\}_s = \left([As]_0 - [As]_{eq}\right) \times \frac{V}{SA} \qquad (4.1)$$

Concentrations of potassium, sulfur and total iron were used to calculate the amount of solid dissolved. The results were normalized with respect to the final mass.

4.1.3 Goethite surface complexation model

Based on the results of this study and on previously reported data (Dzombak and Morel, 1990), a surface complexation model with the Diffuse Double Layer (DDL) model for electrostatics was employed to describe the As(V) sorption edge for goethite. Constants

for protonation of the surface hydroxyl groups and aqueous species were taken from earlier studies (Table 4.1).

Table 4.1. Aqueous protonation constants and intrinsic surface complexation constants.

Arsenate protonation constants[a]	
Reaction	log K
$AsO_4^{-3} + H^+ = HAsO_4^{-2}$	11.60
$AsO_4^{-3} + 2H^+ = H_2AsO_4^-$	18.35
$AsO_4^{-3} + 3H^+ = H_3AsO_4$	20.60
Intrinsic goethite surface complexation constants[b]	
Reaction	log K
$H^+ + Hfo\_sOH = Hfo\_sOH_2^+$	7.47
Hfo_sOH = Hfo_sO- + H+	-9.51
Arsenate adsorption constants[c]	
Reaction	log K
$AsO_4^{-3} + 3H^+ + Hfo\_sOH = Hfo\_sH_2AsO_4 + H2O$	26.27
$AsO_4^{-3} + 2H^+ + Hfo\_sOH = Hfo\_sHAsO_4^- + H2O$	21.15

[a] These reaction constants are taken from the MINEQL$^+$ database (Schecher&McAvoy, 1998)

[b] Liger *et al.* (1999)

[c] *This study*

The stoichiometries of the surface complexes used to fit sorption data are listed in Table 4.1. Similar surface complexes have been used in earlier studies (Manning and Goldberg, 1996; Gao and Mucci, 2001; Goldberg and Johnston, 2001; Dixit and Hering, 2003). The PHREEQC code was used to obtain the intrinsic As(V) surface complexation constants. Surface site densities were set to the values obtained from the sorption isotherms. Model predictions with fixed site densities and complexation constants were performed using the PHREEQC and MINTEQ (Allison *et al.*, 1990) data bases. The ionic strength values of this study were well below 0.7, which is regarded as the upper limit for the application of the extended Debye-Hückel and the ion-association equations that PHREEQC uses for the calculation of activity coefficients of aqueous solutes.

4.2 Results and discussion

4.2.1 Solid phases

Solid phases were characterized before and after reacting with the solutions at the different pH values. XRD patterns are shown in Figure 4.1 and demonstrate that the solids were pure goethite and pure jarosite, respectively.

Concentrations of potassium, sulfur and total iron were used to calculate the amount of solid dissolved. In the case of goethite, the iron concentration corresponded to an amount of solid dissolved less than 1%. In the case of jarosite, the aqueous potassium concentration indicated that the amount of dissolved jarosite ranged from 20-35%.

Given the possibility of precipitation of new phases at the experimental conditions, the saturation indices of the reacted solution with respect to As and Fe-bearing phases were calculated (Table 4.2).

It is observed that all the reacted solutions were undersaturated with respect to all As-bearing phases, including scorodite ($FeAsO_4{:}2H_2O$). Although the solubility product of amorphous Fe(III)-arsenate is unknown, the solubility of the amorphous phase is generally greater than the crystalline phase (Stumm and Morgan, 1996). Therefore, precipitation of As and Fe-As bearing phases during the experiments is discarded. As regards to the Fe-phases, some solutions appear to be supersaturated with respect to hematite. However, hematite is only formed at high temperatures (150-200ºC) in the pH range 0-3 (Robins, 1967). It is worth mentioning that PHREEQC calculations do not consider kinetic aspects, and the formation of goethite in Fe(III) systems is very slow (weeks to months at room temperature) (Schwertmann and Cornell, 1991). Moreover, after reaction XRD patterns of samples only show the presence of goethite and jarosite, discarding the precipitation of any new solid phase.

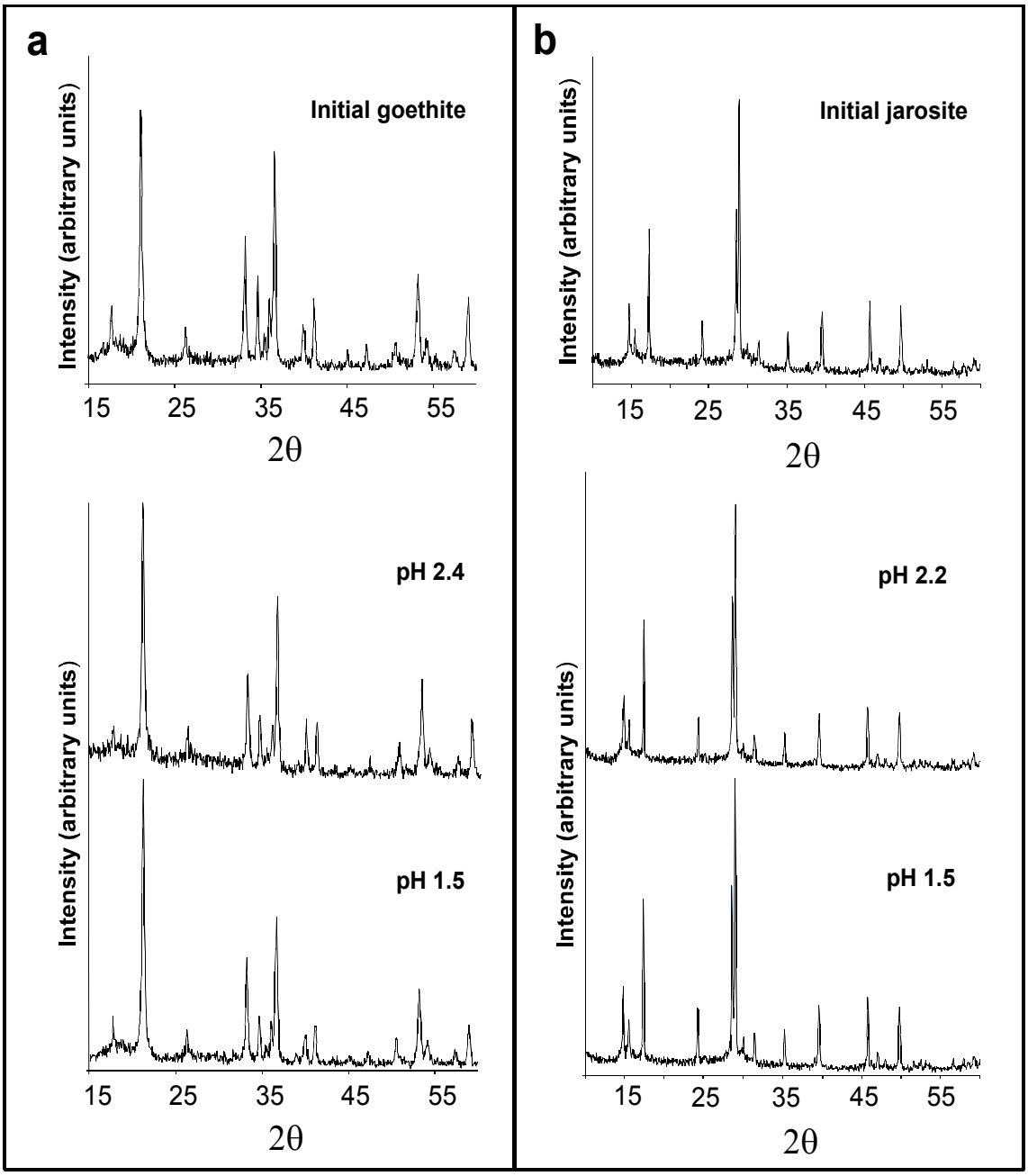

Figure 4.1. Powder X-ray diffraction patterns of initial and residual solids after reaction: (a) at pH 1.5 and 2.4 and 0.15 mol dm^{-3} of ionic strength; (b) at pH 1.5 and 2.2, and 0.15 mol dm^{-3} of ionic strength.

Table 4.2. Calculated saturation index (SI) for Fe-As mineral phases of reacted solutions using the PHREEQC code and the WATEQ4F database with the exception of schwertmannite: logK=10.15 (Yu *et al.*, 1999) and logK=18.0 (Bigham *et al.*, 1996).

Mineral phase	Formula	Solutions reacted with goethite		Solutions reacted with jarosite		
		pH 1.5	pH 2.5	pH 1.5	pH 2	pH 2.7
				No sulphate		
Arsenolite	As_2O_3	-47.02	-47.76	-47.02	-47.29	-48.11
As native	As	-73.56	-73.92	-73.55	-73.69	-74.10
As2O5(cr)	As_2O_5	-12.81	-13.55	-12.81	-13.08	-13.90
As2S3(am)	As_2S_3	-	-	-418.10	-420.75	-425.43
Claudetite	As_2O_3	-47.06	-47.80	-47.06	-47.33	-48.15
Fe(OH)3(a)	$Fe(OH)_3$	-5.07	-4.34	-5.69	-4.23	-2.33
Fe2(SO4)3	$Fe_2(SO_4)_3$	-	-	-25.41	-24.97	-25.17
Goethite	FeOOH	0.82	1.55	0.21	1.66	3.56
Hematite	Fe_2O_3	3.65	5.10	2.42	5.33	9.13
JarositeH	$(H_3O)Fe_3(SO_4)_2(OH)_6$	-	-	-10.73	-7.95	-4.83
Jarosite-K	$KFe_3(SO_4)_2(OH)_6$	-	-	-8.52	-5.24	-1.42
Jarosite-Na	$NaFe_3(SO_4)_2(OH)_6$	-	-	-10.27	-6.99	-3.16
Maghemite	Fe_2O_3	-6.74	-5.29	-7.97	-5.07	-1.27
Schwertmannite (logK=10)	$Fe_8O_8(OH)_{4.5}(SO4)_{1.75}$	-	-	-28.37	-18.13	-5.19
Schwertmannite (logK=18)	$Fe_8O_8(OH)_{4.5}(SO_4)_{1.75}$	-	-	-36.37	-26.13	-13.19
Scorodite	$FeAsO_4{:}2H_2O$	-3.33	-2.97	-3.95	-2.63	-1.14
				Sulphate		
Arsenolite	As_2O_3	-47.02	-47.76	-47.02	-47.27	-48.06
As native	As	-73.55	-73.93	-73.56	-73.68	-74.08
As2O5(cr)	As_2O_5	-12.81	-13.55	-12.81	-13.06	-13.85
As2S3(am)	As_2S_3	-415.25	-420.81	-414.86	-417.25	-421.75
Claudetite	As_2O_3	-47.06	-47.80	-47.06	-47.31	-48.10
Fe(OH)3(a)	$Fe(OH)_3$	-5.58	-4.93	-6.08	-4.80	-2.88
Fe2(SO4)3	$Fe_2(SO_4)_3$	-15.32	-18.97	-15.93	-15.58	-15.55
Goethite	FeOOH	0.32	0.96	-0.19	1.09	3.01
Hematite	Fe_2O_3	2.64	3.92	1.63	4.19	8.03
JarositeH	$(H_3O)Fe_3(SO_4)_2(OH)_6$	-8.50	-9.78	-9.75	-7.34	-4.06
Jarosite-K	$KFe_3(SO_4)_2(OH)_6$	-	-	-7.50	-4.59	-0.61
Jarosite-Na	$NaFe_3(SO_4)_2(OH)_6$	-8.04	-8.37	-9.61	-6.56	-2.55
Maghemite	Fe_2O_3	-7.75	-6.47	-8.76	-6.20	-2.37
Schwertmannite (logK=10)	$Fe_8O_8(OH)_{4.5}(SO4)_{1.75}$	-25.82	-23.50	-29.63	-20.65	-7.46
Schwertmannite (logK=18)	$Fe_8O_8(OH)_{4.5}(SO_4)_{1.75}$	-33.82	-31.50	-37.63	-28.65	-15.46
Scorodite	$FeAsO_4{:}2H_2O$	-3.84	-3.57	-4.34	-3.19	-1.66

4.2.2 Sorption Kinetic considerations

Suspensions were stirred continuously. In the case of goethite, equilibrium was reached after 18 h (Fig. 4.2a). Jarosite-sorption kinetics showed an increase in As sorption even after 53 h, and equilibrium was not attained (Fig. 4.2b). Iron concentration in the goethite solutions was always lower than $3x10^{-4}$ mol dm^{-1}, indicating that less than 1% of initial goethite was dissolved. Concentration of sulfur, potassium or iron increased over the jarosite experimental runs. This increase in metal concentration represented around 35±5 and 22±3 % of dissolved solid at pH 1.5 and 2, respectively. Therefore, at this pH range, goethite hardly dissolved and sorption was the only process that occurred. By contrast, jarosite dissolution occurred together with arsenic sorption.

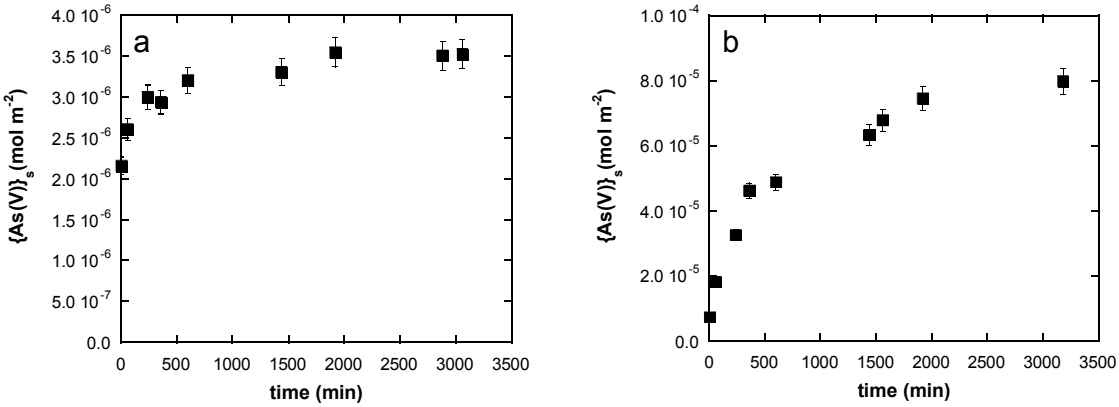

Figure 4.2. Kinetics of As(V) sorption on goethite (a) and jarosite (b). pH_{eq} was 1.5 and $[As(V)]_0$=$1x10^{-3}$ mol dm^{-3} and initial solid was 0.05 g.

4.2.3 As(V) uptake from solution. Effect of arsenic concentration

As(V) removal from aqueous solution was investigated at initial As(V) concentrations of $3x10^{-5}$ to $1x10^{-2}$ mol dm^{-3} at pH_{eq} of 1.5-2.5.

The variation of the As(V) sorbed onto goethite with the equilibrium arsenic concentration in solution is shown in Figure 4.3. The experimental data are fitted with a non-competitive Langmuir isotherm that is expressed as:

$$\Gamma = \Gamma_{max} \frac{K_L \cdot [As]_{eq}}{1 + K_L \cdot [As]_{eq}} \qquad (4.2)$$

where Γ is the quantity of arsenic sorbed on the solid and Γ_{max} is the maximum arsenic sorption in mol m^{-2}, K_L is the Langmuir constant in dm^3 mol and $[As]_{eq}$ is the arsenic concentration in solution at equilibrium in mol dm^{-3}.

The maximum sorption capacity (Γ_{max}) obtained for goethite is 7.0x10 $^{-6}$ mol m^{-2}. The good fitting of the experimental data to the Langmuir isotherm (Fig. 4.3) indicates that the coverage of the sorption sites was in the form of a monolayer, and all surface sites had nearly the same sorption energies. The parameters obtained from the fitting are listed in Table 4.3.

Table 4.3. Parameters of the Langmuir isotherms obtained for As(V) sorption onto goethite as a function of pH and ionic strength.

Experimental conditions		**Results**		
pH_{eq}	Ionic Strength (mol dm^{-3})	K_L (dm^3 mol^{-1})	Γ_{max} (mol m^{-2})	R^2
2.30±0.15	0.02	$9.9 \cdot 10^3$	$6.2 \cdot 10^{-6}$	0.991
2.45±0.20	0.15	$1.4 \cdot 10^4$	$5.7 \cdot 10^{-6}$	0.998
1.59±0.10	0.15	$7.3 \cdot 10^3$	$7.0 \cdot 10^{-6}$	0.995

Earlier spectroscopic studies (e.g. Waychunas *et al.*, 1993; Grossl and Sparks, 1995; Fendorf *et al.*, 1997) have shown that arsenate is sorbed onto iron hydroxides, such as goethite, forming inner sphere surface complexes by ligand exchange with hydroxyl groups at the mineral surface. Waychunas *et al.* (1993) and Sherman and Randall (2003) reported the formation of bidentate complexes, resulting from corner sharing between AsO_4 tetrahedra and edge-sharing pairs of FeO_6 octahedra.

The sorption capacity of jarosite was investigated at the same initial As(V) concentrations and experimental conditions as in goethite experiments (Fig. 4.4).

It is not easy to interpret arsenic sorption on jarosite given jarosite dissolution at this low pH range. The sorption data obtained could not be fitted with a Langmuir or a Freundlich isotherm. Nonetheless, useful quantification was possible. Jarosite sorption kinetics showed that sorption occurred, and that the amount of arsenic sorbed was the

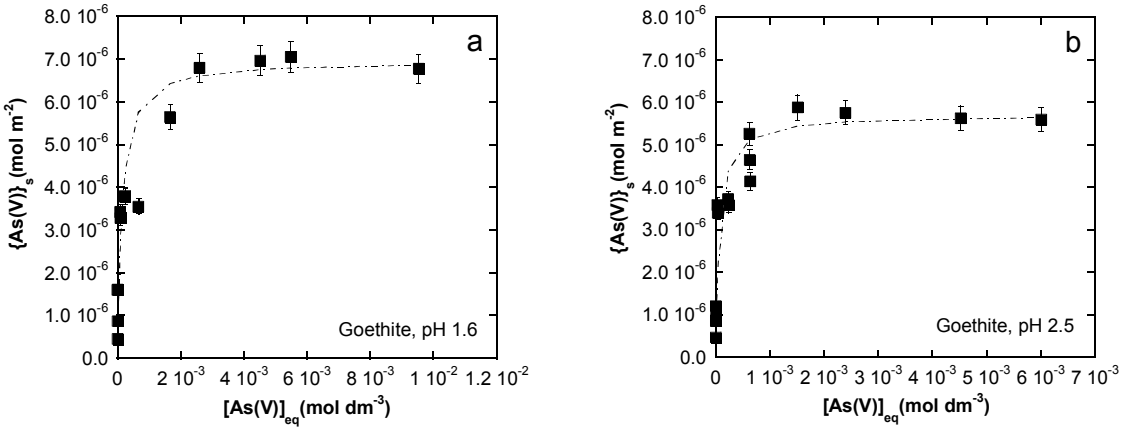

Figure 4.3. As(V) sorption isotherms for goethite. 0.05 g of solid at 0.15 mol dm^{-3} ionic strength and pH_{eq} 1.6 (a) and 2.5 (b). Dotted lines correspond to the fitting data by using a Langmuir isotherm (see text).

maximum after 53 h in all experiments. Thus, the highest amount of arsenic removed calculated by eq. 4.1, was around $1.2\pm0.2 \times 10^{-4}$ mol m^{-2} according to the maximum sorption capacity values of jarosite at the end of the experiments. Hence, jarosite appears to be significantly more effective in sequestering As(V) than goethite (compare Figs. 4.3 and 4.4). This result is in good agreement with Gräfe *et al.* (2008), who observed that the As(V) sorption mechanism on jarosite was substantially different from that on goethite. These authors reported significantly larger surface coverage of As(V) on jarosite with respect to As(V) on goethite. They suggested that As(V) replaced structural sulfate tetrahedra with the result that jarosite was more effective in removing As(V) than goethite owing to the presence of structural sulfate groups.

The As(V) removal capacities obtained in this study for goethite and jarosite were compared with earlier results obtained with natural and synthetic phases (Table 4.4). Comparison was made by normalizing the results with respect to surface area. Our results indicate that the maximum capacity of goethite is between 6 and $7x10^{-6}$ mol m^{-2} at pH 1.5-2.5. These values are very similar to the result reported by Lehmann *et al.* (2005) at pH 3 for natural goethite. At pH 3-7, sorption capacities ranged approximately from $3x10^{-6}$ mol m^{-2} to $4.6x10^{-6}$ mol m^{-2} on both natural and synthetic goethite according to Matis *et al.* (1997), Dixit and Hering (2003) and Giménez *et al.* (2007).

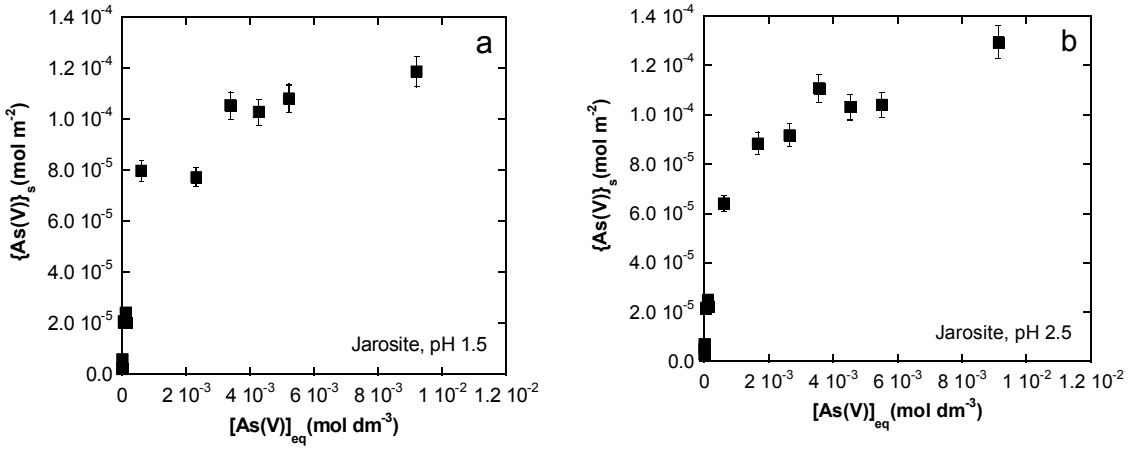

Figure 4.4. As(V) removed by jarosite at pH_{eq} 1.5 (a) and 2.5 (b) and 0.15 mol dm^{-3} ionic strength. Initial solid was 0.05 g.

4.2.4 Effect of pH on As(V) removal

Sorption of As(V) onto iron (oxy)hydroxides is expected to depend on pH because both aqueous arsenate species and the iron (oxy)hydroxide surface charge are pH-dependent. Under acidic conditions, sorbed protons on the functional groups of the surface cause an overall positive surface charge with the result that anions can be sorbed. The aqueous arsenate species present at the pH range studied are H_3AsO_4 and $H_2AsO_4^-$. Although [H_3AsO_4] predominates over [$H_2AsO_4^-$] at pH < 2.3, [$H_2AsO_4^-$] can be preferentially sorbed at this low pH range. Table 4.3 shows that arsenate sorption on goethite decreases slightly

Table 4.4. Summary of experimental conditions and As(V) removal capacities of goethite and jarosite obtained in this study and in earlier works.

	Mineral	Synthesis method	Solid conc. (gL^{-1})	[As] initial ($molL^{-1}$)	Contact time (h)	BET (m^2g^{-1})	pH	As(V) removed (mol m^{-2})
Lehmann *et al*. (2005)	Goethite	*Natural*	1	$1.3\cdot10^{-4}$ to $1.3\cdot10^{-3}$	24	96	3**	$6.3\ 10^{-6}$
Matis *et al*. (1997)	Goethite	Wells (1991)	1	$1.3\cdot10^{-4}$ to $1.3\cdot10^{-3}$	0.5	132	3-3.3†	$4.6\ 10^{-6}$
Dixit and Hering (2003)	Goethite	Schwertmann&Cornwell (1991)	0.5	$1\cdot10^{-5}$ to $1\cdot10^{-4}$	24	54	4†	$3.2\ 10^{-6}$
Giménez *et al*. (2007)	Goethite	*Natural*	5	$1\cdot10^{-6}$ to $3\cdot10^{-3}$	48	2	7.5†	$3.0\ 10^{-6}$
This study	*Goethite*	Schwertmann&Cornell (1991)	2.5	$3\cdot10^{-5}$ to $1\cdot10^{-2}$	48	29	1.6†	$7.0\cdot10^{-6}$
This study	*Goethite*	Schwertmann&Cornell (1991)	2.5	$3\cdot10^{-5}$ to $1\cdot10^{-2}$	48	29	2.3†	$6.2\cdot10^{-6}$
This study	*Goethite*	Schwertmann&Cornell (1991)	2.5	$3\cdot10^{-5}$ to $1\cdot10^{-2}$	48	29	2.5†	$5.7\cdot10^{-6}$
Gräfe *et al.* (2008)	Jarosite*	Sondi et al. (2001)	-	$2.5\cdot10^{-4}$	336	3	5.6†	$1.4\cdot10^{-5}$
This study	*Jarosite*	Baron&Palmer (1996)	2.5	$3\cdot10^{-5}$ to $1\cdot10^{-2}$	48	2	1.5-2.5†	$1.2\cdot10^{-4}$

*Na-Jarosite
** initial pH
† equilibrium pH

with increasing pH. A similar trend has been observed in earlier studies at pH higher than 4.5 (Dixit and Hering, 2003). According to Hsia *et al.* (1994) this behavior is reasonable since surface protonation increases the number of positively charged sites as the pH of the system is lowered. This enhances the attraction force between arsenic anions and the iron oxide surface, thereby increasing the amount of arsenate sorbed on the solid surface.

Jarosite showed no significant differences in the As(V) removal capacity in the short range of pH studied. The sorption mechanism via exchange sulfate-arsenate, suggested by Gräfe *et al.* (2008), could account for the negligible pH effect on the jarosite As(V) removal capacity.

4.2.5 Effect of ionic strength on As(V) removal

The effect of ionic strength on the As(V) sorption was studied by means of experiments carried out at 0.02 mol dm^{-3} and 0.15 mol dm^{-3}. The results plotted in Fig. 4.5 show that As(V) sorption is independent of ionic strength. The results suggest that As(V) adsorption on goethite could proceed via the formation of inner-sphere surface as indicated previously in earlier studies (e.g. Waychunas *et al.*, 1993; Grossl and Sparks, 1995; Fendorf *et al.*, 1997).

4.2.6. Goethite Surface Complexation Model

A surface complexation model based on the diffused double layer (DDL) was applied to elucidate goethite sorption capacity with pH (1.5 <pH <2.5), using the PHREEQC code. Site density was calculated from the maximum sorption density for As(V) (Γ_{max}=7x10^{-6} mol m^{-2}) obtained in this study, yielding 4.19 sites/nm^2, which lies in the range of goethite sorption capacity found in the literature (Lumsdon and Evans, 1994). Sorption data from Matis *et al.* (1997), Dixit and Hering (2003) and Lehmann *et al.* (2005) were used. The arsenate protonation constants and intrinsic surface constants used in the model are given in Table 4.1. Fig. 4.6 shows the good agreement between the model (dotted line)

and the experimental data. As reported in earlier studies (Matis *et al.* 1997; Dixit and Hering, 2003; Giménez *et al.*, 2007), the main trend observed is the decrease in goethite sorption as pH increases.

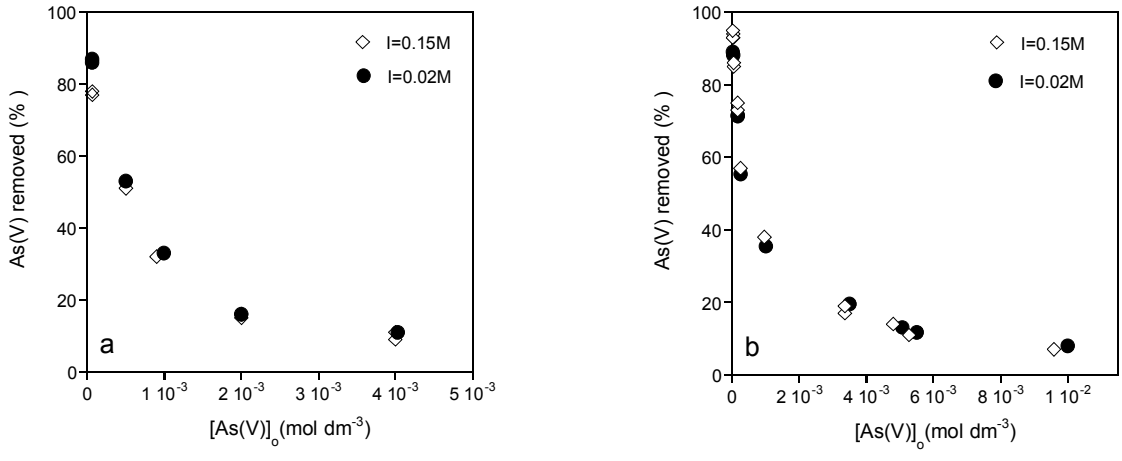

Figure 4.5. Variation of the As(V) sorption onto (a) goethite and (b) jarosite with ionic strength (0.1 and 0.02 mol dm^{-3} NaCl) at pH_{eq} 2 and different arsenic (V) concentrations in solution.

4.2.7 Effect of sulfate on As(V) removal

AMD waters are characterized by exceptionally high sulfate concentrations in waters. These values usually exceed 0.01 mol dm^{-3} (Olías *et al.*, 2004; Dousová *et al.*, 2005; Gault *et al.*, 2005; Acero *et al.*, 2006; Lee and Chon, 2006; Nieto *et al.*, 2007; Asta *et al.*, 2008a), and are possibly higher than 0.2 mol dm^{-3} in tailing pore waters (Al *et al.*, 2000; Moncur *et al.*, 2005; Acero *et al.*, 2007d). Competitive effects of co-occurring solutes such as sulfate have been demonstrated in earlier works (Wilkie and Hering, 1996).

Table 4.5 shows that the quantity of arsenate sorbed onto both solids decreased as sulfate concentration increased. This decrease is marked in the case of jarosite even at low sulfate concentrations (e.g. percentage sorbed is around 1-4% in the presence of sulfate and 38% in the sulfate free solution; Table 4.4). The inhibition of arsenate sorption in goethite was much lower than in jarosite in sulfate rich solutions (Table 4.5). The effect of sulfate was significant when sulfate concentrations exceeded 0.28 mol dm^{-3} at the pH

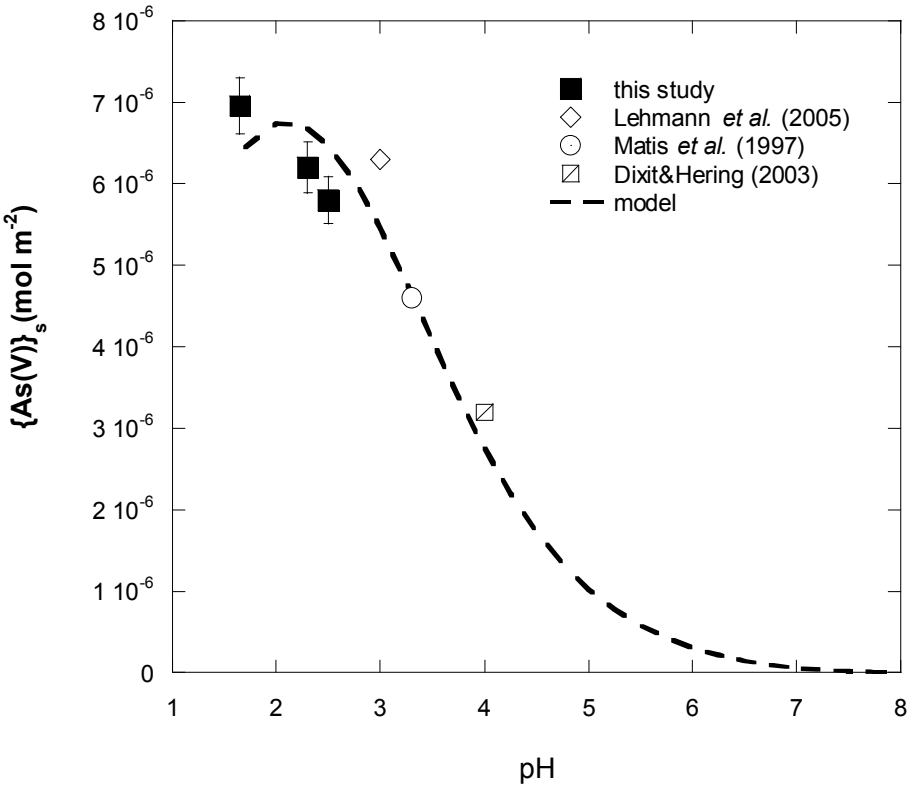

Figure 4.6. Comparison of As(V) sorption edge based on experimental data and DDL model (dotted line) based on the parameters listed in Table 4.1. pH values correspond to the final pH (pH_{eq}) except that of Lehmann *et al.*(2005), which corresponds to the initial pH value.

range studied. A similar decrease in sorption of As(V) in the presence of sulfate was obtained by Wilkie and Hering (1996), who studied the competitive effects of sulfate and arsenic sorption on hydrous ferric oxide (HFO).

Our results are consistent with the different sorption mechanisms reported in earlier studies that indicate that sorption capacity of goethite is slightly affected by sulfate, whereas jarosite, which exchanges sulfate groups for arsenate groups, decreases its exchange capacity as sulfate increases in solution.

Table 4.5. Comparison of the % As(V) sorbed in the presence and absence of sulfate at pH 2 and $[As(V)]_0=1x10^{-3}$ mol dm^{-3}.

	$[SO_4^{2-}]$ (mol dm^{-3})	% As sorbed
Jarosite	-	38
	0.005	4
	0.020	1
	0.280	0
Goethite	-	32
	0.005	31
	0.015	28
	0.020	25
	0.280	0

4.3 Conclusions

The results of this study show that goethite and jarosite are effective As(V) sorbents in highly acidic pH. In the absence of sulfate, the As(V) maximum sorption capacities of goethite and jarosite were 15 mg g^{-1} and 21 mg g^{-1}, respectively, under the similar experimental conditions of this study. These values are considerably lower than those reported by Fukushi *et al.* (2002, 2003b, 2004) for As(V) sorption capacity of schwertmannite (80 mg g^{-1} for synthetic and 60 mg g^{-1} for natural schwertmannite in AMD). This suggests a net release of As(V) to the waters during schwertmannite transformation to jarosite or goethite. Moreover, if these solids were dragged to reductive environments (e.g. pit bottoms), the potential risk of arsenic release would be higher in the case of schwertmannite. In the light of our results, ionic strength has no substantial effect on the sorption of arsenic on jarosite and goethite. However, the sulfate content in the AMD impacted areas has a greater effect on the arsenate sorption capacity of jarosite than on that of goethite. In the absence of competitive effects, As(V) sorption on jarosite is higher than that on goethite under the studied conditions.

Part III

Arsenic mobilization in the context of the Iberian Pyritic Belt

Chapter 5

Arsenic speciation in different Fe(III) minerals: an AMD field case study

In mine wastes (e.g. mine tailings and mine dumps), acid mine drainage (AMD) results from the sulfide oxidative dissolution that leads to generation of free acidity and soluble metals and metalloids, causing a major environmental problem (Bowell and Bruce, 1995; Younger, 1997; Olías *et al.*, 2004). Arsenic, a common constituent of mine waters, can reach very high concentrations in AMD (hundreds of mg L^{-1}), and it can be discharged to fluvial environments, threatening indigenous microorganisms, plants and animals (e.g. Cullen and Reimer, 1989; Foster *et al.*, 1998; Foster and Ashley, 2002).

Most geochemical processes involve the transfer of chemical elements between a fluid phase and a solid mineral phase and occur at solid-water interface (Stumm, 1987; Lasaga, 1990). The dynamics controlling all such processes are governed by the detailed structure and chemical bonding of the mineral surface in contact with the fluid. Among various physical and chemical processes taking place in the systems, sorption-desorption reactions are among the most important. Sorption reactions have been recognized as a

mechanism for the control of metal(loid) concentrations. Soils and sediments, at the solid-water interface represent the major sinks for metal(loid)s released to the environment.

As mentioned in chapter 4, arsenic mobilization in soils and acidic waters is controlled by sorption on newly formed precipitates (schwertmannite, jarosite and goethite), causing natural arsenic attenuation. These new phases effectively sorb As(V) and decrease arsenic concentrations in waters (Fukushi, *et al.* 2003a; Gault *et al.*, 2005; Sánchez-España *et al.* 2005; Acero *et al.*, 2006; Lee and Chon, 2006), playing a key role in the removal of arsenic and other trace elements from solution by adsorption and co-precipitation (Bigham *et al.*, 1994; Benjamin, 1983; Johnson, 1986; Stumm and Sulzberger, 1992; Webster *et al.*, 1998). Since the sorption capacity of these solids is very different (see chapter 4), the study of the mineral phases implicated in the effective arsenic mitigation in natural waters, as well as their temporal and spatial distribution, is of major importance to understand the arsenic evolution in waters.

To study the speciation of trace elements in solids, in other words, the compounds containing a trace element in a sample, a relatively simple and well-adopted procedure is the sequential extraction method.

Ideally, in a sequential extraction method each reagent should target a specific solid phase associated with the trace element of interest. Since the stepwise fractionation cannot be quantitatively delineated, the extracted pools are operationally defined. However, the main limitations of sequential extraction techniques are the lack of selectivity of the reagents and the possible metal readsorption and redistribution during the treatments (Bermond and Yousfi, 1997; Gómez-Ariza *et al.*, 2000). Moreover, the metal partitioning obtained by such techniques is operationally defined by the methods of extraction used (Abollino *et al.*, 2005). Nevertheless, such procedures have found widespread use in environmental sciences: as long as the results are interpreted with full awareness of their limitations, they provide very useful information on the behavior of metals in solid matrices, and help in the assessment of possible contamination risks. In line with this situation, the complexity of the arsenic mineralogy and the widespread

occurrence of As-bearing iron oxyhydroxides require that further detailed speciation and characterization studies be undertaken at the molecular scale to better determine the form, nature, and distribution of As in sediments (Paktunc *et al.*, 2003). X-ray absorption spectroscopy (XAS) has been used succesfully by a number of researchers to investigate solid phase speciation of As in the environment (Foster *et al.*, 1998; Savage *et al.*, 2000; Strawn *et al.*, 2002; Paktunc *et al.*, 2003; Gault *et al.*, 2003, 2005; Impellitteri, 2005; Arai *et al.*, 2006; Charnock *et al.*, 2007; Slowey *et al.*, 2007; Cancès *et al.*, 2008; Román-Ross *et al.*, 2009). These studies made it clear that an understanding of the geochemical processes controlling arsenic mobility cannot be achieved unless the mineralogical/chemical composition of the arsenic sources at molecular scale is known. The speciation of arsenic in these precipitates is critical for the determination of its environmental fate and for the development of effective management strategy for AMD.

To study the natural arsenic mitigation processes in a natural system, the waters and sediments of the acid discharge at the abandoned Tinto Santa Rosa mine were examined (Fig. 5.1). This acid stream is located in the Iberian Pyritic Belt (IPB), one of the most important metallogenetic provinces of volcanic-hosted massive sulfide deposits in the world (e.g. Leistel *et al.*, 1998). Mining activities in this area have generated enormous amounts of mining waste over many centuries, which continue to generate acidity and metal pollution affecting streams and rivers in the Tinto and Odiel drainage basins (Olías *et al.*, 2006; Nieto *et al.*, 2007; Sarmiento *et al.*, 2009). Pyrite is the most abundant mineral in the massive sulfide deposits and in the mining waste. In addition to pyrite, other minor metallic sulfides such as chalcopyrite, galena, sphalerite and arsenopyrite dissolve and contribute to the high concentrations of metals and arsenic to surface and groundwaters.

The acidic discharge of the abandoned Tinto Santa Rosa mine transports high concentrations of acidity, sulfate and metal(loid)s (e.g., Fe, As, Co, Ni, Cu, Pb, and Mn). This acid stream presents similar features to the acidic solutions that emerge from mines, waste rock piles and/or tailings ponds at other locations of the Iberian Pyrite Belt (IPB)

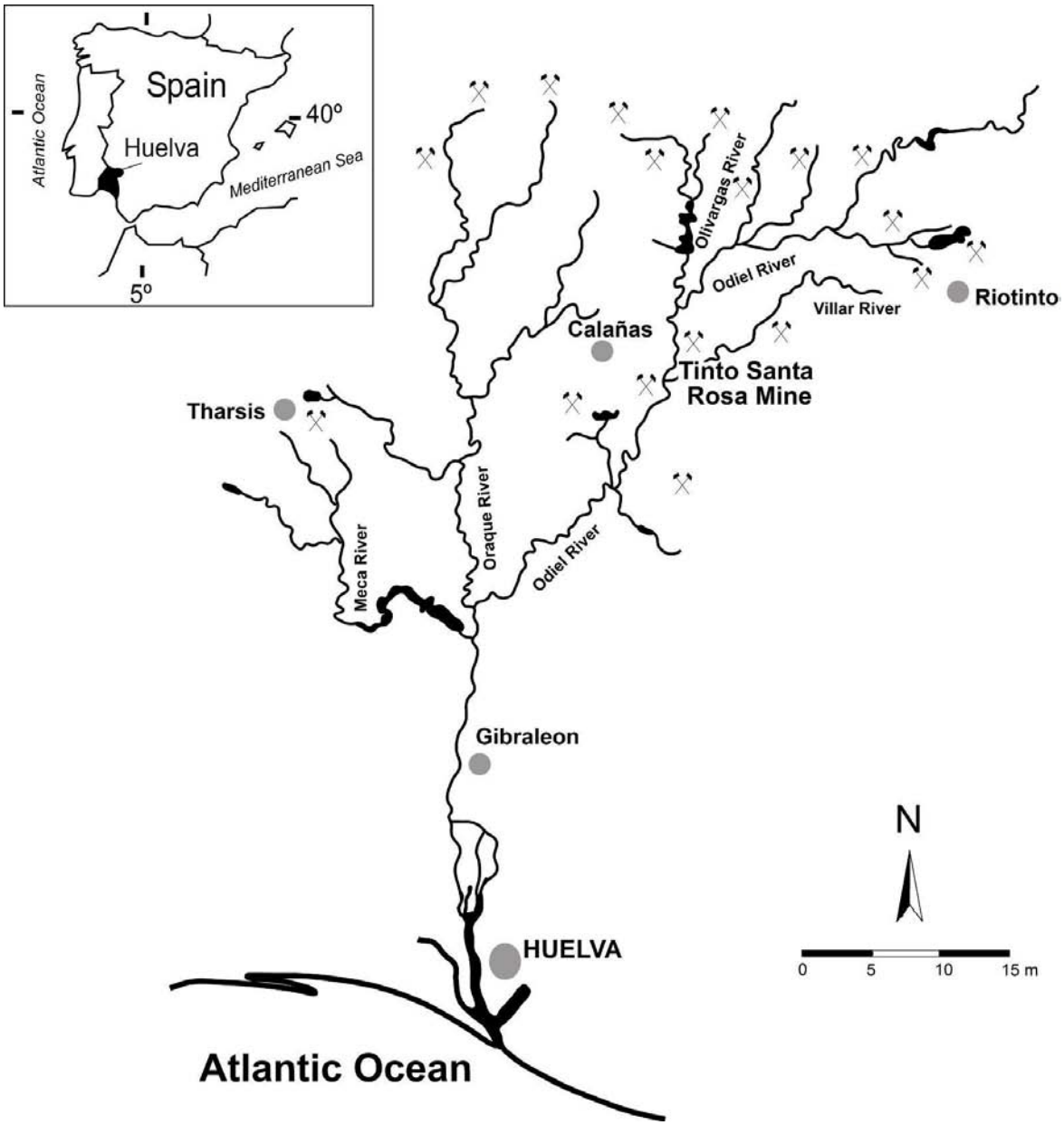

Figure 5.1. Map of Rio Odiel watershed with some of the most important mines. Site of field study (abandoned Tinto Santa Rosa mine). Modified after Sarmiento *et al.*, 2006, with permission from the author.

(see for example Olías *et al.*, 2004; Sánchez-España *et al.*, 2005a,b, 2007; Sánchez-Rodas *et al.*, 2005; Sarmiento *et al.*, 2005, 2007; Acero *et al.*, 2006; Nieto *et al.*, 2007).

Stream beds in acid mine drainage are often covered with highly contaminated sediments. Bulk arsenic concentrations in the Tinto Santa Rosa stream ranged from 0.75 to 40 mg g^{-1}. The environmental impact assessment of these precipitates and their attenuation capacity require the identification and quantification of the arsenic in the sediments and the link between the evolution of the relative proportions of these species with the physico-chemical and mineralogical characteristics of the sediments.

With the aim of gathering the necessary information on the evolution of the chemical forms of arsenic and its association with the sediments, a combination of methods were used: 1) X-ray diffraction (XRD) was carried out to identify the potential As-bearing phases in the sediments; 2) total acid digestion and X-Ray Fluorescence were used to quantify the solid phase element concentrations; 3) the mineralogical and chemical results were confirmed by synchrotron-based X-ray spectroscopy (X-Absorption Spectroscopy, XAS). X-ray Absorption Near Edge Structure (XANES) spectra of the stream bed sediment samples indicated that As occurs mainly as As(V) and yield direct evidence of changes in As speciation with depth. Taken together, these data allow us to fully understand how arsenic sequestration proceeds and to identify which phases are the main arsenic scavengers in the acid stream, and how water-sediment interaction contributes to the chemical evolution of the stream water, with particular emphasis on As geochemistry.

5.1 Materials and Methods

5.1.1 Field site and sampling description

All the water and sediment samples described in this study were collected in July and November of 2006, March of 2007 and February of 2008 from the acid discharge of the abandoned Tinto Santa Rosa mine. This shallow stream (approximately 100-150 cm wide

by 20-45 cm) was studied from the adit mouth to approximately 300 m downstream where it flows into the Villar River (Fig. 5.2). The stream flows down a narrow channel (1.5-2 m) over terraces of ochreous sediment, forming different terrace levels along the channel. The stream bed is covered with several centimetres (up to 10 cm) of yellowish and reddish loose and crusty precipitates, creating different terrace levels along the channel (Fig. 5.3). In order to study the water geochemistry as well as the mineralogy and chemistry of the solids of the Tinto Santa Rosa stream samples were collected in different campaigns.

At each sampling point, pH, temperature, Eh and conductivity were measured *in situ* and three water samples were taken in acid-pre-washed polyethylene bottles, after rinsing thoroughly with filtered local water. Two of the samples were filtered through a 0.1-μm pore membrane filter. One sample (15 mL) was acidified with 1 mL of concentrated HNO_3 solution for major and trace element analysis, while the other sample was acidified with HCl, adjusting its pH to less than 1, for dissolved Fe(II)/Fe(III) determination. The third water sample, for arsenic speciation determination, was taken following the preservation method of Oliveira *et al.* (2006). This sample was filtered through a 0.2-μm pore membrane filter, acidified with HCl and was eluted at a flow rate of ca. 2mL min^{-1} through 10 g of cationic exchange resin placed in a glass column (25 cm height, 1.5 cm i.d.). The first 10 mL of eluted sample were discarded and the following 20 mL were collected for analysis. All the water samples were preserved in the dark at 4ºC until analyzed. Fe and As speciation was analyzed in less than 72 h and 48 h, respectively, since the samples were taken.

Solid samples of the terraces and loose precipitates were also taken from the surface of the stream bed and at different depths and at the sampling points (Fig. 5.2). Samples were dried at room temperature prior to mineralogical and chemical determinations.

The water flow varies seasonally and ranges from an average of 1.4 L s^{-1} (after a very rainy period of time, November 2006) to 0.70 L s^{-1} (March, 2007). Reported values for the water flow are in the same range from 0.5 to 1.8 L s^{-1} (Sánchez-España *et al.*, 2005). The

residence time of water from the adit mouth to downstream where it flows into the Villar River varies from 2 to 3.5 h depending on the flow.

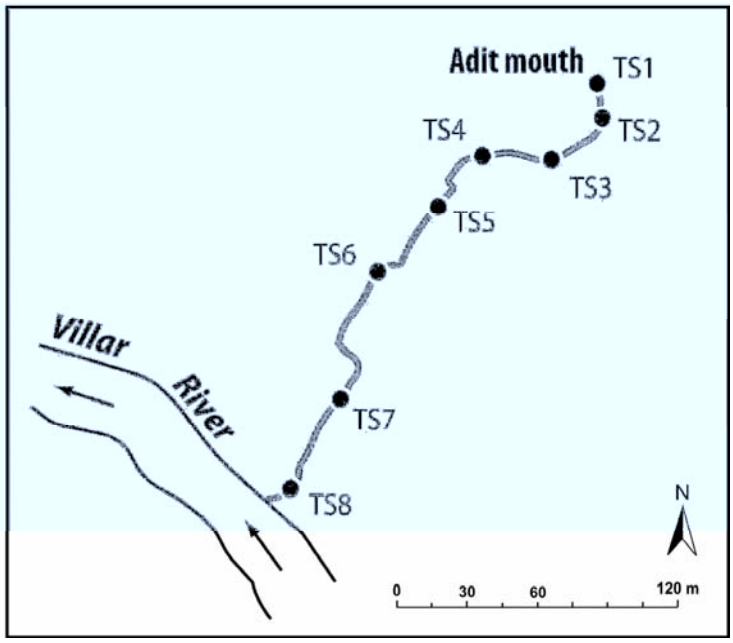

Figure 5.2. Schematic representation of the water sampling points in the acid discharge of the Tinto Santa Rosa mine (see Table 5.1).

5.1.2 Analytical methods

Water pH was measured in the field using a Crison® glass electrode with temperature compensation after calibration with standard buffer solutions of pH 2 and 7. Redox potential was measured using a Pt combination electrode (ThermoOrion SureFlow®) and checked before using by solutions of 220 and 468 mV. The measurements were corrected to the Standard Hydrogen Electrode *(SHE)* to calculate pe. Electrical conductivity was measured with a Pt cell calibrated with KCl 0.1 and 0.01 m solutions. The measurement errors for pH, Eh and conductivity were ≤ 0.05 pH units, ≤ 5 mV and ±1%, respectively.

Concentrations of major elements in solution were measured by Inductively Coupled Plasma Atomic Emission Spectrometry (ICP-AES) using a Perkin-Elmer®

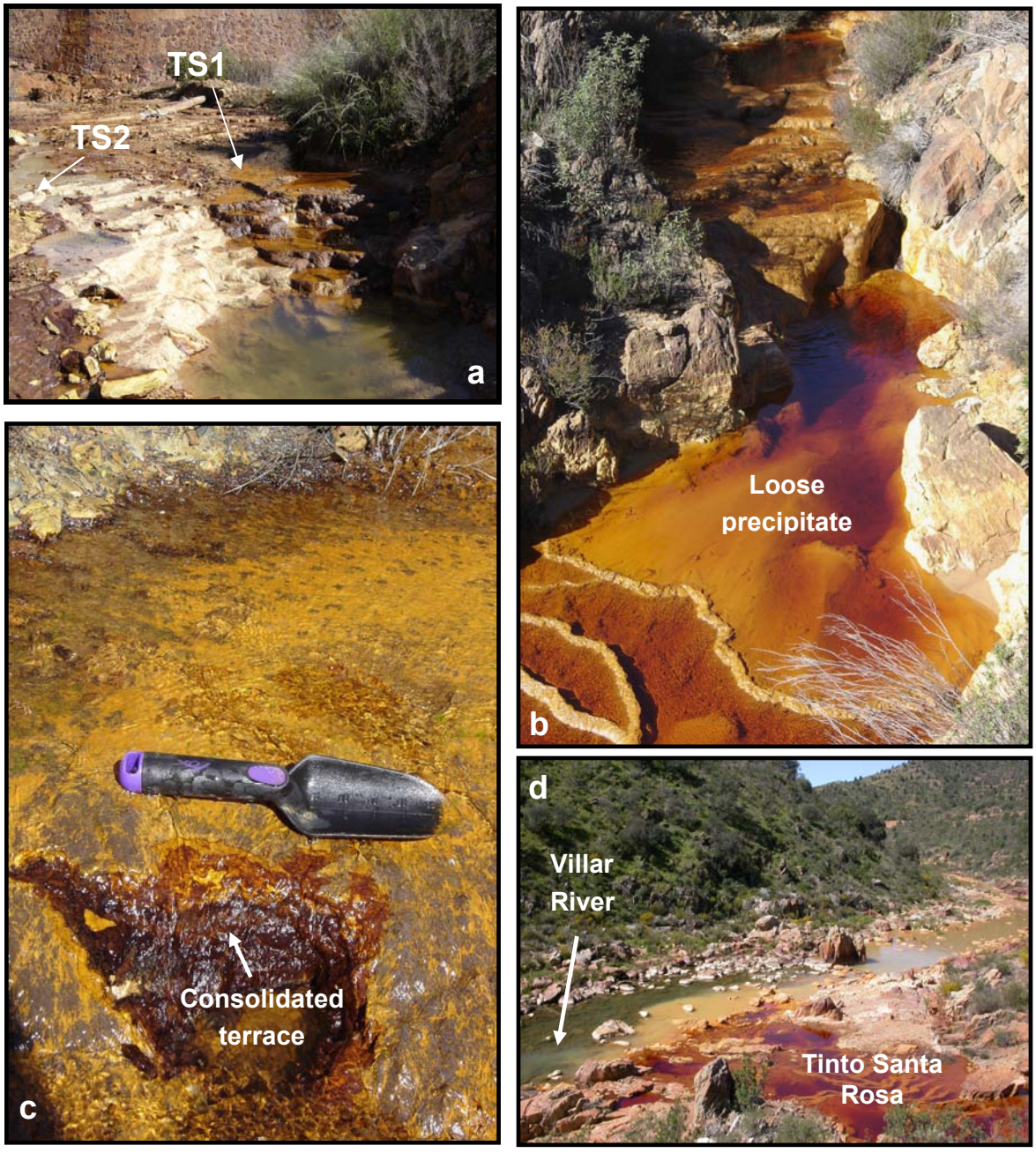

Figure 5.3. Different locations of Tinto Santa Rosa sampling site. (a) View of the area where the two AMD sources are mixing (TS1 and TS2); (b) terraces and fresh sediment of the bedstream at sampling point TS4; (c) close up view of a terrace (TS3); (d) overview of the stream (TS8) where it flows into the Villar River, wich contributes to Odiel River.

Optima 3200 RL. Detection limits were 0.1 mg L^{-1} for Al and S; 0.05 mg L^{-1} for Ca and Mg; 0.1 mg L^{-1} for Si; 0.5 mg L^{-1} for K, 0.025 mg L^{-1} for Fe, Zn, Cu and Mn and 2 mg L^{-1} for Na. The error was estimated to be below 3% (more than ten times the detection limit). Concentrations of trace metals (Ni, Cd, Co, As, Pb, Sb, Ti and V) were analyzed by Inductively coupled plasma mass spectroscopy (ICP-MS) using a Perkin-Elmer® Sciex Elan 6000 instrument. Detection limits were on the order of 1 μg L^{-1} and the error was estimated to be below 5%. In the analyses of ICP-AES and ICP-MS, calibration with sets of standards was performed and the regression coefficients exceeded 0.999. To check the accuracy of the results, three laboratory standards were analyzed every 15 samples. Blanks and duplicates were also analyzed with each batch of samples. In ICP-AES and ICP-MS analyses, dilutions from 1:10 to 1:20 were performed to ensure that the concentration of the samples was within the concentration range of the standards.

Ferrous and total dissolved iron concentrations were determined by colorimetry using the ferrozine method (Stookey, 1970; To *et al.*, 1999) in a UV–VIS HP Spectrophotometer within three days of sampling. Fe(III) was taken as the difference between Fe(tot) and Fe(II). The quality of the results was assured by measuring several standards, blanks and duplicates. Fe(tot) concentrations matched ICP-AES results within 10%.

Arsenic species (As(III) and As(V)) from water samples collected in November of 2006 and March 2007 were analyzed by Liquid Chromatography coupled to Hydride Generation Atomic Fluorescence Spectroscopy (LC-HG-AFS) (Vilanó *et al.*, 2000). Analytical determinations were carried out with a Perkin Elmer 250 LC binary pump (CT, USA), equipped with a Rheodyne 7125 injector (Cotati, CA, USA) with a 100 μL loop; anion-exchange Hamilton PRP-X100 column (250 mm × 4.1 mm, 10 μm i.d.) (Reno, NV, USA) with spherical poly (styrene-divinylbenzene) trimethylammonium exchangers with 10 μm particle size (250mm x 4.1mm i.d.). This instrument was coupled to a P.S. Analytical model Excalibur atomic fluorescence spectrometer equipped with a hollow cathode lamp (current intensities: primary=27.5 mA, boost=35.0 mA) and a Perma Pure

drying membrane (Perma Pure Products, Farmingdale, NJ, USA) which was used for drying the hydride generated. Measuring wavelength was 193.7 nm. Chromatographic separation of As(III) and As(V) was performed using a phosphate buffer (20mM $NH_4H_2PO_4$) as the mobile phase (pH 6), filtered through a 0.22 μm nylon membrane at a flow rate of 1.5 mL min^{-1}. Data acquisition was performed with a microcomputer and homemade software (Pendragon 1.0). Peak heights and peak areas were measured using custom-developed software running with Matlab language. The method detection limits are 0.2 μg L^{-1} for As(III) and As(V).

In the case of the determinations of the arsenic species (As(III) and As(V)) from water samples collected in February of 2008, analyses were performed by High Performance Liquid Chromatography- Inductively Coupled Plasma Mass Spectroscopy (HPLC-ICP-MS). The microHPLC system consisted of an Agilent 1100 Series (Agilent, Waldbronn, Germany) binary pump and auto injector with a programmable sample loop (20 μL maximum). The separations were performed on a PRP-X100 (Hamilton, Reno, NV, USA) anion exchange column (100 mm × 1 mm, 7 μm i.d.) and a phosphate buffer (H_3PO_4 12 mM,) as a mobile phase (pH 3) at a flow rate of 80 μL min^{-1}. The microbore column was connected directly to a Micromist nebulizer and a high-efficiency nebulizer (HEN) using its own capillary (480 mm × 0.25 mm and 480 mm × 0.10 mm, respectively). An HP 4500 ICP-MS instrument (Yokogawa Analytical Systems, Tokyo, Japan) was used for the determinations. For microHPLC-ICP-MS data acquisition, the "time resolved analysis" mode was used with 1 s of integration time per mass. Measurement arsenic mass selected was *m*/*z* 75. Operational conditions were flow rate of 80 μL min^{-1} and injected volume of 5 μL. For tuning of ICP-MS, a solution containing 10 μg L^{-1} of arsenic made up in double deionised water filtered through 0.22 μm was monitored at *m*/*z* 75; the ion intensity was optimized. Then, resolution and mass axis were also optimized. Detection limit for the arsenic species was < 0.05 μg L^{-1}. The quality of the LC-HG-AFS and HPLC-ICP-MS results was assured by measuring several standards, blanks and duplicates. As(tot) concentrations matched ICP-AES results within 15%.

5.1.3 Sediment characterization

Solid samples were air-dried at room temperature after that they were preserved at 4ºC. The major and trace element concentrations of the precipitates were determined by X-Ray Fluorescence using a wavelength dispersion X-ray fluorescence spectrometer (Bruker S4 Explorer) and following the total acid digestion according to the method developed by Querol *et al.* (1996). Concentrations of the resultant solutions of digestions were determined by ICP-AES for major elements and by ICP-MS for trace elements.

The mineralogical composition of the precipitates was determined by X-ray diffractometry (XRD) using a Bruker D5005 diffractometer with Cu Kα radiation. Powered samples were scanned from 0 to 60 degrees 2θ using a scan speed of 0.0014 degrees 2θ per second. Samples of precipitates were observed under field-emission scanning electron microscopy (SEM) using a Hitachi H-4100FE with intensity current of 10 kV.

The specific surface area of the solid samples was determined by the BET-method (Brunauer *et al.*, 1938) with a Micromeritics ASAP 2000 using 5 point N_2-adsorption isotherms.

X-ray absorption spectra from the precipitates (loose precipitates and terraces) were collected at the As K-edge at the European Synchrotron Radiation Facility (ESRF, Grenoble, France) on beamline BM8 (Gilda). Samples were prepared as pellets and they were measured in fluorescence mode with a Ge 13-element detector. Two or three scans were collected for each sample, depending on arsenic concentration. Synthetic standards of arsenic adsorbed onto schwertmannite, goethite and jarosite were prepared in the laboratory to be used as models compounds. Schwertmannite, goethite and jarosite were synthesized following the laboratory procedures described in Schwertmann and Cornell (1996). These protocols correspond to pure phases. Schwertmannite was precipitated by adding ferric chloride to sodium sulfate solutions, heating to 60 °C for 12 min, cooling at room temperature and dialysing the suspension for a period of 30 days. Goethite was

prepared by mixing potassium hydroxide and ferric nitrate solutions and aging for 60 h at 70 ºC. Jarosite was synthesized by dissolving potassium hydroxide and ferric sulfate in water in a covered beaker on a hot plate at 95 ºC and stirring continuously for 4 h. After the mineral synthesis, pure synthetic specimens were placed in contact with a solution 100 mM of As as disodium arsenate heptahydrate (adjusted to pH 2.0 or 4.0 by adding HCl) in a solid/liquid ratio of 1:20 and stirred during 4 h. The As concentration added to each synthesis corresponds to a Fe:As molar ratio of 20 that it is the ratio reported for acid mine drainage from Iberian Pyrite Belt (Sánchez-España *et al.*, 2005b).

Data reduction of experimental XAFS spectra, obtained at the ESRF, was carried out using the WinXAS 95 1.1 package software (Ressler, 1998). The energy threshold of the reference metal foil (Au), $E_{0,ref}$, was determined from the first inflection point in the spectrum (Wong *et al.*, 1984), and raw data were linearly calibrated against the difference between the obtained $E_{0,ref}$ and the tabulated absorption edge energy for As K-edge. Pre-edge background substraction and XANES normalization were carried out by fitting a linear polynomial to the pre-edge and a square polynomial to the post-edge region of the absorption spectrum.

Least-squares fitting (LSF) procedure was applied to determine the amount of each reference in the field samples. This procedure consists of using a set of arsenic model reference compounds and determines the amount of each reference in the field samples. The fitting procedure yielded the relative proportions. Therefore, a sum of the reference spectra was refined to each field sample XANES spectra. The employed nonlinear LSF procedure is based on the Levenberg-Marquardt algorithm (Malinowski, 1991) to minimize the difference between the experimental and the simulated XANES spectrum.

The quality of the fits was quantified by the normalized sum-squares residuals in the 11.85-11.92 keV range according to the following equation (Isaure *et al.*, 2006):

$$NSS = \frac{\sum\left(Xanes_{\text{experimental}} - Xanes_{\text{fit}}\right)^2}{\sum\left(Xanes_{\text{experimental}}\right)^2} \times 100 \qquad (5.1)$$

Additionally, arsenic and iron K-edge X-ray absorption spectra of four samples were obtained at the CCLRC Daresbury Synchrotron Radiation. Arsenic K-edge X-ray absorption spectra were obtained on station 16.5 operating at 2 GeV with a beam current of between 130 and 240 mA. Station 16.5 is equipped with a Si(220) double crystal monochromator, with harmonic contamination of the beam minimized by a vertically focusing mirror in addition to detuning to 70%. The monochromator was calibrated using the L(III) edge of a gold foil. The freeze dried acid mine drainage (AMD) sediments and As(III)- or As(V)-bearing iron (oxyhydr)oxide wet pastes were mounted in an aluminium sample holder with Sellotape windows. Data were collected at liquid nitrogen temperature with the station operating in fluorescence mode using an Ortec 30 element solid state Ge detector. Multiple scans (3 – 4) were collected for each sample and summed to improve signal to noise. Standards of sodium arsenite, disodium arsenate heptahydrate, orpiment and arsenopyrite were diluted with boron nitride and collected at room temperature in transmission mode.

Iron K-edge X-ray absorption spectra were obtained on station 7.1. A sagitally bent focusing Si(111) double crystal monochromator was utilized, with second order harmonic contamination of the beam minimized by a vertically collimating plane mirror as well as to detuning to 70%. Before collecting data, the monochromator was calibrated using a 5 μm iron foil. The AMD samples were diluted with boron nitride as appropriate and presented to the beam in an aluminium sample holder with Sellotape windows. Sample data were collected in a liquid nitrogen cooled cryostat in either transmission or fluorescence mode; a 13 element solid state Ge detector was used to collect data in the latter mode. Two scans were collected and summed for each sample. Hematite, 2-line ferrihydrite, schwertmannite and jarosite were collected at liquid nitrogen temperature in transmission mode after appropriate dilute with boron nitride. The XAS analysis of the

goethite standard was conducted at cryogenic temperature (80 K) on station 8.1 of the Daresbury SRS. A Si(220) monochromator was used, detuned to 50% of the maximum intensity to minimise harmonic contamination. The monochromator energy was calibrated using a 5 μm iron foil.

The proportion of different arsenic or iron phases of the samples studied in stations 16.5 and 7.1 at the UK CCLRC Daresbury Synchrotron Radiation Source (SRS), was established by fitting the summed sample X-ray absorption near edge structure (XANES) or extended X-ray absorption fine structure (EXAFS) spectra, respectively, to a combination of end-member standard spectra using the Solver package included in Microsoft Excel, with the relative contribution of each standard determined by minimizing a least squares residual. In addition, the arsenic data were background subtracted and analysed in EXCURV98 using full curved wave theory (Gurman *et al.*, 1984; Binsted, 1998), with phase shifts calculated *ab initio* using Hedin-Lundqvist potentials and von Barth ground states (Hedin and Lundqvist, 1969). The experimental data were fitted by defining a theoretical model and comparing the calculated EXAFS spectrum with the experimental data. Shells of backscatterers were added around the central absorber atom and the absorber-scatterer distance (r), Fermi energy and Debye-Waller factor ($2\sigma^2$) were refined until a least squares residual was minimised. For each shell of scatterers, the number of atoms in the shell was chosen as the integer or half integer to give the best fit, but was not further refined. Additional shells of scatterers were only considered justified if they improved the final fit of the data significantly.

5.1.4 Geochemical modeling

Model simulations carried out in this chapter include speciation-solubility calculations, which were performed with the PHREEQC code (Parkhurst and Appelo, 1999) using the WATEQ4F thermodynamic database (Ball and Nordstrom, 1991) that was enlarged with data from Bigham *et al.* (1996) and Yu *et al.* (1999) to account for schwertmannite solubility. Additionally, WATEQ4F database was used to calculate solution charge

balance used as Quality Assurance and Quality Control (QA/QC) measure for solution compositions.

5.2 Results and discussion

5.2.1 AMD water chemistry

AMD water discharged from the abandoned Tinto Santa Rosa mine has a pH variability from 2.93 to 3.49 and high concentrations of Fe and SO_4 with a noticeable content of trace elements (TS1 in Table 5.1). This water is mixed with groundwater approximately seven meters away from the first source (Fig. 5.2a). The chemical composition of this second source shows some differences with respect to the acid mine discharge (TS2 in data of November 2006, March 2007 and February 2008). It contains the highest concentrations of arsenic and lead. As(III) comprised a much larger proportion of the dissolved arsenic in the TS2 waters (35 – 49%) compared to that in the adit-mouth waters (TS1 < 31%).

Element concentrations show different patterns from the adit mouth downstream (Table 5.1). In all the field samplings a systematic decrease in ferrous and total dissolved iron concentration accompanied by a decrease in pH was observed (Fig. 5.4). This fact indicates that Fe(II) was oxidized to Fe(III) which, in turn, was removed from the solution by precipitation of hydroxides and hydroxysulfates of iron such as schwertmannite, goethite and jarosite. The overall precipitation is evidenced along the stream in the form of loose and crusty precipitates that cover the bed of the stream (Fig. 5.3).

The total dissolved arsenic concentration decreases downstream from 1867 to 127 $\mu g\ L^{-1}$ in July and from 4280 to 1260 $\mu g\ L^{-1}$ in November. Although the dominant As species is generally As(V), As(III) is supplied by a subterranean source. Downstream, a general increase in As(V)/As(III) ratio is observed due to arsenite oxidation in the stream water (see Table 5.1 and Fig. 5.5)

There are some elements that usually present a constant concentration (conservative elements) due to their low reactivity during transport in aquatic systems at the range of

Table 5.1. Hydrogeochemistry of the Tinto Santa Rosa stream waters during the samplings.

	Sample	T		Eh	Conductivity	mg L^{-1}												μg L^{-1}									
	(filtered)	(ºC)	pH	(mV)	(μS cm^{-1})	Ca	Mg	Na	K	Al	SO42-	Fe TOT	Fe(III)	Fe (II)	Mn	Si	Zn	Cu	As TOT	As(V)	As(III)	As(V)/As(III)	Pb	Ni	Sb	Ti	V	Cd	Co
February 2008	TS1	18.9	3.49	561.5	3750	167	133	26.54	2	83	2893	749	165	584	38	37	69	17	1956	1348	608	2.2	1	490.1	*bdl*	4	55	82	858
	TS2	18.7	3.53	510.5	3200	169	135	26.85	2	81	2853	726	162	564	39	37	68	15	2382	1362	1020	1.3	387	493.2	4.1	4	55	82	855
	TS3	18.1	3.41	598.5	2620	171	136	26.75	1	84	2861	722	188	534	39	38	69	17	1351	962	389	2.5	129	491.9	*bdl*	3	30	84	855
	TS4	15.3	3.37	603.5	2890	171	136	26.51	1	84	2885	708	185	523	39	38	69	17	1412	1064	348	3.1	127	485.7	*bdl*	3	33	84	862
	TS5	19.1	3.26	613.5	2480	172	138	27.14	1	86	2876	683	195	488	39	39	70	17	1145	855	290	2.9	127	511.7	*bdl*	3	25	86	886
	TS6	15.2	3.27	620.5	3150	171	135	26.32	1	84	2866	664	204	460	38	38	68	17	1064	783	281	2.8	118	490.4	*bdl*	3	24	83	847
	TS7	12.5	3.25	624.5	3030	172	136	26.48	2	85	2899	666	213	453	39	39	70	17	991	706	285	2.5	118	502.0	*bdl*	3	23	84	863
	TS8	14.9	3.16	634.5	2580	170	136	26.84	2	86	2865	645	238	407	39	38	69	17	863	656	207	3.2	113	487.4	*bdl*	3	20	82	836
March 2007	TS1	15.1	2.93	580.7	3490	187	153	26	5	116	3623	845	187	658	45	37	83	46	1365	1349	16	84.3	1	904	4	54	102	146	1306
	TS2	18.5	2.97	546.1	3220	172	138	26	4	97	3024	694	151	543	39	34	68	33	2731	1763	968	1.8	654	754	24	42	74	118	1078
	TS3	12	2.95	614.5	3270	194	157	27	4	118	3563	779	247	532	45	40	80	43	1401	1196	205	5.8	211	836	7	46	70	135	1184
	TS4	13.4	2.81	617.5	3150	183	149	26	4	112	3353	719	313	406	43	39	76	41	1384	1271	113	11.2	214	895	7	49	70	146	1277
	TS5	12.9	2.78	627.5	4050	195	159	27	4	119	3563	759	427	332	46	41	82	44	1149	1119	29	38.3	196	827	5	42	53	130	1170
	TS6	13.3	2.76	632.5	3900	188	154	26	3	115	3503	717	340	377	44	41	80	42	1155	1128	27	41.4	202	869	5	47	54	139	1243
	TS7	12.6	2.79	635.5	3040	190	155	27	3	116	3443	711	347	364	44	41	79	42	948	948	*bdl*	-	175	777	3	40	42	123	1104
	TS8	13.2	2.67	643.5	3020	193	159	27	2	118	3563	708	372	336	45	42	81	43	953	953	*bdl*	-	191	856	3	48	43	137	1214
November 2006	TS1	21.2	3.32	567.6	4550	203	172	26	2	128	4170	1055	364	691	49	38	107	76	1400	1400	*bdl*	-	1	842	4	*bdl*	*bdl*	4	1394
	TS2	22.2	2.94	581.1	4530	180	143	22	3	109	3353	786	278	508	36	42	74	49	4280	2199	2081	1	783	675	3	37	66	153	1025
	TS3	20.3	2.85	615.5	4450	191	154	24	1	114	3570	805	360	444	41	43	83	54	2450	1749	701	2	435	372	7	22	29	71	1156
	TS4	21.2	2.87	622.5	4340	189	152	23	2	114	3420	746	358	387	40	44	81	51	2130	2030	100	20	491	813	7	46	51	168	1087
	TS5	21.6	2.83	640.5	4050	184	146	22	3	111	3360	707	434	272	39	45	78	49	1850	1750	100	18	407	774	5	41	40	155	1037
	TS6	20.3	2.81	643.5	3900	173	138	22	1	101	3120	639	414	225	36	44	73	44	1610	1368	242	6	395	746	4	36	31	149	952
	TS7	17.6	2.85	645.5	3820	167	134	21	1	99	2919	599	395	204	35	42	69	43	1470	1127	343	3	356	682	3	35	25	138	916
	TS8	19.5	2.78	653.5	3810	166	135	20	1	98	2970	568	421	146	34	43	69	41	1260	1260	*na*	-	331	674	3	33	24	133	913
July 2006	TS1	-	3.42	-	-	181	145	2	3	88	4026	996	116	881	45	7	85	23	1867	*na*	*na*	-	*bdl*	616	*na*	*na*	*na*	148	1101
	TS3	-	3.01	-	-	175	100	1	4	60	3375	656	112	544	31	19	57	15	803	*na*	*na*	-	76	427	*na*	*na*	*na*	99	759
	TS5	-	2.92	-	-	218	138	2	2	86	3168	832	294	538	42	17	77	20	774	*na*	*na*	-	74	576	*na*	*na*	*na*	131	1026
	TS6	-	2.80	-	-	223	101	*na*	1	62	3035	587	288	299	31	13	56	15	240	*na*	*na*	-	55	409	*na*	*na*	*na*	91	728
	TS8	-	2.62	-	-	180	103	*na*	1	64	2705	561	327	234	31	18	57	15	127	*na*	*na*	-	59	458	*na*	*na*	*na*	101	802

na: not analyzed

bdl: below detection limit

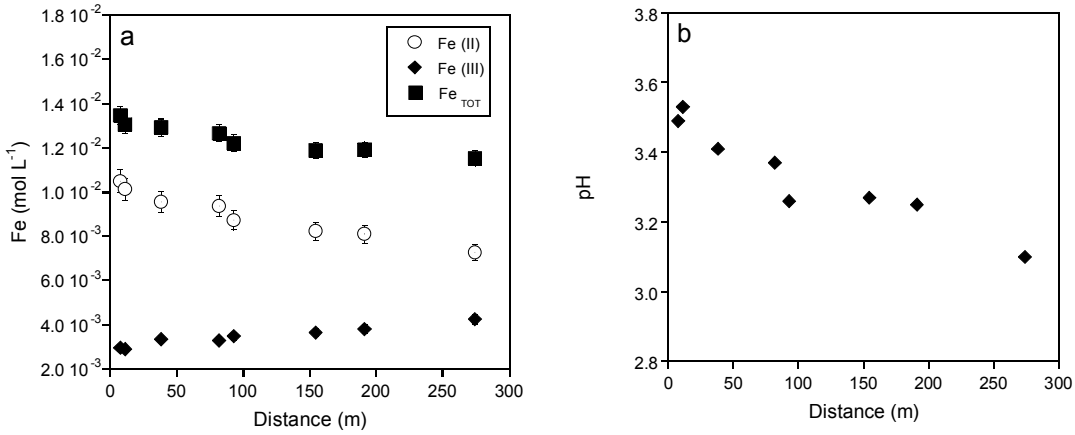

Figure 5.4. Evolution of (a) aqueous concentration of total dissolved iron, Fe(II)and Fe(III) and (b) pH versus distance in the Tinto Santa Rosa stream. Each point corresponds to the different sampling points (TS_i) on February 2008.

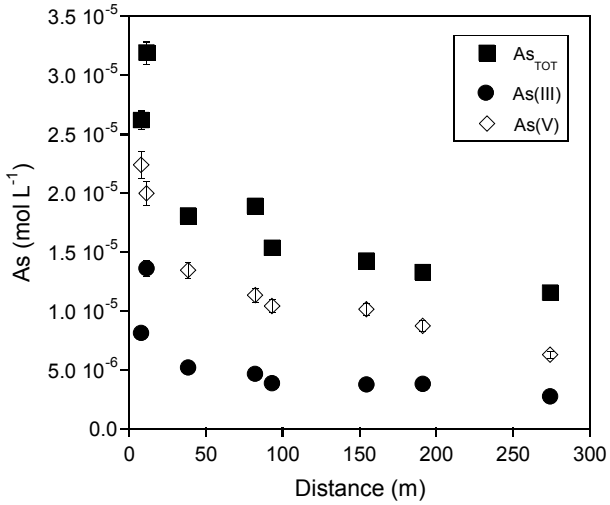

Figure 5.5. Evolution of aqueous concentration of total dissolved arsenic, As (III) and As(V) versus distance in the Tinto Santa Rosa stream. Each point corresponds to the different sampling points (TS_i) on February 2008.

pH studied (such as Na, Mg, Zn, Mn, Al, Cu, Co, Ni and sulfate). Nonetheless, a little decrease in their concentration was observed in the July and November sampling campaigns. This effect could be caused by diffuse water inflows or streams flowing into

the studied stream, resulting in a dilution of the dissolved metal load; only in November additional water inputs were detected in the field. To ensure that no diffuse inflows were affecting the aquatic system an examination of the concentration of the conservative elements along the stream was carried out. The plots of these elements versus distance to adit mouth depict the conservative behavior (Fig. 5.6). Likewise, ratios between several concentrations of these conservative elements versus distance show the same trend (Fig. 5.7).

According to the results, the trace elements present different patterns. The concentration of Cd, Ti and Co does not vary significantly with distance, and that of Pb, Sb, mainly supplied by the subterranean source TS2, and V shows a slight decrease downstream; dissolved As concentration drops systematically from the adit mouth downstream.

As mentioned before, it is well known that concentration of trace metals is controlled by sorption onto mineral surfaces (Stumm, 1992). In this case, the variations in the behavior of these trace elements could likely be attributed to the different affinity of each aqueous species to the surface of the precipitates (schwertmannite, goethite and jarosite) assuming (i) there are no other sources for these elements other than the AMD discharge, and (ii) there are no streams flowing into the Tinto Santa Rosa which may dilute the dissolved metal load. This situation could be assumed for the system in March 2007 and February 2008, according to the non variability of the conservative elements' concentration. Therefore, it is reasonable to attribute the progressive decrease in the aqueous metal concentrations observed in these samplings to the adsorption and/or coprecipitation processes.

5. 2.1.1 Metal(oid) speciation in aqueous solution

The ionic strength of the acidic water, varies, depending on the sampling, from 0.14 to 0.19. These values are well below the value of 0.7 which is conventionally considered as

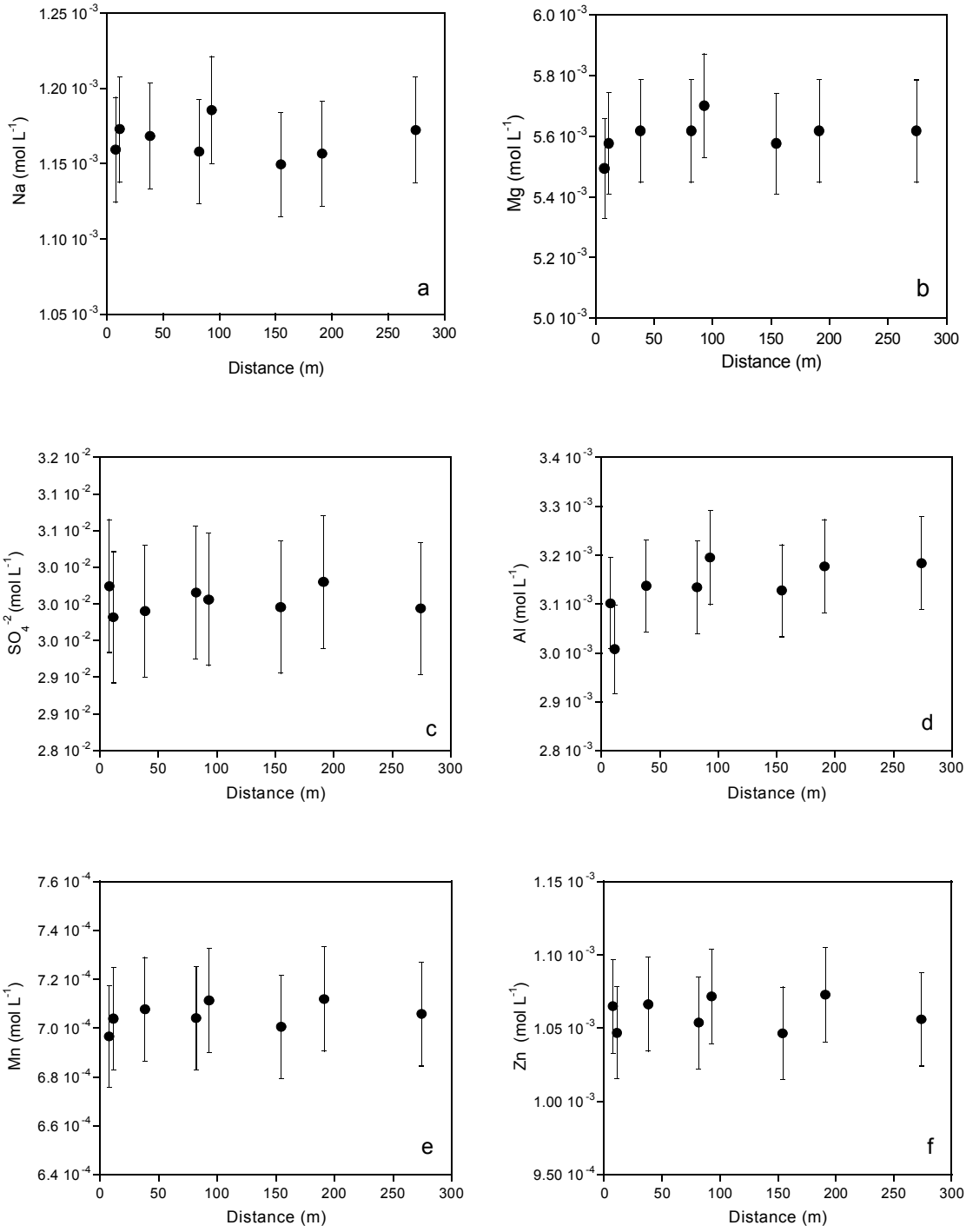

Figure 5.6. Evolution of the concentration of Na, Mg, sulfate, Al, Mn and Zn (Februay 2008 data). These elements present a conservative behavior over the Tinto Santa Rosa stream.

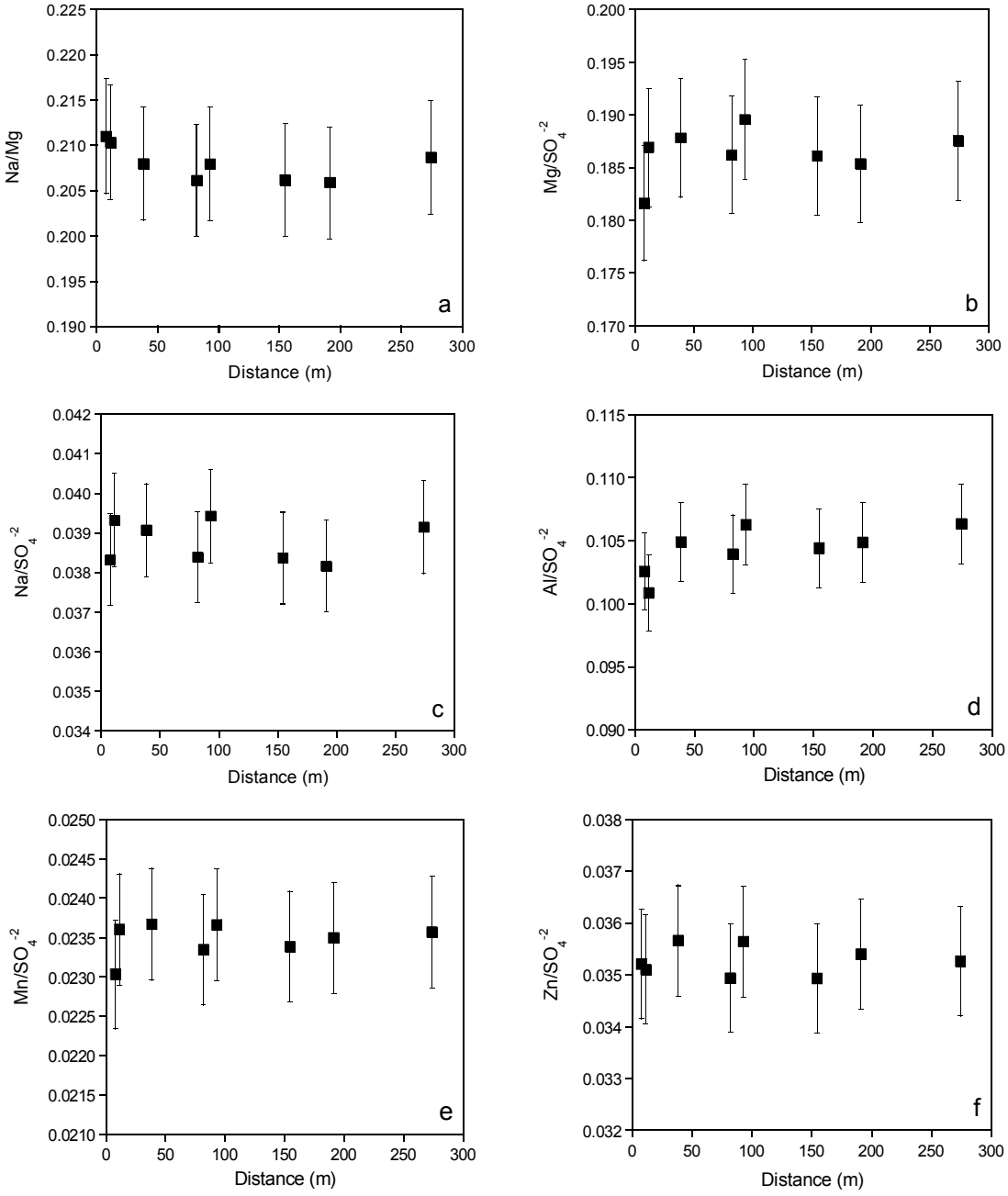

Figure 5.7. Variation of the molar ratio of the conservative element to sulfate in the Tinto Santa Rosa stream versus distance (Februay 2008 data).

an upper limit for the application of the extended Debye-Hückel and the ion-association equations for the calculation of activity coefficients of aqueous solutes.

Metal(oid) speciation was calculated using the PHREEQC code (Parkhurst and Appelo, 1999) and the WATEQ4F database (Ball and Nordstrom, 1991) (Table 5.2). Calculations show that at the acidic pH range measured, divalent metals can be present either as free aqueous ions or complexed with sulfate species. All these species are unlikely sorbed onto the precipitates found in the AMD sediment, since their surfaces exhibit a net positive charge at pH~3 (Stumm, 1992), resulting in minor changes in the dissolved concentrations of Cd, Ni, Cu, Pb and Zn observed along the stream. Conversely, under such acidic conditions, $H_2AsO_4^-$ is the thermodynamically stable arsenate aqueous species, and its sorption onto the positively charged surfaces is favored, resulting in a dramatic drop in aqueous arsenic concentration with distance from the contaminant point sources.

This metal(loid) behavior is in agreement with other metal-sorption trends observed in AMD systems (e.g. Smith, 1999; Fukushi *et al.*, 2003a; Gault *et al.*, 2005; Sánchez-España *et al.*, 2005; Acero *et al.*, 2006; Lee and Chon, 2006).

5.2.1.2 Saturation indices

The saturation index, SI, is defined as the logarithm of the ratio of the ion-activity product to the solubility product constant. If the solution is in equilibrium with a mineral, the ion-activity product is equal to solubility product constant, and SI is 0. If the SI is greater than 0, the solution is supersaturated, and the mineral tends to precipitate; if the SI is less than 0, the solution is undersaturated and the mineral tends to dissolve.

AMD solutions are commonly supersaturated with respect to a number of iron minerals such as goethite, jarosite and schwertmannite, the latter of which is normally the mineral favored to precipitate at pH around 3.5 under oxidizing conditions (Eh > 700 mV). Table 5.3 lists the calculated saturation index (SI) values of the Tinto Santa Rosa stream water with respect to these minerals according to the pH measured. Considering

Table 5.2. PHREEQC results of metal speciation of the waters collected in March 2007.

Sample	pH	Cd^{+2}	Cu^{+2}	$CuSO_4$	Mn^{+2}	Ni^{+2}	$NiSO_4$	Pb^{+2}	$PbSO_4$	Zn^{+2}	$ZnSO_4$
		(mol L^{-1})									
TS1	2.93	6.29×10^{-7}	4.48×10^{-4}	2.72×10^{-4}	5.59×10^{-4}	9.86×10^{-6}	5.61×10^{-6}	1.62×10^{-9}	2.61×10^{-9}	6.98×10^{-4}	4.82×10^{-4}
TS2	2.97	5.37×10^{-7}	3.32×10^{-4}	1.88×10^{-4}	4.95×10^{-4}	8.40×10^{-6}	4.49×10^{-6}	1.14×10^{-6}	1.86×10^{-6}	5.99×10^{-4}	3.88×10^{-4}
TS3	2.95	5.94×10^{-7}	4.29×10^{-4}	2.51×10^{-4}	5.74×10^{-4}	9.26×10^{-6}	5.05×10^{-6}	3.47×10^{-7}	6.12×10^{-7}	6.90×10^{-4}	4.58×10^{-4}
TS4	2.81	$6.68x\ 10^{-7}$	4.17×10^{-4}	2.30×10^{-4}	5.49×10^{-4}	1.01×10^{-5}	5.22×10^{-6}	3.69×10^{-7}	$6.11x\ 10^{-7}$	6.76×10^{-4}	4.24×10^{-4}
TS5	2.78	5.99×10^{-7}	4.47×10^{-4}	2.43×10^{-4}	5.93×10^{-4}	9.38×10^{-6}	4.77×10^{-6}	3.41×10^{-7}	5.57×10^{-7}	7.34×10^{-4}	4.54×10^{-4}
TS6	2.76	6.27×10^{-7}	4.22×10^{-4}	2.38×10^{-4}	5.65×10^{-4}	9.73×10^{-6}	5.14×10^{-6}	3.43×10^{-7}	5.80×10^{-7}	6.99×10^{-4}	4.49×10^{-4}
TS7	2.79	5.62×10^{-7}	4.28×10^{-4}	2.36×10^{-4}	5.72×10^{-4}	9.77×10^{-6}	4.53×10^{-6}	3.01×10^{-7}	5.00×10^{-7}	7.05×10^{-4}	4.42×10^{-4}
TS8	2.67	6.23×10^{-7}	4.34×10^{-4}	2.41×10^{-4}	5.78×10^{-4}	9.63×10^{-6}	5.02×10^{-6}	3.27×10^{-7}	5.46×10^{-7}	7.71×10^{-4}	4.54×10^{-4}

Table 5.3. Saturation index calculations made with the PHREEQC geochemical code with respect to schwertmannite, goethite and jarosite of the water samples.

	Sample (filtered)	pH	Goethite	Jarosite-K	Jarosite-Na	Jarosite-H_3O	Schwertmannite (logK=18)	Schwertmannite (logK=10)
February 2008	TS1	3.49	6.5	6.7	4.1	10.2	11.8	19.8
	TS2	3.53	6.6	6.8	4.2	10.3	12.4	20.4
	TS3	3.41	6.3	6.4	3.8	10.1	11.0	19.0
	TS4	3.37	6.2	6.0	3.5	9.6	10.6	18.6
	TS5	3.26	6.0	5.7	3.2	9.7	8.4	16.4
	TS6	3.27	5.9	5.6	3.1	9.4	9.1	17.1
	TS7	3.25	5.8	5.5	2.9	9.1	9.2	17.2
	TS8	3.16	5.5	5.0	2.4	8.9	6.6	14.6
March 2007	TS1	2.93	4.9	4.1	1.0	7.3	1.9	9.9
	TS2	2.97	5.0	4.2	1.3	7.6	2.1	10.1
	TS3	2.95	5.0	4.3	1.3	7.4	3.6	11.6
	TS4	2.81	4.7	3.9	1.0	7.4	1.8	9.8
	TS5	2.78	4.8	4.1	1.2	7.6	2.3	10.3
	TS6	2.76	4.6	3.7	0.8	7.2	1.0	9.0
	TS7	2.79	4.7	3.9	0.9	7.3	1.8	9.8
	TS8	2.67	4.4	3.1	0.3	6.9	-0.5	7.5
November 2006	TS1	3.32	6.3	8.6	4.2	3.9	-0.2	7.8
	TS2	2.94	5.3	6.5	2.0	2.2	-6.8	1.2
	TS3	2.85	5.1	5.8	1.7	1.9	-4.5	3.5
	TS4	2.87	5.2	6.2	1.9	2.1	-3.3	4.7
	TS5	2.83	5.2	6.5	2.0	2.2	-2.0	6.0
	TS6	2.81	5.1	5.8	1.7	1.9	-2.6	5.5
	TS7	2.85	5.1	5.8	1.8	1.8	-2.1	5.9
	TS8	2.78	5.0	5.6	1.5	1.8	-2.5	5.5
July 2006	TS1	3.42	6.1	6.1	3.2	9.7	8.6	16.6
	TS2	3.01	5.0	4.0	0.8	8.0	1.1	9.1
	TS3	2.92	5.2	4.5	1.8	8.9	3.3	11.3
	TS4	2.80	4.9	3.7	-	8.4	0.8	8.8
	TS5	2.62	4.5	2.9	-	7.8	-1.8	6.2

the schwertmannite solubility product proposed by Bigham *et al.* (1996) (logK = 18±2.5), some of the water samples appear to be undersaturated with respect to schwertmannite, which seems to contradict the field evidence of schwertmannite precipitation. Hence, the use of the solubility constant value of 10.5, proposed by Yu *et al.* (1999), is supported by schwertmannite precipitation as is similarly observed by Fukushi *et al.* (2003a); Regenspurg *et al.* (2004); Acero *et al.* (2006). Thus, according to the calculated SI values, the water samples are strongly supersaturated with respect to schwertmannite, goethite and jarosite.

5.2.2 Chemistry and mineralogy of AMD sediments

Due to the inherent complexity of characterization of the sediments of the Tinto Santa Rosa stream bed, a combination of methods such as X-Ray Difraction (XRD), Differential X-Ray Difraction (DXRD), Scanning Electron Microscopy (SEM), total solid digestions, X-Ray Fluorescence (XRF) and X-Ray Absorption Spectroscopy (XAS) was employed to understand the role played by solids in the arsenic mobilization.

Tables 5.4 and 5.5 show the chemical and mineralogical composition of the Tinto Santa Rosa precipitates. The stream bed is covered by a yellowish to reddish surface layer and gradually changes from fine-grained to loose consolidation with depth. Consolidated terrace sediments show colour changes in depth from yellowish to brownish. Likewise, banded structures are observed in these consolidated terraces as shown in Fig. 5.8.

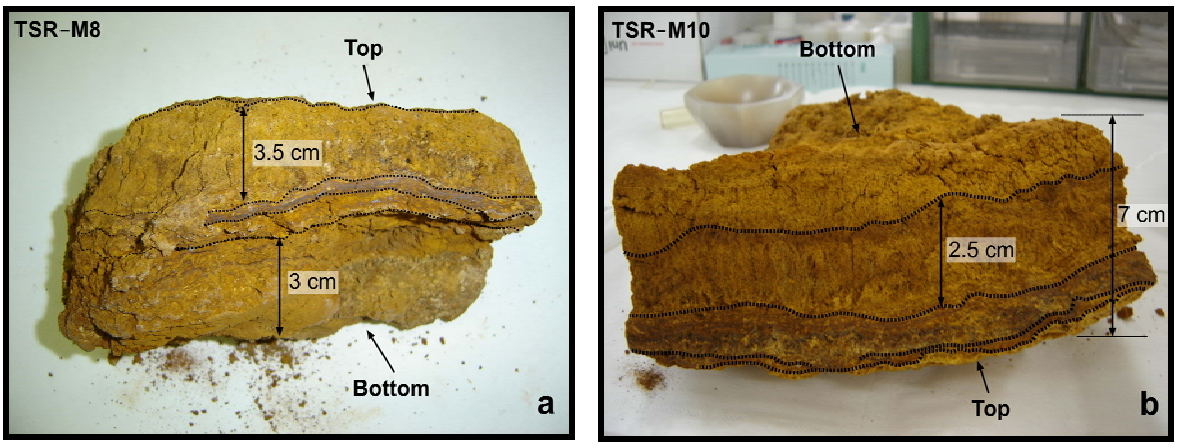

Figure 5.8. Detailed of the consolidated terrace sediments: TSR-M8 (a) and TSR-M10 (b) collected on February 2008. It is observed banded structures and colour changes in depth.

5.2.2.1 Sediment chemical characterization

The major constituents (wt %) and trace elements obtained by total acid digestion and XRF analysis of the solids are shown in Table 5.4. Iron and sulfur are the major chemical components of all the solids (terraces, crusty and loose precipitates). The terraces are

Table 5.4. Major constituents (wt %) and trace metals in the precipitates collected from the Tinto Santa Rosa discharge. The water sample collected at the same sampling time as solids is also indicated.

				Major oxides (wt %)									Trace metals (mg kg^{-1})									
Type of solid	Sample	Water sample	Sampling date	Na_2O	MgO	Al_2O_3	SiO_2	SO_3	K_2O	CaO	Fe_2O_3	As_2O_3	Cu	Mn	Zn	As	Cd	Ni	Sb	V	Pb	Co	Sr
Loose precipitate*	**TSR-J-1**	**TS2**	July 06	0.40	0.81	17.00	42.90	6.80	3.13	0.11	23.02	0.50	600	340	250	3810	*na*	*na*	*na*	*na*	1860	*na*	*na*
Loose precipitate*	**TSR-J-2**	**TS5**	July 06	0.40	0.71	18.30	43.50	5.91	3.07	0.13	23.25	0.35	630	300	200	2620	*na*	*na*	*na*	*na*	1940	*na*	*na*
Consolidated terrace*	**TSR-J-3**	**TS1**	July 07	*bdl*	1.24	0.30	0.69	12.80	0.03	0.03	60.16	3.38	330	60	50	25600	*na*	*na*	*na*	*na*	*bdl*	*na*	*na*
Consolidated terrace*	**TSR-J-4**	**TS1**	July 08	*bdl*	1.06	0.41	0.83	14.00	0.04	0.03	70.09	3.21	370	bdl	120	24300	*na*	*na*	*na*	*na*	*bdl*	*na*	*na*
Loose precipitate	**TSR-N-1**	**TS1**	November 06	*na*	0.09	3.81	0.01	8.43	0.08	0.09	84.60	6.25	396	210	360	32400	1	4	14	502	3	4	23
Loose precipitate	**TSR-N-2**	**TS4**	November 06	*na*	0.25	15.21	0.01	7.72	1.05	0.14	77.74	8.76	540	300	426	39900	1	10	74	297	1446	7	22
Loose precipitate	**TSR-N-3**	**TS5**	November 06	*na*	0.43	31.48	0.07	7.75	3.88	0.15	67.46	0.84	500	300	220	3000	1	27	68	107	1597	5	62
Loose precipitate	**TSR-N-4**	**TS7**	November 06	*na*	0.73	20.48	0.08	5.39	6.50	0.23	52.72	1.04	800	340	200	3500	1	43	118	163	2524	8	95
Loose precipitate	**TSR-N-5**	**TS8**	November 06	*na*	0.68	*bdl*	0.11	5.42	5.64	0.18	58.05	0.80	460	260	134	1900	1	39	99	145	2169	7	91
Consolidated terrace	**TSR-N-6**	**TS1**	November 06	*na*	0.06	1.74	0.02	8.37	0.13	0.04	87.98	2.87	248	200	120	17400	1	1	16	502	7	1	2
Consolidated terrace	**TSR-N-7**	**TS3**	November 06	*na*	0.15	2.11	0.02	8.53	0.53	0.05	86.97	1.45	150	180	105	6600	1	4	15	110	230	3	7
Consolidated terrace	**TSR-N-8**	**TS8**	November 06	*na*	0.09	*bdl*	0.01	8.63	0.42	0.05	88.53	0.36	180	360	135	1800	1	4	11	72	290	1	14
Loose precipitate	**TSR-M-1**	**TS1**	March 07	0.03	0.02	9.55	0.02	8.92	0.01	0.05	83.76	6.64	192	70	118	34200	*bdl*	*bdl*	14	397	*bdl*	2	2
Loose precipitate	**TSR-M-2**	**TS7**	March 07	*bdl*	0.38	12.28	0.06	12.94	0.02	0.58	84.68	0.24	840	1120	1496	1176	72	64	2	84	92	26	5
Loose precipitate	**TSR-M-3**	**TS8**	March 07	*bdl*	0.09	*bdl*	0.06	9.96	0.01	0.14	76.70	0.16	2816	420	400	756	72	36	2	64	100	4	2
Crusty precipitate	**TSR-M-4**	**TS3**	March 07	0.26	0.16	7.26	0.04	6.59	2.30	0.09	77.29	1.19	618	127	129	4829	bdl	11	136	184	5743	3	27
Crusty precipitate	**TSR-M-5**	**TS6**	March 07	0.25	0.11	7.74	0.04	8.16	1.39	0.07	82.57	0.81	1176	115	602	3616	15	5	27	69	6535	3	23
Crusty precipitate	**TSR-M-6**	**TS7**	March 07	0.26	0.16	1.26	0.06	7.82	1.63	0.14	81.55	0.33	332	400	180	1436	52	16	39	136	1204	4	27
Consolidated terrace	**TSR-M-7-(0-3.5 cm)**	**TS1**	March 07	0.02	0.03	0.20	0.08	9.03	0.08	0.33	88.42	1.69	332	584	248	11280	100	44	17	640	196	28	1
Consolidated terrace	**TSR-M-7-(3.5-5.5 cm)**		March 07	*bdl*	*bdl*	*bdl*	0.03	8.40	0.10	0.05	87.49	3.71	140	460	128	22040	72	*bdl*	26	820	128	2	2
Consolidated terrace	**TSR-M-8-(0-0.5 cm)**	**TS3**	March 07	*bdl*	0.01	1.40	0.09	8.25	0.17	0.22	88.03	2.37	168	476	148	14240	70	*bdl*	9	220	372	1	4
Consolidated terrace	**TSR-M-8-(0.5-4 cm)**		March 07	*bdl*	*bdl*	0.72	0.06	9.73	0.31	0.05	86.12	2.02	168	360	132	9880	72	12	71	320	352	2	6
Consolidated terrace	**TSR-M-8-(4-4.5 cm)**		March 07	*bdl*	0.01	0.38	0.03	8.32	0.07	0.08	88.85	2.11	220	572	220	14320	100	16	21	320	256	7	3
Consolidated terrace	**TSR-M-8-(4.5-7 cm)**		March 07	*bdl*	0.05	0.00	0.05	8.50	0.10	0.13	89.10	1.58	340	528	368	8320	112	*bdl*	7	220	264	5	3
Consolidated terrace	**TSR-M-9-(0-5 cm)**	**TS6**	March 07	*bdl*	0.03	1.18	0.06	8.82	0.26	0.09	88.97	0.52	200	456	160	2784	88	16	15	180	480	2	5
Consolidated terrace	**TSR-M-9-(5-10 cm)**		March 07	*bdl*	0.02	*bdl*	0.05	7.79	0.25	0.12	89.98	0.65	280	472	180	3628	80	*bdl*	8	148	448	2	5
Consolidated terrace	**TSR-M-10-(0-2 cm)**	**TS8**	March 07	*bdl*	0.01	0.27	0.06	8.93	0.17	0.10	89.42	0.53	140	48	180	3236	92	*bdl*	8	136	332	2	4
Consolidated terrace	**TSR-M-10-(2-4.5 cm)**		March 07	0.61	bdl	2.26	0.05	7.43	0.09	0.11	90.90	0.48	180	404	168	2340	64	*bdl*	3	96	28	2	3
Consolidated terrace	**TSR-M-10-(4.5-7 cm)**		March 07	*bdl*	0.01	*bdl*	0.03	4.57	0.08	0.04	93.86	0.32	220	1056	1500	3340	200	*bdl*	10	160	352	14	7

* X-ray Fluorescence results

bdl : below detection limit; ***na***: not analized

J: July 2006; **N**: november 2006; **M**: March 2007

Numbers in brackets "( )" indicate the depth at which the solid samples of the consolidated terraces of March 2007 were collected

Table 5.5. Mineralogy of the collected samples.

Type of solid	Sample	Location	Sampling date	Mineralogy
Loose precipitate*	**TSR-J-1**	Middstream	July 06	Qtz, Ill, Kln, Sch, Gt, Jrs
Loose precipitate*	**TSR-J-2**	Downstream	July 06	Qtz, Ill, Kln, Sch, Gt, Jrs
Consolidated terrace*	**TSR-J-3**	Upperstream	July 06	Sch
Consolidated terrace*	**TSR-J-4**	Upperstream	July 06	Sch
Loose precipitate	**TSR-N-1**	Upperstream	November 06	Sch
Loose precipitate	**TSR-N-2**	Upperstream	November 06	Qtz, Ill, Kln, Sch
Loose precipitate	**TSR-N-3**	Middstream	November 06	Qtz, Ill, Kln, Gt, Jrs, Sch
Loose precipitate	**TSR-N-4**	Downstream	November 06	Qtz, Ill, Kln, Gt, Jrs, Sch
Loose precipitate	**TSR-N-5**	Downstream	November 06	Qtz, Ill, Kln,Gt, Jrs, Sch
Consolidated terrace	**TSR-N-6**	Upperstream	November 06	Sch
Consolidated terrace	**TSR-N-7**	Upperstream	November 06	Sch, Gt
Consolidated terrace	**TSR-N-8**	Down stream	November 06	Sch, Gt, Jrs
Consolidated terrace	**TSR-M-7-(0-3.5 cm)**	Upper stream	March 07	Sch
Consolidated terrace	**TSR-M-7-(3.5-5.5 cm)**		March 07	Sch
Consolidated terrace	**TSR-M-8-(0-0.5 cm)**	Middstream	March 07	Qtz, Sch, Gt, Jrs
Consolidated terrace	**TSR-M-8-(0.5-4 cm)**		March 07	Qtz, Sch, Gt
Consolidated terrace	**TSR-M-8-(4-4.5 cm)**		March 07	Sch, Gt
Consolidated terrace	**TSR-M-8-(4.5-7 cm)**		March 07	Sch, Gt
Consolidated terrace	**TSR-M-9-(0-5 cm)**	Downstream	March 07	Qtz, Sch, Gt
Consolidated terrace	**TSR-M-9-(5-10 cm)**		March 07	Sch, Gt
Consolidated terrace	**TSR-M-10-(0-2 cm)**	Down stream	March 07	Qtz, Sch, Gt
Consolidated terrace	**TSR-M-10-(2-4.5 cm)**		March 07	Qtz, Sch, Gt
Consolidated terrace	**TSR-M-10-(4.5-7 cm)**		March 07	Qtz, Sch, Gt

J: July 2006; **N**: november 2006; **M**: March 2007

Numbers in brackets "( )" indicate the depth at which the solid samples of the consolidated terraces of March 2007 were collected

Qtz: quartz; **Ill**: illite; **Kln**: Kaolinite; **Sch**: schwertmannite; **Gt**: goethite; **Jrs**: jarosite

strongly enriched in Fe and S suggesting they are made up of Fe oxy-hydroxides (goethite) and Fe-hydroxy-sulfates (schwertmannite and jarosite). Loose and crusty precipitates show a noticeable content of Al_2O_3, SiO_2 and K_2O as well as Fe_2O_3 that indicates the presence of aluminosilicate detrital material.

The most concentrated element amongst the "trace" elements analyzed is arsenic. Its concentration is very high compared to that of the other trace elements (Table 5.4). The arsenic concentration decreases downstream in the loose, crusty and consolidated terraces, as well as with depth in the consolidated terraces. This evolution is discussed later.

Nonetheless, the content of the rest of elements is significant, especially Mn, Cu and Pb and to a lesser extent Zn, Cd, Ni, Sb, V, Co and Sr. Their concentration in the loose, crusty and consolidated terraces (see Table 5.4) does not follow a systematic trend downstream, suggesting that these metals are unlikely to be involved in sediment-sorption processes. In contrast, the arsenic content systematically decreases downstream, mirroring its behavior in the stream water concentration. No systematic variation in the trace element concentrations was observed with depth in the consolidated terrace samples. This low variability is probably due to the fact that the sediment bands' composition is the result of the superposition of different processes with time.

5.2.2.2 Sediment mineralogical characterization

Schwertmannite is ubiquitous as the primary precipitating mineral during the hydrolysis of Fe(III) in acidic waters with pH between 2.8 and 4.5 and high sulfate concentrations (1000-3000 mg L^{-1}) (Bigham *et al.*, 1994). Ideally, schwertmannite has a Fe/S molar ratio of 8 but the amount of SO_4 is variable due to adsorbed SO_4, yielding a structural formula as $Fe_8O_8(OH)_{8-2x}(SO4)_x \cdot nH_2O$ where $1 \leq x \leq 1.75$, although higher values ($1.75 \leq x \leq 1.86$) have been reported by Yu *et al.* (1999). Goethite (FeOOH) and jarosite ($KFe_3(SO_4)_2(OH)_6$) are also common minerals in these AMD environments.

Schwertmannite is found in all the sediments collected from Tinto Santa Rosa stream (Fig. 5.9). Loose precipitates consist of detrital silicates (quartz, illite, kaolinite), and Fe-hydroxides and Fe-oxy-hydroxy-sulfates (e.g. schwertmannite, jarosite and goethite). Terraces are mostly made up of schwertmannite, goethite and jarosite with minor amounts of quartz.

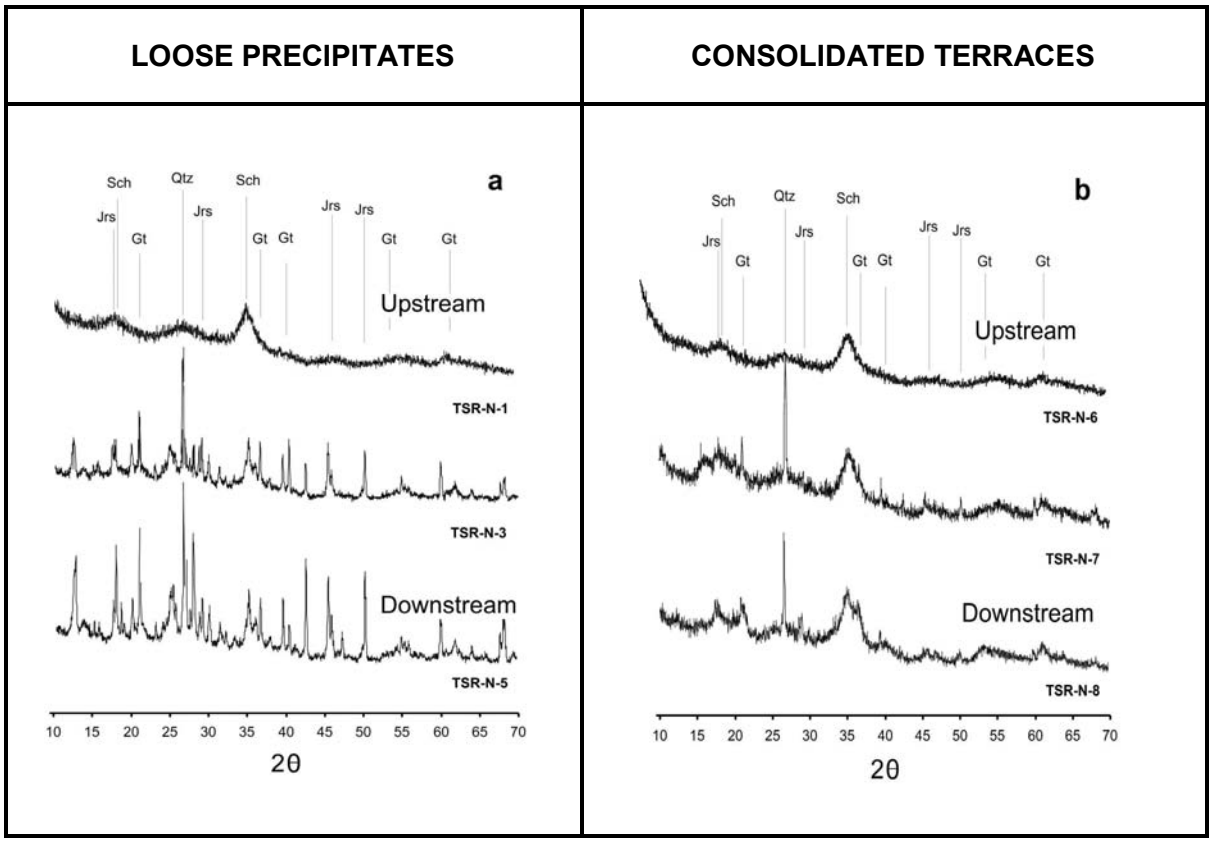

Figure 5.9. XRD patterns for loose precipitates (a) and consolidated terraces (b) along the Tinto Santa Rosa acid mine discharge (Sch: schwertmannite; Jrs: jarosite; Gt: goethite; Qtz: quartz). Samples collected in November 2006.

In the collected samples, the low-intensity XRD peaks of schwertmannite are often hidden by high intense peaks of more crystalline minerals, such as goethite. Differential XRD (DXRD) has been used to identify schwertmannite (Dold, 2003). The technique of DXRD consisted of a sequence of examinations followed by partial extractions of the mineral mixture in acidic oxalate solutions (pH 3, 0.2 M, in darkness) (Dold, 2003). As

low-crystallinity iron oxides, such as schwertmannite, are readily dissolved in acidic oxalate solutions (Bigham and Nordstrom, 2000) the difference between the two spectra will ideally identify the dissolved phase. In some of the samples, such as TSR-N-1, TSR-N-6 or TSR-M-7, the solid was almost totally dissolved in acidic oxalate indicating that schwertmannite was the main phase.

Mineralogical characterization of the solids is consistent with both the elemental composition of the sediments (Table 5.4), and the SI calculations (Table 5.3), which revealed supersaturation of the studied waters with respect to schwertmannite, goethite and jarosite along the stream.

Usually, schwertmannite, which is the main Fe-phase of the collected samples, forms characteristic pin cushion-like aggregates (about 200-500 nm in diameter) leading to a rather high surface area of about 100-300 $m^2\ g^{-1}$ (Bigham *et al.*, 1994; Cornell and Schwertmann, 1996). The pin cushion morphology is not always detectable, especially if samples are taken from consolidated sediments or surface crusts (Bigham and Nordstrom, 2000). The dried samples were examined by SEM (Fig. 5.10) and the pin cushion morphology was not observed. According to Jönsson *et al.* (2005) washing and grinding sample could have contributed to lose this morphology.

The BET surface areas of all the samples (loose precipitates and terraces) were determined to be in the range of 15-50 $m^2\ g^{-1}$. These values are much lower than compared BET values of 100-300 $m^2\ g^{-1}$ that were determined for schwertmannite by Bigham *et al.* (1994) and Cornell and Schwertmann (1996), but similar to those obtained by Webster *et al.* (1998) and Jönsson *et al.* (2005) (55 and 43 $m^2\ g^{-1}$, respectively). These lower BET surface area values could be attributed to the sphere cementation observed. On the other hand, a decrease in surface area could be caused by aggregation of the sulfate-rich particles while drying (Jönsson *et al.*, 2005).

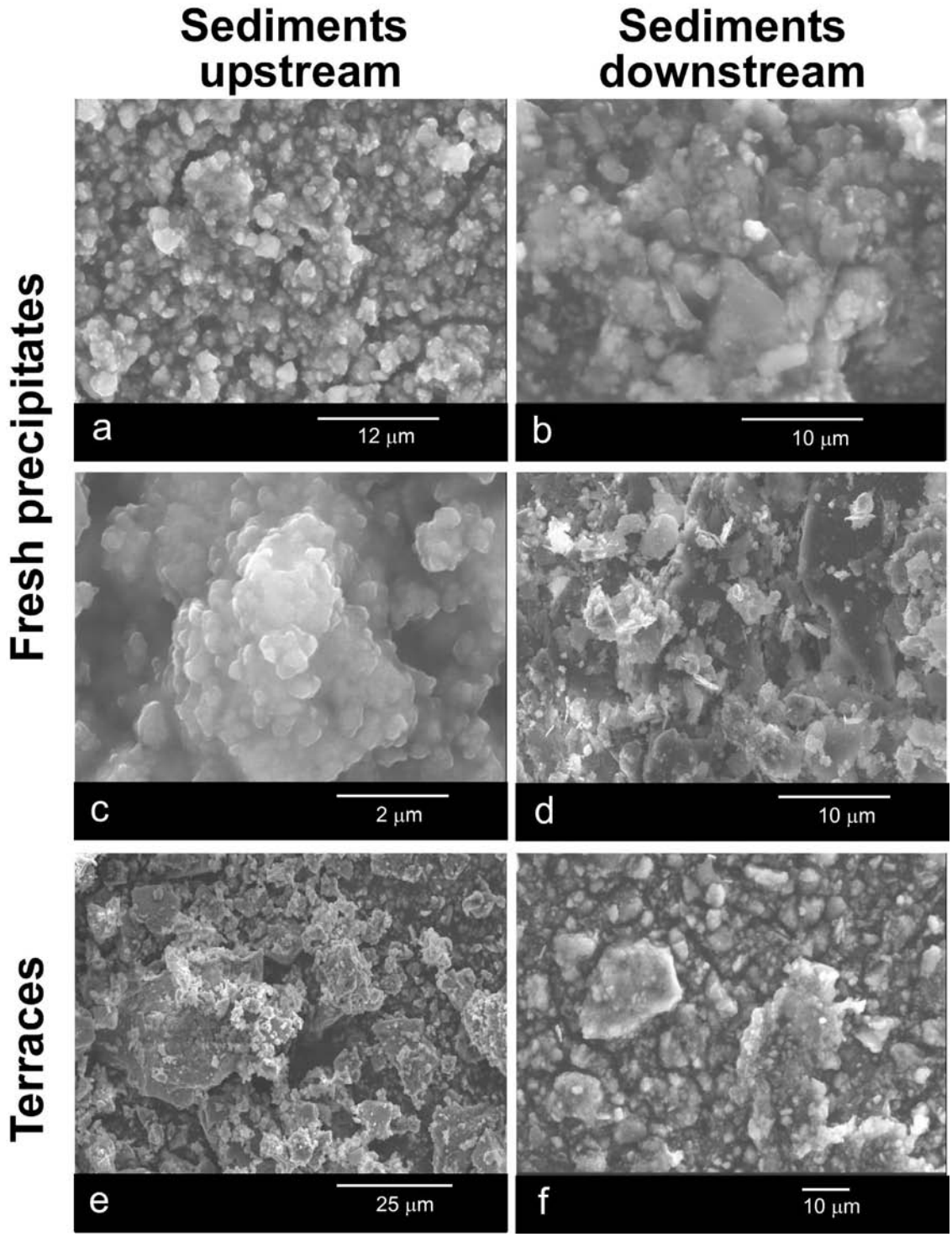

Figure 5.10. SEM pictures of some representative samples of the bed-stream sediments: TSR-J1 (a); TSR-N4 (b); TSR-N1 (c); TSR-J2 (d); TSR-J3 (e); TSR-N8 (f). Upstream sediments appear formed by rounded aggregates, whereas downstream, sediments show elongated and sharp shapes. In the case of consolidated terraces, rounded shapes are less evident, probably due to washing and grinding of the samples.

5.2.2.3 Arsenic association in the sediment

The high arsenic concentration in the precipitates (Table 5.4) indicates that arsenic has been selectively incorporated into the solids probably due to sorption processes at the acidic pH (see Chapter 4), demonstrating the efficiency of AMD precipitates in sequestering arsenic. Determination of the oxidation state of arsenic in waters and the sedimentary arsenic speciation is necessary to link arsenic mobilization with the sorption processes and to determine any potential hazardous effects.

With this in mind, the arsenic and iron associated with the AMD precipitates in the Tinto Santa Rosa stream was studied using extended X-ray absorption fine structure (EXAFS) spectroscopy in two representative samples that correspond to a consolidated terrace sediment and a loose solid precipitate (TSR-J2 and TSR-J3) both collected in July 2006.

The pattern fitting of the Fe K-edge EXAFS spectra shown in Fig. 5.11a indicated that the iron mineralogy was dominated by schwertmannite, with lesser amounts of goethite (11% in TSR-J3) and jarosite/goethite (29% of H-jarosite and 24% of goethite in TSR-J2), which were previously detected by XRD (Fig. 5.11b).

Normalized As K-edge EXAFS spectra are relatively similar for samples TSR-J2 and TSR-J3 (Fig. 5.12a). The oscillations giving rise to the first peak in the Fourier transform (Fig. 5.12b) were best fitted with a shell of four arsenic atoms at 1.68 Å (see Table 5.6). The coordination number, As-O bond distance and position of the absorption edges indicate that the arsenic in the samples is dominated by As(V) (Farquhar *et al.*, 2002). The inclusion of multiple scattering of the outgoing photoelectron within the arsenate tetrahedron in the fit further improved the least squares residual. A second shell interaction between arsenic and iron was fitted at 3.30-3.32 Å. The fitted As-Fe distances do not allow us to unambiguously identify the host-bearing phase that harbours arsenic. However, reported values for EXAFS analyses of the local environment of arsenate in jarosite, ferric oxihydroxides and goethite revealed As-Fe interaction at 3.26-3.32 Å,

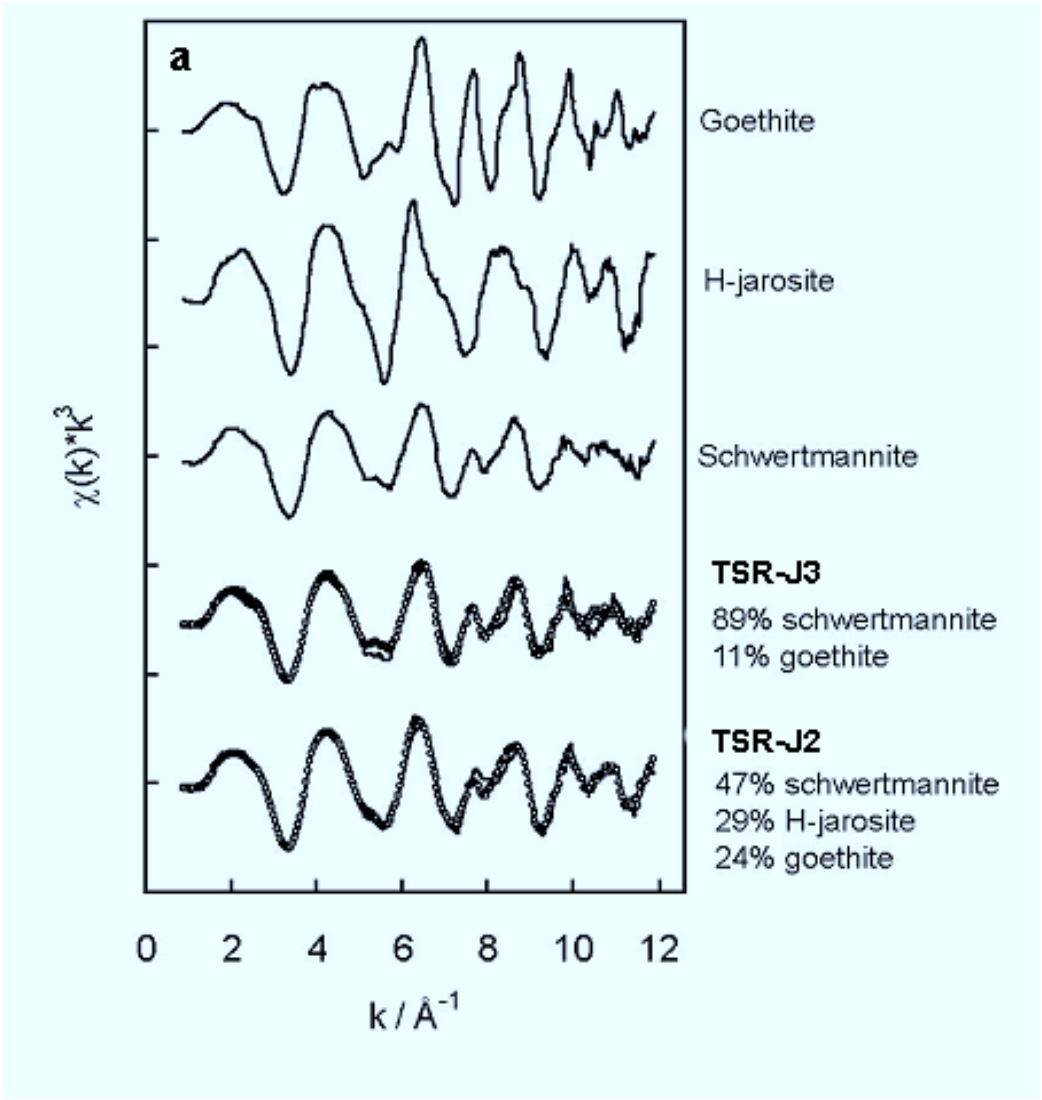

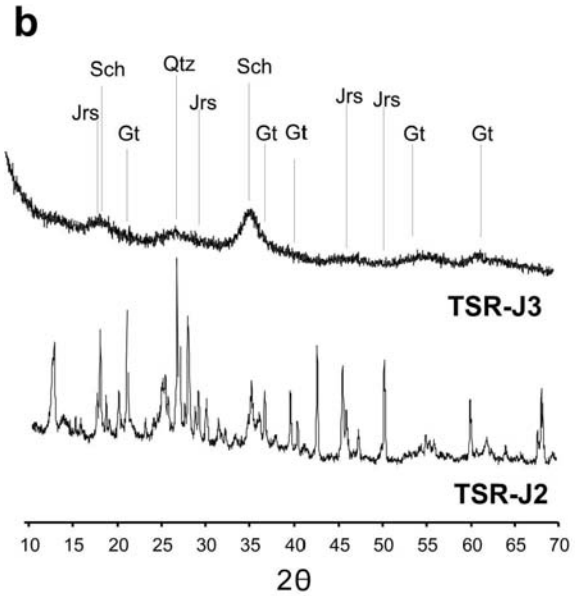

Figure 5.11. Normalised Fe K-edge EXAFS spectra of Fe (oxyhydr)oxide model compounds and two AMD samples. The experimental spectra and best fit of the data are displayed as solid and dotted lines respectively (TSR-J2: 47% schwertmannite, 29% H-jarosite, 23% goethite; TSR-J3: 89% schwertmannite, 11% goethite) (a); XRD patterns for the TSR-J3 and TSR-J2 samples (Sch: schwertmannite; Jrs: jarosite; Gt: goethite; Qtz: quartz) (b). AMD samples were collected in July 2006; TSR-J3 is consolidated terrace in the adit mouth, and TSR-J2 is loose precipitate located downstream before the stream flows into Villar River.

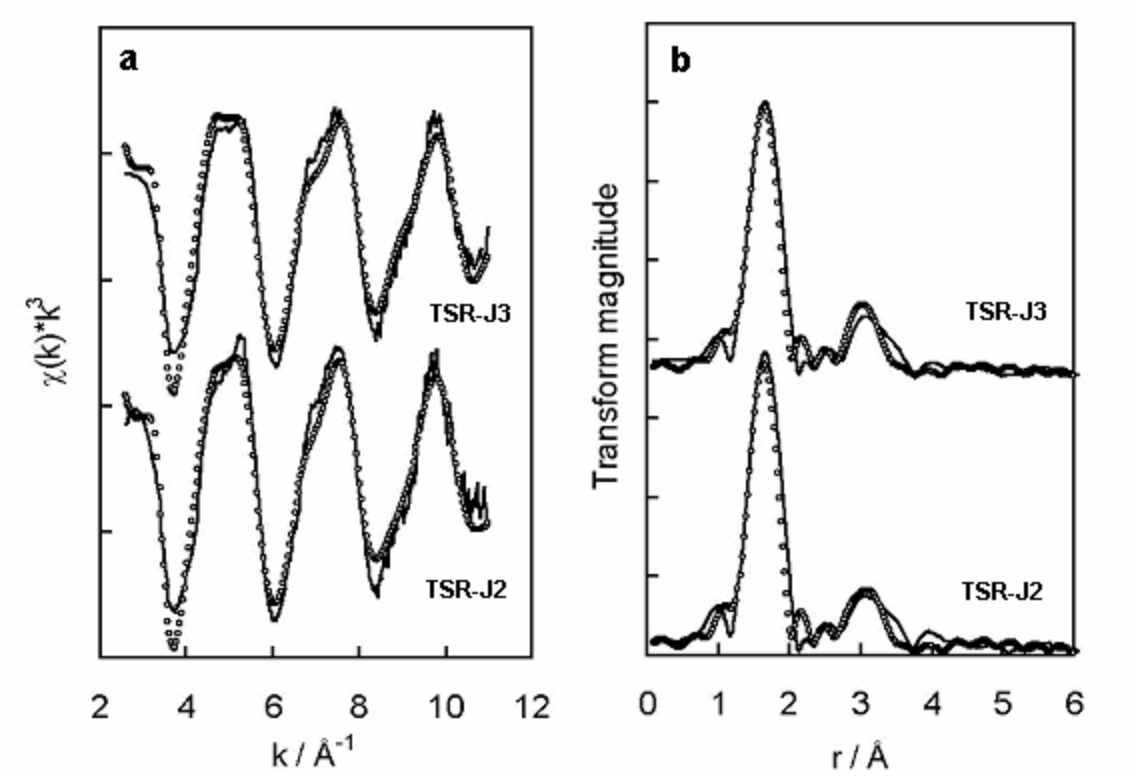

Figure 5.12. Normalised As K-edge EXAFS spectra (a) and radial distribution function (b) of two AMD samples collected in July 2006 (TSR-J3 is consolidated terrace at the adit mouth, and TSR-J2 is loose precipitate located downstream before the stream flows into Villar River). Solid lines represent experimental data, and dotted lines are the least squares best fit using the parameters listed in Table 5.6.

Table 5.6. Paramaters obtained from fitting As K-edge EXAFS spectra for AMD samples[a].

		EXAFS fit		
Sample	Scatterer	N	r / Å	$2\sigma^2$ / Å^2
TSR-J2	O	4	1.68	0.005
	Fe	2	3.32	0.016
TSR-J3	O	4	1.68	0.006
	Fe	2	3.30	0.015

[a] N is the coordination number (±25%), r is the interatomic distance (±0.02 Å for the first shell, ±0.05 Å for more distant shells) and $2\sigma^2$ is the Debye-Waller factor (±25%).

suggesting that the arsenic associated with the AMD samples was associated with an iron mineral assemblage (Gault *et al.*, 2005). This As-Fe interaction is consistent with bidentate arsenic oxyanions occupying corner sharing positions at the apices of iron oxyhydroxide octahedra (Waychunas *et al.*, 1993, Fendorf *et al.*, 1997, Farquhar *et al.*, 2002, Sherman and Randall, 2003) or compatible with arsenate substitution for sulfate in the jarosite structure (Savage *et al.*, 2000; Paktunc and Dutrizac, 2003).

A thorough examination of the samples collected was carried out by means of the arsenic X-ray absorption near edge structure (XANES) spectra of many of the samples collected in November 2006 and March 2007. As K-edge XANES spectra were used to determine the arsenic oxidation state in bulk sediments at different depth profiles (to study the temporal variation) and along the stream (to study the spatial variation).

The normalized XANES spectra of most of the samples are shown in Fig. 5.13. In all samples, arsenic was present in its oxidised pentavalent state (absorption maxima 11.873 keV), As(III) was found to be less than 10% in all the samples. These results are consistent with the AMD water chemistry results, indicating that arsenate is more effectively removed from solution than arsenite Arsenate uptake explains the decrease in aqueous As(V) along the stream. Therefore, according to XANES and EXAFS results, arsenic is present mainly as arsenate associated to the Fe-compounds found in the sediments.

Using a set of arsenic model compounds, the As-bearing components in the studied samples were speciated to determine the amount of each reference in the field sample using the least-squares fitting (LSF) procedure (Ressler *et al.*, 2000). The fitting procedure yielded the relative proportions listed in Table 5.7. The values correspond to the amount of the respective normalized reference spectra required to yield a good match between simulated and experimental XANES spectra. Uncertainties in the fit results are estimated to be in the range of 10%. The quality of the fits was quantified by the normalized sum-squares residuals $NSS=\Sigma(Xanes_{experimental}-Xanes_{fit})^2/\Sigma(Xanes_{experimental})^2 \times 100$, in the 11.850-11.920 keV range. The improvement of adding a new component was calculated by $I=100-(NSS_{two\text{-}components} * 100/NSS_{best\text{-}one\ fit\ component})$ or $I=100-(NSS_{three\text{-}components} * 100/NSS_{best\text{-}two\ fit}$

components) (Isaure *et al.*, 2006). If the fit improvement (I) was more than 20% the addition of the new component was considered and then the simulation with both components was retained. Comparison between experimental and transformation results are shown in Figs. 5.14 and 5.15.

Table 5.7. Quantitative As speciation in samples estimated by LSF and XANEs spectra. The sum of percentages is not always equal to 100% because a tolerance of 10% is admitted.

Sample	Depth (cm)	% As sorbed		
		Schw	Gt	Jt
TSR-N1	-	100	-	-
TSR-N3	-	12	68	19
TSR-N4	-	18	62	19
TSR-N5	-	12	64	18
TSR-N6	-	100	-	-
TSR-N7	-	100	-	-
TSR-N8	-	14	86	-
TSR-M-8	0-0.5	100	-	-
	0.5-4	23	69	-
	4-4.5	22	68	-
	4.5-7	< 10	95	-
TSR-M-10	0-2	14	86	-
	2-4.5	-	100	-
	4.5-6	-	100	-
	6-7	-	100	-

According to the XANES results, the main As(V) scavenger phase upstream (samples TSR-N1, TSR-N6 and TSR-N7) is schwertmannite, whereas downstream (samples TSR-N3, TSR-N4, TSR-N5 and TSR-N8) the percentage of As associated to schwertmannite decreased as goethite and jarosite increased. Downstream, most of the arsenic is associated to goethite, which has a high As(V) sorption capacity even in presence of sulfate as explained in Chapter 4. Lower As(V) percentages are found in jarosite (18-19% in samples TSR-N3, TSR-N4 and TSR-5). These results are, in general, in good agreement with the sediment mineralogical distribution over the stream determined by XRD.

At the adit mouth area (upstream) loose precipitates are composed mainly by schwertmannite with minor quantities of goethite and quartz (Table 5.5). Downstream, solids are made up of detrital silicates, Fe-oxides and Fe-oxy-hydroxy-sulfates, such as

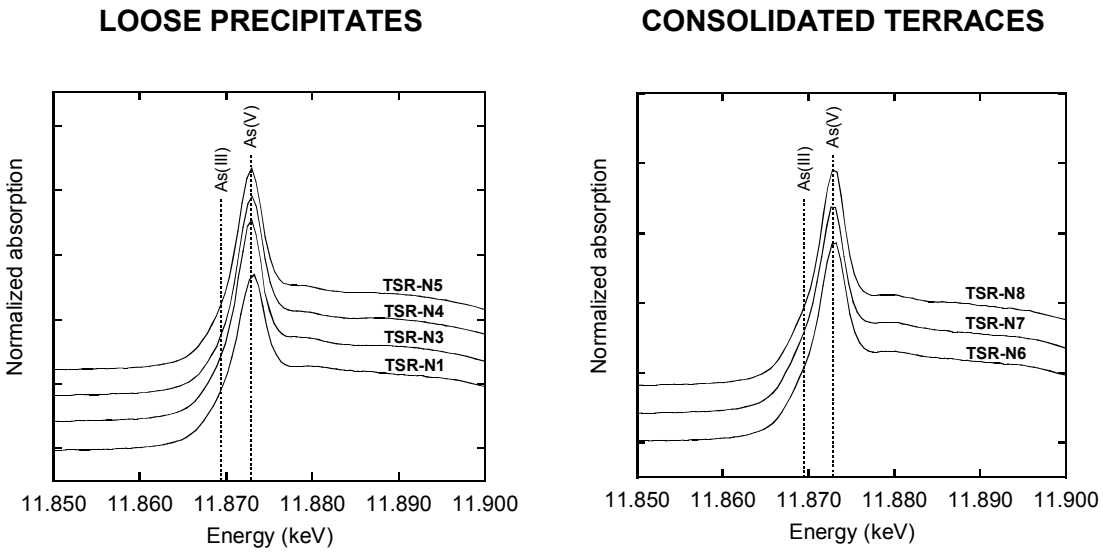

Figure 5.13. As K-edge XANES spectra of the AMD samples with peak height positions of As(III) and As(V) indicated.

schwertmannite, jarosite and goethite (Fig. 5.9). This mineralogical evolution is attributed to either a pH decrease along the stream, favoring the precipitation of jarosite and goethite directly from the solution, or to the displacement of some particles from the upper-stream precipitates and terraces downstream. Nevertheless, the schwertmannite aging process, which is the schwertmannite transformation to goethite and jarosite cannot be discarded.

As it is shown in the XRD patterns depicted in Fig. 5.16 the consolidated terraces exhibite a mineralogical evolution in depth. This evolution is assumed to represent the temporal evolution of the precipitates. The XRD patterns of sediments collected at the upper part (0-4 cm) of the consolidated terraces, TSR-M7 and TSR-M8, showed that they are composed primarily of schwertmannite, with minor amounts of goethite and quartz. Likewise, XRD patterns of sediment downstream (TSR-M-10) showed the presence of schwertmannite and goethite at the surficial sediment. While the sediment in TSR-M7 showed no significant change of solid crystallinity with depth, the sediments of consolidated terraces TSR-M-8 and TSR-M-10 showed an increase in crystallinity with

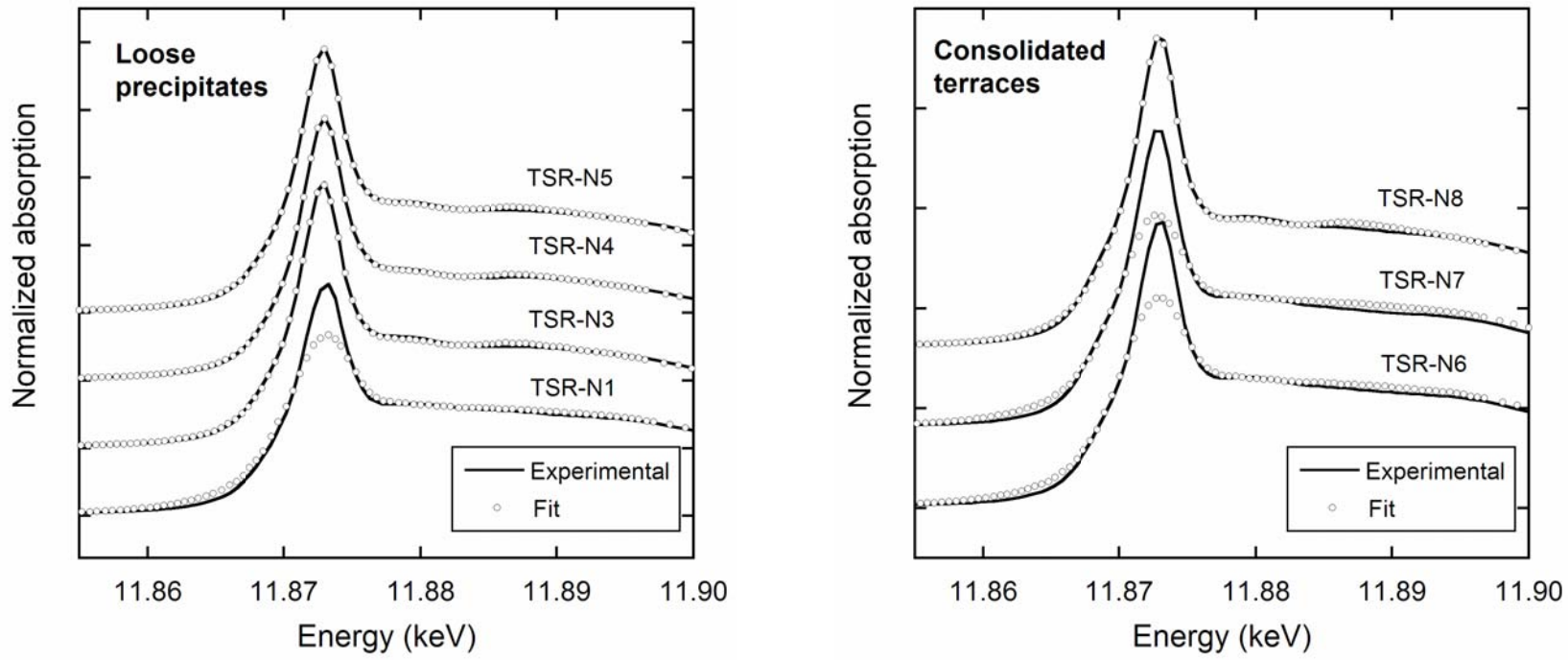

Figure 5.14. Experimental and least-squares fits for the AsK-edge XANES spectra of the collected samples in November 2006. The relative proportions obtained by the least-square fitting (LSF) procedure are shown in Table 5.7.

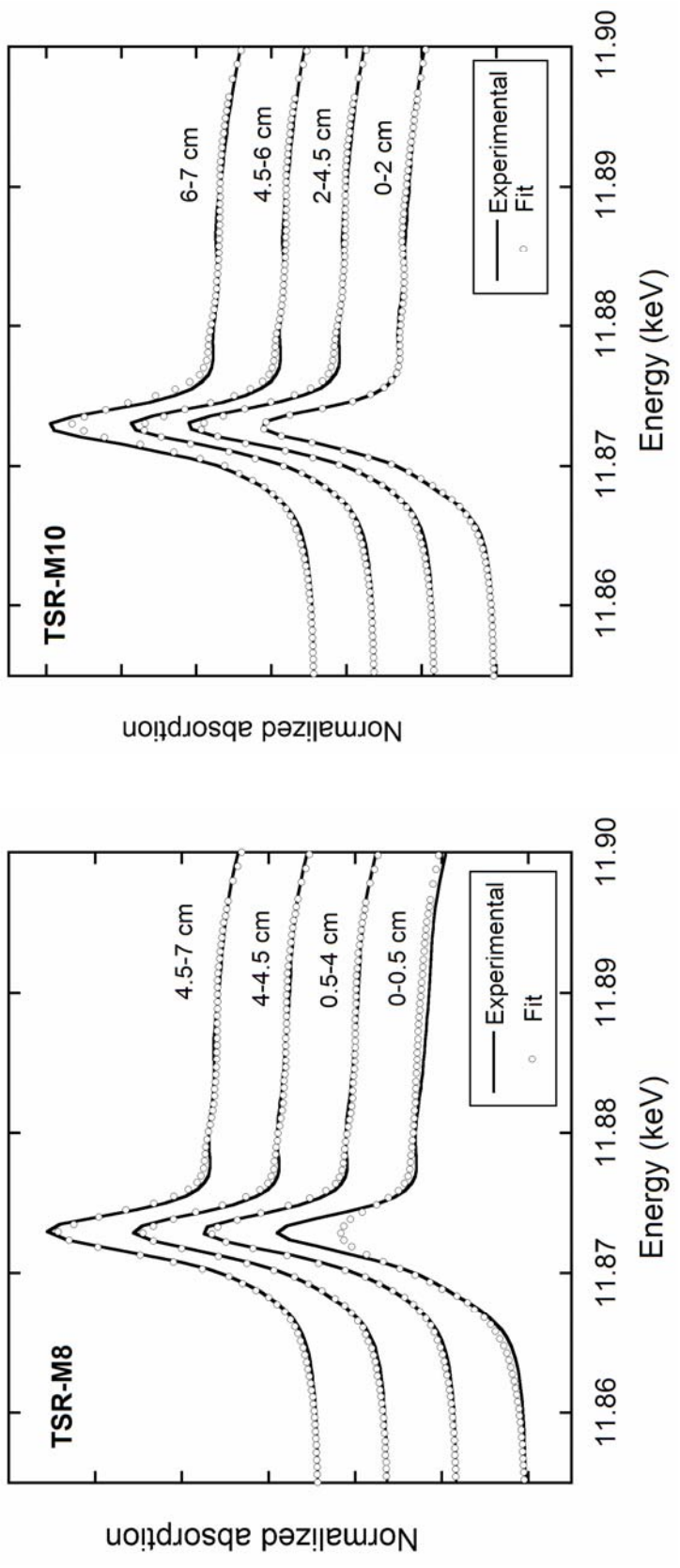

Figure 5.15. Experimental and least-squares fits for the AsK-edge XANES spectra of the collected consolidated terrace samples at different depths. The relative proportions obtained by the least-square fitting (LSF) procedure are shown in Table 5.7.

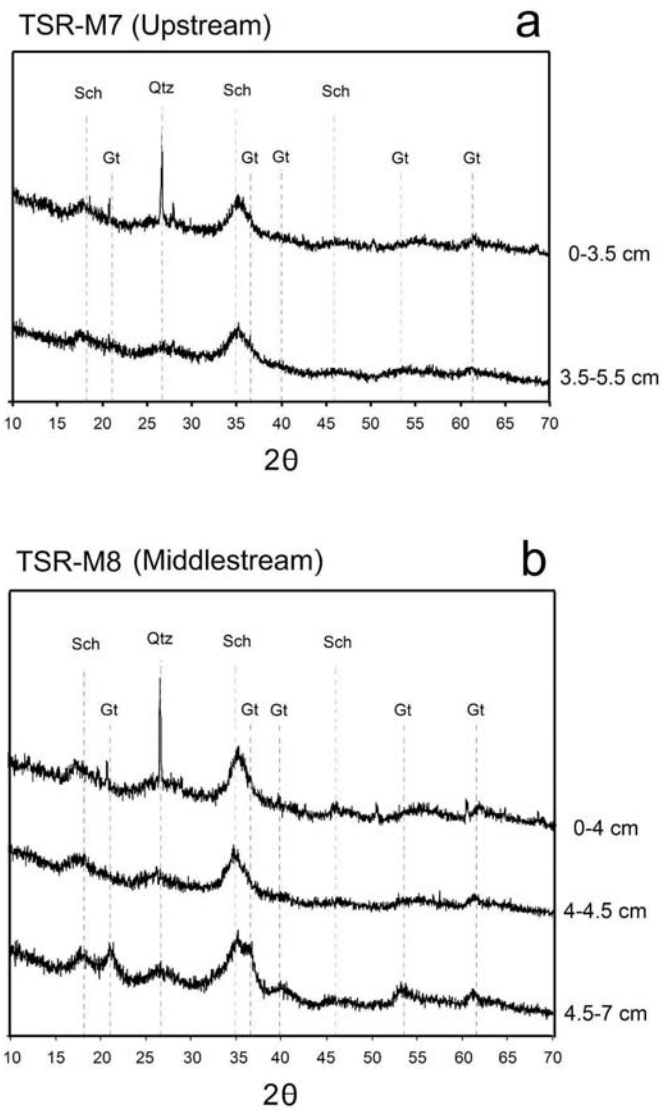

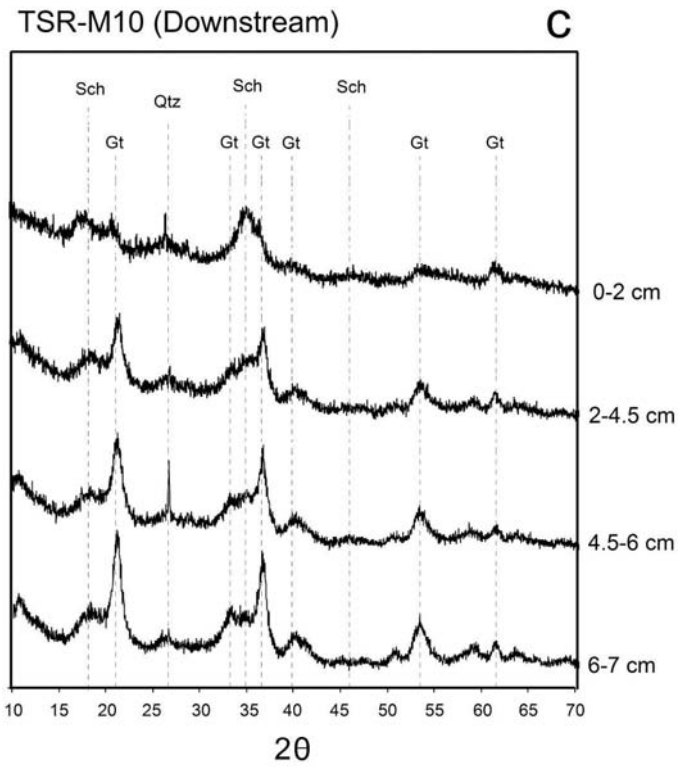

Figure 5.16. X-ray diffraction patterns for the consolidated terrace stream sediments taken at different depth in March 2008 in the upstream (a), midstream (b) and downstream (c) of the Tinto Santa Rosa. XRD patterns show a schwertmannite-rich sediment at the top of the sediment. With depth goethite is dominant in the consolidated terraces located middle and upstream, suggesting a schwertmannite transformation into goethite. Sch: schwertmannite; Jrs: jarosite; Gt: goethite; Qtz: quartz.

depth, associated with the more prominent goethite reflections. The arsenic associated with the Fe-phases in the terrace TSR-M-8 showed a similar trend: in the upper sediments, As(V) is found associated mainly to schwertmannite, which is the main phase observed by XRD. At depth, the amount of As(V) sorbed on goethite increased, accompanying the increased proportion of goethite in the sediment. In the case of terrace TSR-M-10, although a slight increase in arsenic associated to goethite is observed, is very homogeneous.

Comparing the mineralogical percentages of the sediments obtained by XANES to the As concentration in these solids it is observed that the highest arsenic concentrations are associated with sediments made up of mainly schwertmannite, corresponding to the loose precipitates and upper stream terraces. When the precipitates consisted mostly of goethite and/or jarosite, which have lower sorption capacities than schwertmannite (see Chapter 4), the arsenic concentration in the sediment was lower.

The mineralogical evolution with depth observed in the sediments could be explained by schwertmannite transformation into more stable minerals (e.g. goethite) over timescales of weeks to months (Bigham *et al.*, 1996; Peine *et al.* 2000, Gagliano *et al.* 2004, Jönsson *et al.*, 2005, Acero *et al.*, 2006), and jarosite (Acero *et al.*, 2006; Wang *et al.*, 2006 and Kawano and Tomita, 2001). This transformation is inhibited by the presence of arsenate sorbed onto schwertmannite (Fukushi *et al.*, 2003a). This arsenate inhibition could account for the difference in the schwertmannite transformation degree in depth and over the Tinto Santa Rosa stream bed. Upstream sediments with high arsenic concentrations consisted of schwertmannite and minor quantities of goethite, whereas in downstream sediments with low arsenic contents and high amounts of goethite, schwertmannite transformation to goethite and/or jarosite probably occurred.

5.3 Conclusions

The acidic discharge of the abandoned Tinto Santa Rosa mine in the Iberian Pyritic Belt (SW, Spain) transports high concentrations of acidity, sulfate and metal(loid)s (e.g., Fe,

As, Co, Ni, Cu, Pb, and Mn). Although the concentration of arsenic, which is found as As(III) and As(V), is high (up to 4 mg L^{-1}), arsenic is naturally attenuated by sorption onto Fe-oxyhydroxide and Fe-oxyhydroxysulfate phases that made up the stream bed precipitates. Although the dissolved arsenic concentration is reduced over the stream, it reaches to approximately 127 μg L^{-1}, still exceeding the As limit (10 μg L^{-1}) for potable waters (EU guideline).

To unravel the complex nature of the AMD sediments of the stream bed, XRD and XAS characterization methods, together with total acid digestions and XRF analyses were used, providing the mineralogical content, the arsenic chemical speciation, spatial distribution, and the mineralogical association of arsenic in the collected sediment.

XRD and DXRD results indicate that schwertmannite is the dominant secondary phase in the loose sediments and consolidated terraces of the Tinto Santa Rosa stream bed. Loose and crusty precipitates consist of hydroxides and oxy-hydroxy-sulfates of iron such as schwertmannite, jarosite and goethite, as well as some amounts of detrital silicates (quartz, illite, kaolinite). The sediments of the consolidated terraces are made up of schwertmannite, goethite, jarosite and minor amounts of quartz. This mineralogical content is consistent with the saturation index calculations with the PHREEQC code and WATEQ4F database, which revealed supersaturation of the stream water with respect to schwertmannite, goethite and jarosite along the length of the stream.

The mineralogical distribution over the stream indicates that schwertmannite is the dominant phase of the upstream loose sediments, and its amount decreases in the sediments downstream, accompanied by an increase in the content of goethite and jarosite. Likewise, the mineralogical content of the consolidated terraces at depth shows that in the upstream sediments schwertmannite dominates and downstream terraces exhibit an increase in crystallinity with depth, reflected in the presence of enhanced goethite XRD reflections. The synchrotron-based iron K-edge X-ray spectroscopy of the sediments allowed quantification of the mineral content in contrast to the qualitative XRD content.

Based on total acid digestion and XRF analyses, arsenic is mainly associated with Fe-oxyhydroxides and Fe-oxyhydroxysulfates. This arsenic identification in the sediment was confirmed by synchrotron-based X-ray spectroscopy using a least-square fitting (LSF) procedure on the XANES spectra, indicating that: (1) As occurs mainly as As(V); (2) upstream arsenic is sorbed onto the main phase, schwertmannite, whereas downstream it appears mainly sorbed onto goethite and jarosite and (3) changes in As speciation with depth are observed in the consolidated terrace sediments, where arsenic mainly associated to schwertmannite in the upper part of the terraces, and increasing arsenic is primarily associated with goethite at depth.

Accordingly, based on the exhaustive characterization of the sedimentary and aqueous arsenic evolution along the stream it is possible to recapitulate that:

(1) From the comparison between the mineralogical content and the arsenic concentration in the identified Fe-phases the highest arsenic concentration is associated with sediments that are made up mainly of schwertmannite, corresponding to upstream precipitates and terraces. Downstream sediments, where precipitates consisted mostly of goethite and/or jarosite, contained lower arsenic concentrations, likely due to the lower sorption capacity of goethite and jarosite compared to schwertmannite.

(2) The mineralogical differences observed in the loose sediments could be attributed to (i) differences on pH along the stream that would favor precipitation of jarosite and goethite, (ii) erosional transport of some particles from the upstream sediments, and (iii) aging of metastable schwertmannite.

(3) The mineralogical distribution in the consolidated terraces with depth is a consequence of the temporal evolution of the precipitates as a result of schwertmannite transformation into more stable minerals, such as goethite and jarosite, over timescales of weeks to months.

(4) Arsenic sequestration depends on the rapid oxidation of As(III) and Fe(II), with the subsequent hydrolysis of Fe(III) causing precipitation of poorly crystallized minerals

such as schwertmannite that can remove arsenic from solution. To quantify the proposed processes responsible of arsenic attenuation in the AMD Tinto Santa Rosa, reactive transport modelling that couples advective flux and the main geochemical reactions observed in the field was performed using the PHREEQC code. Resulting calculations are presented in Chapter 6.

Chapter 6

Geochemical modeling of arsenic in AMD environments

As discussed in the earlier chapters, arsenic, which is one of the priority pollutants in AMD (La Force *et al.*, 2000; Savage *et al.*, 2000), could under extremely acid conditions reach very high concentrations (in the order of hundreds of mg L^{-1}; e.g. Nordstrom and Alpers, 1999; Plumlee *et al.*, 1999). The primary source of arsenic is the oxidation of As-bearing sulfides such as arsenopyrite, marcasite and As-rich pyrite. This process, which is one of the main causes of arsenic contamination of surface and groundwaters in regions of active and historic mining activities world-wide (Ball and Nordstrom, 1985; Prior and Williams, 1996; Smedley *et al.*, 1996; Armienta *et al.*, 1997), has also been identified as a source of arsenic in non-mining areas (Peters *et al.*, 1999).

The geochemistry of arsenic in natural systems is complex. The main processes that control the mobility and fate of arsenic in surface and groundwaters are: (1) redox reactions; (2) sorption/desorption; (3) solid phase precipitation and dissolution and (4) biological activity (Cheng *et al.*, 2008). The occurrence and removal of arsenic in natural

water bodies are, therefore, related to water pH, redox conditions, the arsenic oxidation state, and sorption (or exchange) reactions. Effective remediation of streams and rivers affected by acid mine drainage demands a comprehensive knowledge of the dominant mechanisms that determine arsenic content in order to curb arsenic pollution and improve water treatment.

The characterization of arsenic sources in mining areas, the mechanisms controlling arsenic release and mobility, and its natural attenuation processes have been studied (e.g. Fukushi *et al.*, 2003a; Frau and Ardau, 2003; Casiot *et al.*, 2005; Gault *et al.*, 2005). On the other hand, there are a number of studies based on geochemical modeling of arsenic behaviour. Welch and Lico (1998) made a forward model that included a surface complexation model using PHREEQC to determine the role of adsorption and potential arsenic sources and sinks in the Carson Desert, Nevada. A surface complexation modeling was also used to simulate the behaviour of arsenic at an industrially contaminated site by Lumsdon *et al.* (2001). Stollenwerk *et al.* (2007) studied arsenic attenuation by the oxidized aquifer sediments in Bangladesh including competitive sorption and As(III) oxidation processes. As regards sulfide oxidation, Schreiber *et al.* (2000) proposed pyrite oxidation as the potential As source in eastern Winconsin by means of an inverse modeling made with NETPATH. Carrillo-Chavez *et al.* (2000) using inverse and forward modeling, studied the processes controlling arsenic in a mining district close to La Paz, Baja California (Mexico), and Armienta *et al.* (2001) predicted the water chemistry evolution using an inverse modeling for mass balance at Zimapán Valley (Mexico).

However, there are a few studies that combine an exhaustive arsenic characterization and the geochemical quantification in AMD environments. For example, most works deal with the arsenic source without considering arsenic oxidation (e.g. Schreiber *et al.*, 2000). Additionally, surface oxidation processes were not considered, and surface complexation modelling based on hydrous ferric oxide (HFO) surface-site parameters was used to compute schwertmannite sorption. Thus, these models despite

being useful in some cases have been found to underestimate arsenic removal (Tonkin *et al.*, 2002). There are no works that have used the sorption capacity of schwertmannite combined with arsenate sorption and precipitation processes coupled to the iron and arsenic oxidation reactions to simulate arsenic mobility under field conditions.

Accordingly, a geochemical model is proposed in this chapter in order to quantify the geochemical processes involved in the arsenic fate along an AMD discharge. The model is simple and is based on the processes quantified in earlier studies and previous chapters, i.e. oxidation of iron and arsenic, arsenate sorption on Fe-precipitates (e.g., schwertmannite), and schwertmannite precipitation. The rate laws and sorption constants for the different reactions involved are calibrated against the evolution of the water concentration along an AMD where active precipitation of schwertmannite occurs.

6.1 Model description

6.1.1 Conceptual model

The chemical water and sediment characterization along the stream was fully discussed in Chapter 5. The main features in the stream water were a decrease in pH from 3.5 and 3 to 3 and 2.7, accompanied by a systematic decrease in the concentrations of ferrous, total iron, As(III), As(V) and total arsenic.

The conceptual model of the processes involved in arsenic attenuation consists of: (1) Fe(II) oxidation to Fe(III), (2) oxidation of As(III) to As(V), (3) Fe(III) precipitation as hydroxides and hydroxysulfates that causes a decrease in pH, and (4) sorption of As(V) onto the solid Fe(III)-phases. The reactions are shown in Table 6.1 (eq. 6.1 to 6.4).

In the presence of oxygen, ferrous iron produced by sulfide oxidation is oxidized by oxygen (eq. 6.1). This reaction is known to be very slow at low pH (Singer and Stumm, 1970) except in the presence of microorganisms, that increases the rate of Fe(III) production by up to six orders of magnitude, which will be discussed below.

Table 6.1. Main reactions and rate laws used in the model and rate constant values and k_d obtained from the Tinto Santa Rosa field data (March 2007 and February 2008 campaigns).

Equation	Reaction	Rate expression (mol L^{-1} s^{-1})	Model rate constant		Reported and calculated rate constant values	
	Fe(II) oxidation		mar-07	feb-08		
(6.1)	$Fe^{2-} + 0.25\,O_2(aq) + H^- = Fe^{3+} + 0.5\,H_2O$	$r_{Fe(II)} = \frac{-d[Fe(II)]}{dt} = k\,[Fe(II)]\,f_{O2}$	$10^{-3.55}$	$10^{-3.75}$	$10^{-3.43}$ $10^{-3.47}$ $10^{-3.9}$ - $10^{-5.2}$	(1) (2) (3)
	As(III) oxidation (a)					
(6.2)	$2Fe^{3+} + H_3AsO_3 + H_2O + h\nu = 2Fe^{2+} + H_3AsO_4 + 2H^+$	$r_{As(III)} = \frac{-d[As(III)]}{dt} = k[As(III)]\,[Fe(III)]$	$10^{-1.20}$	$10^{-1.20}$	$10^{-2.2}$ $10^{-2.8}$	(3)
	Schwertmannite precipitation (b)					
(6.3)	$8Fe^{3+} + 2.07SO_4^{2-} + 11.86H_2O = Fe_8O_8(SO_4)_{2.07}(OH)_{3.86} + 19.86H^+$	$r_{Sch\ precipitation} = k\ (1-\Omega)$	10^{-15}	10^{-24}	-	-
		$r_{Sch\ precipitation} = k\ [Fe(III)]\,[H^+]^{-1}$	$10^{-8.0}$	$10^{-8.5}$	$10^{-8.10}$	(4)
	As(V) sorption (c)					
(6.4)	$Schwertmannite + H_3AsO_4 + 0.24OH^- = As\text{-}Schw + 0.62\,SO_4^{2-} + 0.24\,H_2O + H^+$	$r_{As(V)\ sorption} = r_{Sch\ precipitation}\ k_d\ [As(V)]$	$10^{3.42}$	$10^{3.90}$	$10^{4.5}$-$10^{5.0}$	(5)

"$h\,\nu$" is photons
(a) Reaction proposed by Emett and Khoe (2001)
(b) Calculated schwertmannite composition of Tinto Santa Rosa acid discharge
(c) Reaction proposed byFukushi *et al*. (2003b)
Ω = saturation index
K_d = distribution coefficient

(1) The fO_2 (fO_2 equal to $10^{-0.67}$) was included in the rate constant reported by McKnight and Bencala (1989)
(2) The fO_2 (fO_2 equal to $10^{-0.67}$) was included in the rate constant reported by McKnight*et al.* (1988)
(3) Chapter 3 this volume; Table 3.2
(4) Calculated modelling the data of Acero*et al.* (2006)
(5) Calculated from the data of Fukushi*et al.* (2003b)

The rate of Fe(II) oxidation was found to be proportional to Fe(II) concentration, indicating first-order kinetics. This dependence that was proposed in systems under steady-state conditions (or equivalent) (Nordstrom, 1985), was implemented in the model by using the expression of Singer and Stumm (1970) for pH below 3.5:

$$r_{Fe(II)} = \frac{-d[Fe(II)]}{dt} = k[Fe(II)]\ f_{O2} \qquad (6.1)$$

where $r_{Fe(II)}$ is the oxidation rate expressed in mol L^{-1} s^{-1}, [Fe(II)] is the ferrous iron concentration (mol L^{-1}) at a time t (s), fO_2 is the oxygen fugacity and k (s^{-1}) is the rate constant of the kinetic expression.

An important consequence of Fe(II) oxidation to Fe(III) is the precipitation of secondary ferric phases that remove dissolved iron (and other elements such as arsenic) from the solution and cause the pH to decrease progressively downstream.

Arsenite oxidation by oxygen is very slow (Tallman and Shaikh, 1980; Eary and Schramke, 1990) even in Fe(III) solutions (Manning *et al.*, 2002, Roberts *et al.*, 2004, McCleskey *et al.* 2004; Johnston and Singer, 2007). However, the rate of oxidation of As(III) to As(V) by oxygen and Fe(III) is increased by several orders of magnitude by the presence of near ultraviolet light since the reaction takes place in conjunction with the photochemical reduction of Fe(III) (eq. 6.2; Table 6.1; Emett and Khoe, 2001; Hug *et al.*, 2001; Bednar *et al.*, 2002; McCleskey *et al.* 2004). Likewise, microbes could catalyze arsenic oxidation in natural waters (e.g. Wakao *et al.*, 1988; Wilkie and Hering, 1998; Santini *et al.*, 2002; Nakazawa and Hareyama, 2007). In the case of AMD waters, the arsenic speciation and redox chemistry is controlled by dissolved Fe in AMD systems (Bednar *et al.*, 2005, Sarmiento *et al.*, 2007). This is in good agreement with the results obtained in Chapter 3, where simultaneous iron and arsenic oxidation was studied under laboratory conditions similar to those in the field. The results suggested that Fe(II) oxidation was biotically catalyzed and the resulting Fe(III) catalyzed As(III) oxidation to As(V). Although earlier works have proposed pseudo-first order kinetics in iron mediated oxidation of As(III)

(Leuz *et al.*, 2006), Fe(III) has been demonstrated to be involved in As(III) oxidation. Therefore, a second-order kinetic equation that takes into account the effect of As(III) and Fe(III) was proposed for the field model (equation 6.2):

$$r_{As(III)} = \frac{-d[As(III)]}{dt} = k\,[As(III)]\,[Fe(III)]^n \qquad (6.2)$$

where k is the oxidation coefficient (L mol^{-1} s^{-1}), [As (III)] and [Fe(III)] are the arsenite and ferric iron concentrations, respectively, in mol L^{-1} after time t, and n is the reaction order with respect to ferric iron concentration that was found experimentally to be one.

The oxidation of As(III) to As(V) plays a central role in arsenic attenuation since Fe(III) precipitates that cover the stream bed show a larger capacity to sorb As(V) than As(III). Therefore, oxidation of As(III) to As(V) substantially enhances the arsenic removal capacity of stream solids.

Apart from oxidation reactions, the precipitation of secondary phases is another process mainly involved in the arsenic evolution along the acid stream. The usual Fe(III) phase formed after Fe(II) oxidation at many sites of the IPB is schwertmannite (Sánchez-España *et al.*, 2005b, 2007; Acero *et al.*, 2006). The mineral paragenesis may also include variable amounts of goethite and jarosite as detected by X-Ray Diffraction. Although the solubility calculations performed with the PHREEQC code indicate supersaturation with respect to these phases, it should be noted that the PHREEQC calculations do not consider kinetic aspects, and the formation of goethite and jarosite in Fe(III) systems at low temperature (15-20ºC) is very slow (weeks to months at room temperature) (Schwertmann and Cornell, 1991). In addition, transformation of schwertmannite into goethite and/or jarosite is also a very slow process (Bigham *et al.*, 1996; Regenspurg *et al.*, 2004; Jönsson *et al.*, 2005 and Acero *et al.*, 2006). Furthermore, transformation is retarded by the presence of arsenate sorbed onto schwertmannite (Fukushi *et al.*, 2003a), which is expected to occur in the sediments of the Tinto Santa Rosa stream. Given that the water residence time considered in the stream is 2.1 to 3.2 h, direct precipitation of goethite and

jarosite and transformation of schwertmannite into goethite and/or jarosite were not considered in the model. Therefore, for modeling purposes, the amount of ferric iron removed from water between the mixing point and TS8 (Fig. 5.2; Chapter 5) was exclusively ascribed to precipitated schwertmannite.

As regards the rate of mineral precipitation, it is reasonable to assume that this rate is proportional to the degree of supersaturation. Kinetic expressions that consider the saturation index (as eq. 6.3) have been widely used for model precipitation of many minerals (see for example, Molson *et al.*, 2008):

$$r_{Sch\ precipitation} = k\ (1\text{-}\Omega) \qquad (6.3)$$

where Ω is the schwertmannite saturation index, defined as the ratio of the ion activity product and the solubility product and k is the rate constant (mol L^{-1} s^{-1}). The high variability in the saturation indices for schwertmannite demanded the use of very different rate constants in the model (see Table 6.1). Accordingly, the prediction of schwertmannite precipitation was impossible because the rate constant seemed to vary widely in time even though this process was apparently constant in the field. Therefore, a simple kinetic expression that ultimately depends on the saturation state of the solution was used to account for schwertmannite precipitation:

$$r_{Sch\ precipitation} = k\ [Fe(III)][H^+]^{-1} \qquad (6.4)$$

where $r_{Sch\ precipitation}$ is the rate of schwertmannite precipitation in mol L^{-1} s^{-1}, [Fe(III)] and [H^+] are the ferric iron and proton concentration in mol L^{-1}, and k is the rate constant in mol L^{-1} s^{-1}.

It is worth noting that this expression is sufficiently close to eq. 6.3, which considers that the rate is proportional to the degree of supersaturation, since the sulfate concentration displays a conservative behaviour in AMD waters (it is assumed as constant and integrated in the k value) and since [H^+] scarcely varies along the stream.

According to the total acid digestion analyses and the X-Ray Fluorescence results, the arsenic content in the Tinto Santa Rosa precipitates was very high, which demonstrated the efficiency of the AMD precipitates to sequester arsenic. In addition, XANES spectra indicated that the arsenic sequestered in the precipitates was mainly in its oxidized pentavalent state. Given the absence of waters flowing into the Tinto Santa Rosa stream to dilute the dissolved metal load, at least during the campaign of March 2007 and February 2008 (see Figs. 5.6 and 5.7; Chapter 5), the decrease in aqueous As(III) concentration with time was attributed to arsenite oxidation to arsenate. Depletion of As(III) was accompanied by production of As(V) which was, in part, sorbed onto schwertmannite. This Fe(III)-oxyhydroxysulfate is known to act as a usual sink for As(V) in AMD due to sorption processes (e.g. Fukushi *et al.*, 2003a,b; 2004) (eq. 6.4; Table 6.1). Hence, the last process included in the model was the arsenic decrease due to As(V) sorption onto schwertmannite.

Sorption of As(V) can occur through true adsorption (or surface complexation) or co-precipitation (forming a mixed precipitate or solid solution). In the case of schwertmannite, the uptake mechanism of As(V) by schwertmannite in co-precipitation is identical to that in the adsorption (Fuskhusi *et al.*, 2004) and consists of a replacement of AsO_4 by SO_4 groups. Furthermore, the evolution of changes in composition has proved to be similar in adsorption (Fukushi *et al.*, 2004) and co-precipitation (Carlson *et al.*, 2002). Owing to the similar composition in the resultant As(V) complexes in both systems, the following simple kinetic co-precipitation rate was included in the model:

$$r_{As(V)_{sorption}} = r_{Sch\ precipitation}\ k_d [As(V)] \qquad (6.5)$$

where $r_{As(V)\ sorption}$ is the As(V) sorption rate (mol L^{-1} s^{-1}), $r_{Sch\ precipitation}$ is the schwertmannite precipitation rate (mol L^{-1} s^{-1}), [As(V)] is the arsenate concentration in mol L^{-1} and K_d represents the distribution coefficient for As(V) into schwertmannite. This expression was used to calculate the distribution coefficient for As(V) from the laboratory data of Fukushi *et al.* (2003b). The obtained values were compared with these of our model.

6.1.2 Reactive transport model implementation

The one dimensional (1D) reaction-transport model PHREEQC (Parkhurst and Appelo, 1999) and the WATEQ4F thermodynamic database (Ball and Nordstrom, 1991) were used to simulate the evolution of the water composition along the stream.

In the simulations, a 1D column containing 20 cells, 15 m each in length, with 1 kg of water each cell was used with a time step of 800 and 500 s, yielding an average linear velocity of 0.02 and 0.03 m s^{-1} (March 2007 and February 2008 data, respectively). The advective transport time (for a chemically conservative constituent) was 10000 s and 16000 s to model the March 2007 and February 2008 data, respectively, in the 300 m length of the column.

At each time step, PHREEQC simulated the four processes affecting arsenic mobility (eq. 6.1 to 6.4, see Table 6.1). The reactions considered in the advective transport model were calculated by kinetic laws.

Model inputs included measured temperature, pH, pe and the concentration of anions and cations. The water composition that resulted from the mixing water of the two contaminant sources (TS1 and TS2 in a mixing ratio of 0.7TS1/0.3TS2 in both samplings; see Table 5.1 and Fig. 5.2, Chapter 5) was used as the initial water composition. Therefore, in addition to aqueous speciation, the reactions included in the model were those with the most significant impact on arsenic behaviour.

6.2 Results and discussion

Figures 6.1 and 6.2 display the pH and dissolved concentrations of total iron and Fe(II), Fe(III), total arsenic, As(III) and As(V) along the Tinto Santa Rosa stream and the resulting simulations.

The measured pH was suitably fitted. This evolution trend was mainly controlled by iron geochemistry. The iron removal from the dissolved phase demands the oxidation of

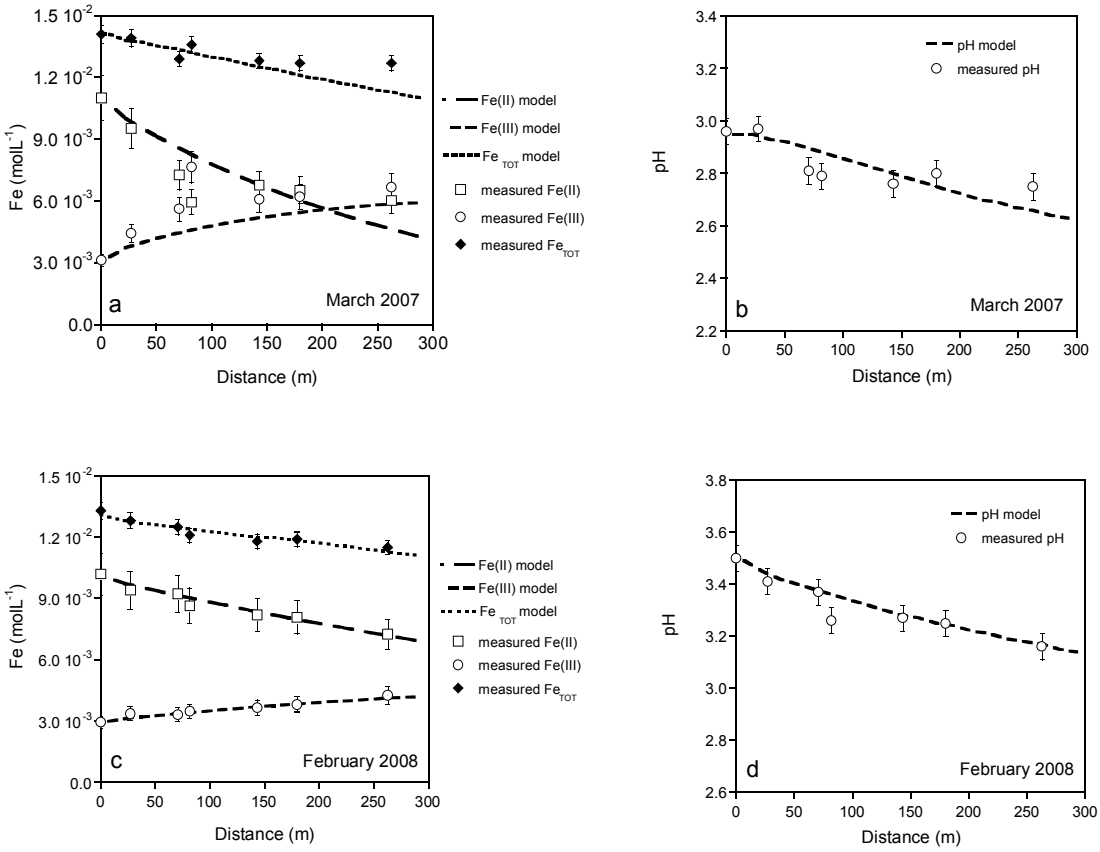

Figure 6.1. Comparison between simulated and measured data for pH and concentration of Fe(II), Fe(III) and total iron in the Tinto Santa Rosa stream. Error bars correspond to the analytical error (10% for Fe(II) and Fe(III), 3% for total iron and 0.05 for pH). The calculated values reproduced satisfactorily the measured data. The distances between the different sampling points, located by GPS in the field, were calculated by means of ArcGIS 9 over the aerial orthoimage of the Tinto Santa Rosa stream. The travelling time between points was estimated with the flow rate and the stream section measured in the field.

ferrous iron, hydrolysis of ferric iron and the formation of Fe-precipitates. Ferric iron hydrolysis releases protons, thereby decreasing pH.

The rate of Fe(II) oxidation was calculated from the decrease in the Fe(II) concentration between the TS1 and TS2 mixing point and point TS8 (see Table 5.1 and Fig. 5.2, Chapter 5). The residence time of water estimated between the TS1-TS2 mixing point and TS8 was 3.2 and 2.1 h, depending on the flow rate (Q=0.71 and 1.1 L/s,

respectively). The resulting Fe(II)-oxidation field rate ranged from $3.4x10^{-7}$ mol L^{-1} s^{-1} to $4.3x10^{-7}$ mol L^{-1} s^{-1}. These rates are 5 orders of magnitude higher than the value of $3.0x10^{-12}$ mol L^{-1} s^{-1} proposed by Singer and Stumm (1968). This difference between laboratory and field Fe(II)-oxidation rates is classically attributed to the catalyzing effect of bacteria (Noike *et al.*, 1983; Nordstrom, 1985; Kirby and Elder Brady, 1998; Sánchez-España *et al.*, 2007). The iron oxidation rates obtained correspond to rate constant values of $10^{-3.55}$ and $10^{-3.75}$ L mol^{-1} s^{-1} (or $10^{-4.2}$-$10^{-4.4}$ s^{-1}) including the atmospheric pO_2 in rate constant). These kinetic contant values are slightly higher than those obtained by using the same first-order kinetic expression under laboratory conditions ($10^{-4.1}$ to $10^{-5.2}$ L mol^{-1} s^{-1}). But they are comparable to the calculated first-order ferrous iron oxidation rate constant of $10^{-4.1}$ s^{-1} (including pO_2 in the rate constant) for microbial oxidation of ferrous iron calculated by McKnight *et al.* (1988) or McKnight and Bencala (1989) under field conditions.

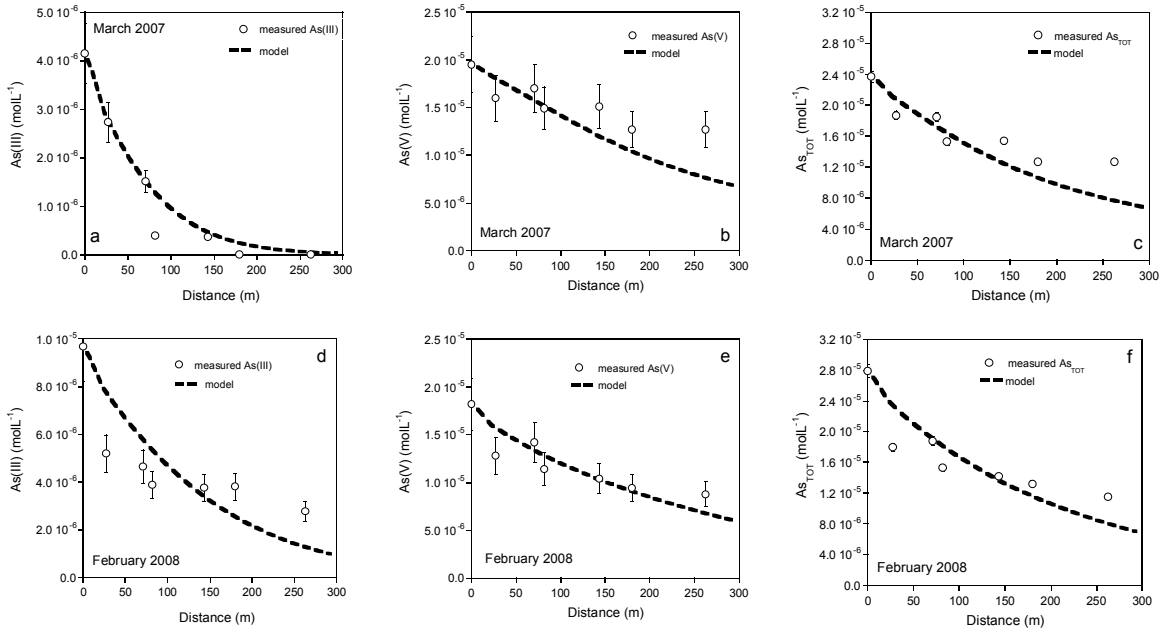

Figure 6.2. Comparison between simulated and measured data for concentration of As(III), As(V) and total arsenic in the Tinto Santa Rosa stream. Error bars correspond to the analytical error (15% for As(III) and As(V) and 3% for total arsenic).

After fixing the oxidation rate of Fe(II), As(III) oxidation and Fe(III) precipitation were fitted simultaneously. As in Fe(II), the As(III) oxidation rate at the field scale was calculated from the decrease in As(III) concentration between the mixing point TS1 and TS2 and TS8 and the time required for water to travel this distance. The calculated oxidation rate constant is in the order of $10^{-1.2}$ L mol^{-1} s^{-1}. This value is one order of magnitude faster than those obtained in this study under laboratory conditions (see Chapter 3; As(III) oxidation rate constants ranged from $10^{-2.2}$ to $10^{-2.8}$ L mol^{-1} s^{-1}). As stated above, iron and arsenic oxidation occurs simultaneously and iron oxidizes arsenic. Therefore, the higher As(III) oxidation rate observed in the field is probably due to the catalytic effect of ferric iron and solar light although a biocatalyzed process cannot be ruled out. The model adequately predicted the general As(III) evolution using the proposed kinetic expression (eq. 6.2). Nonetheless, a marked decrease in the As(III) dissolved concentration on February 2008 is observed in the upper reaches of the stream (between TS1-TS2 mixing point and TS3) and is not totally reproduced (Fig. 6.2d). This discrepancy between the measured and the predicted values is difficult to interpret. It could be attributed to differences in solar irradiation during day time sampling since ultraviolet light induces rapid photooxidation of As(III) to As(V), and also to the fact that high Fe(II)/Fe(III) ratio (as observed upstream) raises hydroxyl radical production, increasing the oxidation rate of As(III) (Sarmiento, 2007).

The schwertmannite precipitation rate was calculated from the Fe(III) concentration differences along the stream (eq. 6.3; Table 6.1). The estimated rate for schwertmannite precipitation was around $3.1x10^{-7}$ and $1.7x10^{-7}$ mol L^{-1} s^{-1} for the data of March 2007 and February 2008, respectively. These rate values would be $1.3x10^{-7}$ and $2.4x10^{-7}$ mol L^{-1} s^{-1} using the differences of total dissolved iron along the Tinto Santa Rosa stream as reported in Sánchez-España *et al.* (2007). These values would be in the range of $1.7x10^{-6}$ to 10^{-7} mol L^{-1} s^{-1} reported by Sánchez-España *et al.* (2007) for other AMD impacted sites in the Iberian Pyritic Belt.

The determination of the rate constant value for schwertmannite precipitation is complicated because schwertmannite is an amorphous Fe-phase with a solubility constant value that covers a range of several orders of magnitude (Bigham *et al.*, 1996; Yu *et al.*, 1999). Using rate constants of $10^{-8.0}$ and $10^{-8.5}$ mol L^{-1} s^{-1}, the model adequately reproduces the field data. Given the absence of similar precipitation expressions in the literature, the same kinetic expression was used to model the reported data by Acero *et al.* (2006) of January 2004 in the Cueva de la Mora stream (located close to the Tinto Santa Rosa mine). A precipitation constant of $10^{-8.1}$ mol L^{-1} s^{-1} was obtained by coupling the Fe(II) oxidation (with the same oxidation rate constant of $10^{-3.75}$ L mol^{-1} s^{-1}) as that of the February data model) and the schwertmannite precipitation processes. The rate constant obtained is in good agreement with the one obtained for schwertmannite precipitation in the Tinto Santa Rosa acid discharge.

The partitioning of an element into preferential solid and aqueous phases is useful in predicting the amount of each element that is incorporated into the solid phase. The distribution coefficient (K_d) for As(V) into schwertmannite was obtained from laboratory data by Fukushi *et al.* (2003b). Kinetic sorption of As(V) onto schwertmannite was modelled by incorporating As(V) as a minor constituent into precipitated schwertmannite (eq. 6.4; Table 6.1). Although the model is simplified by omitting the water chemistry, the calculated data adequately predict the evolution of the measured As(V) when the distribution coefficients are equal to $10^{3.42}$ and $10^{3.90}$. These values are respectively lower than $10^{4.5}$ and $10^{5.0}$, which were calculated from the data of Fukushi *et al.* (2003b) under similar As(V) concentrations to those of this study. This discrepancy could be attributed to the higher sulfate concentration in the Tinto Santa Rosa stream, that ranges from 2800 to 3500 mg L^{-1}), than in the laboratory experiments (10-70 mg L^{-1}). Schwertmannite sorption mechanism was suggested to occur via sulfate-arsenate exchange (Fukushi *et al.*, 2003b; Fukushi et al., 2004) similar to that proposed for jarosite. Therefore, the schwertmannite exchange capacity could decrease as sulfate increases in solution as observed for jarosite (see Chapter 4). The model reproduced suitably the arsenic field data. Only in the lower reaches did the predicted evolution slightly overestimate the field

values. This slight discrepancy may be attributed to the fact that a uniform stream bed in which only schwertmannite was considered as the Fe(III)-phase was assumed. As discussed in Chapter 4, the As(V) sorption capacities of schwertmannite, goethite and jarosite are very different.

6.3 Conclusions

A 1-D reactive transport model coupling advective flux and several chemical reactions has proved to be useful in elucidating the geochemical behaviour of an AMD stream. A remarkable innovation in this model is the incorporation of key chemical reactions such as iron and arsenic oxidation, precipitation of schwertmannite and arsenic sorption onto the newly precipitated schwertmannite on the stream bed.

Our geochemical modeling highlights the importance of iron oxidation, which ultimately induces all the geochemical changes observed in the system. On the one hand, Fe(III) is capable of oxidizing As(III), and on the other hand the precipitation of Fe(III) phases favors the As(V) sorption onto them. Therefore, the main mechanism to attenuate naturally arsenic in AMD discharges is schwertmannite precipitation together with arsenite oxidation to arsenate.

Despite the simplicity of our model, the simulations satisfactorily reproduced the main chemical features of the stream water such as the pH decrease downstream and the accompanying changes in arsenic (As(III), As(V), As_{TOT}) and iron (Fe(II), Fe(III) and Fe_{TOT}) concentrations. The fitted kinetic constants for iron oxidation are comparable to those reported in earlier studies with the same rate law under field and laboratory biotic conditions. The distribution coefficient of arsenate onto schwertmannite was lower than that calculated from data obtained under laboratory conditions. This is probably due to the fact that the schwertmannite sorption mechanism, which was suggested to occur via sulfate-arsenate exchange, is likely affected by high sulfate concentrations. The model calibration demonstrated the need for scaling the arsenic oxidation rate obtained under laboratory conditions since it was 1-2 orders of magnitude lower. As for the rate constant

of schwertmannite precipitation, this constant was calibrated to reproduce the iron evolution observed given the absence of these values in the literature. This value proved to be similar in both samplings and was suitable for modeling schwertmannite precipitation at another AMD site in the Iberian Pyritic Belt.

Chapter 7

General conclusions

This chapter summarizes the main contributions of this thesis.

The **first part of this thesis** is concerned with flow-through experiments designed to obtain the dissolution rate laws applicable to the prediction of the long-term dissolution of arsenopyrite and marcasite, the main contributors with pyrite of arsenic to waters.

The arsenopyrite dissolution rate law at pH range 1-6 and 25 ˚C can be expressed as:

$$R_{arsenopyrite}(mol\ m^{-2}\ s^{-1})_{25^\circ C} = 10^{-8.07\pm0.25} \cdot a_{O_2}^{0.60\pm0.05} \cdot a_{H^+}^{-0.05\pm0.05} \quad (7.1)$$

The marcasite dissolution rate law at pH between 1 and 3 and 25 ˚C can be expressed as:

$$R_{marcasite}(mol\ m^{-2}\ s^{-1})_{25^\circ C} = 10^{-9.10\pm0.14} \cdot a_{O_2}^{0.33\pm0.03} \cdot a_{H^+}^{-0.08\pm0.04} \quad (7.2)$$

Under the experimental conditions of this study, arsenopyrite and marcasite dissolution rates are significantly dependent on dissolved oxygen, decreasing as the

dissolved oxygen concentration is diminished. By contrast, pH has little effect on dissolution.

The apparent activation energy is 29.4 and 14.1 kJ mol^{-1} for arsenopyrite and marcasite dissolution, respectively. These rather low values suggest that the overall dissolution reaction is controlled by transport processes or mixed-controlled by surface reactions and transport processes.

In acidic solutions (pH ≤ 3) a sulfur-enriched layer is created over the two sulfide surfaces. The originated layers are mainly made up of polysulfides and sulfates and the presence of elemental sulfur cannot be ruled out. These layers do not exert a passivating effect and the steady state is attained.

The iron released from arsenopyrite and marcasite dissolved under mildly acid to basic pH, precipitates as Fe-oxyhydroxide phases over the surfaces. This Fe-coating slows down diffusion of aqueous species through it. This results in a decrease in metal release, preventing the attainment of the steady state. The formation of these Fe-coatings is important at remediated AMD sites since these coatings passivate the surfaces of the metal-rich sulfides. These coatings become the sink of toxic metal(oid)s (e.g., arsenic) in AMD waters because of their high stability and retention capacities.

The **second part of this thesis** deals with the oxidation of As(III) to As (V) in the presence of iron, and As(V) sorption on goethite and jarosite under laboratory conditions similar to those found in AMD waters. Arsenic retention capacities of goethite and jarosite are compared to that of schwertmannite.

Arsenic speciation and redox chemistry seem to be controlled by aqueous Fe in AMD waters. Under AMD biotic conditions, ferrous iron and arsenite oxidize simultaneously. Despite reports on the presence of arsenite-oxidizing bacteria in mine-drainage waters, our findings suggest that Fe(III), which resulted from microbial oxidation of ferrous iron, abiotically oxidized As(III). As(III) oxidation to As(V) by Fe(III)

is slow under abiotic conditions. Arsenite oxidation is greatly enhanced by light in the presence of chloride and by Fe(III) in solution.

Arsenic mobilization in soils and waters is mainly controlled by sorption processes. Acid Rock Drainage (ARD) and Acid Mine Drainage (AMD) impacted areas usually show high arsenic contents that decrease with the distance from the polluting source (mine adit, tailings, heaps, etc.). Natural attenuation of arsenic in AMD areas is controlled by new iron precipitates (e.g., schwertmannite ($Fe_8O_8(OH)_{5.5}(SO_4)_{1.25}$), jarosite ($KFe_3(SO_4)_2(OH)_6$) and goethite (FeOOH)) that sorb aqueous arsenate. Sorption capacity of goethite and jarosite was studied using batch experiments with synthetic K-jarosite and goethite at highly acidic pH (1.5-2.5). The effect of ionic strength and sulfate concentration on arsenic removal was also investigated. The two minerals were able to remove arsenic from aqueous solutions. In the absence of competitive effects of other anions, K-jarosite presented better removal efficiency than goethite for As(V). The maximum sorption capacity was respectively estimated to be $1.2 \cdot 10^{-4}$ and $7.0 \cdot 10^{-6}$ mol m^{-2} under similar experimental conditions. Ionic strength and pH had little effect on the sorption capacity of goethite and jarosite in the small range of pH studied. The presence of sulfate, which is the main anion in AMD natural systems, had a negative effect on arsenic removal, since sulphate competes with arsenate for surface sorption sites.

The sorption capacities obtained are considerably lower than that reported by schwertmannite. This suggests that a net release of As(V) to water could take place during schwertmannite transformation to jarosite or goethite.

The **last part of this thesis** is devoted to the characterization of the geochemical processes involved in arsenic natural mitigation at the AMD sites located in the Iberian Pyritic Belt (SW, Spain). To this end, the chemistry of waters and sediments of the Tinto Santa Rosa acid mine discharge is discussed.

The most striking feature observed in the Tinto Santa Rosa AMD waters is the reduction of pH downstream accompanied by a decrease in ferrous and total iron. These

observations indicate that bacterially mediated oxidation of ferrous to ferric iron takes place simultaneously with Fe(III) removal by precipitation of Fe(III)-phases, which cover the bed stream. Dissolved arsenic concentration decreases as As(III) is oxidized to As(V) downstream.

The bed-stream precipitates show a high arsenic concentration, which is mainly in its pentavalent state, indicating that arsenic is selectively incorporated into the solids probably due to sorption processes at acidic pH. This demonstrates the efficiency of AMD precipitates in sequestering arsenic. Mineralogically, loose and crusty precipitates consist of detritic silicates and oxihydroxides and oxy-hydroxy-sulfates of iron such as schwertmannite, jarosite and goethite. Consolidated terraces are made up of schwertmannite, goethite, jarosite and small amounts of quartz.

A comparison of sediment mineralogy and arsenic concentration in the identified Fe-phases shows that the highest arsenic concentration is associated with the sediments largely made up of schwertmannite corresponding to loose precipitates and terraces upstream. Arsenic concentration was lower downstream, where precipitates consist largely of goethite and/or jarosite with As(V) sorption capacities lower than that of schwertmannite.

The main geochemical processes observed in the field and studied under laboratory conditions were quantified by a 1-D reaction-transport model using the PHREEQC code. In the light of our findings, the model, despite its simplicity, satisfactorily reproduces the arsenic mobilization data along the Tinto Santa Rosa acid discharge.

Bibliography

Abollino O., Giacomino A., Malandrino M., and Mentasti E. (2005) The use of sequential extraction procedures for the characterization and management of contaminated soils. *Annali di Chimica* **95,** 525-538.

Acero P., Ayora C., Torrentó C., and Nieto J. M. (2006) The role of trace elements during schwertmannite precipitation and subsequent transformation into goethite and jarosite. *Geochimica et Cosmochimica Acta* **70**, 4130-4139.

Acero P., Cama J., and Ayora C. (2007a) Sphalerite dissolution kinetics in acidic environment. *Applied Geochemistry* **22**, 1872-1883.

Acero P., Cama J., and Ayora C. (2007b) Kinetics of chalcopyrite dissolution at pH 3. *European Journal of Mineralogy* **19**, 173-182.

Acero P., Cama J., and Ayora C. (2007c) Rate law for galena dissolution in acidic environment. *Chemical Geology* **245**, 219-229.

Acero P., Ayora C., and Carrera J. (2007d) Coupled thermal, hydraulic and geochemical evolution of pyritic tailings in unsaturated column experiments. *Geochimica et Cosmochimica Acta* **71**, 5325-5338.

Acero P., Cama J., Ayora C., and Asta M. P. (2009) Chalcopyrite dissolution rate law from pH 1 to 3. *Geologica Acta,* **In press**.

Al T. A., Martin C. J., and Blowes D. W. (2000) Carbonate-mineral/water interactions in sulfide-rich mine tailings. *Geochimica et Cosmochimica Acta* **64**, 3933-3948.

Allison J. D., Brown D. S., and Novo-Gradac K. L. (1990) MINTEQA2/PRODEFA2, A Geochemical Assessment Model for Environmental Research Laboratory, Office of Research and Development, U.S. EPA.

Aposhian H. V., Zakharyan R. A., Avram M. D., Sampayo-Reyes A., and Wollenberg M. L. (2004) A review of the enzymology of arsenic metabolism and a new potential role of hydrogen peroxide in the detoxication of the trivalent arsenic species. *Toxicology and Applied Pharmacology* **198**, 327-335.

Appleyard E. C. and Blowes D. W. (1994) Applications of Mass-Balance Calculations to Weathered Sulfide Mine Tailings. In *Environmental Geochemistry of Sulfide Oxidation*, Vol. 550, pp. 516-534.

Arai Y., Lanzirotti A., Sutton S. R., Newville M., Dyer J., and Sparks D. L. (2006) Spatial and temporal variability of arsenic solid-state speciation in historically lead arsenate contaminated soils. *Environmental Science and Technology* **40,** 673-679.

Armienta M. A., Rodriguez R., Aguayo A., Ceniceros N., Villaseñor G., and Cruz O. (1997) Arsenic contamination of groundwater at Zimapán, Mexic. *Hydrogeology Journal* **5**, 39-46.

Armienta M. A., Villaseñor G., Rodriguez R., Ongley L. K., and Mango H. (2001) The role of arsenic-bearing rocks in groundwater pollution at Zimapán Valley, Mexico. *Environmental Geology* **40**, 571-581.

Asta M. P., Cama J., Gault A. G., Charnock J. M., and Queralt I. (2007) Characterization of AMD sediments in the discharge of the Tinto Santa Rosa mine (Iberian Pyritic Belt, SW Spain). *Proceedings IMWA Symposium 2007 Water in Mining Envrionments*, 391-395.

Asta M. P., Cama J., and Ayora C. (2008a) Atenuación Natural de Arsénico en el Drenaje Acido de Mina. *Macla* **9**, 35-36.

Asta M. P., Cama J., Soler J. M., Arvidson R. S., and Lüttge A. (2008b) Interferometric study of pyrite surface reactivity in acidic conditions. *American Mineralogist* **93,** 508-519.

Ball J. W. and Nordstrom D. K. (1985) Major and trace-element analyses of acid mine waters in the Leviathan Mine drainage basin, California/Nevada. In *U.S. Geological Survey Water-Resources Investigations Report 85-4169*, pp. 46.

Ball J. W. and Nordstrom D. (1991) User's manual for WATEQ4F with revised thermodynamic database and test cases for calculating speciation of major, trace and redox elements in natural waters. U.S. Geological Survey Water-Resources Investigation Report 91–183.

Baron D. and Palmer C. D. (1996) Solubility of jarosite at 4-35°C. *Geochimica et Cosmochimica Acta* **60**, 185-195.

Barrante J. R. (1974) Applied Mathematics for Physical Chemistry. Prentice-Hall, Inc.

Beattie M. J. V. and Poling G. W. (1987) A Study of the Surface Oxidation of Arsenopyrite Using Cyclic Voltammetry. *International Journal of Mineral Processing* **20**, 87-108.

Bednar A. J., Garbarino J. R., Ranville J. F., and Wildeman T. R. (2002) Preserving the distribution of inorganic arsenic species in groundwater and acid mine drainage samples. *Environmental Science and Technology* **36**, 2213-2218.

Bednar A. J., Garbarino J. R., Ranville J. F., and Wildeman T. R. (2005) Effects of iron on arsenic speciation and redox chemistry in acid mine water. *Journal of Geochemical Exploration* **85**, 55-62.

Benjamin M. M. (1983) Adsorption and surface precipitation of metals of amorphous iron oxyhidroxide. *Environmental Science and Technology* **17**, 686-692.

Bermond A. P. and Yousfi I. (1997) Reliability of comparisons based on sequential extraction procedures applied to soil samples: The thermodynamic point of view [Etude de la validite de comparaisons fondees sur l'application de procedures d'extractions sequentielles appliquees a des echantillons de terre]. *Environmental Technology* **18,** 219-224.

Berner R. (1980) *Early diagenesis; a theoretical approach.* Princeton Series in Geochemistry.

Bigham J. M. and Nordstrom D. K. (2000) Iron and aluminum hydroxysulfates from acid sulfate waters. *Sulfate Minerals - Crystallography, Geochemistry and Environmental Significance* **40**, 351-403.

Bigham J. M., Carlson L., and Murad E. (1994) Schwertmannite, a new iron oxyhydroxysulphate from Pyhasalmi, Finland, and others localities. *Mineralogical Magazine* **58**, 641-648.

Bigham J. M., Schwertmann U., Traina S. J., Windland R. L., and Wolf M. (1996) Schwermannite and the chemical modelling or iron in acid sulfate waters. *Geochimica et Cosmochimica Acta* **12**, 2111-2121.

Binsted N. (1998) CLRC Daresbury Laboratory EXCURV98 program, CLRC Daresbury Laboratory, Warrington, UK.

Bonnissel-Gissinger P., Alnot M., Ehrhardt J. J., and Behra P. (1998) Surface oxidation of pyrite as a function of pH. *Environmental Science and Technology* **32**, 2839-2845.

Borda M. J., Strongin D. R., and Schoonen M. A. (2004) A vibrational spectroscopic study of the oxidation of pyrite by molecular oxygen. *Geochimica et Cosmochimica Acta* **68**, 1807-1813.

Bowell R. J. (1994) Sorption of Arsenic by Iron-Oxides and Oxyhydroxides in Soils. *Applied Geochemistry* **9**, 279-286.

Bowell R. J. and Bruce I. (1995) Geochemistry of iron ochres and mine waters from Levant Mine, Cornwall. *Applied Geochemistry* **10**, 237-250.

Brandt F., Bosbach D., Krawczyk-Barsch E., Arnold T., and Bernhard G. (2003) Chlorite dissolution in the acid pH-range: A combined microscopic and macroscopic approach. *Geochimica et Cosmochimica Acta* **67**, 1451–1461.

Brantley S. L. (2008) Kinetics of Mineral Dissolution. In *Kinetics of Water-Rock interaction* (ed. J. D. Kubicki, S.L. Brantley , A.F. White), pp. 151-196. Springer. NewYork.

Brantley S. L. and Conrad C. F. (2008) Analysis of Rates of Chemical Reactions. In *Kinetics of Water-Rock Interaction* (ed. J. D. Kubicki, S.L. Brantley , A.F. White), pp. 1-35. Springer, NewYork.

Breed A. W., Harrison S. T. L., and Hansford G. S. (1997) A preliminary investigation of the ferric leaching of a pyrite/arsenopyrite flotation concentrate. *Minerals Engineering* **10**, 1023-1030.

Brookins D. G. (1988) *Eh-pH diagrams for geochemistry.* Springer-Verlag, Berlin.

Brunauer S., Emmett P. H., and Teller E. (1938) Adsorption of gases in multimolecular layers. *Journal of the American Chemical Society* **60**, 309-319.

Bruneel O., Personné J. C., Casiot C., Leblanc M., Elbaz-Poulichet F., Mahler B. J., Le Flèche A., and Grimont P. A. D. (2003) Mediation of arsenic oxidation by *Thiomonas sp.* in acid mine drainage (Carnoulès, France). *Journal of Applied Microbiology* **95**, 492-499.

Buckley A. N. and Walker G. W. (1988) The surface-composition of arsenopyrite exposed to oxidizing environments. *Applied Surface Science* **35**, 227-240.

Buckley A. N. and Woods R. (1985) X-Ray photoelectron spectroscopy of oxidized pyrrothite surfaces. I Expose to air. *Applied Surface Science* **22**, 280-287.

Buckley A. N. and Woods R. (1987) The Surface Oxidation of Pyrite. *Applied Surface Science* **27**, 437-452.

Bunnell J. E., Finkelman R. B., Centeno J. A., and Selinus O. (2007) Medical geology: a globally emerging discipline. *Geologica Acta* **5**, 273-281.

Cama J. and Acero P. (2005) Dissolution of minor sulfides present in a pyritic sludge at pH 3 and 25ºC. *Geologica Acta* **3**, 15-26.

Cama J., Acero P., Ayora C., and Lobo A. (2005) Galena surface reactivity at acidic pH and 25ºC based on flow-through and in situ AFM experiments. *Chemical Geology* **214**, 309-330.

Cama J., Asta M. P., Acero P., and De Giudicci G. (2008) Dissolution kinetics of arsenopyrite and its implication on arsenic speciation in the environment. In *Natural Arsenic in Latin America*, pp. 273-280. Balkema.

Cancès B., Juillot F., Morin G., Laperche V., Polya D., Vaughan D. J., Hazemann J.-L., Proux O., Brown Jr. G. E., and Calas G. (2008) Changes in arsenic speciation through a contaminated soil profile: A XAS based study. *Science of the Total Environment* **397,** 178-189.

Carlson L., Bigham J. M., Schwertmann U., Kyek A., and Wagner F. (2002) Scavenging of As from acid mine drainage by schwertmannite and ferrihydrite: a comparison with syntethic analogues. *Environmental Science and Technology* **36**, 1712-1719.

Carrillo-Chavez A., Drever J. I., and Martinez M. (2000) Arsenic content and groundwater geochemistry of the San Antonio-El Triunfo, Carrizal and Los Planes aquifers in southernmost Baja California, Mexico. *Environmental Geology* **39**, 1295-1303.

Casiot C., Leblanc M., Bruneel O., Personne J. C., Koffi K., and Elbaz-Poulichet F. O. (2003a) Geochemical processes controlling the formation of As-rich waters within a tailings impoundment (Carnoulès, France). *Aquatic Geochemistry.* **9**, 273-290.

Casiot C., Morin G., Juillot F., Bruneel O., Personne J. C., Leblanc M., Duquesne K., Bonnefoy V., and Elbaz-Poulichet F. (2003b) Bacterial immobilization and oxidation of arsenic in acid mine drainage (Carnoules creek, France). *Water Research* **37**, 2929-2936.

Casiot C., Lebrun S., Morin G., Bruneel O., Personne J. C., and Elbaz-Poulichet F. O. (2005) Sorption and redox processses controlling arsenic fate and transport in a stream impacted by acid mine drainage. *Science of the Total Environment* **347**, 122-130.

Charnock J. M., Polya D. A., Gault A. G., and Morgan A. J. (2007) XAS studies of arsenic in the environment. *AIP Conference Proceedings 882*, 211-213.

Cheng H., Hu Y., Luo J., Xu b., and Zhao J. (2008) Geochemical processes controlling fate and transport of arsenic in acid mine drainage (AMD) and natural systems. *Journal of hazardous materials,* **doi: 10.1016/j.hazmat.2008.10.070**.

Cherry J. A., Shaikh A. U., Tallman D. E., and Nicholson R. V. (1979) Arsenic Species as an Indicator of Redox Conditions in Groundwater. *Journal of Hydrology* **43**, 373-392.

Cornell R. M. and Schwertmann U. (1996) *The iron oxides: structure, properties, reactions, occurrence and uses.* VCH Verlagsgesellschaft, Weinheim.

Courtin-Nomade A., Bril H., Néel C., and Lenain J. F. (2003) Arsenic in iron cements developed within tailings of a former metallic mine- Enguialès, Aveyron, France. *Applied Geochemistry* **18**, 395-408.

Craw D., Falconer D., and Youngson J. H. (2003) Environmental arsenopyrite stability and dissolution: theory, experiment, and field observations. *Chemical Geology* **199**, 71-82.

Cullen W. R. and Reimer K. J. (1989) Arsenic speciation in the environment. *Chemical Reviews* **89**, 713-764

Daus B., Mattusch J., Wennrich R., and Weiss H. (2002) Investigation on stability and preservation of arsenic species in iron rich water samples. *Talanta* **58**, 57-65.

Davis J. A. and Kent D. B. (1990) Surface complexation modelling in aqueous geochemistry. *Reviews in Mineralogy and Geochemistry* **23**, 177-260.

De Giudici G. and Zuddas P. (2001) In situ investigation of galena dissolution in oxygen saturated solution: evolution of surface features and kinetic rate. *Geochimica et Cosmochimica Acta* **65**, 1381-1389.

Descostes M., Vitorge P., and Beaucaire C. (2004) Pyrite dissolution in acidic media. *Geochimica et Cosmochimica Acta* **68**, 4559-4569.

Dixit S. and Hering J. G. (2003) Comparison of arsenic (V) and arsenic (III) sorption onto iron oxide minerals: Implications for arsenic mobility. *Environmental Science and Technology* **37**, 4182-4189.

Dold B. (2003) Dissolution kinetics of schwertmannite and ferrihydrite in oxidized mine samples and their detection by differential X-ray diffraction (DXRD). *Applied Geochemistry* **18**, 1531-1540.

Domènech C., de Pablo J., and Ayora C. (2002) Oxidative dissolution of pyritic sludge from the Aznalcollar mine (SW Spain). *Chemical Geology* **190**, 339-353.

Dousová B., Kolousek D., Kovandaa F., Machovic V., and Novotná M. (2005) Removal of As(V) species from extremely contaminated mining water. *Applied Clay Science* **28**, 31-42.

Duquesne K., Lieutaud A., Ratouchniak J., Yarzábal A., and Bonnefoy V. (2007) Mechanisms of arsenite elimination by *Thiomonas* sp. isolated from Carnoulès acid mine drainage. *European Journal of Soil Biology* **43**, 351-355.

Dzombak D. A. and Morel F. M. (1990) *Surface complexation modeling, Hydrous Iron Oxide*. John Wiley & Sons.

Eary L. E. and Schramke J. A. (1990) Rates of Inorganic Oxidation Reactions Involving Dissolved-Oxygen. *Chemical Modeling of Aqueous Systems II* **416**, 379-396.

Elsetinow A. R., Strongin D. R., Borda M. J., Schoonen M. A., and Rosso K. M. (2003) Characterization of the structure and the surface reactivity of a marcasite thin film. *Geochimica et Cosmochimica Acta* **67**, 807-812.

Emett M. T. and Khoe G. H. (2001) Photochemical oxidation of arsenic by oxygen and iron in acidic solutions. *Water Research* **35**, 649-656.

Farquhar M. L., Charnock J. M., Livens F. R., and Vaughan D. J. (2002) Mechanisms of arsenic uptake from aqueous solution by interaction with goethite, lepidocrocite, mackinawite, and pyrite: An X-ray absorption spectroscopy study. *Environmental Science Technology* **36**, 1757-1762.

Fendorf S., Eick M. J., Grossl P., and Sparks D. L. (1997) Arsenate and chromate retention mechanisms on goethite. 1. Surface structure. *Environmental Science Technology* **31**, 315-320.

Ferguson J. E. (1990) *The heavy elements-chemistry, environmental impact and health effects.* Pergamon Press.

Ficklin W. H. and Mosier E. L. (1999) Field methods for sampling and analysis of environmental samples for unstable and selected stable constituents. In *The environmental geochemistry of mineral deposits, Part A. Processes, Techniques, and Health Issues*: Society of Economic Geologists, Vol. Rev Econ Geol 6A (ed. Plumlee GS, M.J. Losdon), pp. 249–264.

Foster A. L., Brown G.E. J., Tingle T. N., and Parks G. A. (1998) Quantitative arsenic speciation in mine tailings using X-ray absorption spectroscopy. *American Mineralogist* **83,** 553-568

Foster A. L. and Ashley R. P. (2002) Characterization of arsenic species in microbial mats from an inactive gold mine. *Geochemistry: Exploration, Environment, Analysis* **2**, 253-261.

Frau F. and Ardau C. (2003) Geochemical controls on arsenic distribution in the Baccu Locci stream catchment (Sardinia, Italy) affected by past mining. *Applied Geochemistry* **18**, 1373-1386.

Fukushi K., Sato T., and Yanase N. (2002) Sorption of As(V) onto schwertmannite and its effect on the transformation. *Goldschmidt Conference Abstracts*, A249.

Fukushi K., Sasaki M., Sato T., Yanase N., Amano H., and Ikeda H. (2003a) A natural attenuation of arsenic in drainage from an abandoned arsenic mine dump. *Applied Geochemistry* **18**, 1267-1278.

Fukushi K., Sato T., and Yanase N. (2003b) Solid-solution reactions in As(V) sorption by schwertmannite. *Environmental Science and Technology* **37**, 3581-3586.

Fukushi K., Sato T., Yanase N., Minato J., and Yamada H. (2004) Arsenate sorption on schwertmannite. *American Mineralogist* **89**, 1728-1734.

Gagen P. M. (1987) The oxidation rates of arsenopyrite and chalcopyrite in acidic ferric chloride solutions at 0 to 60 °C. Ph. D. Thesis, Virginia Polytechnic Institute and State University.

Gagliano W. B., Brill M. R., Bingham J. M., Jones F. S., and Traina S. J. (2004) Chemistry and mineralogy of ochreous sediments in a constructed mine drainage wetland. *Geochimica et Cosmochimica Acta* **68**, 2119-2128.

Gao Y. and Mucci A. (2001) Acid base reactions, phosphate and arsenate complexation, and their competitive adsorption at the surface of goethite in 0.7 M NaCl solution. *Geochimica et Cosmochimica Acta* **65**, 2361-2378.

Gault A. G., Polya D. A., Lythgoe P. R., Farquhar M. L., Charnock J. M., and Wogelius R. A. (2003) Arsenic speciation in surface waters and sediments in a contaminated waterway: An IC-ICP-MS and XAS based study. *Applied Geochemistry* **18,** 1387-1397.

Gault A. G., Cooke D. R., Townsend A. T., Charnock J. M., and Polya D. A. (2005) Mechanisms of arsenic attenuation in acid mine drainage from Mount Bischoff, western Tasmania. *Science of Total Environment* **345**, 219-228.

Giménez J., Martínez M., De Pablo J., Rovira M., and Duro L. (2007) Arsenic sorption onto natural hematite, magnetite, and goethite. *Journal of Hazardous Materials* **141**, 575-580.

Goldberg S. and Johnston C. T. (2001) Mechanisms of Arsenic Adsorption on Amorphous Oxides Evaluated Using Macroscopic Measurements, Vibrational Spectroscopy, and Surface Complexation Modeling. *Journal of Colloid and Interface Science* **234**, 204-216.

Gómez Ariza J. L., Giráldez I., Sánchez-Rodas D., and Morales E. (2000) Selectivity assessment of a sequential extraction procedure for metal mobility characterization using model phases. *Talanta* **52,** 545-554.

Gräfe M. and Sparks D. L. (2005) Kinetics of zinc and arsenate co-sorption at the goethite-water interface. *Geochimica et Cosmochimica Acta* **69**, 4573-4595.

Gräfe M., Beattie D. A., Smith E., Skinner W. M., and Singh B. (2008) Copper and arsenate co-sorption at the mineral-water interfaces of goethite and jarosite. *Journal of Colloid and Interface Science* **322**, 399-413.

Grossl P. R. and Sparks D. L. (1995) Evaluation of contaminant ion adsorption/desorption on goethite using pressure-jump relaxation kinetics. *Geoderma* **67**, 87-101.

Gurman S. J., Binsted N., and Ross I. (1984) A rapid, exact curved-wave theory for EXAFS calculations. *Journal of Physics C: Solid state physics* **17**, 143-151.

Hacquard E., Bessiere J., Alnot M., and Ehrhardt J. J. (1999) Surface spectroscopic study of the adsorption of Ni(II) on pyrite and arsenopyrite at pH 10. *Surface and Interface Analysis* **27**, 849-860.

Harmer S. L. and Nesbitt H. W. (2004) Stabilization of pyrite (FeS2),marcasite (FeS2), arsenopyrite (FeAsS) and loellingite (FeAS(2)) surfaces by polymerization and auto-redox reactions. *Surface Science* **564**, 38-52.

Hedin L. and Lundqvist S. (1969) Effects of electron-electron and electron-phonon interactions on the one-electron states of solids. *Journal of Physics C: Solid state physics* **23**, 1-181.

Hernández-García M. E. and Custodio E. (2004) Natural baseline quality of madrid tertiary detrital aquifer groundwater (Spain): A basis for aquifer management. *Environmental Geology* **46**, 173-188.

Herrera L., Ruiz P., Aguillon J. C., and Fehrmann A. (1989) A New Spectrophotometric Method for the Determination of Ferrous Iron in the Presence of Ferric Iron. *Journal of Chemical Technology and Biotechnology* **44**, 171-181.

Hsia T. H., Lo S. L., Lin C. F., and Lee D. Y. (1994) Characterization of arsenate adsorption on hydrous iron oxide using chemical and physical methods. *Colloids and Surfaces A: Physicochemical and Engineering Aspects* **85**, 1-7.

Hug S. J., Canonica L., Wegelin M., Gechter D., and Von Gunten U. (2001) Solar oxidation and removal of arsenic at circumneutral pH in iron containing waters. *Environmental Science and Technology* **35**, 2114-2121.

Impellitteri C. A. (2005) Effects of pH and phosphate on metal distribution with emphasis on As speciation and mobilization in soils from a lead smelting site. *Science of the Total Environment* **345,** 175-190.

Isaure M.-P., Fayard B., Sarret G., Pairis S., and Bourguignon J. (2006) Localization and chemical forms of cadmium in plant samples by combining analytical electron microscopy and X-ray spectromicroscopy. *Spectrochimica Acta - Part B Atomic Spectroscopy* **61**, 1242-1252.

Janzen M. P., Nicholson R. V., and Scharer J. M. (2000) Pyrrhotite reaction kinetics: Reaction rates for oxidation by oxygen, ferric iron, and for nonoxidative dissolution. *Geochimica et Cosmochimica Acta* **64**, 1511-1522.

Johnson C. A. (1986) The regulation of trace element concentrations in river and estuarine waters contaminated with acid mine drainage: the adsorption of Cu and Zn on amorphous Fe oxyhydroxides. *Geochimica et Cosmochimica Acta* **50**, 2433-243.

Johnston R. B. and Singer P. C. (2007) Redox reactions in the Fe-As-O_2 system. *Chemosphere* **69**, 517-525.

Jönsson J., Persson P., Sjoberg S., and Lovren L. (2005) Schwertmannite precipitated from acid mine drainage: phase transformation, sulphate release and surface properties. *Applied Geochemistry* **20**, 179-191.

Kamei G. and Ohmoto H. (2000) The kinetics of reactions between pyrite and O-2-bearing water revealed from in situ monitoring of DO, Eh and pH in a closed system. *Geochimica et Cosmochimica Acta* **64**, 2585-2601.

Kawano M. and Tomita K. (2001) Geochemical modeling of bacterially induced mineralization of schwertmannite and jarosite in sulfuric acid spring water. *American Mineralogist* **86**, 1156-1165.

Khoe G. H., Brown P. L., and Sylva R. N. (1986) The hydrolysis of metal ions: Part 9. Iron (III) in perchloric, nitrate, and chloride media (1 mol dm^{-3}). *Journal of the Chemical Society, Dalton Transactions* **9,** 1901–1906.

Kirby C. S. and Elder Brady J. A. (1998) Field determination of Fe2+ oxidation rates in acid mine drainage using a continuously-stirred tank reactor. *Applied Geochemistry* **13**, 509-520.

Kläning U. K., Bielski B. H. J., and Sehested K. (1989) Arsenic(IV). A pulse-radiolysis study. *Inorganic Chemistry* **28**, 2717-2724.

Koslides T. and Ciminelli V. S. T. (1992) Pressure Oxidation of Arsenopyrite and Pyrite in Alkaline-Solutions. *Hydrometallurgy* **30**, 87-106.

Krause E. and Ettel V. A. (1988) Solubility and stability of scorodite, FeAsO4 2H2O: New data and further discussion. *American Mineralogist* **73**, 850-854.

Kupka D., Rzhepishevska O. I., Dopson M., Lindström E. B., Karnachuk O. V., and Tuovinen O. H. (2007) Bacterial oxidation of ferrous iron at low temperatures. *Biotechnology and Bioengineering* **97,** 1470-1478.

La Force M. J., Hansel C. M., and Fendorf S. (2000) Arsenic speciation, seasonal transformations and co-distribution with iron in a mine waste-influenced palustrine emergent wetland. *Environmental Science and Technology* **34**, 3937-3943.

Lasaga A. C. (1990) Atomic treatment of mineral-water surface reactions. In *Mineral-water interface geochemistry*, Vol. 23 (ed. Michael F. Hochella, Arthur F. White), pp. 17-85. Reviews in Mineralogy.

Lasaga A. C. (1998) *Kinetic Theory in the Earth Sciences.* Princeton University Press.

Lazareva E. V., Shuvaeva O. V., and Tsimbalist V. G. (2002) Arsenic speciation in the tailings impoundment of a gold recovery plant in Siberia. *Geochemistry: Exploration, Environment Analysis* **2**, 263-268.

Leblanc M., Achard B., Othman D. B., Luck J. M., Bertrand-Sarfati J., and Personneé J. C. (1996) Accumulation of arsenic from acidic mine waters by ferruginous bacterial accretions (stromatolites). *Applied Geochemistry* **11**, 541-554.

Leblanc M., Casiot C., Elbaz-Poulichet F., and Personné J. C. (2002) Arsenic removal by oxidizing bacteria in a heavily arsenic contaminated acid mine drainage system (Carnoulès, Francia). In *Mine Water Hydrogeology and Geochemistry*, pp. 267-275. Special Publication, Geological Society.

Lee J. S. and Chon H. T. (2006) Hydrochemical characteristics of acid mine drainage in the vicinity of an abandoned mine, Daduk Creek, Korea. *Journal of Geochemical Exploration* **88**, 37-40.

Lee P. K., Kang M. J., Choi S. H., and Touray J. C. (2005) Sulfide oxidation and the natural attenuation of arsenic and trace metals in the waste rocks of the abandoned Seobo tungsten mine, Korea. *Appied Geochemistry* **20**, 1687-1703.

Lehmann M., Zouboulis A. I., Matis K. A., and Grohmann A. (2005) Sorption of arsenic oxyanions from aqueous solution on goethite: study of process modelling. *Microchimica Acta* **151**, 269-275.

Leistel J. M., Marcoux E., Pascual E., Quesada C., Sanchez A., and Thieblemont D. (1998) The massive sulphide deposits of the Iberian Pyrite Belt. Review and preface to the special issue. *Mineralium Deposita* **33**, 2-30.

Lengke M. F. and Tempel R. N. (2002) Reaction rates of natural orpiment oxidation at 25 to 40 degrees C and pH 6.8 to 8.2 and comparison with amorphous As2S3 oxidation. *Geochimica et Cosmochimica Acta* **66**, 3281-3291.

Lengke M. F. and Tempel R. N. (2003) Natural realgar and amorphous AsS oxidation kinetics. *Geochimica et Cosmochimica Acta* **67**, 859-871.

Leonard P., Estrada Rendon C. M., Amara G., Rousey J. M., Tobin J. M., and Degorce-Dumas J. R. (1999) Natural attenuation study of the impact of acid mine drainage (AMD) in the site of Carnoulès. In *Biohydrometallurgy and the environment toward the*

minig of the 21st century (ed. R. Amils, and A. Ballester), pp. 587-594. Elsevier, Amsterdam. The Netherlands.

Leuz A.-K., Hug S. J., Wehrli B., and Johnson C. A. (2006) Iron-mediated oxidation of antimony(III) by oxygen and hydrogen peroxide compared to arsenic(III) oxidation. *Environmental Science and Technology* **40,** 2565-2571.

Levine I. N. (1978) *Physical Chemistry*. McGraw Hill, New York.

Liger E., Charlet L., and Van Cappellen P. (1999) Surface catalysis of uranium(VI) reduction by iron(II) . *Geochimica et Cosmochimica Acta* **63**, 2939-2955.

Lochmann J. and Pedlik M. (1995) Kinetic Anomalies of Dissolution of Sphalerite in Ferric Sulfate-Solution. *Hydrometallurgy* **37**, 89-96.

Lumsdon D. G. and Evans L. J. (1994) Surface complexation model parameters for goethite (α-FeOOH). *Journal of Colloid and Interface Science* **164**, 119-125.

Lumsdon D. G., Meeussen J. C. L., Paterson E., Garden L. M., and Anderson P. (2001) Use of solid phase characterisation and chemical modelling for assessing the behaviour of arsenic in contaminated soils. *Applied Geochemistry* **16**, 571-581.

Malinowski E. R. (1991) Factor analysis in chemistry. 2nd ed: John Willey.

Malmström M. E. and Collin C. (2004) Sphalerite weathering kinetics: effect of ph and particle size. *Proc. 11th Symp. Water-Rock Interaction*, 849-852.

Manaka M., Kawasaki M., and Honda A. (2000) Measurements of the effective diffusion coefficient of dissolved oxygen and oxidation rate of pyrite by dissolved oxygen in compacted sodium bentonite. *Nuclear Technology* **130**, 206-217.

Manaka M. (2007) Comparison of rate laws for the oxidation of five pyrites by dissolved oxygen in acidic solution. *Journal of Mineralogical and Petrological Sciences* **102**, 24-38.

Manning B. A. and Goldberg S. (1996) Modeling competitive adsorption of arsenate with phosphate and molybdate on oxide minerals. *Soil Science Society of America* **60**, 121-131.

Manning B. A., Hunt M. L., Amrhein C., and Yarmoff J. A. (2002) Arsenic(III) and arsenic(V) reactions with zerovalent iron corrosion products. *Environmental Science and Technology* **36**, 5455-5461.

Mathews C. T. and Robins R. G. (1972) The oxidation of iron disulphide by ferric sulphate. *Australian Chemical Engineering* **13,** 21-25.

Mathews C. T. and Robins R. G. (1974) Oxidation of iron disulfide by molecular oxygen. *Australian Chemical Engineering* **15**, 19-24.

Matis K. A., Zouboulis F. B., Malamas M. D., Ramos Alfonso M. D., and Hudson M. J. (1997) Flotation removal of As(V) onto goethite. *Environmental Pollution* **97**, 239-245.

McCleskey R. B., Nordstrom D. K., and Ball J. W. (2003) Metal interferences and their removal prior to the determination of As(T) and As(III) in acid mine waters by hydride generation atomic absorption spectrometry In *Water-resources investigations report; 2003-4117.*

McCleskey R. B., Nordstrom D. K., and Maest A. S. (2004) Preservation of water samples for arsenic(III/V) determinations: an evaluation of the literature and new analytical results. *Applied Geochemistry* **19**, 995-1009.

McGuire M. M., Banfield J. F., and Hamers R. J. (2001) Quantitative determination of elemental sulfur at the arsenopyrite surface after oxidation by ferric iron: mechanistic implications. *Geochemical Transactions* **2**, 25-29.

McKibben M. A. (1984) Kinetics of aqueous oxidation of pyrite by ferric ion, oxygen and hydrogen peroxide from pH 1-4 and 20-40ºC. Ph.D. Thesis., Pennsylvania State University, U.S.A.

McKibben M. A. and Barnes H. L. (1986) Oxidation of Pyrite in Low-Temperature Acidic Solutions - Rate Laws and Surface Textures. *Geochimica et Cosmochimica Acta* **50**, 1509-1520.

McKibben M. A., Tallant B. A., and del Angel J. K. (2008) Kinetics of inorganic arsenopyrite oxidation in acidic aqueous solutions. *Applied Geochemistry* **23**, 121-135.

McKnight D. M. and Bencala K. E. (1989) Reactive iron transport in an acidic mountain stream in Summit County, Colorado: A hydrologic perspective. *Geochimica et Cosmochimica Acta* **53,** 2225-2234.

McKnight D. M., Kimball B. A., and Bencala K. E. (1988) Iron photoreduction and oxidation in an acidic mountain stream. *Science* **240 (4852),** 637-640.

Metz V. and Ganor J. (2001) Stirring effect on kaolinite dissolution rate. *Geochimica et Cosmochimica Acta* **65**, 3475–3490.

Mikhlin Y. L., Romanchenko A. S., and Asanov I. P. (2006) Oxidation of arsenopyrite and deposition of gold on the oxidized surfaces: A scanning probe microscopy, tunneling spectroscopy and XPS study. *Geochimica et Cosmochimica Acta* **70**, 4874-4888.

Molson J., Aubertin M., Bussière B., and Benzaazoua M. (2008) Geochemical transport modelling of drainage from experimental mine tailings cells covered by capillary barriers. *Applied Geochemistry* **23,** 1-24.

Moncur M. C., Ptacek C. J., Blowes D. W., and Jambor J. L. (2005) Release, transport and attenuation of metals from an old tailings impoundment. *Applied Geochemistry* **20**, 639-659.

Moses C. O. and Herman J. S. (1991) Pyrite Oxidation at Circumneutral pH. *Geochimica et Cosmochimica Acta* **55**, 471-482.

Mycroft J. R., Bancroft G. M., McIntyre N. S., Lorimer J. W., and Hill I. R. (1990) Detection of Sulfur and Polysulfides on Electrochemically Oxidized Pyrite Surfaces by X-Ray Photoelectron-Spectroscopy and Raman-Spectroscopy. *Journal of Electroanalytical Chemistry* **292**, 139-152.

Nakazawa H. and Hareyama W. (2007) Biological oxidation of arsenite in strong acid water. *Resources Processing* **54**, 182-186.

Nesbitt H. W. and Muir I. J. (1994) X-Ray Photoelectron Spectroscopic Study of a Pristine Pyrite Surface Reacted with Water-Vapor and Air. *Geochimica et Cosmochimica Acta* **58**, 4667-4679.

Nesbitt H. W. and Muir I. J. (1998) Oxidation states and speciation of secondary products on pyrite and arsenopyrite reacted with mine waste waters and air. *Mineralogy and Petrology* **62**, 123-144.

Nesbitt H. W., Muir L. J., and Pratt A. R. (1995) Oxidation of Arsenopyrite by Air and Air-Saturated, Distilled Water, and Implications for Mechanism of Oxidation. *Geochimica et Cosmochimica Acta* **59**, 1773-1786.

Nicholson R. V., Gilham R. V., and Reardon E. J. (1988) Pyrite oxidation in carbonate-buffered solutions:1. experimental kinetics. *Geochimica et Cosmochimica Acta* **52**, 1077-1085.

Nicholson R. V., Gilham R. V., and Reardon E. J. (1990) Pyrite oxidation in carbonate-buffered solutions: 2. rate control by oxide coatings. *Geochimica et Cosmochimica Acta* **54**, 395-402.

Nieto J. M., Sarmiento A. M., Olías M., Canovas C. R., Riba I., Kalman J., and Delvalls T. A. (2007) Acid mine drainage polluiton in the Tinto and Odiel rivers (Iberian Pyritic Belt, SW Spain) and bioavailability of the transported metals to Huelva Estuary. *Environment International* **33**, 445-455.

Noike T., Nakamura K., and Matsumoto J. I. (1983) Oxidation of Ferrous Iron by Acidophilic Iron-Oxidizing Bacteria from a Stream Receiving Acid-Mine Drainage. *Water Research* **17**, 21-27.

Nordstrom D. K. (1985) The rate of ferrous iron oxidation in a stream receiving acid mine effluent. In *Selected papers in hydrologic sciences*, pp. 113-119. USGS Water Supply Paper 2270.

Nordstrom D. K. (2000) Aqueous Redox Chemistry and the Behaviour of Iron in Acid Mine Waters. In Proceedings of the 18 Workshop on Monitoring Oxidation-Reduction Processes for Groundwater Restoration. (ed. R.T., Wilkin, R.D., Ludwig and R.G., Ford), pp. 43–47. Environmental Protection Agency, EPA /600/R-02/002.

Nordstrom D. K. (2002) Worldwide occurences of arsenic in ground water. *Science* **296**, 2143+2145.

Nordstrom D. K. (2003) Effects of microbiological and geochemical interactions in mine drainage. In *Environmental aspects of mine wastes.*, Vol. 31 (ed. J. L. Jambor, D.W. Blowes, A.I.M. Ritchie). Mineral. Assoc. Can. Short Course.

Nordstrom D. K. and Alpers C. N. (1999) Negative pH, efflorescent mineralogy, and consequences for environmental restoration at the Iron Mountain Superfund site, California. *Proceedings of the National Academy of Sciences of the United States of America* **96**, 3455–3462.

Nordstrom D. K. and Southam G. (1997) Geomicrobiology of sulfide mineral oxidation. In *Geomicrobiology: Interactions between microbes and minerals*, Vol. 35 (ed. J.F. Banfield and K.H. Nealson), pp. 361-390. Reviews in Mineralogy.

Olías M., Nieto J. M., Sarmiento A. M., Cerón J. C., and Cánovas C. R. (2004) Seasonal water quality variations in a river affected by acid mine drainage: The Odiel River (South West Spain). *Science of the Total Environment* **333**, 267-281.

Oliveira V., Sarmiento A. M., Gómez-Ariza J. L., Nieto J. M., and Sánchez-Rodas D. (2006) New preservation method for inorganic arsenic speciation in acid mine drainage samples. *Talanta* **69**, 1182-1189.

Paktunc D. and Dutrizac J. E. (2003) Characterization of arsenate-for-sulfate substitution in synthetic jarosite using X-ray diffraction and X-ray absorption spectroscopy. *Canadian Mineralogist* **41,** 905-919.

Paktunc D., Foster A., and Laflamme G. (2003) Speciation and characterization of arsenic in Ketza River mine tailings using x-ray absorption spectroscopy. *Environmental Science and Technology* **37,** 2067-2074.

Parkhurst D. L. and Appelo C. A. J. (1999) User's Guide to PHREEQC (Version 2), a computer program for speciation, batch reaction, one-dimensional transport, and inverse geochemical calculations. In *Water Resources Research Investigations Report 99-4259*, pp. 312.

Parks G. A. (1990) Surface Energy and Adsorption at Mineral/Water Interfaces: An Introduction In Mineral-water interface geochemistry, Vol. 23 (ed. Michael F. Hochella, Arthur F. White), pp. 133-175. Reviews in Mineralogy.

Peine A., Tritschler A., Küsel K., and Peiffer S. (2000) Electron flow in an iron-rich acidic sediment - evidence for an acidity-driven iron cycle. *Limnology and Oceanography* **45**, 1077-1087.

Pérez-López R., Cama J., Nieto J. M., and Ayora C. (2007) The iron-coating role on the oxidation kinetics of a pyritic sludge doped with fly ash. *Geochimica et Cosmochimica Acta* **71**, 1921-1934.

Peters S. C., Blum J. D., Klaue B., and Karagas M. R. (1999) Arsenic occurrence in New Hampshire drinking water. *Environmental Science and Technology* **33,** 1328-1333.

Pfeifer H. R., Häussermann A., Lavanchy J. C., and Halter W. (2007) Distribution and behavior of arsenic in soils and waters in the vicinity of the former gold-arsenic mine of Salanfe, Western Switzerland. *Journal of Geochemical Exploration* **93**, 121-134.

Plumlee G. S., Smith K. S., Montour M. R., Ficklin W. H., and Mosier E. L. (1999) Geologic controls on the composition of natural waters and mine waters draining diverse mineral-deposit types. In *The Environmental Geochemistry of Mineral Deposits, Part B: Case Studies and Research Topics,* Vol. 6B. Society of Economic Geologists (ed. Filipek, L.H. and Plumlee, G.S.), pp. 381–402. Inc.

Pratt A. R., Nesbitt H. W., and Muir I. J. (1994) Generation of Acids from Mine Waste - Oxidative Leaching of Pyrrhotite in Dilute H_2SO_4 Solutions at pH 3.0. *Geochimica et Cosmochimica Acta* **58**, 5147-5159.

Pratt A. R., McIntyre N. S., and Splinter S. J. (1998) Deconvolution of pyrite marcasite and arsenopyrite XPS spectra using the maximum entropy method. *Surface Science* **396**, 266-272.

Prior H. L. and Williams G. A. (1996) Some mines and minerals of Morgan County, Missouri. *Rocks and Minerals* **71**, 102.

Querol X., Alastuey A., Lopez-Soler A., Mantilla E., and Plana F. (1996) Mineral composition of atmospheric particulates around a large coal-fired power station. *Atmospheric Environment* **30**, 3557-3572.

Regenspurg S. and Peiffer S. (2005) Arsenate and chromate incorporation in schwertmannite. *Applied Geochemistry* **20**, 1226-1239.

Regenspurg S., Brand A., and Peiffer S. (2004) Formation and stability of schwertmannite in acidic mining lakes. *Geochimica et Cosmochimica Acta* **68**, 1185–1197.

Ressler T. (1998) WinXAS: A program for X-ray absorption spectroscopy data analysis under MS-Windows. *Journal of Synchrotron Radiation* **5,** 118-122.

Ressler T., Wong J., Roos J., and Smith I. L. (2000) Quantitative speciation of Mn-bearing particulates emitted from autos burning (methylcyclopentadienyl)manganese tricarbonyl-added gasolines using XANES spectroscopy. *Environmental Science and Technology* **34**, 950-958.

Richardson S. and Vaughan D. J. (1989) Arsenopyrite - a Spectroscopic Investigation of Altered Surfaces. *Mineralogical Magazine* **53**, 223-229.

Rimstidt J. D. and Vaughan D. J. (2003) Pyrite oxidation: A state-of-the-art assessment of the reaction mechanism. *Geochimica et Cosmochimica Acta* **67**, 873-880.

Rinker M. J., Nesbitt H. W., and Pratt A. R. (1997) Marcasite oxidation in low-temperature acidic (pH 3.0) solutions: Mechanism and rate laws. *American Mineralogist* **82**, 900-912.

Roberts L. C., Hug S. J., Ruettimann T., Billah M., Khan A. W., and Rahman M. T. (2004) Arsenic Removal with Iron(II) and Iron(III) in Waters with High Silicate and Phosphate Concentrations. *Environmental Science and Technology* **38**, 307-315.

Robins R. G. (1967) Hydrothermal precipitation in solutions of thorium nitrate, ferric nitrate and aluminium nitrate. *Journal of inorganic and Nuclear Chemistry* **29**, 431-435.

Román-Ross G., Pérez-Lopez R., Ayora C., Fernández A., Bardelli F., and Cuello G. J. (2009) Arsenic fate during Schwertmannite transformation: an EXAFS approach. *In preparation*.

Rosman T. G., Uddin A. N., and Burns F. J. (2004) Evidence that arsenic acts as a carcinogen in skin cancer. *Toxicology and Applied Pharmacology* **198**, 394-404.

Ruitenberg R., Hansford G. S., Reuter M. A., and Breed A. W. (1999) The ferric leaching kinetics of arsenopyrite. *Hydrometallurgy* **52**, 37-53.

Sáez R., Pascual E., Toscano M., and Almodovar G. R. (1999) The Iberian type of volcanosedimentary massive sulphide deposits. *Mineralium Deposita* **34**, 549–570.

Salzsauler K. A., Sidenko N. V., and Sherriff B. L. (2005) Arsenic mobility in alteration products of sulfide-rich, arsenopyrite-bearing mine wastes, snow lake, manitoba, Canada. *Applied Geochemistry* **20**, 2303-2314.

Sánchez-España J. S., López E., Santofimia E., Reyes J., and Martín J. A. (2005a) The natural attenuation of two acidic effluents in Tharsis and La Zarza-Perrunal mines (Iberian Pyritic Belt, Huelva, Spain). *Environmental Geology* **49**, 253-266.

Sánchez-España J., Pamo E. L., Santofimia E., Aduvire O., Reyes J., and Barettino D. (2005b) Acid mine drainage in the Iberian Pyrite Belt (Odiel river watershed, Huelva, SW Spain): Geochemistry, mineralogy and environmental implications. *Applied Geochemistry* **20**, 1320-1356.

Sánchez-España J., López Pamo E., and Santofimia Pastor E. (2007) The oxidation of ferrous iron in acidic mine effluents from the Iberian Pyrite Belt (Odiel Basin, Huelva, Spain): Field and laboratory rates. *Journal of Geochemical Exploration* **92**, 120-132.

Sánchez-Rodas D., Gomez-Ariza J. L., Giraldez I., Velasco A., and Morales E. (2005) Arsenic speciation in river and estuarine waters from southwest Spain. *Science of the Total Environment* **345**, 207-217.

Santini J. M., Sly L. I., Wen A., Comrie D., De Wulf-Durand P., and Macy J. M. (2002) New arsenite-oxidizing bacteria isolated from Australian gold mining environments - Phylogenetic relationships. *Geomicrobiology Journal* **19,** 67-76.

Sarmiento A. M. (2007) Estudio de la contaminación por drenajes ácidos de mina de las aguas superficiales en la cuenca del río Odiel (SO España), Huelva. Ph.D. Thesis, Huelva University, Spain.

Sarmiento A. M., Casiot C., Nieto J. M., Elbaz-Poulichet F., and Olias M. (2005) Seasonal variations in Fe and As speciation and mobility in waters affected by acid mine drainage in the Odiel river basin (Huelva, Spain). *Geogaceta* **37**, 115-118.

Sarmiento A. M., Nieto J. M., Olias M., and Canovas C. R. (2006) Pollution of a river basin impacted by acid mine drainage in the Iberian Pyrite Belt (SW Spain). *Proceedings of the 7th International Conference on Acid Rock Drainage (ICARD)*, St. Louis, MO.

Sarmiento A. M., Oliveira V., Gómez-Ariza J. L., Nieto J. M., and Sánchez-Rodas D. (2007) Diel cycles of arsenic speciation due to photooxidation in acid mine drainage from the iberian pyrite belt (sw spain). *Chemosphere* **66**, 677-683.

Sarmiento A. M., Nieto J. M., Casiot C., Elbaz-Poulichet F., and Egal M. (2009) Inorganic arsenic speciation at river basin scales: The Tinto and Odiel Rivers in the Iberian Pyrite Belt, SW Spain. *Environmental Pollution*, **doi: 10.1016/j.envpol.2008.12.002**, **in press**.

Savage K. M., Tingle T. N., O'Day P. A., Waychunas G. A., and Bird D. K. (2000) Arsenic speciation in pyrite and secondary weathering phases, Mother Lode Gold District, Tulomne County, California. *Applied Geochemistry* **15**, 1219-1244.

Savage K. M., Bird D. K., and O'Day P. A. (2005) Arsenic speciation in synthetic jarosite. *Chemical Geology* **215**, 473-498.

Schaufuss A. G., Nesbitt H. W., Scaini M. J., Hoechst H., Bancroft M. G., and Szargan R. (2000) Reactivity of surface sites on fractured arsenopyrite (FeAsS) toward oxygen. *American Mineralogist* **85**, 1754-1766.

Schecher W. D. and McAvoy D. C. (1998) MINEQL+, V. 4.5, Users Manual, Hallowell, ME.

Schreiber M. E., Simo J. A., and Freiberg P. G. (2000) Stratigraphic and geochemical controls on naturally occurring arsenic in groundwater, eastern Wisconsin, USA. *Hydrogeology Journal* **8**, 161-176.

Schrenk M. O., Edwards K. J., Goodman R. M., Hamers R. J., and Banfield J. F. (1998) Distribution of Thiobacillus Ferrooxidans and Leptospirillum ferrooxidans: Implications for generation of acid mine drainage. *Science* **279**, 1519-1522.

Schwertmann U. and Cornell R. M. (1991) *Iron oxides in the Laboratory*.

Schwertmann U. and Murad E. (1983) The effect of pH on the formation of goethite and hematite from ferrihydrite. *Clays and Clay Minerals* **31**, 277-284.

Sherman D. M. and Randall S. R. (2003) Surface complexation of arsenic(V) to iron(III) (hydr)oxides: Structural mechanism from ab initio molecular geometries and EXAFS spectroscopy. *Geochimica et Cosmochimica Acta* **67**, 4223-4230.

Silverman M. P. and Lundgren D. G. (1959) Studies on the Chemoautotrophic Iron Bacterium Ferrobacillus-Ferrooxidans .1. An Improved Medium and a Harvesting Procedure for Securing High Cell Yields. *Journal of Bacteriology* **77**, 642-647.

Singer P. C. and Stumm W. (1968) Kinetics of the oxidation of ferrous iron. *Proceedings of the Second Symposium on Coal Mine Drainage Research.*

Singer P. C. and Stumm W. (1970) Acidic mine drainage: the rate-limiting step. *Science* **167**, 1121-1123.

Slowey A. J., Johnson S. B., Newville M., and Brown Jr. G. E. (2007) Speciation and colloid transport of arsenic from mine tailings. *Applied Geochemistry* **22,** 1884-1898.

Smedley P. L. and Kinniburgh D. G. (2002) A review of the source, behaviour and distribution of arsenic in natural waters. *Applied Geochemistry* **17**, 517-568.

Smedley P. L., Edmunds W. M., and Pelig-Ba K. B. (1996) Mobility of arsenic in groundwater in the Obuasi gold-mining area of Ghana: Some implications for human health. *Special Publications of the Geological Society of London* **113**, 163-181.

Smedley P. L., Knudsen J., and Maiga D. (2007) Arsenic in groundwater from mineralized Proterozoic basement rocks of Burkina Faso. *Applied Geochemistry* **22**, 1074-1092.

Smith E. E. and Schumate K. S. (1970) *Sulfide to sulfate reaction mechanism.* Federal Water Quality Administration.

Smith K. S. (1999) Metal sorption on mineral surfaces: an overview with examples relating to mineral deposits. In *The environmental geochemistry of mineral deposits, Part A. Processes, Techniques, and Health Issues*: Society of Economic Geologists, Vol. Rev Econ Geol 6A (ed. Plumlee GS, M.J. Losdon), pp. 161-182.

Sondi I., Shi I., and Matijevic E. (2001) Precipitation of monodispersed basic iron(III) sulfate (sodium jarosite) particles. *Colloid and Polymer Science* **279**, 161-165.

Stollenwerk K. G., Breit G. N., Welch A. H., Yount J. C., Whitney J. W., Foster A. L., Uddin M. N., Majumder R. K., and Ahmed N. (2007) Arsenic attenuation by oxidized aquifer sediments in Bangladesh. *Science of the Total Environment* **379**, 133-150.

Stookey L. L. (1970) Ferrozine - A new spectrophotometric reagent for iron. *Analytical Chemistry* **42,** 779-781.

Strawn D., Doner H., Zavarin M., and McHugo S. (2002) Microscale investigation into the geochemistry of arsenic, selenium, and iron in soil developed in pyritic shale materials. *Geoderma* **108**, 237-257.

Strömberg B. and Banwart S. (1994) Kinetic modelling of geochemical reactions at the Aitik mining waste rock site in northern Sweden. *Applied Geochemistry* **9**, 583-595.

Stumm W. (1987) *Aquatic surface chemistry*. John Willey, New York.

Stumm W. (1992) *Chemistry of the Soil-Water interaction*. Wiley and Sons, New York.

Stumm W. and Morgan J. J. (1996) *Aquatic Chemistry, Chemical Equilibria and Rates in Natural Waters*. John Wiley & Sons, Inc., New York, 1022p.

Stumm W. and Sulzberger B. (1992) The cycling of iron in natural environments: considerations based on laboratory studies of heterogeneous redox processes. *Geochimica et Cosmochimica Acta* **56**, 3233-3257.

Tallant B. A. and McKibben M. A. (2005) Arsenic mineral kinetics: Arsenopyrite oxidation. *Geochimica et Cosmochimica Acta* **69**, A820-A820.

Tallman D. E. and Shaikh A. U. (1980) Redox stability of inorganic arsenic(III) and arsenic(V) in aqueous solution. *Analytical Chemistry* **52**, 196-199.

To T., Nordstrom K. D., Cunningham K., Ball J., and McCleskey B. (1999) New method for the direct determination of dissolved Fe(III) concentration in acid mine waters. *Environmental Science Technology* **33**, 807-813.

Tomioka Y. (2006) Dissolution mechanisms of arsenopyrite and removal of extracted arsenic by co-existing minerals. *Proceedings of the 19th International Meeting of the International Mineralogical Association*, 77-78.

Tonkin J. W., Balistrieri L. S., and Murray J. W. (2002) Modeling metal removal onto natural particles formed during mixing of acid rock drainage with ambient surface water. *Environmental Science Technology* **36**, 484-492.

Uhlig I., Szargan R., Nesbitt H. W., and Laajalehto K. (2001) Surface states and reactivity of pyrite and marcasite. *Applied Surface Science* **179**, 222-229.

Verplanck P. L., Mueller S. H., Goldfarb R. J., and Nordstrom D. K. (2007) Elevated arsenic in ground water, Ester dome (Alaska). *Proceedings IMWA Symposium 2007: Water in Mining Environments*, 473-477.

Vilanó M., Padró A., and Rubio R. (2000) Coupled techniques based on liquid chromatography and atomic fluorescence detection for arsenic speciation. *Analytica Chimica Acta* **411**, 71-79.

Wakao N., Koyatsu H., Komai Y., Shimokawara H., Sakurai Y., and Shiota H. (1988) Microbial Oxidation of Arsenite and Occurrence of Arsenite-Oxidizing Bacteria in Acid-Mine Water from a Sulfur-Pyrite Mine. *Geomicrobiology Journal* **6**, 11-24.

Walker F. P., Schreiber M. E., and Rimstidt J. D. (2006) Kinetics of arsenopyrite oxidative dissolution by oxygen. *Geochimica et Cosmochimica Acta* **70**, 1668-1676.

Waltham C. A. and Eick M. J. (2002) Kinetics of arsenic adsorption on goethite in the presence of sorbed silicic acid. *Soil Science Society of America* **66**, 812-825.

Wang H., Bigham J. M., and Tuovinen O. H. (2006) Formation of schwertmannite and its transformation to jarosite in the presence of acidophilic iron-oxidizing microorganisms. *Materials Science and Engineering C* **26**, 588-592.

Waychunas G. A., Rea B. A., Fuller C. C., and Davis J. A. (1993) Surface-chemistry of ferrihydrite 1. EXAFS studies of the geometry of coprecipitated and adsorbed arsenate. *Geochimica et Cosmochimica Acta* **57**, 2251-2269.

Webster J. G., Swedlund P. J., and Webster K. S. (1998) Trace metal adsorption onto an acid mine drainage iron (III) oxy hydroxy sulfate. *Environmental Science and Technology* **32**, 1361-1368.

Weisener C. G., Smart R. S. C., and Gerson A. R. (2003) Kinetics and mechanisms of the leaching of low Fe sphalerite. *Geochimica et Cosmochimica Acta* **67**, 823-830.

Weisener C. G., Smart R. S. C., and Gerson A. R. (2004) A comparison of the kinetics and mechanism of acid leaching of sphalerite containing low and high concentrations of iron. *International Journal of Mineral Processing* **74**, 239-249.

Welch A. H. and Lico M. S. (1998) Arsenic in groundwater of the Western United States. *Ground Water* **26**, 333-347.

Welch A. H. and Stollenwerk K. G. E. (2003) *Arsenic in Ground Water: Geochemistry and Occurrence.* Kluwer Academic Publishers.

Wells D. J. (1991) Extraction of the perrhenate and pertechnetate solutions from aqueous solutions using inorganic ion exchangers, Reading University, UK.

Wen C. Y. (1968) Noncatalytic solid-fluid reaction models. *Industrial and Engineering Chemistry Research* **60**, 34-54.

WHO (2004). *Guidelines for drinking water quality*. Volume 1: Recommendations, 3rd ed. World Health Organization. Geneva, Switzerland.

Wiersma C. L. (1982) Relative rates of reaction of pyrite and marcasite with ferric iron at low pH. Virginia Polytechnic Institute and State University.

Wiersma C. L. and Rimstidt J. D. (1984) Rates of Reaction of Pyrite and Marcasite with Ferric Iron at Ph-2. *Geochimica et Cosmochimica Acta* **48**, 85-92.

Wilke C. R. and Chang P. (1955) Correlation of diffusion coefficients in dilute solutions. *AIChE Journal* **1**, 264-270.

Wilkie J. A. and Hering J. G. (1996) Adsorption of arsenic onto hydrous ferric oxide: Effects of adsorbate/adsorbent ratios and co-occurring solutes. *Colloids and Surfaces a-Physicochemical and Engineering Aspects* **107**, 97-110.

Wilkie J. A. and Hering J. G. (1998) Rapid oxidation of geothermal arsenic(III) in streamwaters of the eastern Sierra Nevada. *Environmental Science Technology* **32**, 657-662.

Williams M. (2001) Arsenic in mine waters: an international study. *Environmental Geology* **40**, 267-278.

Williamson M. A. and Rimstidt J. D. (1994) The Kinetics and Electrochemical Rate-Determining Step of Aqueous Pyrite Oxidation. *Geochimica et Cosmochimica Acta* **58**, 5443-5454.

Wong J., Lytle F. W., Messmer R. P., and Maylotte D. H. (1984) K-edge absorption spectra of selected vanadium compounds. *Physical Review B* **30**, 5596 - 5610.

Younger P. L. (1997) The longevity of minewater pollution: A basis for decision-making. *Science of the Total Environment* **194**, 457-466.

Yu J. Y., Heo B., Choi I. K., Cho J. P., and Chang H. W. (1999) Apparent solubilities of schwertmannite and ferrihydrite in natural stream waters polluted by mine drainage. *Geochimica et Cosmochimica Acta* **63**, 3407-3416.

Yu Y. M., Zhu Y. X., Williams-Jones A. E., Gao Z. M., and Li D. X. (2004) A kinetic study of the oxidation of arsenopyrite in acidic solutions: implications for the environment. *Applied Geochemistry* **19**, 435-444.

Yu Y. M., Zhu Y., Gao Z., Gammons C. H., and Li D. (2007) Rates of arsenopyrite oxidation by oxygen and Fe(III) at pH 1.8-12.6 and 15-45 ºC. *Environmental Science Technology* **41**, 6460-6464.

Appendix:

Experimental data from the flow-through experiments

Table A.1: Experimental data from the flow-through experiments presented in this thesis. Time periods in bold letters correspond to the considered steady-state (n.a.: not analyzed; b.d.l.: below detection limit).

Sample	Time (h)	flow rate (mL min^{-1})	As	S $\mu mol\ L^{-1}$	Fe
ASP-25-1-1	0	0.040	61.24	95678	122.36
ASP-25-1-2	20	0.042	17.79	97362	52.07
ASP-25-1-3	96	0.043	9.28	96738	35.63
ASP-25-1-4	119	0.043	9.75	97424	31.72
ASP-25-1-5	144	0.043	11.13	97112	33.05
ASP-25-1-6	187	0.043	20.27	97549	36.03
ASP-25-1-7	264	0.043	37.88	97861	45.62
ASP-25-1-8	288	0.043	39.05	98110	45.23
ASP-25-1-9	311	0.043	47.44	97923	53.18
ASP-25-1-10	336	0.043	30.59	98609	34.84
ASP-25-1-11	358	0.043	29.47	98235	34.50
ASP-25-1-12	432	0.044	25.11	98796	28.58
ASP-25-1-13	456	0.044	32.86	97424	38.07
ASP-25-1-14	479	0.045	33.29	97923	38.64
ASP-25-1-15	504	0.045	30.97	97985	36.13
ASP-25-1-16	526	0.033	30.97	97486	36.49
ASP-25-1-17	600	0.042	66.10	98983	72.01
ASP-25-1-18	623	0.046	41.67	98859	48.45
ASP-25-1-19	646	0.046	26.20	99857	29.77
ASP-25-1-20	672	0.048	34.46	99170	39.61
ASP-25-1-21	692	0.047	32.89	99732	37.31
ASP-25-1-22	767	0.048	30.91	100293	35.48
ASP-25-1-23	792	0.049	31.50	99358	35.19
ASP-25-1-24	816	0.050	30.54	100231	34.59
ASP-25-1-25	840	0.048	31.66	100418	35.79
ASP-25-1-26	862	0.038	35.42	99545	39.89
ASP-25-1-27	936	0.038	33.08	100356	36.38
ASP-25-1-28	**959**	0.038	30.75	100667	34.12
ASP-25-1-29	**983**	0.038	31.42	101042	36.03
ASP-25-1-30	**1007**	0.039	32.06	100106	35.81
ASP-25-1-31	**1031**	0.039	27.31	98983	30.24
ASP-25-1-32	**1100**	0.039	28.59	100231	31.95
ASP-25-1-33	**1125**	0.040	29.36	98983	32.29
ASP-25-1-34	**1148**	0.039	31.82	100605	35.74
ASP-25-1-35	**1176**	0.040	31.82	100543	35.39
ASP-25-1-36	**1198**	0.040	27.39	99919	30.93

Table A.2: Experimental data from the flow-through experiments presented in this thesis. Time periods in bold letters correspond to the considered steady-state (n.a.: not analyzed; b.d.l.: below detection limit).

.

Sample	Time (h)	flow rate (mL min^{-1})	As	S $\mu mol\ L^{-1}$	Fe
ASP-25-2-1	0	0.040	29.77	970	40.86
ASP-25-2-2	20	0.042	14.05	970	14.05
ASP-25-2-3	96	0.043	9.59	954	7.40
ASP-25-2-4	119	0.043	6.76	968	4.58
ASP-25-2-5	144	0.043	5.29	971	3.91
ASP-25-2-6	187	0.043	5.31	975	5.01
ASP-25-2-7	264	0.043	7.82	990	12.15
ASP-25-2-8	288	0.043	10.08	974	19.84
ASP-25-2-9	311	0.043	14.18	981	32.46
ASP-25-2-10	336	0.043	12.31	970	28.95
ASP-25-2-11	358	0.043	13.30	968	32.82
ASP-25-2-12	432	0.044	17.11	993	40.36
ASP-25-2-13	456	0.044	17.57	1012	40.72
ASP-25-2-14	479	0.045	20.50	1000	43.92
ASP-25-2-15	504	0.045	30.39	1008	47.97
ASP-25-2-16	526	0.033	39.12	995	43.46
ASP-25-2-17	600	0.042	36.87	1000	39.07
ASP-25-2-18	623	0.046	39.26	1004	41.50
ASP-25-2-19	**646**	0.046	30.94	952	33.57
ASP-25-2-20	**672**	0.048	36.23	977	40.41
ASP-25-2-21	**692**	0.047	35.30	952	39.12
ASP-25-2-22	**767**	0.048	34.45	968	38.48
ASP-25-2-23	**792**	0.049	33.66	972	36.85
ASP-25-2-24	**816**	0.050	33.17	948	36.42
ASP-25-2-25	**840**	0.048	35.14	961	39.09

Table A.3: Experimental data from the flow-through experiments presented in this thesis. Time periods in bold letters correspond to the considered steady-state(n.a.: not analyzed; b.d.l.: below detection limit).

Sample	Time (h)	flow rate (mL min^{-1})	As	S $\mu mol\ L^{-1}$	Fe
ASP-25-3-1	0	0.016	81.27	51.24	156.38
ASP-25-3-2	47	0.036	36.84	24.61	88.61
ASP-25-3-3	73	0.036	24.21	20.59	63.72
ASP-25-3-4	96	0.028	17.79	15.24	50.81
ASP-25-3-5	168	0.037	11.20	10.00	30.06
ASP-25-3-6	192	0.037	10.04	8.38	26.30
ASP-25-3-7	216	0.037	11.64	8.12	28.00
ASP-25-3-8	240	0.038	16.88	9.11	38.30
ASP-25-3-9	262	0.038	21.85	10.34	35.51
ASP-25-3-10	337	0.038	33.66	15.29	41.56
ASP-25-3-11	357	0.037	76.53	22.48	89.78
ASP-25-3-12	385	0.037	56.49	15.96	60.32
ASP-25-3-13	408	0.037	67.23	22.52	74.32
ASP-25-3-14	432	0.037	53.16	18.15	59.14
ASP-25-3-15	504	0.037	58.72	23.78	65.23
ASP-25-3-16	527	0.037	53.34	24.34	58.76
ASP-25-3-17	552	0.037	52.02	21.15	56.67
ASP-25-3-18	577	0.037	50.56	22.48	55.49
ASP-25-3-19	600	0.037	48.28	19.08	52.52
ASP-25-3-20	672	0.037	46.69	18.52	51.26
ASP-25-3-21	696	0.037	41.63	20.95	46.55
ASP-25-3-23	744	0.037	39.26	18.80	43.56
ASP-25-3-25	839	0.037	38.83	19.97	43.13
ASP-25-3-27	887	0.037	37.28	18.66	41.27
ASP-25-3-29	**1006**	0.037	36.76	20.06	40.39
ASP-25-3-31	**1055**	0.037	34.45	17.87	37.80
ASP-25-3-33	**1103**	0.037	34.77	18.47	38.14
ASP-25-3-35	**1200**	0.038	32.92	17.57	35.95
ASP-25-3-37	**1247**	0.038	33.61	17.87	36.47

Table A.4: Experimental data from the flow-through experiments presented in this thesis. Time periods in bold letters correspond to the considered steady-state (n.a.: not analyzed; b.d.l.: below detection limit).

Sample	Time (h)	flow rate (mL min^{-1})	As	S $\mu mol\ L^{-1}$	Fe
ASP-25-4-1	0	0.032	33.61	86.17	17.52
ASP-25-4-2	24	0.033	49.04	69.23	27.54
ASP-25-4-3	47	0.033	63.12	58.82	69.58
ASP-25-4-4	72	0.034	63.97	45.72	81.25
ASP-25-4-5	96	0.034	55.79	38.30	73.79
ASP-25-4-6	168	0.034	49.07	34.24	62.92
ASP-25-4-7	192	0.034	44.55	33.77	56.54
ASP-25-4-8	216	0.034	44.45	31.47	56.31
ASP-25-4-9	240	0.034	47.58	33.24	59.66
ASP-25-4-10	262	0.034	46.69	30.51	56.11
ASP-25-4-11	336	0.034	45.21	29.00	53.00
ASP-25-4-12	357	0.034	22.08	22.55	n.a.
ASP-25-4-13	384	0.034	42.31	24.81	49.90
ASP-25-4-14	407	0.034	44.11	25.74	52.26
ASP-25-4-15	432	0.034	37.64	24.78	44.28
ASP-25-4-16	503	0.034	39.44	25.18	45.66
ASP-25-4-17	527	0.034	38.51	23.00	43.49
ASP-25-4-18	552	0.034	36.99	21.26	41.04
ASP-25-4-19	576	0.034	36.29	21.10	40.18
ASP-25-4-20	600	0.035	35.09	19.59	38.03
ASP-25-4-21	672	0.035	32.74	22.59	36.67
ASP-25-4-22	720	0.035	32.92	22.83	37.19
ASP-25-4-23	768	0.035	33.86	22.72	35.33
ASP-25-4-24	863	0.035	35.09	21.85	38.14
ASP-25-4-25	1030	0.035	33.94	19.79	36.08
ASP-25-4-26	1077	0.035	33.74	20.27	36.24
ASP-25-4-27	1174	0.035	33.60	20.41	36.28
ASP-25-4-28	**1224**	0.037	30.59	18.76	32.55
ASP-25-4-29	**1272**	0.038	30.99	20.07	32.01
ASP-25-4-30	**1416**	0.038	29.93	17.67	31.23
ASP-25-4-31	**1512**	0.038	29.14	17.36	30.56
ASP-25-4-32	**1560**	0.038	27.80	16.58	29.27
ASP-25-4-33	**1608**	0.038	29.55	19.75	30.13

Table A.5: Experimental data from the flow-through experiments presented in this thesis. Time periods in bold letters correspond to the considered steady-state(n.a.: not analyzed; b.d.l.: below detection limit).

Sample	Time (h)	flow rate (mL min^{-1})	As	S $\mu mol\ L^{-1}$	Fe
ASP-25-12-1	0	0.040	112.72	48.96	197.53
ASP-25-12-2	117	0.042	77.77	34.93	107.70
ASP-25-12-3	287	0.041	72.89	33.37	87.10
ASP-25-12-4	378	0.042	63.08	30.93	69.96
ASP-25-12-5	502	0.042	79.87	35.52	87.64
ASP-25-12-6	619	0.042	66.70	31.22	72.30
ASP-25-12-7	714	0.042	71.19	32.46	80.48
ASP-25-12-8	839	0.042	75.83	33.77	80.03
ASP-25-12-9	958	0.042	71.41	31.81	75.33
ASP-25-12-10	1050	0.042	64.46	31.93	71.58
ASP-25-12-11	1174	0.042	63.80	32.59	69.16
ASP-25-12-12	1295	0.041	66.24	31.56	71.33
ASP-25-12-13	1386	0.042	64.29	32.87	71.34
ASP-25-12-14	1505	0.042	54.06	31.22	57.59
ASP-25-12-15	1554	0.038	57.99	30.88	64.22
ASP-25-12-16	1632	0.042	47.69	27.37	54.72
ASP-25-12-17	1676	0.042	54.82	30.20	61.85
ASP-25-12-18	1700	0.042	52.09	16.46	57.11
ASP-25-12-19	1797	0.042	48.15	20.45	51.56
ASP-25-12-20	1846	0.042	48.69	23.79	51.67
ASP-25-12-21	1896	0.042	46.39	22.87	50.61
ASP-25-12-22	1964	0.042	40.15	17.41	44.90
ASP-25-12-23	2058	0.042	44.58	23.83	47.35
ASP-25-12-24	2155	0.041	47.96	33.45	52.09
ASP-25-12-25	2299	0.041	50.78	26.19	53.96
ASP-25-12-26	2394	0.041	50.78	21.61	52.96
ASP-25-12-27	**2465**	0.041	47.86	27.54	52.66
ASP-25-12-28	**2513**	0.041	51.52	35.52	53.86
ASP-25-12-29	**2561**	0.042	50.51	24.56	54.33
ASP-25-12-30	**2633**	0.041	54.06	29.16	56.89
ASP-25-12-31	**2681**	0.041	51.32	33.15	55.16
ASP-25-12-32	**2729**	0.041	48.54	22.08	53.61
ASP-25-12-33	**2803**	0.041	46.92	26.81	48.92
ASP-25-12-34	**2852**	0.041	49.71	23.71	54.56
ASP-25-12-35	**2897**	0.041	52.51	27.34	55.76

Table A.6: Experimental data from the flow-through experiments presented in this thesis. Time periods in bold letters correspond to the considered steady-state (n.a.: not analyzed; b.d.l.: below detection limit).

Sample	Time (h)	flow rate (mL min^{-1})	As	S $\mu mol\ L^{-1}$	Fe
ASP-25-13-1	0	0.046	127.85	8.06	155.24
ASP-25-13-2	123	0.048	75.98	4.84	87.16
ASP-25-13-3	195	0.048	82.08	2.89	96.70
ASP-25-13-4	293	0.048	74.26	1.73	91.75
ASP-25-13-5	383	0.049	80.44	52.42	93.65
ASP-25-13-6	507	0.050	101.35	347.71	105.64
ASP-25-13-7	625	0.049	92.05	585.56	48.85
ASP-25-13-8	719	0.048	77.28	700.88	0.25
ASP-25-13-9	845	0.048	61.17	712.17	0.09
ASP-25-13-10	964	0.048	42.79	733.72	0.04
ASP-25-13-11	1056	0.049	90.18	375.42	177.50
ASP-25-13-12	1180	0.049	143.33	154.33	221.23
ASP-25-13-13	1348	0.049	92.39	148.77	111.46
ASP-25-13-14	1466	0.048	88.19	86.00	100.08
ASP-25-13-15	1560	0.044	72.03	85.02	84.61
ASP-25-13-16	1682	0.046	63.27	70.31	71.72
ASP-25-13-17	1803	0.049	64.36	65.66	75.05
ASP-25-13-18	1847	0.048	64.40	45.33	72.59
ASP-25-13-19	1894	0.049	54.82	60.15	62.65
ASP-25-13-20	1970	0.050	59.00	68.57	66.37
ASP-25-13-21	2014	0.050	61.04	59.29	70.55
ASP-25-13-22	2062	0.050	63.90	60.73	73.13
ASP-25-13-23	2136	0.050	69.89	69.26	77.54
ASP-25-13-24	2161	0.049	70.54	57.95	78.80
ASP-25-13-25	2236	0.046	70.03	57.44	78.15
ASP-25-13-26	2305	0.034	89.96	80.51	100.24
ASP-25-13-27	2353	0.025	111.35	90.22	126.17
ASP-25-13-28	2399	0.026	86.95	63.54	98.78
ASP-25-13-29	2471	0.026	87.45	82.41	99.93
ASP-25-13-30	2520	0.026	85.30	74.98	97.91
ASP-25-13-31	**2567**	0.026	95.73	84.56	106.61
ASP-25-13-32	**2639**	0.025	97.02	91.62	111.16
ASP-25-13-33	**2687**	0.026	97.00	81.42	111.69
ASP-25-13-34	**2735**	0.026	94.08	89.61	104.56
ASP-25-13-35	**2809**	0.026	96.97	83.37	108.27
ASP-25-13-36	**2857**	0.025	94.80	79.56	108.19

Table A.7: Experimental data from the flow-through experiments presented in this thesis. Time periods in bold letters correspond to the considered steady-state (n.a.: not analyzed; b.d.l.: below detection limit).

Sample	Time (h)	flow rate (mL min^{-1})	As	S $\mu mol\ L^{-1}$	Fe
ASP-25-5-1	0	0.036	39.63	36.39	66.46
ASP-25-5-2	24	0.018	17.37	16.04	44.01
ASP-25-5-3	97	0.017	9.66	9.30	29.58
ASP-25-5-4	122	0.037	5.21	6.46	18.44
ASP-25-5-5	145	0.037	4.40	6.35	16.02
ASP-25-5-6	169	0.037	4.13	5.61	14.76
ASP-25-5-7	191	0.037	2.63	3.89	9.83
ASP-25-5-8	266	0.036	2.78	5.81	9.39
ASP-25-5-9	286	0.036	4.80	5.39	14.49
ASP-25-5-10	314	0.036	12.90	7.64	22.44
ASP-25-5-11	337	0.036	13.10	n.a.	17.35
ASP-25-5-12	361	0.036	5.23	n.a.	7.18
ASP-25-5-13	432	0.036	6.07	n.a.	9.85
ASP-25-5-14	456	0.036	8.68	n.a.	12.66
ASP-25-5-15	481	0.036	10.22	n.a.	13.49
ASP-25-5-16	506	0.036	7.76	n.a.	10.00
ASP-25-5-17	529	0.036	5.74	n.a.	7.57
ASP-25-5-18	601	0.036	8.27	n.a.	11.40
ASP-25-5-19	625	0.036	8.74	n.a.	11.70
ASP-25-5-20	649	0.036	9.30	n.a.	12.15
ASP-25-5-21	673	0.034	10.47	8.55	12.28
ASP-25-5-23	768	0.034	10.10	4.59	13.05
ASP-25-5-25	816	0.035	11.08	5.03	13.35
ASP-25-5-27	935	0.035	11.24	5.47	14.00
ASP-25-5-29	**984**	0.035	7.01	3.74	8.37
ASP-25-5-31	**1032**	0.032	7.76	4.88	9.10
ASP-25-5-33	**1128**	0.035	7.94	4.08	9.60
ASP-25-5-35	**1177**	0.035	8.04	4.65	9.58

Tables A.8 and A.9: Experimental data from the flow-through experiments presented in this thesis. Time periods in bold letters correspond to the considered steady-state (n.a.: not analyzed; b.d.l.: below detection limit).

Sample	Time (h)	flow rate (mL min^{-1})	As	S $\mu mol\ L^{-1}$	Fe
ASP-25-24-1	0	0.034	180.01	132.26	245.16
ASP-25-24-2	63	0.037	30.42	26.82	41.94
ASP-25-24-3	142	0.037	16.39	14.07	25.80
ASP-25-24-4	191	0.037	17.17	15.98	25.00
ASP-25-24-5	236	0.037	16.73	19.57	22.62
ASP-25-24-6	307	0.036	17.18	b.d.l.	22.35
ASP-25-24-7	357	0.036	19.38	16.28	23.65
ASP-25-24-8	401	0.036	22.31	15.01	27.20
ASP-25-24-9	569	0.036	19.32	19.77	23.79
ASP-25-24-10	641	0.036	21.04	19.14	25.74
ASP-25-24-11	696	0.036	15.43	1.60	21.19
ASP-25-24-12	808	0.035	17.24	2.60	21.84
ASP-25-24-13	861	0.035	15.59	20.15	20.44
ASP-25-24-14	909	0.035	18.18	14.49	22.20
ASP-25-24-15	984	0.034	23.85	22.16	29.07
ASP-25-24-16	**1027**	0.035	18.04	34.02	21.34
ASP-25-24-17	**1078**	0.036	16.04	19.90	20.96
ASP-25-24-18	**1166**	0.036	16.60	26.40	21.78
ASP-25-24-19	**1199**	0.036	16.40	28.05	22.09
ASP-25-24-20	**1246**	0.036	19.25	28.63	23.65

Sample	Time (h)	flow rate (mL min^{-1})	As	S $\mu mol\ L^{-1}$	Fe
ASP-25-25-1	0	0.035	115.59	57.67	208.70
ASP-25-25-2	63	0.039	21.66	n.a.	51.98
ASP-25-25-3	142	0.038	18.82	7.60	43.58
ASP-25-25-4	191	0.038	18.69	4.28	41.41
ASP-25-25-5	236	0.038	18.12	2.74	34.55
ASP-25-25-6	307	0.037	18.41	7.15	31.99
ASP-25-25-7	357	0.038	19.70	6.08	31.56
ASP-25-25-8	401	0.038	19.60	9.43	29.21
ASP-25-25-9	569	0.036	18.44	7.74	23.30
ASP-25-25-10	641	0.038	17.01	2.77	22.65
ASP-25-25-11	696	0.039	14.42	17.26	20.53
ASP-25-25-12	808	0.038	15.79	17.13	20.25
ASP-25-25-13	861	0.038	15.22	26.37	19.05
ASP-25-25-14	909	0.038	15.39	10.94	21.14
ASP-25-25-15	984	0.038	19.82	24.46	23.65
ASP-25-25-16	1027	0.039	15.38	13.49	19.42
ASP-25-25-17	**1078**	0.039	15.07	23.96	19.02
ASP-25-25-18	**1166**	0.038	16.72	23.09	20.20
ASP-25-25-19	**1199**	0.038	14.66	18.97	17.64
ASP-25-25-20	**1247**	0.038	16.11	25.71	18.72

Tables A.10: Experimental data from the flow-through experiments presented in this thesis. Time periods in bold letters correspond to the considered steady-state (n.a.: not analyzed; b.d.l.: below detection limit).

Sample	Time (h)	flow rate (mL min^{-1})	As	S $\mu mol\ L^{-1}$	Fe
ASP-25-6-1	0	0.018	111.33	119878	10276
ASP-25-6-2	49	0.037	55.78	117913	9825
ASP-25-6-3	120	0.037	36.09	120938	10025
ASP-25-6-4	144	0.037	33.41	122061	10061
ASP-25-6-5	169	0.038	29.99	125023	10286
ASP-25-6-6	193	0.038	27.83	118537	9785
ASP-25-6-7	217	0.038	26.41	121998	10032
ASP-25-6-8	289	0.038	25.88	123558	10149
ASP-25-6-9	313	0.038	25.99	121998	9941
ASP-25-6-10	337	0.038	24.35	122435	10007
ASP-25-6-11	361	0.038	24.24	120907	9812
ASP-25-6-12	385	0.038	24.55	122030	9937
ASP-25-6-13	456	0.038	25.47	121562	9955
ASP-25-6-14	480	0.038	22.29	121437	9950
ASP-25-6-15	503	0.038	22.90	124337	10254
ASP-25-6-16	527	0.038	23.84	119410	9755
ASP-25-6-17	623	0.038	21.48	122529	9982
ASP-25-6-18	647	0.038	22.41	122996	9939
ASP-25-6-19	671	0.038	21.36	124337	10082
ASP-25-6-20	694	0.038	23.41	123277	10086
ASP-25-6-21	719	0.038	21.57	121718	9893
ASP-25-6-22	791	0.038	20.85	121437	9894
ASP-25-6-23	816	0.038	20.85	124774	10125
ASP-25-6-24	841	0.038	22.81	122684	9957
ASP-25-6-25	864	0.038	22.49	121655	9878
ASP-25-6-26	889	0.038	23.21	121312	9833
ASP-25-6-27	**1009**	0.038	20.25	130543	10349
ASP-25-6-28	**1033**	0.038	20.97	127924	10272
ASP-25-6-29	**1057**	0.038	20.85	122684	9955
ASP-25-6-30	**1129**	0.038	21.77	130824	10421
ASP-25-6-31	**1153**	0.038	21.26	130325	10331
ASP-25-6-32	**1177**	0.038	22.49	127144	10278
ASP-25-6-33	**1201**	0.038	23.01	129171	10403
ASP-25-6-34	**1225**	0.038	21.05	122466	9996
ASP-25-6-35	**1297**	0.038	21.77	123183	9964

Table A.11: Experimental data from the flow-through experiments presented in this thesis. Time periods in bold letters correspond to the considered steady-state (n.a.: not analyzed; b.d.l.: below detection limit).

Sample	Time (h)	flow rate (mL min^{-1})	As	S $\mu mol\ L^{-1}$	Fe
ASP-25-7-1-a	0	0.032	18.93	76.03	22.90
ASP-25-7-2-a	28	0.038	5.30	9.15	10.62
ASP-25-7-3-a	311	0.038	2.11	4.10	5.67
ASP-25-7-4-a	459	0.038	b.d.l	b.d.l	2.38
ASP-25-7-5-a	627	0.038	b.d.l	b.d.l	1.08
ASP-25-7-6-a	797	0.038	b.d.l	b.d.l	0.64
ASP-25-7-7-a	1132	0.035	b.d.l	b.d.l	0.47
ASP-25-7-8-a	1157	0.039	b.d.l	b.d.l	0.46
ASP-25-7-9-a	**1179**	0.038	b.d.l	b.d.l	0.93
ASP-25-7-10-a	**1202**	0.032	b.d.l	b.d.l	0.59
ASP-25-7-11-a	**1275**	0.038	b.d.l	b.d.l	0.56
ASP-25-7-12-a	**1300**	0.038	b.d.l	b.d.l	0.68
ASP-25-7-13-a	**1324**	0.038	b.d.l	b.d.l	1.01
ASP-25-7-1-b	1347	0.038	1.70	b.d.l	1.99
ASP-25-7-2-b	1444	0.038	4.18	b.d.l	4.60
ASP-25-7-3-b	1491	0.038	4.82	3.49	5.38
ASP-25-7-4-b	1540	0.037	5.73	4.04	6.21
ASP-25-7-5-b	1636	0.038	4.75	3.62	5.29
ASP-25-7-6-b	1683	0.037	5.28	3.81	5.79
ASP-25-7-7-b	1780	0.038	4.74	3.62	5.27
ASP-25-7-8-b	**1828**	0.037	4.68	3.81	5.16
ASP-25-7-9-b	**1876**	0.037	5.37	4.24	5.28
ASP-25-7-10-b	**2020**	0.037	4.53	3.65	4.97
ASP-25-7-11-b	**2163**	0.037	5.18	4.00	5.39
ASP-25-7-12-b	**2308**	0.037	4.53	3.50	4.84
ASP-25-7-13-b	**2452**	0.037	4.03	3.39	4.20
ASP-25-7-15-b	**2549**	0.036	4.25	3.42	4.70
ASP-25-7-16-b	**2643**	0.036	4.12	3.42	4.40
ASP-25-7-17-b	2860	0.037	5.42	3.93	5.78
ASP-25-7-1-c	2979	0.004	46.32	32.18	43.76
ASP-25-7-2-c	3219	0.036	17.10	17.09	15.19
ASP-25-7-3-c	3340	0.036	20.78	22.48	21.81
ASP-25-7-4-c	3460	0.035	18.63	24.03	19.86
ASP-25-7-5-c	3508	0.036	21.35	26.36	22.20
ASP-25-7-6-c	3724	0.036	21.26	14.50	20.02
ASP-25-7-7-c	**3820**	0.036	18.00	12.23	16.88
ASP-25-7-8-c	**3868**	0.036	16.16	10.05	17.42
ASP-25-7-9-c	**3892**	0.036	16.69	11.71	18.42
ASP-25-7-10-c	**3983**	0.036	17.95	18.22	17.83
ASP-25-7-11-c	**4012**	0.036	16.36	10.45	17.29

Table A.12: Experimental data from the flow-through experiments presented in this thesis. Time periods in bold letters correspond to the considered steady-state (n.a.: not analyzed; b.d.l.: below detection limit).

Sample	Time (h)	flow rate (mL min^{-1})	As	S $\mu mol\ L^{-1}$	Fe
ASP-25-32-1	0	0.007	166.27	70.01	217.37
ASP-25-32-2	127	0.015	89.42	47.95	151.55
ASP-25-32-3	151	0.015	56.02	41.99	121.61
ASP-25-32-4	174	0.014	28.63	23.46	78.58
ASP-25-32-5	238	0.015	12.64	24.44	55.94
ASP-25-32-6	289	0.013	10.85	10.11	38.46
ASP-25-32-7	342	0.016	9.57	20.74	34.87
ASP-25-32-8	409	0.015	11.07	30.00	31.30
ASP-25-32-9	459	0.012	8.71	25.33	25.37
ASP-25-32-10	503	0.016	7.98	7.44	20.85
ASP-25-32-11	579	0.013	8.64	11.32	15.71
ASP-25-32-12	676	0.016	5.22	4.92	11.41
ASP-25-32-13	**771**	0.015	4.26	10.71	9.07
ASP-25-32-14	**841**	0.015	4.41	4.31	7.50
ASP-25-32-15	**915**	0.015	4.83	18.60	7.79
ASP-25-32-16	**967**	0.012	4.01	5.60	6.96

Table A.13: Experimental data from the flow-through experiments presented in this thesis. Time periods in bold letters correspond to the considered steady-state (n.a.: not analyzed; b.d.l.: below detection limit).

Sample	Time (h)	flow rate (mL min^{-1})	As	S $\mu mol\ L^{-1}$	Fe
ASP-25-34-1-a	0	0.016	350.47	170.09	541.93
ASP-25-34-2-a	54	0.049	170.86	70.20	309.47
ASP-25-34-3-a	95	0.048	50.78	20.77	87.40
ASP-25-34-4-a	167	0.048	39.67	18.63	53.88
ASP-25-34-5-a	213	0.045	35.11	16.10	41.74
ASP-25-34-6-a	262	0.046	26.14	13.20	31.04
ASP-25-34-7-a	333	0.027	24.68	13.22	28.15
ASP-25-34-8-a	384	0.047	22.54	12.04	25.94
ASP-25-34-9-a	406	0.047	20.85	n.a.	24.08
ASP-25-34-10-a	430	0.047	19.30	n.a.	21.97
ASP-25-34-11-a	502	0.046	21.69	n.a.	22.68
ASP-25-34-12-a	526	0.046	20.31	n.a.	20.71
ASP-25-34-13-a	549	0.047	19.06	n.a.	19.82
ASP-25-34-14-a	579	0.046	16.97	9.72	18.84
ASP-25-34-15-a	606	0.046	18.30	10.77	19.02
ASP-25-34-16-a	676	0.040	18.35	12.12	22.92
ASP-25-34-17-a	723	0.047	15.88	9.09	17.61
ASP-25-34-18-a	749	0.047	15.99	8.87	16.94
ASP-25-34-19-a	773	0.016	14.61	9.45	16.40
ASP-25-34-20-a	845	0.141	15.35	9.03	16.94
ASP-25-34-21-a	**870**	0.006	13.33	9.75	16.15
ASP-25-34-22-a	**894**	0.047	15.08	9.01	15.75
ASP-25-34-23-a	**940**	0.046	12.69	n.a.	15.77
ASP-25-34-24-a	**1013**	0.046	13.88	9.01	15.79
ASP-25-34-25-a	**1036**	0.046	14.15	9.42	15.79
ASP-25-34-26-a	**1060**	0.047	13.88	8.10	15.38
ASP-25-34-27-a	**1080**	0.005	14.95	9.01	15.03
ASP-25-34-28-a	1102	0.055	14.55	10.44	16.08
ASP-25-34-29-a	1165	0.031	14.95	10.61	19.10
ASP-25-34-30-a	1201	0.047	12.55	10.04	18.82
ASP-25-34-31-a	1221	0.047	12.68	8.63	17.20
ASP-25-34-32-a	1246	0.047	13.48	8.63	15.32
ASP-25-34-33-a	1269	0.014	10.41	8.93	15.18
ASP-25-34-34-a	1342	0.050	7.74	4.22	4.81
ASP-25-34-1-b	1368	0.052	6.54	3.57	4.23
ASP-25-34-2-b	1391	0.051	2.80	3.60	5.00
ASP-25-34-3-b	1414	0.052	4.00	4.22	5.79
ASP-25-34-4-b	1437	0.051	2.80	5.30	6.55
ASP-25-34-5-b	1510	0.007	5.87	4.63	6.12
ASP-25-34-6-b	1536	0.048	6.41	3.60	6.12
ASP-25-34-7-b	1557	0.026	6.81	4.73	6.67
ASP-25-34-8-b	1581	0.001	2.94	4.52	6.12
ASP-25-34-9-b	**1605**	0.044	3.87	4.30	6.14
ASP-25-34-10-b	**1677**	0.049	1.44	3.95	4.09
ASP-25-34-11-b	**1702**	0.049	4.02	4.14	3.81
ASP-25-34-12-b	**1725**	0.049	2.80	3.16	3.49

Table A.14: Experimental data from the flow-through experiments presented in this thesis. Time periods in bold letters correspond to the considered steady-state (n.a.: not analyzed; b.d.l.: below detection limit).

Sample	Time (h)	flow rate (mL min^{-1})	As	S $\mu mol\ L^{-1}$	Fe
ASP-50-1-1	0	0.053	132.50	64.06	606.05
ASP-50-1-2	24	0.039	89.48	46.28	259.79
ASP-50-1-3	99	0.036	80.83	39.04	125.30
ASP-50-1-4	120	0.036	79.12	43.05	123.30
ASP-50-1-5	146	0.036	75.59	37.96	98.56
ASP-50-1-6	171	0.036	74.46	41.66	91.26
ASP-50-1-7	195	0.037	70.28	48.79	82.40
ASP-50-1-8	264	0.037	65.43	40.86	77.80
ASP-50-1-9	291	0.036	64.14	44.21	76.40
ASP-50-1-10	315	0.037	64.69	39.84	75.28
ASP-50-1-11	338	0.037	63.95	38.68	74.47
ASP-50-1-12	362	0.037	61.12	44.22	70.89
ASP-50-1-13	435	0.037	59.67	26.35	68.36
ASP-50-1-14	456	0.037	58.58	40.02	67.70
ASP-50-1-15	483	0.037	59.81	42.65	68.74
ASP-50-1-16	507	0.036	60.56	38.11	67.78
ASP-50-1-17	530	0.034	62.51	41.43	71.61
ASP-50-1-18	603	0.030	70.24	43.13	79.20
ASP-50-1-19	626	0.025	77.88	49.36	87.61
ASP-50-1-20	650	0.023	81.98	54.24	94.95
ASP-50-1-21	794	0.020	143.22	75.41	153.21
ASP-50-1-22	842	0.023	84.42	43.22	88.16
ASP-50-1-23	933	0.031	61.52	32.31	64.26
ASP-50-1-24	962	0.031	61.20	33.12	63.56
ASP-50-1-25	988	0.031	58.46	31.17	61.15
ASP-50-1-26	1011	0.031	60.32	32.87	63.08
ASP-50-1-27	1033	0.031	57.33	28.58	59.66
ASP-50-1-28	1107	0.032	55.82	30.80	58.03
ASP-50-1-29	1131	0.032	55.63	29.83	58.28
ASP-50-1-30	**1154**	0.032	54.24	29.35	56.78
ASP-50-1-31	**1179**	0.032	53.36	29.11	55.67
ASP-50-1-32	**1204**	0.033	51.62	30.37	54.00
ASP-50-1-33	**1275**	0.033	51.07	29.80	53.59
ASP-50-1-34	**1298**	0.032	49.47	28.41	52.19
ASP-50-1-35	**1325**	0.032	51.49	29.27	53.70
ASP-50-1-36	**1346**	0.033	51.70	29.54	54.18
ASP-50-1-37	**1365**	0.033	51.80	27.08	54.07

Tables A.15 and A.16: Experimental data from the flow-through experiments presented in this thesis. Time periods in bold letters correspond to the considered steady-state (n.a.: not analyzed; b.d.l.: below detection limit).

Sample	Time (h)	flow rate (mL min^{-1})	As	S $\mu mol\ L^{-1}$	Fe
ASP-50-4-1	0	0.031	365.72	251.67	348.97
ASP-50-4-2	45	0.036	141.48	n.a	n.a.
ASP-50-4-3	93	0.035	136.15	83.45	125.60
ASP-50-4-4	164	0.035	119.46	72.79	90.42
ASP-50-4-5	214	0.036	105.45	65.12	91.19
ASP-50-4-6	260	0.036	95.70	58.85	74.16
ASP-50-4-7	332	0.035	90.36	53.67	82.70
ASP-50-4-8	380	0.035	86.49	52.36	78.12
ASP-50-4-9	429	0.035	75.95	50.21	63.01
ASP-50-4-10	500	0.035	83.29	47.81	74.41
ASP-50-4-11	549	0.035	77.82	48.15	73.91
ASP-50-4-12	598	0.035	77.82	47.37	75.34
ASP-50-4-13	678	0.035	73.41	n.a.	n.a.
ASP-50-4-14	727	0.035	64.47	n.a.	n.a.
ASP-50-4-15	**769**	0.035	54.06	33.09	47.56
ASP-50-4-16	**840**	0.035	54.73	33.49	55.54
ASP-50-4-17	**885**	0.035	56.06	34.05	55.81
ASP-50-4-18	**932**	0.035	52.72	33.77	53.57
ASP-50-4-19	**1004**	0.034	57.93	35.21	56.99
ASP-50-4-20	**1052**	0.035	62.33	36.86	60.00

Sample	Time (h)	flow rate (mL min^{-1})	As	S $\mu mol\ L^{-1}$	Fe
ASP-70-5-1	0	0.019	797.01	341.72	1139.87
ASP-70-5-2	30	0.026	452.00	228.20	762.78
ASP-70-5-3	74	0.025	138.75	117.73	196.38
ASP-70-5-4	146	0.029	89.49	86.73	133.52
ASP-70-5-5	198	0.027	74.89	63.86	96.60
ASP-70-5-6	247	0.027	56.49	61.93	75.46
ASP-70-5-7	319	0.027	38.75	60.75	56.66
ASP-70-5-8	340	0.027	34.92	52.14	49.62
ASP-70-5-9	385	0.027	32.15	50.47	42.32
ASP-70-5-10	484	0.027	32.12	44.32	42.27
ASP-70-5-11	**536**	0.027	30.51	50.90	40.80
ASP-70-5-12	**580**	0.026	31.38	41.71	41.86
ASP-70-5-13	**656**	0.026	31.91	32.08	43.65
ASP-70-5-14	**703**	0.026	34.09	43.57	42.65
ASP-70-5-15	**744**	0.026	26.97	41.43	37.44

Table A.17: Experimental data from the flow-through experiments presented in this thesis. Time periods in bold letters correspond to the considered steady-state (n.a.: not analyzed; b.d.l.: below detection limit).

Sample	Time (h)	flow rate (mL min^{-1})	As	S $\mu mol\ L^{-1}$	Fe
ASP-70-1-1	0	0.030	304.56	132.77	959.23
ASP-70-1-2	28	0.034	167.12	84.06	269.43
ASP-70-1-3	100	0.035	107.84	66.50	122.03
ASP-70-1-4	123	0.035	96.78	54.28	111.45
ASP-70-1-5	148	0.035	79.32	43.05	90.75
ASP-70-1-6	171	0.035	69.80	57.19	79.88
ASP-70-1-7	196	0.035	56.94	46.30	65.21
ASP-70-1-8	268	0.035	55.00	38.25	76.41
ASP-70-1-9	292	0.035	49.86	16.97	57.11
ASP-70-1-10	315	0.035	47.68	23.80	56.10
ASP-70-1-11	340	0.035	47.02	32.10	53.78
ASP-70-1-12	364	0.036	46.36	28.92	51.92
ASP-70-1-13	455	0.036	45.22	29.83	50.57
ASP-70-1-14	484	0.036	44.61	41.78	49.12
ASP-70-1-15	508	0.036	41.84	19.09	49.76
ASP-70-1-16	531	0.036	38.84	25.29	47.49
ASP-70-1-17	604	0.036	39.53	27.18	45.18
ASP-70-1-18	627	0.036	38.91	29.58	44.61
ASP-70-1-19	652	0.036	37.79	23.60	42.31
ASP-70-1-20	676	0.036	38.55	17.94	43.89
ASP-70-1-21	700	0.036	35.86	21.96	41.03
ASP-70-1-22	772	0.036	37.10	29.36	42.84
ASP-70-1-23	796	0.036	38.28	22.91	42.43
ASP-70-1-24	820	0.036	37.26	21.76	42.74
ASP-70-1-25	844	0.036	38.33	21.00	43.25
ASP-70-1-26	868	0.036	36.16	20.83	41.34
ASP-70-1-27	940	0.036	36.55	25.26	42.56
ASP-70-1-28	964	0.036	36.27	19.27	41.96
ASP-70-1-29	988	0.036	36.39	22.60	42.09
ASP-70-1-30	1011	0.036	35.20	14.57	40.06
ASP-70-1-31	1108	0.036	30.71	31.20	35.01
ASP-70-1-32	1132	0.036	30.36	18.18	35.08
ASP-70-1-33	1154	0.036	31.33	24.92	36.03
ASP-70-1-34	1181	0.036	31.07	20.99	37.26
ASP-70-1-35	**1201**	0.036	31.34	29.96	36.60
ASP-70-1-36	**1278**	0.037	33.06	30.92	36.16
ASP-70-1-37	**1304**	0.036	32.48	25.61	37.12
ASP-70-1-38	**1327**	0.037	31.61	25.82	36.75
ASP-70-1-39	**1347**	0.037	30.36	31.93	35.94
ASP-70-1-40	**1438**	0.037	30.95	24.65	35.43
ASP-70-1-41	**1466**	0.037	31.42	31.23	34.93
ASP-70-1-42	**1492**	0.037	29.43	30.70	34.84
ASP-70-1-43	**1513**	0.037	29.06	19.23	34.40

Table A.18: Experimental data from the flow-through experiments presented in this thesis. Time periods in bold letters correspond to the considered steady-state (n.a.: not analyzed; b.d.l.: below detection limit).

Sample	Time (h)	flow rate (mL min^{-1})	As	S $\mu mol\ L^{-1}$	Fe
ASP-25-8-1	0	0.034	49.95	53.88	22.23
ASP-25-8-2	47	0.037	67.11	75.22	45.40
ASP-25-8-3	190	0.037	52.80	67.18	39.21
ASP-25-8-4	240	0.037	54.37	55.51	41.71
ASP-25-8-5	333	0.037	46.31	48.03	35.91
ASP-25-8-6	432	0.037	42.81	48.63	35.92
ASP-25-8-7	525	0.037	42.62	61.96	35.73
ASP-25-8-8	577	0.037	50.66	68.17	42.75
ASP-25-8-9	719	0.029	44.73	43.13	28.08
ASP-25-8-10	887	0.038	78.84	70.10	50.87
ASP-25-8-11	937	0.038	49.63	51.54	33.62
ASP-25-8-12	1080	0.037	51.55	43.59	34.62
ASP-25-8-13	1177	0.037	40.60	35.84	29.42
ASP-25-8-14	1273	0.037	44.13	45.24	30.86
ASP-25-8-15	1368	0.037	43.85	52.21	30.58
ASP-25-8-16	1394	0.037	43.84	46.55	31.33
ASP-25-8-17	1416	0.037	46.79	25.89	31.68
ASP-25-8-18	1512	0.037	40.16	47.66	30.93
ASP-25-8-19	1536	0.036	39.14	43.96	29.50
ASP-25-8-20	1560	0.037	36.84	31.01	27.75
ASP-25-8-21	1608	0.037	40.47	52.89	33.12
ASP-25-8-22	1677	0.037	44.16	47.52	31.11
ASP-25-8-23	1728	0.036	41.66	52.17	31.14
ASP-25-8-24	1752	0.036	42.66	46.66	32.58
ASP-25-8-25	1770	0.036	40.90	42.58	30.63
ASP-25-8-26	1869	0.036	37.11	24.09	25.95
ASP-25-8-27	1920	0.034	35.99	40.28	26.93
ASP-25-8-28	2041	0.031	42.34	45.97	30.72
ASP-25-8-29	2090	0.036	34.92	20.99	26.59
ASP-25-8-30	**2183**	0.038	35.05	44.34	27.16
ASP-25-8-31	**2207**	0.038	34.46	28.94	25.87
ASP-25-8-32	**2232**	0.038	33.49	42.38	26.41
ASP-25-8-33	**2255**	0.038	36.58	35.18	27.01
ASP-25-8-34	**2280**	0.038	33.89	36.66	25.80
ASP-25-8-35	**2352**	0.038	32.75	36.28	26.65
ASP-25-8-36	**2376**	0.039	30.64	34.20	22.74
ASP-25-8-37	**2400**	0.039	32.93	37.21	25.81

Table A.19: Experimental data from the flow-through experiments presented in this thesis. Time periods in bold letters correspond to the considered steady-state (n.a.: not analyzed; b.d.l.: below detection limit).

Sample	Time (h)	flow rate (mL min^{-1})	As	S $\mu mol\ L^{-1}$	Fe
ASP-25-9-1	0	0.029	53.25	73.70	16.67
ASP-25-9-2	47	0.033	77.20	87.54	29.42
ASP-25-9-3	93	0.033	53.32	78.31	22.54
ASP-25-9-4	189	0.034	44.22	68.13	19.41
ASP-25-9-5	333	0.034	29.88	41.15	12.41
ASP-25-9-6	384	0.034	28.47	29.73	12.86
ASP-25-9-7	431	0.035	19.65	30.88	9.62
ASP-25-9-8	525	0.034	17.49	29.98	7.64
ASP-25-9-9	672	0.035	21.51	26.86	11.03
ASP-25-9-10	719	0.029	20.73	29.44	4.60
ASP-25-9-11	887	0.035	19.42	28.97	3.52
ASP-25-9-12	937	0.035	20.19	23.40	5.20
ASP-25-9-13	1057	0.035	19.38	25.27	4.77
ASP-25-9-14	1080	0.035	19.83	25.34	5.10
ASP-25-9-15	1176	0.035	16.78	16.17	3.21
ASP-25-9-16	1201	0.035	15.63	15.19	2.17
ASP-25-9-17	1248	0.035	16.26	17.72	0.19
ASP-25-9-18	1344	0.035	18.13	18.25	1.47
ASP-25-9-19	1394	0.035	19.91	12.34	3.68
ASP-25-9-20	1435	0.035	18.74	1.79	4.31
ASP-25-9-21	1535	0.034	18.65	19.41	1.94
ASP-25-9-22	1560	0.035	18.23	13.44	1.14
ASP-25-9-23	1584	0.034	17.50	23.28	1.45
ASP-25-9-24	1607	0.035	17.41	7.54	1.15
ASP-25-9-25	1677	0.035	19.41	17.62	1.18
ASP-25-9-26	1703	0.035	22.36	22.62	0.83
ASP-25-9-27	1728	0.035	19.71	15.02	1.61
ASP-25-9-28	1752	0.035	21.17	23.78	1.16
ASP-25-9-29	1769	0.035	21.58	15.66	2.18
ASP-25-9-30	1868	0.035	19.29	21.19	2.34
ASP-25-9-31	1919	0.002	32.13	n.a.	2.16
ASP-25-9-32	2041	0.036	17.16	10.82	3.71
ASP-25-9-33	**2064**	0.036	16.50	11.60	3.67
ASP-25-9-34	**2089**	0.035	15.36	9.07	4.39
ASP-25-9-35	**2107**	0.035	19.79	15.51	2.68
ASP-25-9-36	**2183**	0.036	18.69	27.29	8.72
ASP-25-9-37	**2207**	0.035	17.96	12.17	6.10
ASP-25-9-38	**2231**	0.036	19.69	17.19	6.85

Tables A.20 and A.21: Experimental data from the flow-through experiments presented in this thesis. Time periods in bold letters correspond to the considered steady-state (n.a.: not analyzed; b.d.l.: below detection limit).

Sample	Time (h)	flow rate (mL min^{-1})	As	S $\mu mol\ L^{-1}$	Fe
ASP-25-23-1	0	0.036	176.00	214.95	96.01
ASP-25-23-2	102	0.037	108.96	132.08	54.55
ASP-25-23-3	149	0.037	92.70	114.22	45.03
ASP-25-23-4	193	0.036	86.57	102.36	39.53
ASP-25-23-5	270	0.036	90.14	106.14	42.11
ASP-25-23-6	319	0.036	87.96	99.06	35.48
ASP-25-23-7	365	0.036	79.58	92.18	34.29
ASP-25-23-8	436	0.036	74.33	84.81	23.82
ASP-25-23-9	485	0.035	82.15	94.32	33.93
ASP-25-23-10	530	0.035	79.99	98.78	35.37
ASP-25-23-11	697	0.035	78.61	96.40	30.17
ASP-25-23-12	776	0.035	76.18	99.78	29.21
ASP-25-23-13	818	0.035	78.96	95.10	36.80
ASP-25-23-14	871	0.035	71.91	81.68	34.98
ASP-25-23-15	962	0.035	66.60	73.10	31.58
ASP-25-23-16	**990**	0.035	65.48	92.82	31.24
ASP-25-23-17	**1038**	0.035	66.88	90.59	35.42
ASP-25-23-18	**1113**	0.035	66.86	92.13	35.51
ASP-25-23-19	**1155**	0.035	65.25	89.41	38.01

Sample	Time (h)	flow rate (mL min^{-1})	As	S $\mu mol\ L^{-1}$	Fe
ASP-70-4-1	0	0.019	365.61	564.52	210.43
ASP-70-4-2	54	0.024	157.88	261.47	88.63
ASP-70-4-3	127	0.029	108.92	173.14	63.19
ASP-70-4-4	169	0.024	102.75	159.65	61.28
ASP-70-4-5	214	0.026	81.69	128.13	47.12
ASP-70-4-6	290	0.026	76.15	123.41	42.84
ASP-70-4-7	335	0.026	64.30	93.09	39.72
ASP-70-4-8	382	0.026	49.35	70.71	35.31
ASP-70-4-9	459	0.026	78.91	113.44	48.86
ASP-70-4-10	509	0.027	74.82	96.92	41.50
ASP-70-4-11	552	0.027	57.60	78.24	28.40
ASP-70-4-12	630	0.027	51.79	77.57	25.14
ASP-70-4-13	675	0.027	55.81	87.27	29.56
ASP-70-4-14	724	0.027	49.96	76.69	23.43
ASP-70-4-15	845	0.028	52.94	67.62	24.80
ASP-70-4-16	886	0.028	53.09	70.23	28.52
ASP-70-4-17	964	0.029	47.63	63.22	25.56
ASP-70-4-19	**1055**	0.030	45.09	61.10	24.03
ASP-70-4-20	**1132**	0.031	44.48	58.73	22.79
ASP-70-4-21	**1181**	0.031	46.64	57.55	22.26
ASP-70-4-23	**1297**	0.030	48.93	69.07	25.25
ASP-70-4-24	**1346**	0.030	47.39	64.80	23.97

Table A.22: Experimental data from the flow-through experiments presented in this thesis. Time periods in bold letters correspond to the considered steady-state (n.a.: not analyzed; b.d.l.: below detection limit).

Sample	Time (h)	flow rate (mL min^{-1})	As	S $\mu mol\ L^{-1}$	Fe
ASP-25-19-1-a	0	0.033	58.25	49.86	78.13
ASP-25-19-2-a	73	0.038	14.04	5.91	18.84
ASP-25-19-3-a	122	0.038	7.98	4.12	10.71
ASP-25-19-4-a	165	0.038	4.10	3.00	5.50
ASP-25-19-5-a	240	0.038	3.29	1.27	4.42
ASP-25-19-6-a	285	0.037	4.89	2.00	6.56
ASP-25-19-7-a	334	0.037	4.57	7.14	6.13
ASP-25-19-8-a	408	0.037	1.53	n.a.	2.05
ASP-25-19-9-a	458	0.036	2.49	n.a.	3.34
ASP-25-19-10-a	501	0.036	b.d.l.	n.a.	0.71
ASP-25-19-11-a	573	0.036	b.d.l.	n.a.	0.75
ASP-25-19-12-a	630	0.037	b.d.l.	n.a.	0.55
ASP-25-19-13-a	676	0.037	b.d.l.	n.a.	b.d.l.
ASP-25-19-14-a	749	0.039	1.30	11.52	1.74
ASP-25-19-15-a	796	0.041	b.d.l.	n.a.	4.20
ASP-25-19-16-a	840	0.041	b.d.l.	0.56	0.89
ASP-25-19-17-a	**915**	0.044	1.30	1.20	b.d.l.
ASP-25-19-18-a	**959**	0.041	1.31	2.92	b.d.l.
ASP-25-19-19-a	**1113**	0.037	1.34	3.54	b.d.l.
ASP-25-19-1-b	1208	0.004	210.94	266.26	0.20
ASP-25-19-2-b	1515	0.032	125.48	139.04	3.17
ASP-25-19-3-b	1583	0.029	107.98	121.92	7.34
ASP-25-19-4-b	1661	0.032	84.63	81.89	2.25
ASP-25-19-5-b	**1704**	0.031	68.42	77.43	16.45
ASP-25-19-6-b	**1943**	0.035	52.40	64.78	14.02

Table A.23: Experimental data from the flow-through experiments presented in this thesis, (n.a.: not analyzed; b.d.l.: below detection limit).

Sample	Time (h)	flow rate (mL min^{-1})	As	S $\mu mol\ L^{-1}$	Fe
ASP-25-10-1	0.0	0.018	21.42	27.49	b.d.l.
ASP-25-10-2	49.2	0.037	8.01	24.29	b.d.l.
ASP-25-10-3	121.4	0.037	3.58	7.54	b.d.l.
ASP-25-10-4	145.2	0.037	3.28	12.85	b.d.l.
ASP-25-10-5	169.5	0.037	3.83	5.31	b.d.l.
ASP-25-10-6	192.6	0.037	2.73	7.96	b.d.l.
ASP-25-10-7	313.1	0.038	2.05	1.16	b.d.l.
ASP-25-10-8	335.0	0.037	1.74	9.40	b.d.l.
ASP-25-10-9	361.7	0.037	1.71	b.d.l.	b.d.l.
ASP-25-10-10	619.3	0.037	4.15	5.98	b.d.l.
ASP-25-10-11	864.1	0.035	2.60	b.d.l.	b.d.l.
ASP-25-10-12	889.5	0.035	1.45	3.37	b.d.l.
ASP-25-10-13	1052.6	0.018	5.04	3.10	b.d.l.
ASP-25-10-14	1128.0	0.013	4.28	2.78	b.d.l.
ASP-25-10-15	1297.6	0.036	b.d.l.	2.88	b.d.l.
ASP-25-10-16	1322.7	0.036	b.d.l.	b.d.l.	b.d.l.
ASP-25-10-17	1369.1	0.035	b.d.l.	b.d.l.	b.d.l.
ASP-25-10-18	1465.5	0.035	2.09	2.06	b.d.l.
ASP-25-10-19	1486.8	0.035	b.d.l.	10.62	b.d.l.
ASP-25-10-20	1512.8	0.035	4.87	b.d.l.	b.d.l.
ASP-25-10-21	1536.9	0.035	n.a.	b.d.l.	b.d.l.
ASP-25-10-22	1560.4	0.035	3.24	11.60	b.d.l.
ASP-25-10-23	1630.0	0.035	n.a.	b.d.l.	b.d.l.
ASP-25-10-24	1654.2	0.035	4.85	b.d.l.	b.d.l.
ASP-25-10-25	1702.7	0.035	5.56	b.d.l.	b.d.l.
ASP-25-10-26	1823.4	0.034	3.22	5.81	b.d.l.
ASP-25-10-27	1968.7	0.034	2.61	5.53	b.d.l.
ASP-25-10-28	2015.2	0.034	4.08	4.30	b.d.l.
ASP-25-10-29	2060.9	0.034	2.63	4.30	b.d.l.
ASP-25-10-30	2158.1	0.034	2.83	4.86	b.d.l.
ASP-25-10-31	2209.7	0.034	3.86	4.50	b.d.l.
ASP-25-10-32	2305.5	0.034	2.61	4.17	b.d.l.
ASP-25-10-33	2353.8	0.033	4.64	4.27	b.d.l.
ASP-25-10-34	2396.8	0.034	b.d.l.	4.43	b.d.l.
ASP-25-10-35	2496.7	0.033	3.81	4.68	b.d.l.

Table A.24: Experimental data from the flow-through experiments presented in this thesis, (n.a.: not analyzed; b.d.l.: below detection limit).

Sample	Time (h)	flow rate (mL min^{-1})	As	S $\mu mol\ L^{-1}$	Fe
ASP-25-21-1	0	0.028	88.05	79.61	b.d.l.
ASP-25-21-2	99	0.038	27.33	34.20	b.d.l.
ASP-25-21-3	141	0.038	23.38	b.d.l.	b.d.l.
ASP-25-21-4	185	0.038	21.10	11.19	b.d.l.
ASP-25-21-5	261	0.037	32.23	53.87	b.d.l.
ASP-25-21-6	307	0.038	28.89	18.51	b.d.l.
ASP-25-21-7	353	0.020	19.20	15.49	b.d.l.
ASP-25-21-8	430	0.023	51.30	83.56	b.d.l.
ASP-25-21-9	480	0.037	15.22	20.36	b.d.l.
ASP-25-21-10	523	0.037	18.41	6.09	b.d.l.
ASP-25-21-11	601	0.037	11.81	27.07	b.d.l.
ASP-25-21-12	646	0.037	2.88	23.05	b.d.l.
ASP-25-21-13	696	0.034	3.60	21.23	b.d.l.
ASP-25-21-14	817	0.036	6.08	25.84	b.d.l.
ASP-25-21-15	858	0.036	6.77	43.08	b.d.l.
ASP-25-21-16	936	0.036	3.21	20.93	b.d.l.
ASP-25-21-17	982	0.036	2.13	b.d.l.	b.d.l.
ASP-25-21-18	1027	0.036	2.58	15.22	b.d.l.
ASP-25-21-19	1152	0.036	5.54	12.95	b.d.l.
ASP-25-21-20	1198	0.036	3.01	13.89	b.d.l.
ASP-25-21-21	1269	0.036	1.75	9.85	b.d.l.
ASP-25-21-22	1318	0.036	b.d.l.	9.61	b.d.l.
ASP-25-21-23	1609	0.036	b.d.l.	27.67	b.d.l.

Table A.25: Experimental data from the flow-through experiments presented in this thesis, (n.a.: not analyzed; b.d.l.: below detection limit).

Sample	Time (h)	flow rate (mL min^{-1})	As	S $\mu mol\ L^{-1}$	Fe
ASP-25-11-1	0	0.020	14.53	16.54	b.d.l.
ASP-25-11-2	49	0.032	9.83	5.61	b.d.l.
ASP-25-11-3	121	0.032	6.62	b.d.l.	b.d.l.
ASP-25-11-4	145	0.032	6.57	3.64	b.d.l.
ASP-25-11-8	361	0.032	6.76	n.a.	b.d.l.
ASP-25-11-11	485	0.032	7.49	n.a.	b.d.l.
ASP-25-11-12	508	0.032	6.97	n.a.	b.d.l.
ASP-25-11-13	528	0.032	6.61	n.a.	b.d.l.
ASP-25-11-14	619	0.032	8.21	n.a.	b.d.l.
ASP-25-11-15	647	0.007	8.55	8.68	b.d.l.
ASP-25-11-16	673	0.025	8.19	n.a.	b.d.l.
ASP-25-11-17	722	0.033	15.11	29.98	b.d.l.
ASP-25-11-18	795	0.022	10.38	20.73	b.d.l.
ASP-25-11-19	864	0.033	8.79	19.70	b.d.l.
ASP-25-11-20	961	0.028	7.75	20.61	b.d.l.
ASP-25-11-21	1011	0.039	5.10	2.12	b.d.l.
ASP-25-11-22	1052	0.023	5.50	13.69	b.d.l.
ASP-25-11-23	1175	0.031	6.53	11.07	b.d.l.
ASP-25-11-24	1224	0.031	11.41	7.28	b.d.l.
ASP-25-11-25	1322	0.031	8.63	12.49	b.d.l.
ASP-25-11-26	1369	0.031	7.71	14.25	b.d.l.
ASP-25-11-27	1465	0.031	8.18	13.53	b.d.l.
ASP-25-11-28	1512	0.030	4.94	8.34	b.d.l.
ASP-25-11-29	1560	0.030	6.65	12.04	b.d.l.
ASP-25-11-30	1654	0.030	6.68	10.10	b.d.l.
ASP-25-11-31	1702	0.030	6.40	11.51	b.d.l.
ASP-25-11-32	1823	0.030	7.64	12.68	b.d.l.
ASP-25-11-33	1873	0.031	8.29	13.22	b.d.l.
ASP-25-11-34	1968	0.031	7.00	11.94	b.d.l.
ASP-25-11-35	2015	0.028	8.03	13.14	b.d.l.
ASP-25-11-36	2061	0.030	10.79	n.a.	b.d.l.
ASP-25-11-37	2158	0.030	12.06	13.04	b.d.l.
ASP-25-11-38	2209	0.030	9.72	11.88	b.d.l.
ASP-25-11-39	2305	0.031	9.58	14.19	b.d.l.
ASP-25-11-40	2353	0.031	9.05	12.33	b.d.l.
ASP-25-11-41	2396	0.031	8.02	12.72	b.d.l.
ASP-25-11-42	2496	0.031	6.33	8.39	b.d.l.
ASP-25-11-43	2544	0.031	6.21	12.90	b.d.l.
ASP-25-11-44	2643	0.031	8.84	11.83	b.d.l.

Table A.26: Experimental data from the flow-through experiments presented in this thesis. Time periods in bold letters correspond to the considered steady-state (n.a.: not analyzed; b.d.l.: below detection limit).

Sample	Time (h)	flow rate (mL min^{-1})	As	S $\mu mol\ L^{-1}$	Fe
ASP-25-15-1	0	0.016	67.66	151.82	b.d.l.
ASP-25-15-2	20	0.028	9.96	30.59	b.d.l.
ASP-25-15-3	91	0.028	b.d.l.	4.36	b.d.l.
ASP-25-15-4	143	0.029	1.37	1.96	b.d.l.
ASP-25-15-5	188	0.029	2.79	2.55	b.d.l.
ASP-25-15-6	262	0.028	4.03	13.79	b.d.l.
ASP-25-15-7	354	0.028	1.52	11.20	b.d.l.
ASP-25-15-8	431	0.028	2.39	6.87	b.d.l.
ASP-25-15-9	523	0.029	3.58	23.58	b.d.l.
ASP-25-15-10	619	0.028	2.15	25.64	b.d.l.
ASP-25-15-11	787	0.029	1.42	24.14	b.d.l.
ASP-25-15-12	833	0.029	2.84	31.90	b.d.l.
ASP-25-15-13	931	0.029	2.76	19.19	b.d.l.
ASP-25-15-14	980	0.029	2.22	27.54	b.d.l.
ASP-25-15-15	1147	0.029	1.74	10.67	b.d.l.
ASP-25-15-16	1196	0.029	2.11	12.91	b.d.l.
ASP-25-15-17	1319	0.029	2.30	11.48	b.d.l.
ASP-25-15-18	1486	0.029	3.06	12.47	b.d.l.
ASP-25-15-19	1533	0.029	2.28	4.58	b.d.l.
ASP-25-15-20	1605	0.028	b.d.l.	12.04	b.d.l.
ASP-25-15-21	1702	0.029	8.18	3.62	b.d.l.
ASP-25-15-22	1821	0.030	3.15	9.14	b.d.l.
ASP-25-15-23	1869	0.029	3.95	14.67	b.d.l.
ASP-25-15-24	1942	0.030	2.69	13.29	b.d.l.
ASP-25-15-25	1990	0.030	4.23	10.44	b.d.l.
ASP-25-15-26	2037	0.029	2.64	15.00	b.d.l.
ASP-25-15-27	2157	0.030	3.46	9.82	b.d.l.
ASP-25-15-28	2204	0.029	2.15	4.98	b.d.l.
ASP-25-15-29	2277	0.030	4.04	8.13	b.d.l.
ASP-25-15-30	2373	0.031	b.d.l.	37.89	b.d.l.
ASP-25-15-31	2497	0.031	b.d.l.	8.78	b.d.l.
ASP-25-15-32	2544	0.031	b.d.l.	10.86	b.d.l.
ASP-25-15-33	2665	0.031	b.d.l.	13.01	b.d.l.
ASP-25-15-34	2784	0.031	4.04	22.03	b.d.l.
ASP-25-15-35	2828	0.031	8.36	24.39	b.d.l.
ASP-25-15-36	2881	0.032	7.14	22.05	b.d.l.
ASP-25-15-37	2971	0.032	7.25	42.05	b.d.l.
ASP-25-15-38	3211	0.034	3.82	3.13	b.d.l.

Table A.27: Experimental data from the flow-through experiments presented in this thesis. Time periods in bold letters correspond to the considered steady-state (n.a.: not analyzed; b.d.l.: below detection limit).

Sample	Time (h)	flow rate (mL min^{-1})	S	Fe
			$\mu mol\ L^{-1}$	
MRC-1-1	0	0.038	157.09	58.77
MRC-1-2	27	0.038	198.31	19.96
MRC-1-5	98	0.030	237.98	57.01
MRC-1-6	171	0.034	209.49	105.98
MRC-1-8	218	0.041	103.25	79.58
MRC-1-9	363	0.043	152.00	109.10
MRC-1-12	436	0.043	141.90	110.84
MRC-1-14	530	0.042	113.90	94.54
MRC-1-16	579	0.043	128.84	98.75
MRC-1-17	601	0.045	108.62	86.41
MRC-1-19	700	0.049	95.60	72.71
MRC-1-21	747	0.052	83.17	69.37
MRC-1-23	843	0.025	88.01	72.03
MRC-1-25	893	0.026	102.91	88.79
MRC-1-27	934	0.027	97.92	82.42
MRC-1-29	1034	0.027	91.16	74.27
MRC-1-31	1083	0.027	84.08	68.93
MRC-1-33	1176	0.027	96.93	77.65
MRC-1-35	1227	0.027	99.17	79.03
MRC-1-37	1268	0.027	97.36	78.39
MRC-1-39	1367	0.027	90.59	70.55
MRC-1-41	1419	0.028	91.25	72.64
MRC-1-42	1443	0.028	98.89	78.55
MRC-1-43	1540	0.028	94.65	73.02
MRC-1-44	1564	0.028	69.20	54.16
MRC-1-45	1588	0.028	79.77	65.77
MRC-1-46	1606	0.028	75.13	61.36
MRC-1-47	1682	0.028	72.10	58.46
MRC-1-49	1731	0.028	69.76	55.95
MRC-1-51	1778	0.028	73.29	58.66
MRC-1-53	1875	0.028	91.06	76.47
MRC-1-55	1918	0.028	80.74	65.85
MRC-1-57	2020	0.029	84.73	63.73
MRC-1-59	2068	0.029	68.35	52.35
MRC-1-61	2186	0.029	72.35	54.94
MRC-1-62	2210	0.029	45.09	51.99
MRC-1-63	2232	0.029	77.44	56.39
MRC-1-64	2259	0.029	80.27	59.90
MRC-1-65	2280	0.029	50.56	48.24
MRC-1-66	**2356**	0.029	67.89	55.56
MRC-1-67	**2383**	0.029	66.62	57.24
MRC-1-68	**2406**	0.029	79.26	55.70
MRC-1-69	**2425**	0.029	72.86	58.60
MRC-1-70	**2516**	0.029	64.14	57.72
MRC-1-71	**2544**	0.029	72.03	62.26
MRC-1-72	**2571**	0.029	70.84	58.43
MRC-1-73	**2591**	0.029	74.58	61.99

Table A.28: Experimental data from the flow-through experiments presented in this thesis. Time periods in bold letters correspond to the considered steady-state, (n.a.: not analyzed; b.d.l.: below detection limit).

Sample	Time (h)	flow rate (mL min^{-1})	S	Fe
			μmol L^{-1}	
MRC-2-1	0	0.008	3080.2	n.a
MRC-2-2	41	0.047	383.9	n.a
MRC-2-3	117	0.047	223.9	n.a
MRC-2-4	161	0.048	213.0	n.a
MRC-2-5	188	0.048	184.0	n.a
MRC-2-6	213	0.047	149.7	n.a
MRC-2-7	287	0.022	163.1	7.77
MRC-2-8	335	0.042	866.0	n.a
MRC-2-9	378	0.048	261.6	n.a
MRC-2-10	454	0.046	276.3	n.a
MRC-2-11	501	0.036	459.4	n.a
MRC-2-12	549	0.049	139.7	2.54
MRC-2-13	619	0.044	205.5	6.22
MRC-2-14	670	0.040	205.5	5.75
MRC-2-15	713	0.042	124.8	32.01
MRC-2-16	812	0.041	117.5	57.35
MRC-2-17	839	0.043	132.3	68.81
MRC-2-18	883	0.041	121.7	77.51
MRC-2-19	957	0.039	130.7	82.09
MRC-2-20	1004	0.038	125.8	87.90
MRC-2-21	1050	0.039	124.9	91.32
MRC-2-22	1126	0.039	117.4	81.52
MRC-2-23	1174	0.042	116.3	78.89
MRC-2-24	1217	0.039	108.4	70.19
MRC-2-25	1294	0.039	117.9	69.31
MRC-2-26	1342	0.045	102.3	64.76
MRC-2-27	1386	0.044	104.5	66.98
MRC-2-28	1460	0.044	103.3	66.12
MRC-2-29	1505	0.043	108.43	70.81
MRC-2-30	1554	0.038	122.15	73.21
MRC-2-31	1632	0.043	100.95	64.30
MRC-2-32	1676	0.043	95.90	64.62
MRC-2-33	1700	0.039	109.43	72.82
MRC-2-34	1797	0.037	133.23	82.18
MRC-2-35	1846	0.036	127.55	79.84
MRC-2-36	1895	0.037	115.48	73.66
MRC-2-37	1964	0.020	172.49	103.56
MRC-2-38	2008	0.026	157.33	104.10
MRC-2-39	2057	0.028	127.02	95.42
MRC-2-40	**2130**	0.028	109.46	89.06
MRC-2-41	**2155**	0.028	108.49	89.49
MRC-2-42	**2230**	0.028	109.90	89.20
MRC-2-43	**2299**	0.028	105.94	87.93
MRC-2-44	**2347**	0.029	99.73	84.23
MRC-2-45	**2393**	0.029	101.54	80.02
MRC-2-46	**2465**	0.028	107.65	83.74
MRC-2-47	**2514**	0.028	102.98	84.60
MRC-2-48	**2561**	0.029	107.81	86.34
MRC-2-49	**2633**	0.028	99.26	83.42

Table A.29: Experimental data from the flow-through experiments presented in this thesis. Time periods in bold letters correspond to the considered steady-state (n.a.: not analyzed; b.d.l.: below detection limit).

Sample	Time (h)	flow rate (mL min^{-1})	S	Fe
			μmol L^{-1}	
MRC-3-1	0	0.013	111.84	231.57
MRC-3-2	51	0.033	89.35	216.76
MRC-3-3	75	0.035	111.04	208.37
MRC-3-4	171	0.033	126.05	180.88
MRC-3-5	218	0.012	94.66	107.56
MRC-3-6	386	0.037	70.72	69.98
MRC-3-7	436	0.038	69.71	60.05
MRC-3-8	530	0.038	29.65	48.14
MRC-3-9	556	0.038	42.82	49.05
MRC-3-10	579	0.038	54.03	46.60
MRC-3-11	601	0.038	39.64	37.83
MRC-3-12	675	0.038	33.01	34.11
MRC-3-13	699	0.038	21.33	34.14
MRC-3-14	722	0.038	33.57	35.64
MRC-3-15	1010	0.038	26.55	23.60
MRC-3-16	1250	0.041	29.04	25.12
MRC-3-17	1418	0.042	24.33	20.84
MRC-3-18	1730	0.044	49.83	40.48
MRC-3-19	1851	0.029	28.43	24.05
MRC-3-20	1922	0.044	29.85	24.71
MRC-3-21	2020	0.044	15.95	18.71
MRC-3-22	2068	0.044	30.20	20.05
MRC-3-23	2186	0.044	15.96	19.20
MRC-3-24	2210	0.044	22.18	19.46
MRC-3-25	2232	0.044	25.79	21.77
MRC-3-26	2259	0.044	14.55	20.06
MRC-3-27	2280	0.044	n.a.	18.59
MRC-3-28	2356	0.044	17.72	20.02
MRC-3-29	**2382**	0.044	31.89	22.29
MRC-3-30	**2406**	0.044	20.37	22.61
MRC-3-31	**2425**	0.043	8.79	21.63
MRC-3-32	**2516**	0.044	18.10	23.06
MRC-3-33	**2544**	0.044	27.39	24.60
MRC-3-34	**2570**	0.044	22.88	25.12
MRC-3-35	**2591**	0.044	27.43	22.09
MRC-3-36	**2619**	0.044	19.19	21.13
MRC-3-37	**2692**	0.030	21.87	25.75

Table A.30: Experimental data from the flow-through experiments presented in this thesis. Time periods in bold letters correspond to the considered steady-state (n.a.: not analyzed; b.d.l.: below detection limit).

Sample	Time (h)	flow rate (mL min^{-1})	S	Fe
			μmol L^{-1}	
MRC-4-1	0	0.033	605.27	2174.72
MRC-4-2	50	0.038	159.12	249.62
MRC-4-3	120	0.039	85.84	107.31
MRC-4-4	171	0.039	79.85	85.31
MRC-4-5	215	0.039	49.25	58.39
MRC-4-6	313	0.040	39.15	45.21
MRC-4-7	340	0.039	56.51	43.39
MRC-4-8	384	0.039	42.11	39.23
MRC-4-9	459	0.039	40.13	37.87
MRC-4-10	505	0.039	61.47	44.28
MRC-4-11	551	0.039	42.78	37.75
MRC-4-12	627	0.039	51.13	34.80
MRC-4-13	675	0.039	42.36	34.40
MRC-4-14	718	0.039	45.92	34.27
MRC-4-15	795	0.039	50.61	33.02
MRC-4-16	844	0.039	44.80	33.65
MRC-4-17	887	0.039	49.40	35.42
MRC-4-18	961	0.039	45.49	32.83
MRC-4-19	1006	0.039	43.18	34.44
MRC-4-20	1055	0.035	40.59	33.86
MRC-4-21	1130	0.039	39.11	28.97
MRC-4-22	1177	0.039	42.41	29.72
MRC-4-23	1201	0.039	44.41	30.99
MRC-4-24	1298	0.039	43.01	30.74
MRC-4-25	1347	0.039	44.75	31.78
MRC-4-26	1396	0.039	37.98	27.93
MRC-4-27	1465	0.039	39.11	28.43
MRC-4-28	1509	0.039	43.07	30.92
MRC-4-29	1559	0.039	66.33	53.63
MRC-4-30	1631	0.039	40.26	37.03
MRC-4-31	1656	0.039	36.42	28.49
MRC-4-32	1731	0.039	35.18	27.05
MRC-4-33	1800	0.039	36.11	27.68
MRC-4-34	1848	0.039	35.49	26.66
MRC-4-35	1895	0.039	34.55	26.84
MRC-4-36	1966	0.039	37.36	28.58
MRC-4-37	**2014**	0.039	38.70	30.12
MRC-4-38	**2062**	0.039	42.23	32.62
MRC-4-39	**2134**	0.039	42.91	34.07
MRC-4-40	**2182**	0.039	42.94	32.75
MRC-4-41	**2230**	0.039	37.30	28.58
MRC-4-42	**2304**	0.039	40.20	30.83
MRC-4-43	**2352**	0.039	40.17	31.75

Table A.31: Experimental data from the flow-through experiments presented in this thesis. Time periods in bold letters correspond to the considered steady-state(n.a.: not analyzed; b.d.l.: below detection limit).

Sample	Time (h)	flow rate (mL min^{-1})	S	Fe
			μmol L^{-1}	
MRC-50-1-1	0	0.031	699.49	n.a.
MRC-50-1-2	22	0.037	577.56	n.a.
MRC-50-1-3	99	0.038	201.15	136.53
MRC-50-1-4	147	0.038	172.43	159.80
MRC-50-1-5	190	0.038	151.47	161.58
MRC-50-1-6	265	0.038	138.43	134.50
MRC-50-1-7	310	0.039	129.23	117.92
MRC-50-1-8	358	0.035	132.07	109.72
MRC-50-1-9	437	0.039	115.92	95.79
MRC-50-1-10	481	0.039	112.27	88.90
MRC-50-1-11	505	0.039	110.68	83.63
MRC-50-1-12	602	0.039	111.55	80.04
MRC-50-1-13	650	0.039	109.24	79.32
MRC-50-1-14	700	0.039	108.46	77.21
MRC-50-1-15	768	0.039	111.64	77.60
MRC-50-1-16	813	0.039	110.46	77.83
MRC-50-1-17	862	0.039	105.94	74.86
MRC-50-1-18	935	0.039	98.48	72.59
MRC-50-1-19	960	0.039	98.64	69.94
MRC-50-1-20	1034	0.039	97.05	67.31
MRC-50-1-21	1104	0.039	95.68	67.11
MRC-50-1-22	1152	0.039	93.74	64.49
MRC-50-1-23	1198	0.039	94.80	64.60
MRC-50-1-24	1269	0.039	92.03	63.76
MRC-50-1-25	1318	0.039	98.77	65.75
MRC-50-1-26	1366	0.039	93.12	62.78
MRC-50-1-27	1438	0.039	95.58	62.70
MRC-50-1-28	1485	0.040	92.72	60.91
MRC-50-1-29	1534	0.041	93.09	61.58
MRC-50-1-30	1607	0.041	96.89	63.46
MRC-50-1-31	1656	0.041	104.41	66.80
MRC-50-1-32	1702	0.043	133.88	79.66
MRC-50-1-33	1776	0.033	106.56	70.33
MRC-50-1-34	1824	0.026	133.04	88.65
MRC-50-1-35	1871	0.027	116.32	76.08
MRC-50-1-36	1944	0.027	109.34	70.10
MRC-50-1-37	1990	0.027	107.19	68.29
MRC-50-1-38	2039	0.027	109.31	65.91
MRC-50-1-39	2112	0.028	111.46	66.67
MRC-50-1-40	**2160**	0.028	109.77	65.38
MRC-50-1-41	**2208**	0.028	111.64	66.38
MRC-50-1-42	**2280**	0.028	108.99	64.37
MRC-50-1-43	**2331**	0.028	107.93	63.52
MRC-50-1-44	**2376**	0.028	109.96	63.32
MRC-50-1-45	**2451**	0.028	109.03	63.26

Table A.32: Experimental data from the flow-through experiments presented in this thesis. Time periods in bold letters correspond to the considered steady-state (n.a.: not analyzed; b.d.l.: below detection limit).

Sample	Time (h)	flow rate (mL min^{-1})	S	Fe
			μmol L^{-1}	
MRC-50-2-1	0	0.033	1057.2	3011.91
MRC-50-2-2	23	0.038	219.8	609.54
MRC-50-2-3	100	0.039	125.9	268.42
MRC-50-2-4	148	0.039	125.2	237.44
MRC-50-2-5	192	0.039	102.7	181.57
MRC-50-2-6	288	0.040	89.0	143.06
MRC-50-2-7	336	0.039	87.6	128.64
MRC-50-2-8	455	0.039	85.9	116.88
MRC-50-2-9	502	0.039	87.6	110.77
MRC-50-2-10	600	0.039	91.3	109.21
MRC-50-2-11	649	0.039	93.4	106.40
MRC-50-2-12	696	0.039	90.4	104.38
MRC-50-2-13	768	0.039	89.8	101.37
MRC-50-2-14	816	0.039	93.5	100.83
MRC-50-2-15	864	0.039	96.6	97.88
MRC-50-2-16	939	0.039	91.2	97.34
MRC-50-2-17	988	0.039	93.5	97.14
MRC-50-2-18	1035	0.039	95.0	94.85
MRC-50-2-19	1105	0.039	97.2	105.99
MRC-50-2-20	1155	0.035	103.4	108.89
MRC-50-2-21	1202	0.039	101.4	107.98
MRC-50-2-22	1274	0.039	110.1	123.00
MRC-50-2-23	1321	0.039	112.6	136.11
MRC-50-2-24	1371	0.039	108.9	131.86
MRC-50-2-25	1441	0.039	108.7	125.22
MRC-50-2-26	1489	0.039	116.7	115.22
MRC-50-2-27	1538	0.039	115.2	110.21
MRC-50-2-28	**1610**	0.039	108.1	104.14
MRC-50-2-29	**1658**	0.039	109.3	104.96
MRC-50-2-30	**1705**	0.039	108.6	100.36
MRC-50-2-31	**1778**	0.039	106.1	98.85
MRC-50-2-32	**1826**	0.039	103.7	96.96
MRC-50-2-33	**1873**	0.039	107.7	97.83
MRC-50-2-34	**1946**	0.039	108.2	102.47

Table A.33: Experimental data from the flow-through experiments presented in this thesis. Time periods in bold letters correspond to the considered steady-state (n.a.: not analyzed; b.d.l.: below detection limit).

Sample	Time (h)	flow rate (mL min^{-1})	S	Fe
			μmol L^{-1}	
MRC-70-1-1	0	0.033	2103.79	3262.31
MRC-70-1-2	25	0.035	272.56	369.02
MRC-70-1-3	72	0.034	111.46	122.38
MRC-70-1-4	141	0.037	99.95	112.00
MRC-70-1-5	196	0.036	117.10	126.30
MRC-70-1-6	243	0.036	114.36	108.88
MRC-70-1-7	315	0.036	107.68	96.45
MRC-70-1-8	363	0.036	129.76	110.76
MRC-70-1-9	408	0.032	153.99	123.80
MRC-70-1-10	483	0.035	62.37	38.14
MRC-70-1-11	527	0.037	95.55	70.99
MRC-70-1-12	580	0.036	120.84	67.04
MRC-70-1-13	**670**	0.036	116.70	55.97
MRC-70-1-14	**747**	0.036	106.25	53.59
MRC-70-1-15	**838**	0.037	129.51	65.28
MRC-70-1-18	**1083**	0.037	109.24	50.24
MRC-70-1-19	**1180**	0.037	120.97	57.10

Table A.34: Experimental data from the flow-through experiments presented in this thesis. Time periods in bold letters correspond to the considered steady-state (n.a.: not analyzed; b.d.l.: below detection limit).

Sample	Time (h)	flow rate (mL min^{-1})	S	Fe
			μmol L^{-1}	
MRC-5-1-a	0	0.025	222.20	297.76
MRC-5-2-a	54	0.018	110.30	157.33
MRC-5-3-a	95	0.052	24.50	40.16
MRC-5-4-a	167	0.048	21.43	34.75
MRC-5-5-a	213	0.045	19.59	29.65
MRC-5-6-a	262	0.048	17.69	25.03
MRC-5-7-a	333	0.043	18.83	26.93
MRC-5-8-a	384	0.048	19.86	27.11
MRC-5-9-a	406	0.048	18.04	25.82
MRC-5-10-a	430	0.048	18.38	25.64
MRC-5-11-a	502	0.047	19.42	27.66
MRC-5-12-a	526	0.047	16.71	23.53
MRC-5-13-a	549	0.048	16.76	22.67
MRC-5-14-a	579	0.047	17.72	23.31
MRC-5-15-a	606	0.026	17.72	23.31
MRC-5-16-a	676	0.071	21.68	27.31
MRC-5-17-a	723	0.046	16.85	23.03
MRC-5-18-a	749	0.045	14.84	21.25
MRC-5-19-a	773	0.045	16.31	21.20
MRC-5-20-a	845	0.046	16.14	20.97
MRC-5-21-a	870	0.042	16.42	20.39
MRC-5-22-a	918	0.095	15.44	18.35
MRC-5-23-a	**940**	0.044	13.32	16.91
MRC-5-24-a	**1013**	0.044	14.06	17.31
MRC-5-25-a	**1036**	0.044	13.97	16.77
MRC-5-26-a	**1060**	0.045	13.78	16.42
MRC-5-27-a	**1080**	0.044	12.54	15.92
MRC-5-28-a	**1102**	0.053	13.16	16.06
MRC-5-29-a	**1165**	0.029	13.43	16.64
MRC-5-30-a	**1201**	0.044	13.65	16.24
MRC-5-31-a	**1221**	0.044	12.13	14.30
MRC-5-32-a	1246	0.045	12.40	15.67
MRC-5-33-a	1269	0.044	11.59	14.69
MRC-5-1-b	1342	0.043	11.29	13.38
MRC-5-2-b	1368	0.045	5.29	7.41
MRC-5-3-b	**1391**	0.046	b.d.l.	4.32
MRC-5-4-b	**1414**	0.045	3.85	4.03
MRC-5-5-b	**1437**	0.045	3.77	4.61
MRC-5-6-b	**1510**	0.041	6.43	7.01
MRC-5-7-b	**1536**	0.045	7.16	8.28
MRC-5-8-b	**1557**	0.049	4.68	6.60
MRC-5-9-b	**1581**	0.045	3.41	4.57
MRC-5-10-b	**1605**	0.044	b.d.l.	3.83

Table A.35: Experimental data from the flow-through experiments presented in this thesis. Time periods in bold letters correspond to the considered steady-state (n.a.: not analyzed; b.d.l.: below detection limit)..

Sample	Time (h)	flow rate (mL min^{-1})	S	Fe
			μmol L^{-1}	
MRC-6-1-a	0	0.020	1790.99	n.a.
MRC-6-2-a	54	0.048	605.31	n.a.
MRC-6-3-a	95	0.048	203.74	n.a.
MRC-6-4-a	167	0.048	104.35	n.a.
MRC-6-5-a	213	0.045	65.30	31.34
MRC-6-6-a	262	0.055	52.77	28.43
MRC-6-7-a	333	0.043	35.74	29.12
MRC-6-8-a	384	0.058	38.86	33.12
MRC-6-9-a	406	0.060	88.94	34.18
MRC-6-10-a	430	0.060	160.64	56.07
MRC-6-11-a	502	0.059	150.53	56.20
MRC-6-12-a	526	0.059	126.52	49.37
MRC-6-13-a	549	0.061	121.94	51.52
MRC-6-14-a	579	0.061	116.29	52.02
MRC-6-15-a	606	0.063	108.46	54.51
MRC-6-16-a	**676**	0.047	109.40	66.52
MRC-6-17-a	**723**	0.063	85.54	60.78
MRC-6-18-a	**749**	0.057	84.08	63.90
MRC-6-19-a	**773**	0.033	140.27	63.00
MRC-6-20-a	**845**	0.060	71.88	64.24
MRC-6-21-a	**870**	0.057	80.12	73.75
MRC-6-22-a	894	0.050	79.18	77.12
MRC-6-1-b	1269	0.034	51.08	64.77
MRC-6-2-b	**1300**	0.080	10.01	23.77
MRC-6-3-b	**1368**	0.085	10.97	22.82
MRC-6-4-b	**1391**	0.084	9.18	20.06
MRC-6-5-b	**1414**	0.084	11.30	16.79
MRC-6-6-b	**1509**	0.084	10.32	18.23

Table A.36: Experimental data from the flow-through experiments presented in this thesis. Time periods in bold letters correspond to the considered steady-state (n.a.: not analyzed; b.d.l.: below detection limit).

Sample	Time (h)	flow rate (mL min^{-1})	S	Fe
			$\mu mol\ L^{-1}$	
MRC-25-7-1	0	0.033	6.51	2.31
MRC-25-7-2	24	0.033	6.62	2.28
MRC-25-7-3	48	0.033	5.06	2.03
MRC-25-7-4	120	0.033	4.32	2.20
MRC-25-7-5	144	0.033	3.55	2.60
MRC-25-7-6	167	0.033	3.46	3.13
MRC-25-7-7	192	0.033	3.25	4.02
MRC-25-7-8	216	0.033	3.18	7.21
MRC-25-7-9	307	0.033	b.d.l.	8.06
MRC-25-7-10	336	0.033	b.d.l.	6.73
MRC-25-7-11	360	0.033	b.d.l.	6.95
MRC-25-7-12	383	0.033	b.d.l.	6.14
MRC-25-7-13	456	0.032	b.d.l.	6.27
MRC-25-7-14	480	0.033	b.d.l.	6.51
MRC-25-7-15	504	0.033	b.d.l.	6.75
MRC-25-7-16	528	0.030	b.d.l.	6.47
MRC-25-7-21	720	0.035	7.54	11.77
MRC-25-7-22	792	0.034	b.d.l.	14.37
MRC-25-7-23	816	0.034	8.07	12.69
MRC-25-7-24	840	0.034	b.d.l.	11.00
MRC-25-7-25	864	0.034	b.d.l.	13.84
MRC-25-7-26	958	0.034	b.d.l.	6.97
MRC-25-7-27	984	0.033	4.65	7.69
MRC-25-7-28	1008	0.033	b.d.l.	7.76
MRC-25-7-29	**1033**	0.033	b.d.l.	9.14
MRC-25-7-30	**1054**	0.033	b.d.l.	6.79
MRC-25-7-32	**1157**	0.030	b.d.l.	5.65
MRC-25-7-33	**1180**	0.033	b.d.l.	6.75
MRC-25-7-34	**1199**	0.033	b.d.l.	5.37
MRC-25-7-35	**1290**	0.033	b.d.l.	5.65

Table A.37: Experimental data from the flow-through experiments presented in this thesis. Time periods in bold letters correspond to the considered steady-state (n.a.: not analyzed; b.d.l.: below detection limit).

Sample	Time (h)	flow rate (mL min^{-1})	S	Fe
			μmol L^{-1}	
MRC-8-1	0	0.057	6749	307.25
MRC-8-2	13	0.032	5972	319.25
MRC-8-3	165	0.034	5956	264.82
MRC-8-4	190	0.034	5985	177.48
MRC-8-5	309	0.025	5900	160.16
MRC-8-6	357	0.034	5891	135.51
MRC-8-7	429	0.034	5841	126.57
MRC-8-8	477	0.034	5844	119.23
MRC-8-9	525	0.034	5844	110.46
MRC-8-10	597	0.033	5844	109.22
MRC-8-11	620	0.033	5844	107.32
MRC-8-12	646	0.033	5844	101.38
MRC-8-13	693	0.033	5844	98.64
MRC-8-14	772	0.033	5844	94.22
MRC-8-15	813	0.033	5844	97.19
MRC-8-16	861	0.033	5844	91.39
MRC-8-17	**932**	0.033	5844	90.08
MRC-8-18	**981**	0.033	5844	91.39
MRC-8-19	**1030**	0.033	5844	85.32
MRC-8-20	**1105**	0.033	5844	87.11
MRC-8-21	**1149**	0.033	5844	86.71
MRC-8-22	**1197**	0.033	5844	86.12
MRC-8-23	**1268**	0.033	5844	84.55
MRC-8-24	**1317**	0.033	5844	84.30
MRC-8-25	**1364**	0.033	5844	84.64

Table A.38: Experimental data from the flow-through experiments presented in this thesis. Time periods in bold letters correspond to the considered steady-state (n.a.: not analyzed; b.d.l.: below detection limit).

Sample	Time (h)	flow rate (mL min^{-1})	S	Fe
			μmol L^{-1}	
MRC-9-1	0	0.041	37578.74	1741.45
MRC-9-2	32	0.031	37578.74	209.38
MRC-9-3	184	0.033	37578.74	175.60
MRC-9-4	209	0.020	37578.74	171.41
MRC-9-5	328	0.023	37578.74	183.12
MRC-9-6	376	0.033	37578.74	141.22
MRC-9-7	448	0.033	37578.74	123.49
MRC-9-8	496	0.033	37578.74	120.54
MRC-9-9	544	0.033	37578.74	116.51
MRC-9-10	616	0.033	37578.74	109.85
MRC-9-11	639	0.033	37578.74	109.79
MRC-9-12	665	0.032	37578.74	124.62
MRC-9-13	712	0.033	37578.74	106.62
MRC-9-14	791	0.032	37578.74	103.78
MRC-9-15	832	0.032	37578.74	100.72
MRC-9-16	879	0.021	37578.74	100.93
MRC-9-17	951	0.023	37578.74	129.88
MRC-9-18	999	0.032	37578.74	93.84
MRC-9-19	**1049**	0.032	37578.74	88.74
MRC-9-20	**1124**	0.032	37578.74	85.46
MRC-9-21	**1168**	0.032	37578.74	86.80
MRC-9-22	**1216**	0.032	37578.74	88.42
MRC-9-23	**1287**	0.032	37578.74	89.96
MRC-9-24	**1336**	0.032	37578.74	85.94
MRC-9-25	**1383**	0.032	37578.74	90.24
MRC-9-26	**1456**	0.032	37578.74	86.42
MRC-9-27	**1503**	0.032	37578.74	89.91

Table A.39: Experimental data from the flow-through experiments presented in this thesis. Time periods in bold letters correspond to the considered steady-state (n.a.: not analyzed; b.d.l.: below detection limit).

Sample	Time (h)	flow rate (mL min^{-1})	S	Fe
			μmol L^{-1}	
MRC-10-1	0	0.044	13160.36	295.79
MRC-10-2	32	0.032	2287.16	303.49
MRC-10-3	184	0.034	648.35	215.94
MRC-10-4	209	0.034	233.14	165.57
MRC-10-5	328	0.025	54.33	98.07
MRC-10-6	376	0.034	89.19	132.66
MRC-10-7	448	0.034	72.63	106.02
MRC-10-8	496	0.034	64.18	97.55
MRC-10-9	544	0.034	65.46	100.32
MRC-10-10	616	0.034	63.46	92.69
MRC-10-11	639	0.034	63.46	90.81
MRC-10-12	665	0.034	63.46	88.59
MRC-10-13	712	0.034	63.46	92.62
MRC-10-14	791	0.033	63.46	86.55
MRC-10-15	832	0.034	71.95	85.00
MRC-10-16	879	0.033	69.92	86.00
MRC-10-17	**951**	0.033	65.74	76.83
MRC-10-18	**999**	0.033	67.39	78.55
MRC-10-19	**1049**	0.034	65.93	77.15
MRC-10-20	**1124**	0.033	63.09	72.75
MRC-10-21	**1168**	0.033	68.23	74.09
MRC-10-22	**1216**	0.033	64.84	73.12
MRC-10-23	**1287**	0.033	65.15	72.14
MRC-10-24	**1336**	0.033	68.55	75.34

Table A.40: Experimental data from the flow-through experiments presented in this thesis, (n.a.: not analyzed; b.d.l.: below detection limit).

Sample	Time (h)	flow rate (mL min^{-1})	S	Fe
			mol L^{-1}	
MRC-11-1	0	0.031	409.34	b.d.l.
MRC-11-2	48	0.036	203.09	b.d.l.
MRC-11-3	122	0.034	148.61	b.d.l.
MRC-11-4	167	0.033	130.00	b.d.l.
MRC-11-5	194	0.033	102.99	b.d.l.
MRC-11-6	218	0.032	111.98	b.d.l.
MRC-11-7	292	0.032	112.51	b.d.l.
MRC-11-8	317	0.032	111.14	b.d.l.
MRC-11-9	341	0.032	116.77	b.d.l.
MRC-11-10	364	0.032	103.76	b.d.l.
MRC-11-11	383	0.032	112.57	b.d.l.
MRC-11-12	460	0.032	132.13	b.d.l.
MRC-11-13	481	0.032	113.36	b.d.l.
MRC-11-14	507	0.032	131.43	b.d.l.
MRC-11-15	531	0.032	128.38	b.d.l.
MRC-11-16	555	0.032	108.25	b.d.l.
MRC-11-17	624	0.032	134.30	b.d.l.
MRC-11-18	649	0.032	135.76	b.d.l.
MRC-11-19	676	0.032	122.91	b.d.l.
MRC-11-20	697	0.032	121.62	b.d.l.
MRC-11-21	719	0.031	132.30	b.d.l.
MRC-11-22	818	0.031	118.39	b.d.l.
MRC-11-23	845	0.031	120.20	b.d.l.
MRC-11-24	868	0.031	126.83	b.d.l.
MRC-11-25	889	0.031	140.94	b.d.l.
MRC-11-26	963	0.030	125.23	b.d.l.
MRC-11-27	985	0.031	118.12	b.d.l.
MRC-11-28	1010	0.030	111.62	b.d.l.
MRC-11-29	1033	0.030	105.73	b.d.l.
MRC-11-30	1055	0.030	120.73	b.d.l.
MRC-11-31	1131	0.029	105.01	b.d.l.
MRC-11-32	1153	0.029	94.11	b.d.l.
MRC-11-33	1179	0.029	105.54	b.d.l.
MRC-11-34	1204	0.036	97.74	b.d.l.
MRC-11-35	1223	0.035	80.46	b.d.l.
MRC-11-36	1300	0.035	84.27	b.d.l.
MRC-11-37	1327	0.035	64.17	b.d.l.
MRC-11-38	1348	0.035	66.17	b.d.l.
MRC-11-39	1369	0.038	66.40	b.d.l.
MRC-11-40	1391	0.038	74.30	b.d.l.

Table A.41: Experimental data from the flow-through experiments presented in this thesis, (n.a.: not analyzed; b.d.l.: below detection limit).

Sample	Time (h)	flow rate (mL min^{-1})	S $\mu mol\ L^{-1}$	Fe
MRC-12-1	0	0.027	104.07	b.d.l.
MRC-12-2	18	0.027	145.92	b.d.l.
MRC-12-3	91	0.028	120.13	b.d.l.
MRC-12-4	136	0.028	108.65	b.d.l.
MRC-12-5	185	0.028	104.94	b.d.l.
MRC-12-6	258	0.029	92.18	b.d.l.
MRC-12-7	306	0.028	93.49	b.d.l.
MRC-12-8	354	0.028	86.32	b.d.l.
MRC-12-9	426	0.029	79.87	b.d.l.
MRC-12-10	477	0.029	66.02	b.d.l.
MRC-12-11	522	0.029	64.96	b.d.l.
MRC-12-12	597	0.028	60.16	b.d.l.
MRC-12-13	645	0.028	68.23	b.d.l.
MRC-12-14	688	0.028	54.76	b.d.l.
MRC-12-15	766	0.028	52.67	b.d.l.
MRC-12-16	814	0.029	50.49	b.d.l.
MRC-12-17	858	0.029	40.85	b.d.l.
MRC-12-18	954	0.029	37.73	b.d.l.
MRC-12-19	1002	0.029	37.36	b.d.l.
MRC-12-20	1121	0.029	23.07	b.d.l.
MRC-12-21	1167	0.029	36.49	b.d.l.
MRC-12-22	1266	0.029	35.21	b.d.l.
MRC-12-23	1314	0.029	35.02	b.d.l.
MRC-12-24	1361	0.029	33.56	b.d.l.
MRC-12-25	1434	0.029	31.62	b.d.l.
MRC-12-26	1482	0.021	33.68	b.d.l.
MRC-12-27	1530	0.029	29.41	b.d.l.
MRC-12-28	1605	0.029	29.64	b.d.l.
MRC-12-29	1654	0.029	28.39	b.d.l.
MRC-12-30	1700	0.029	31.81	b.d.l.
MRC-12-31	1771	0.029	32.43	b.d.l.
MRC-12-32	1821	0.029	32.50	b.d.l.
MRC-12-33	1868	0.029	34.99	b.d.l.
MRC-12-34	1940	0.029	29.93	b.d.l.
MRC-12-35	1987	0.029	30.52	b.d.l.
MRC-12-36	2036	0.029	29.95	b.d.l.
MRC-12-37	2106	0.029	31.56	b.d.l.
MRC-12-38	2155	0.029	30.09	b.d.l.
MRC-12-39	2204	0.029	36.67	b.d.l.
MRC-12-40	2276	0.029	35.66	b.d.l.
MRC-12-41	2324	0.029	30.40	b.d.l.
MRC-12-42	2371	0.029	35.55	b.d.l.
MRC-12-43	2444	0.029	29.51	b.d.l.
MRC-12-44	2492	0.029	29.63	b.d.l.
MRC-12-45	2538	0.029	28.50	b.d.l.
MRC-12-46	2611	0.029	25.96	b.d.l.

Table A.42: Experimental data from the flow-through experiments presented in this thesis, (n.a.: not analyzed; b.d.l.: below detection limit).

Sample	Time (h)	flow rate (mL min^{-1})	S	Fe
			μmol L^{-1}	
MRC-14-1	0	0.032	383.27	b.d.l.
MRC-14-2	116	0.034	161.29	b.d.l.
MRC-14-3	161	0.033	138.84	b.d.l.
MRC-14-4	283	0.033	109.43	b.d.l.
MRC-14-5	379	0.033	94.27	b.d.l.
MRC-14-6	451	0.032	85.98	b.d.l.
MRC-14-7	548	0.032	82.58	b.d.l.
MRC-14-8	671	0.034	83.67	b.d.l.
MRC-14-9	791	0.033	75.13	b.d.l.
MRC-14-10	883	0.032	70.45	b.d.l.
MRC-14-11	1027	0.032	65.30	b.d.l.
MRC-14-12	1193	0.032	59.66	b.d.l.
MRC-14-13	1340	0.032	58.01	b.d.l.
MRC-14-14	1459	0.032	52.30	b.d.l.
MRC-14-15	1555	0.031	50.55	b.d.l.
MRC-14-16	1679	0.031	39.73	b.d.l.
MRC-14-17	1796	0.019	49.43	b.d.l.
MRC-14-18	1893	0.032	29.81	b.d.l.
MRC-14-19	2012	0.031	28.22	b.d.l.
MRC-14-20	2131	0.031	27.82	b.d.l.
MRC-14-21	2229	0.031	27.82	b.d.l.
MRC-14-22	2349	0.031	23.40	b.d.l.
MRC-14-23	2396	0.031	24.16	b.d.l.
MRC-14-24	2469	0.031	24.10	b.d.l.
MRC-14-25	2517	0.031	23.26	b.d.l.
MRC-14-26	2564	0.031	26.45	b.d.l.
MRC-14-27	2637	0.031	53.84	b.d.l.
MRC-14-28	2686	0.031	28.03	b.d.l.
MRC-14-29	2733	0.031	31.93	b.d.l.
MRC-14-30	2802	0.030	29.12	b.d.l.
MRC-14-31	2857	0.031	31.13	b.d.l.
MRC-14-32	2904	0.031	29.63	b.d.l.
MRC-14-33	2976	0.031	26.71	b.d.l.
MRC-14-34	3025	0.031	18.91	b.d.l.
MRC-14-35	3069	0.031	22.08	b.d.l.
MRC-14-36	3144	0.031	21.18	b.d.l.
MRC-14-37	3187	0.031	20.13	b.d.l.
MRC-14-38	3241	0.031	16.18	b.d.l.
MRC-14-39	3331	0.031	13.92	b.d.l.